General Disclaimer

One or more of the Following Statements may affect this Document

- This document has been reproduced from the best copy furnished by the organizational source. It is being released in the interest of making available as much information as possible.

- This document may contain data, which exceeds the sheet parameters. It was furnished in this condition by the organizational source and is the best copy available.

- This document may contain tone-on-tone or color graphs, charts and/or pictures, which have been reproduced in black and white.

- This document is paginated as submitted by the original source.

- Portions of this document are not fully legible due to the historical nature of some of the material. However, it is the best reproduction available from the original submission.

REPORT NO. 4428
COPY NO. 22

Hydraulic Fluid Interaction Servovalve

by

T.A. Phillips and A. Blatter

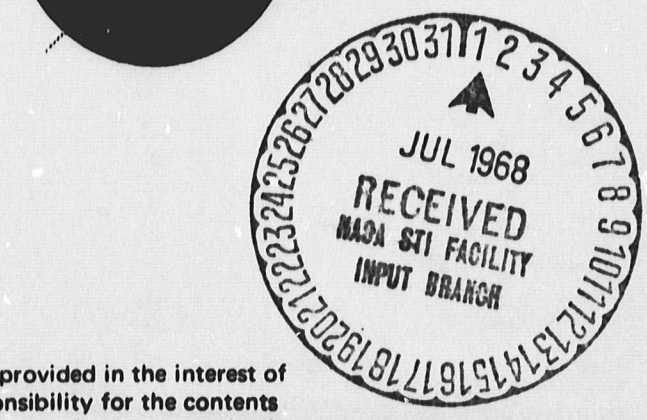

Prepared Under Contract No. NAS 8–11928

NATIONAL AERONAUTICS AND SPACE ADMINISTRATION

Bendix

Research Laboratories

Report No. 4428

Hydraulic Fluid Interaction Servovalve

by

T. A. Phillips and A. Blatter

Prepared Under Contract No. NAS 8–11928

NATIONAL AERONAUTICS AND SPACE ADMINISTRATION

Submitted to:

National Aeronautics and Space Administration
Marshall Space Flight Center
Huntsville, Alabama

Bendix
Research
Laboratories

TABLE OF CONTENTS

LIST OF ILLUSTRATIONS

LIST OF TABLES

HYDRAULIC FLUID INTERACTION SERVOVALVE

By T. A. Phillips and A. Blatter
Bendix Research Laboratories

SUMMARY

This program demonstrated the feasibility of using fluidic vortex valves as the fluid control elements in a hydraulic servoactuator control system. The vortex valves were incorporated into a completely new servovalve concept and physically designed into a package interchangeable with an existing spool-type servovalve. The vortex servovalve offers the advantages of lower cost because of few precision parts and good contamination tolerance due to large flow channels. In addition, the vortex valve has significantly different dynamic characteristics than spool-type servovalves. Analysis has shown that the dynamic pressure feedback compensation now required with some engine gimbaling servoactuators may not be required if a vortex servovalve is used. High flow consumption of the vortex servovalve is compatible with recent trends toward using fuel as the hydraulic servosystem fluid.

Two vortex servovalves, as shown in Figure 1, were fabricated and delivered to the National Aeronautics and Space Administration - Marshall Space Flight Center under Contract NAS8-11928.

The development effort started with basic testing and improvement of the vortex valve. This resulted in a vortex valve momentum efficiency increase of 2 to 1. Configuration variations of the basic vortex valve were evaluated (the double outlet and the radial flow vortex valves) and demonstrated good performance. Detailed circuit analysis was performed in order to define the optimum pilot stage and fluidic element configurations. This analysis indicated the need for improving the vortex valve performance in order to reduce the pilot stage torque motor input power and size requirements. A very high gain reverse-flow flapper-nozzle pilot stage design concept was employed to further reduce the torque motor power and size. This approach led to a pilot stage stability problem.

Hydraulic circuit analysis of the basic servovalve system indicated performance that would adequately surround actual flight loading performance requirements. Servovalve power stage flow-trimming and performance tests were successfully carried out. Pilot stage test results indicated the presence of a dynamic instability. Supported by analysis and test, all feasible modifications to the pilot stage hardware were tested and evaluated but the instability remained.

The power stage of the servovalve and a simulated pilot stage were assembled on the Saturn SI-B servoactuator supplied by NASA. A Bendix servovalve was used as a convenient means of pilot stage flow control. The actuator could be smoothly and accurately stroked. The tests definitely showed the feasibility of employing two vortex valves in a push-pull configuration.

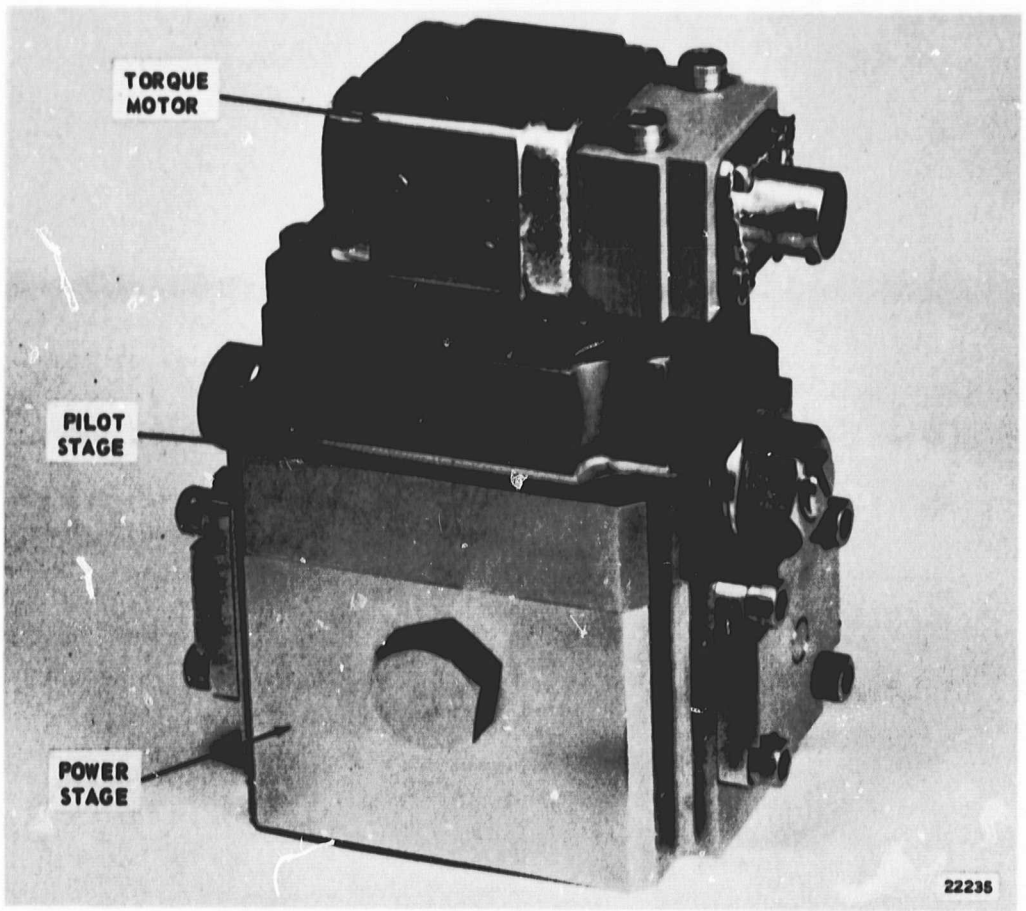

Figure 1 - Hydraulic Vortex Servovalve

One area of potential application of the hydraulic vortex servovalve is in a gimbaling system where the rocket fuel is used for the hydraulic fluid. The corrosion and contamination problems of such a system could be more readily handled with a no-moving part servovalve. Since fuel flow from the actuator returns to the large volume fuel system rather than a servosystem reservoir, heat rejection is not a problem. Furthermore, the higher input electrical power requirements of advanced servoactuators will reduce the high pilot stage power gain requirement.

In summary, this program demonstrated that the hydraulic vortex servovalve offers significant advantages over conventional spool-type servovalves. This program has advanced the development of the basic fluidic vortex valve elements and the understanding of their physical implementation in hydraulic circuitry.

INTRODUCTION

Background and Objectives

In a rocket vehicle flight control system, the thrust vector is commonly controlled by gimbaling the entire rocket engine with hydraulic servoactuators. The spool-type electrohydraulic servovalve is a precision component which is expensive to fabricate and very sensitive to hydraulic contamination and environmental conditions. The application of fluidic control (no-moving part) technology to the hydraulic servovalve offers the potential of increased reliability, nonelectrical signal summing and fabrication cost reduction. The objective of this program was the development of a hydraulic servovalve utilizing the vortex amplifier as the primary flow control element and evaluating its performance on a typical rocket engine gimbaling servoactuator.

Vortex Valve Description

The vortex valve is unique among fluidic control elements in that it is capable of throttling flow, whereas most of the elements function only as flow diverters. The control action is produced by interaction between a properly introduced control flow and the supply flow. A schematic of a vortex valve and its characteristics is shown in Figure 2. The main supply flow is introduced radially into the cylindrical chamber. In the absence of control flow, the main flow proceeds radially toward the center outlet, and the limiting restriction that establishes maximum flow is the outlet orifice at the center of the chamber.

Adding control flow imparts a rotational flow component to the supply flow as it passes the control injector. The flow entering the vortex chamber then has a tangential velocity component in addition to the radial component. As the flow proceeds toward the center of the valve, conservation of its angular momentum causes the tangential velocity to increase. This substantial buildup in tangential velocity of the fluid causes a centrifugal pressure buildup across the vortex flow field in a radial direction. This pressure buildup opposes the incoming supply flow and provides the means for modulating the supply flow.

The strength of the vortex flow field, which is a function of control flow, produces a valving characteristic; i.e., an increase in control flow causes a reduction in total valve flow.

The elementary configuration, shown in Figure 2, is not the most effective vortex valve design. In the configuration shown in Figure 3, the supply flow, instead of being admitted to the vortex chamber at one location, is introduced through an annular slot at the periphery of the chamber. This configuration provides a uniform sheet of supply fluid, allowing the introduction of the control flow at several points. This

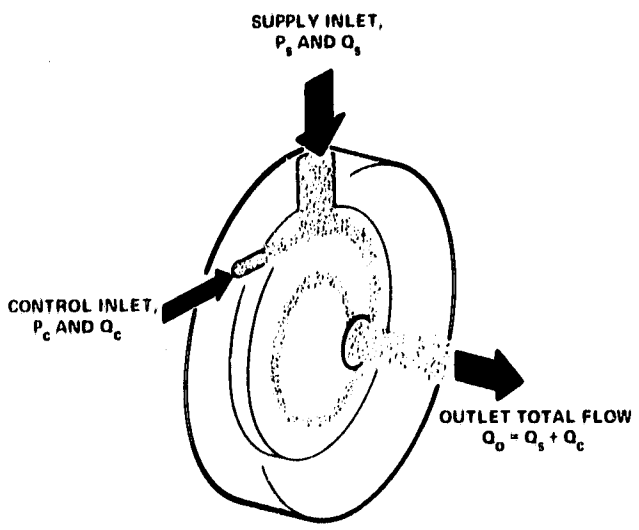

BASIC VORTEX VALVE

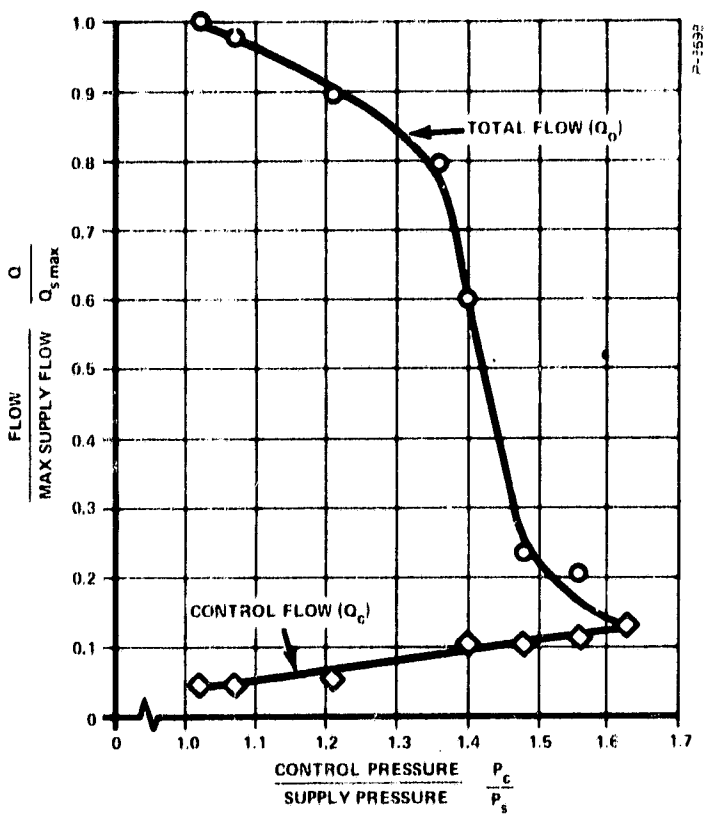

VORTEX VALVE TURNDOWN CHARACTERISTICS

Figure 2 - Vortex Valve Concept

results in a more uniform momentum exchange of the control and supply flows, and in better vortex valve performance.

The vortex valve will operate with any type of fluid. It has been used with gases, hydraulic fluids, liquid metals, liquid propellants, and water. It has been built in sizes ranging from 0.072-inch chamber diameter up to 9 inches.

The basic vortex valve has a typical flow modulation range of 4:1 to 10:1. One of the major developments in the vortex valve investigation was the addition of a flow pickoff to the vortex amplifier. This is shown in Figure 4. It is a simple tubular flow receiver located concentric to the vortex valve outlet hole. With no control flow to the vortex valve, the flow exiting from the vortex chamber is a well-defined jet. This flow is recovered in the flow pickoff. The recovery characteristic is similar to that achieved with a conventional jet pipe valve. When a control flow is introduced into the vortex chamber, it induces a vortex flow field. The flow leaving the vortex chamber now assumes a hollow conical shape resulting from the tangential flow momentum. This cone of fluid impinges on the flow pickoff, and some is diverted to exhaust. Thus, the pickoff increases valve modulation since the introduction of control flow not only lowers total flow but causes only part of this total flow to pass through the pickoff.

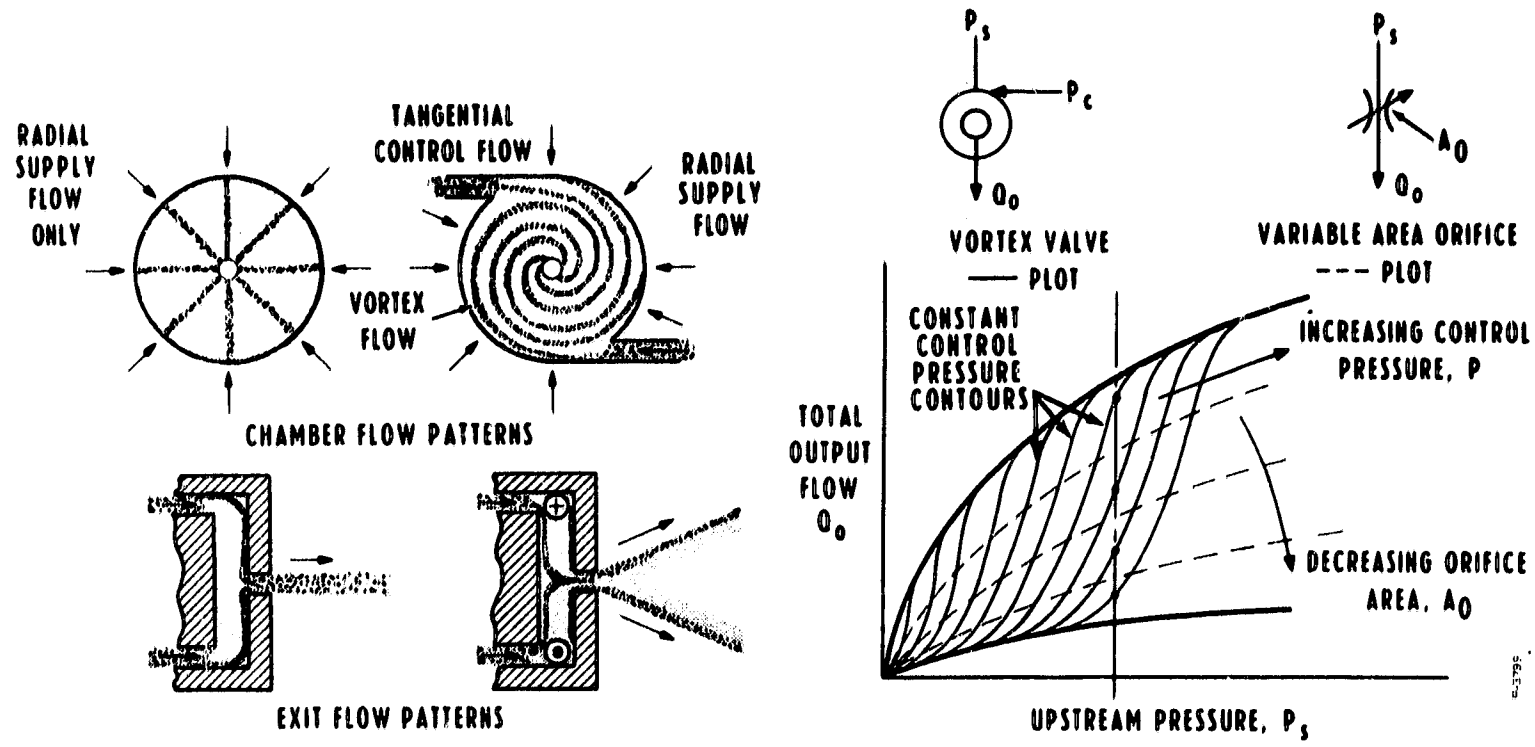

Figure 3 - Vortex Valve Configuration

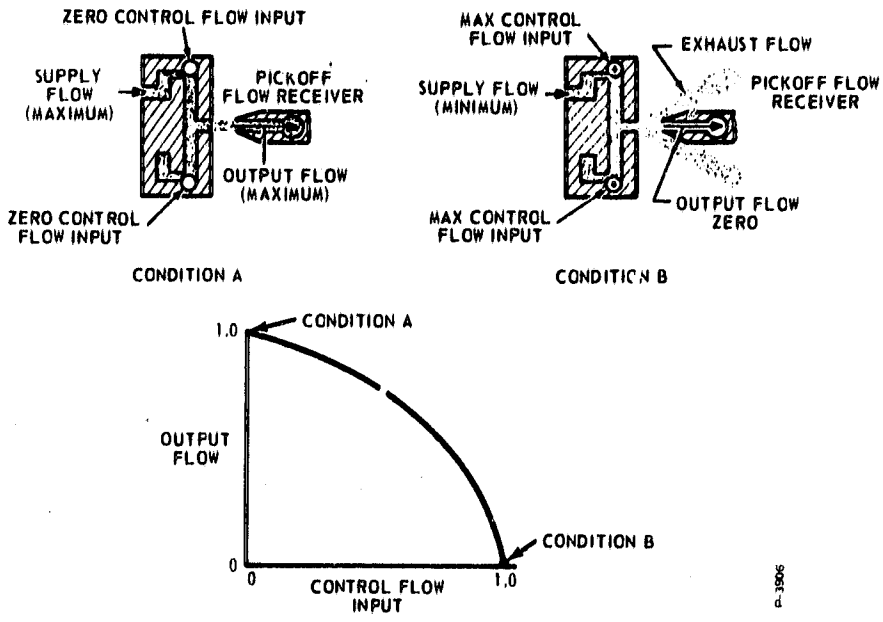

Figure 4 - Vortex Valve with Flow Pickoff

When the control flow is increased further, the cone widens and more of the exiting flow is directed past the pickoff to exhaust. Finally, if the control flow is increased enough, it will cause all of the flow to miss the pickoff. This then produces a valving action with full modulation of flow to zero. The flow pickoff can be connected to a load and back-pressured to develop a pressure-flow characteristic of the load.

Summary of Specifications

The following is a summary of the performance specifications for the hydraulic vortex servovalve:

Fluid Medium	Hydraulic Oil, MIL-H-5606
Supply Pressure	3000 psig
Maximum Flow (3000 psi valve drop)	16.8 $\pm$ 1.6 gpm
Ambient Temperature	0 to 150°F
Differential Current	$\pm$12 ma
Quiescent Current	6 ma
Threshold	0.15 ma
Hysteresis	0.30 ma
Null Shift (3000 $\pm$ 300 psi)	0.36 ma
Vibration	$\pm$6 g
Shock	40 g
Altitude	300,000 ft

HYDRAULIC VORTEX SERVOVALVE CONCEPT, DESIGN, AND PERFORMANCE

The hydraulic vortex servovalve developed during this program consists of a torque motor-driven reversed-flow flapper-nozzle pilot stage providing control flow to two vortex valves which comprise the servovalve power stage. The power stage vortex valves are arranged in a push-pull configuration and incorporate flow receivers to provide full range modulation of actuator flow.

The servovalve hydraulic circuit schematic is shown in Figure 5. The reversed-flow flapper-nozzle valve operates with the flapper-nozzle cavity at the supply pressure level. The flow direction in the nozzles is the opposite of conventional flapper-nozzle flow, and the flapper nozzle becomes the variable upstream orifice of the pilot stage. With this arrangement, the pressures in the nozzles vary with flapper position in such a way that the hydraulic pressure force on the flapper acts like a negative rate spring. By carefully balancing this negative hydraulic

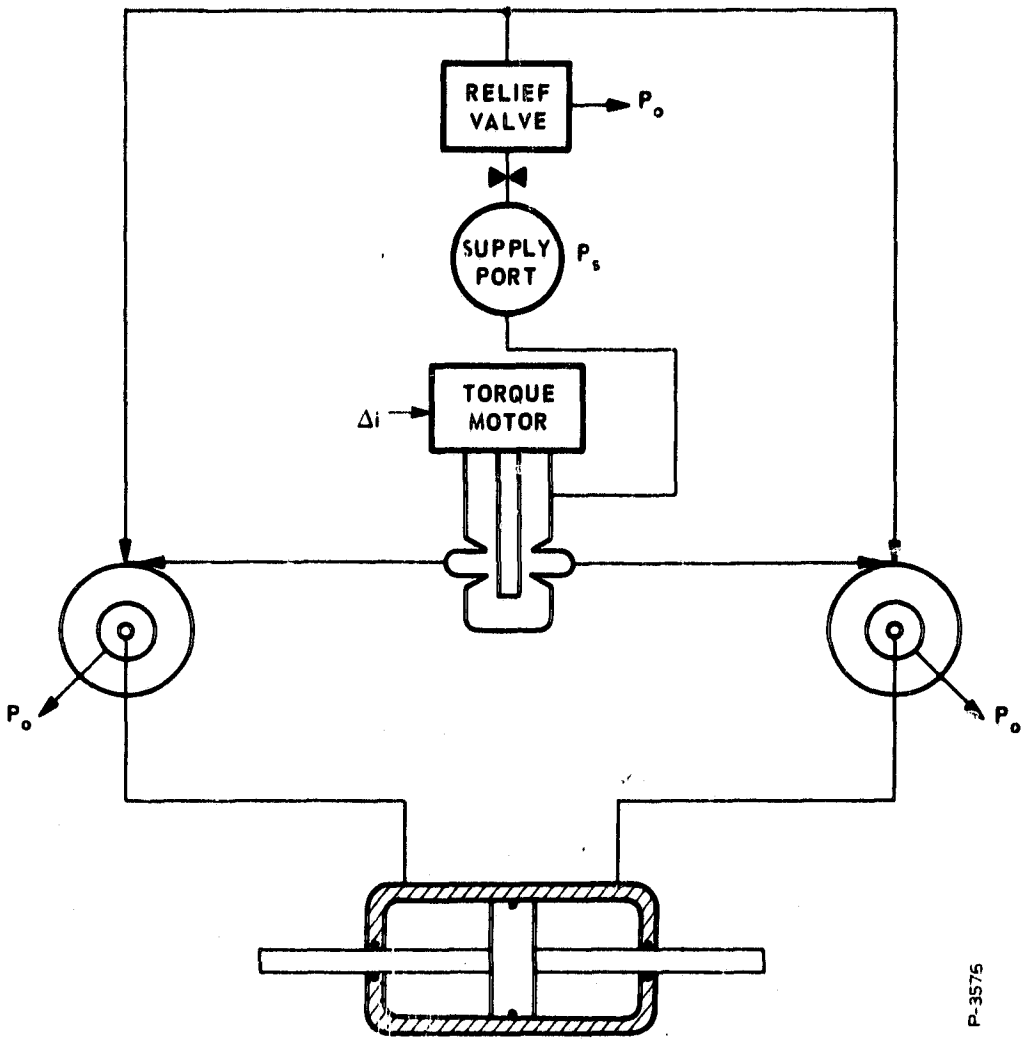

Figure 5 - Hydraulic Circuit Concept for Vortex Servovalve

spring rate with the positive mechanical rates of the torque motor-flapper system, the potential of a lower power torque motor is realized. Furthermore, all of the pilot stage flow enters the vortex valves and none is bled off to the reservoir. By appropriately setting the flapper-nozzle clearance at null, the vortex valves may be readily turned down any desired amount; thus, some control of quiescent flow is possible. This permits the reduction of pump flow requirements and continuous energy dissipation as heat. With the reversed-flow flapper-nozzle system, then, the pilot stage flow and torque motor input power and size requirements could be satisfied.

The power stage, shown schematically in Figure 5, consists of two single outlet vortex valves with integral flow receivers. The output of each flow receiver is channeled to the cylinder ports of the hydraulic actuator. With the pilot stage in the null condition, equal flow passes through the two vortex valves. Under this condition, the flow receivers recover equal pressure and no actuator force is obtained. The pressure level in the flow receivers is a function of the vorticity obtained for the null flapper-nozzle setting. When a differential current is applied to the torque motors, the resultant flapper motion causes an increase in control pressure to one of the vortex valves and a decrease in control pressure to the other vortex valve. With the increase in control pressure, there is a corresponding decrease in recovered presure and flow in the flow receiver. At the same time, the decrease in control pressure in the other vortex valve results in an increase of recovered pressure and flow. A pressure differential is established across the actuator position and a load force is developed. This force can result in motion which draws fluid from one flow receiver and pumps it out through the other flow receiver to return. The flow receiver diameter must be properly sized to provide good flow and pressure recovery characteristics in the normal flow direction while minimizing flow impedance when the flow is reversed. The optimum ratio of flow receiver diameter to vortex valve outlet hole diameter to satisfy this requirement has been established by test to be 1.5.

Figure 6 is a layout drawing of the hydraulic fluidic servovalve. As shown, the pilot and power stage assemblies are individual "modules" which can be tested and modified individually prior to final assembly and test of the complete servovalve.

The pilot stage is designed with adjustable nozzles for setting the null control pressures. A round cantilever spring device is attached to the torque motor output shaft. The diameter and effective length of this device are carefully machined to provide a known positive mechanical spring rate. This positive spring rate combines with the negative hydraulic rate of the flapper-nozzle system to provide a small net positive rate load which can be driven by the torque motor.

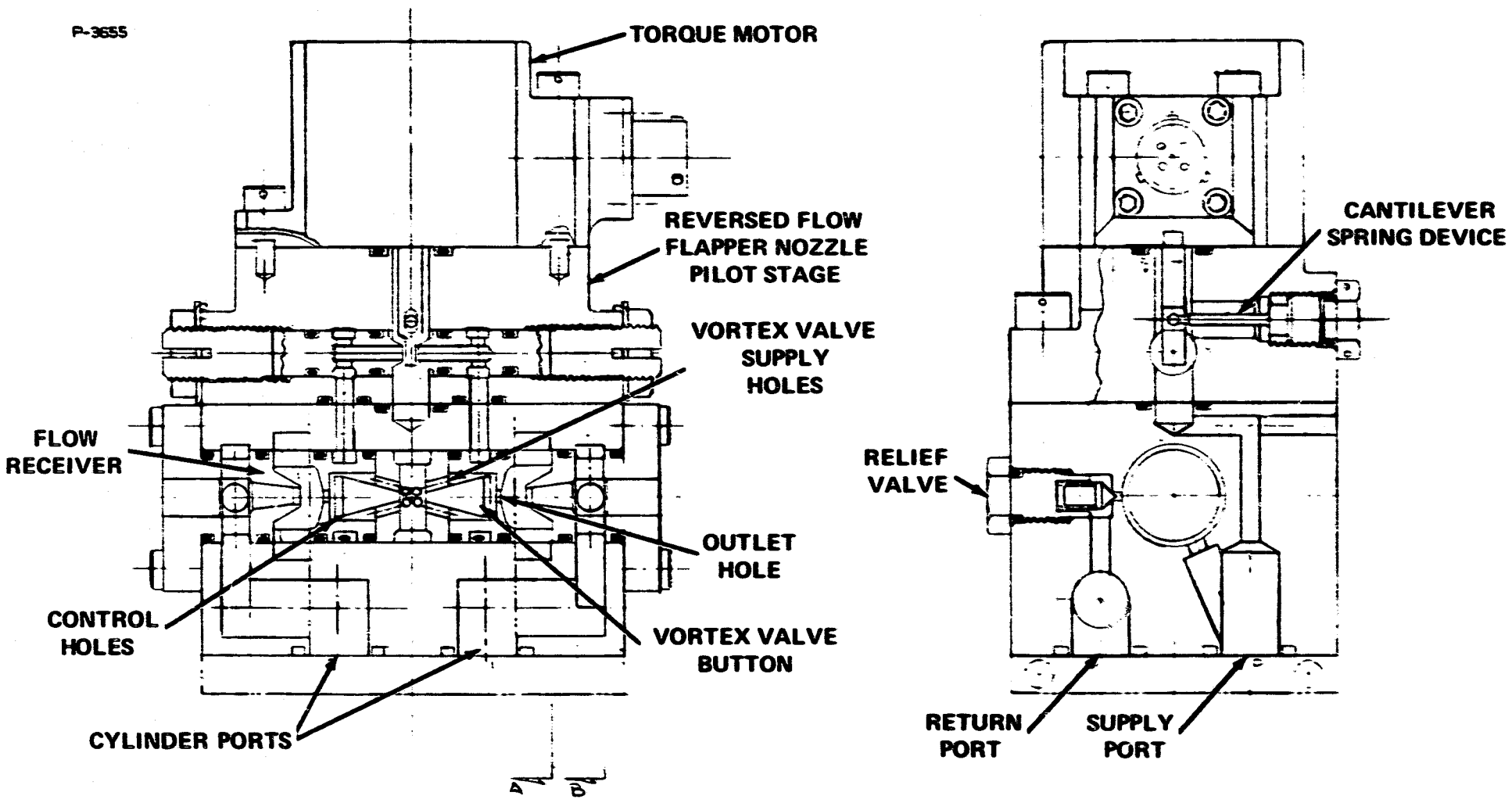

Figure 6 - Hydraulic Fluidic Servovalve

The two power stage vortex valves are placed end-to-end in the power stage body. Supply flow enters each vortex valve through six drilled passages connecting the vortex chamber to a centrally located supply annulus. After passing over the vortex valve button, where control flow is admitted through four tangential holes, the hydraulic fluid exits through the outlet hole. The amount of control flow injected determines the amount of flow recovered in the flow receiver. The receiver flow is then channeled to the actuator cylinder ports. The power stage body was made up of five separate plates which were stacked and copper-brazed together to form the final assembly. Prior to brazing, simple milling operations were used to form communication channels in each plate. In this manner, large area channeling could be obtained without exceeding the space limitations of the servoactuator package.

Figure 7 shows the complete servovalve assembly. The disassembled pilot and power stage assemblies are shown in Figures 8 and 9. Figure 10 shows the two power stage vortex valve assemblies.

Functional testing of the servovalve included performance tests and optimization of the power stage vortex valves. All of the units were designed to have matched performance but some rework was required to bring the performance in line with predicted results. Final turndown performance for all the vortex valves is shown in Figures 11 through 14. The control port flow coefficient was maximized in the final design in

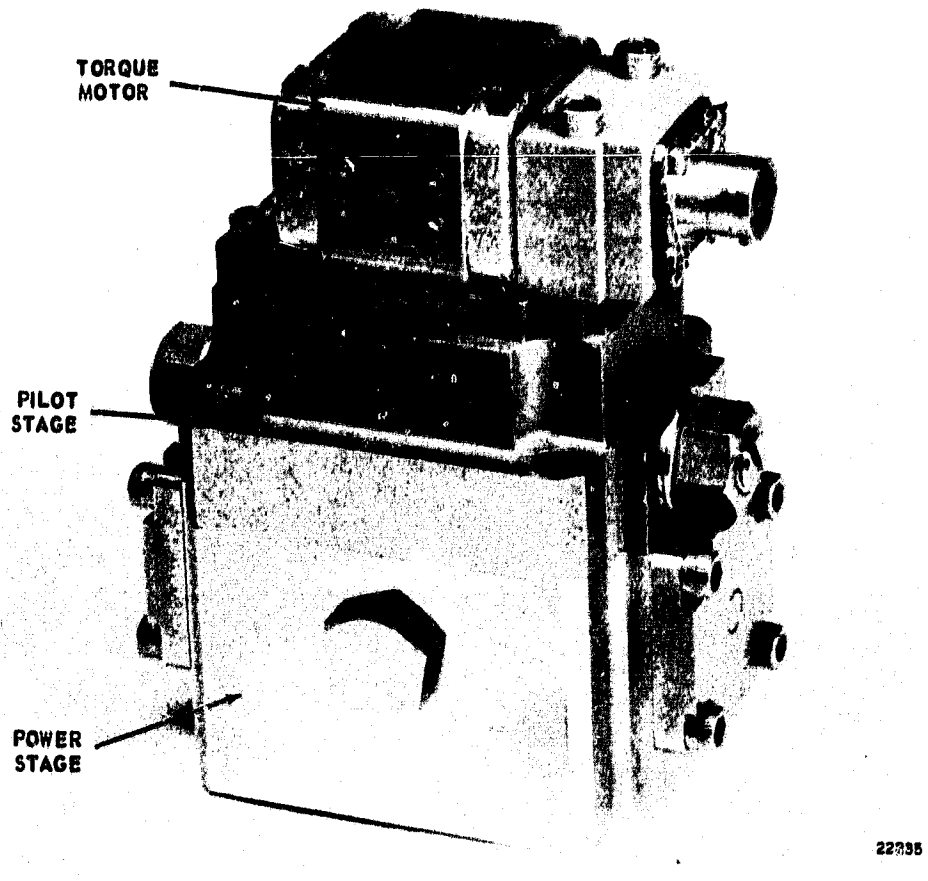

Figure 7 - Hydraulic Vortex Servovalve

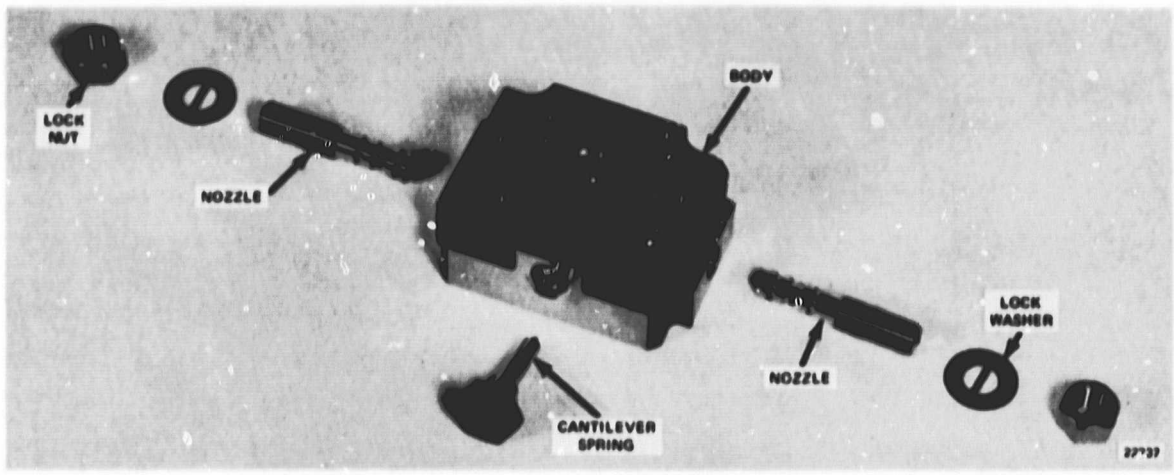

Figure 8 - Pilot Stage - Hydraulic Vortex Servovalve

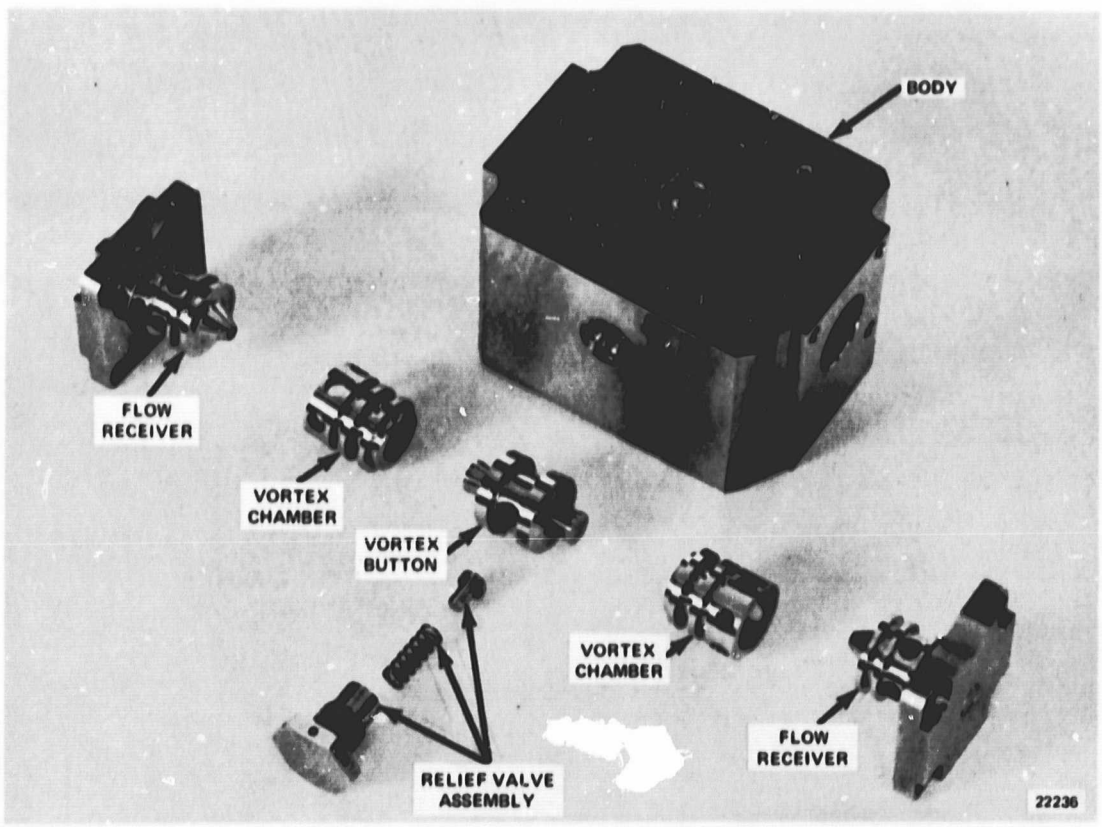

Figure 9 - Power Stage - Hydraulic Vortex Servovalve

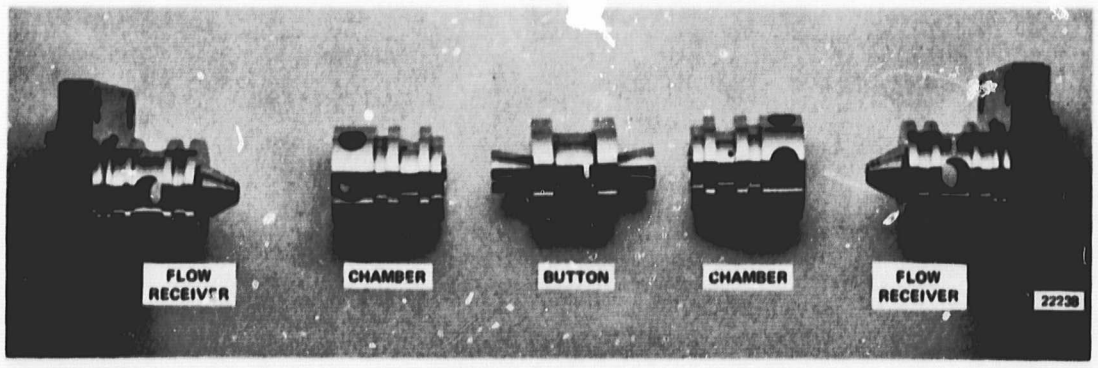

Figure 10 - Power Stage Vortex Valves

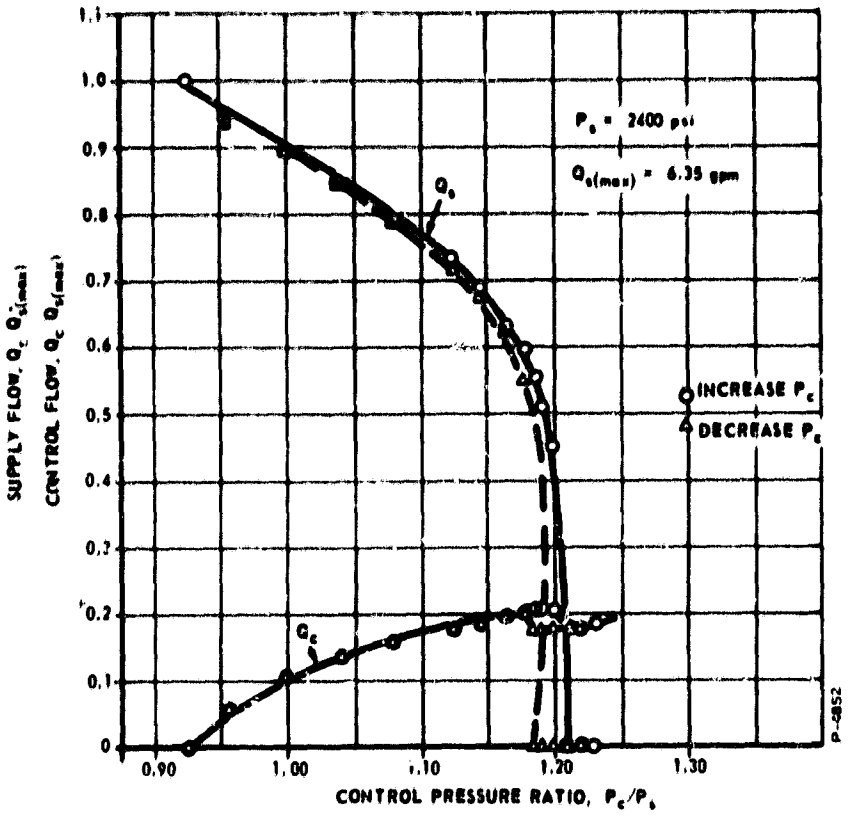

Figure 11 - Vortex Valve Performance - Assembly No. 1; Vortex Valve No. 1

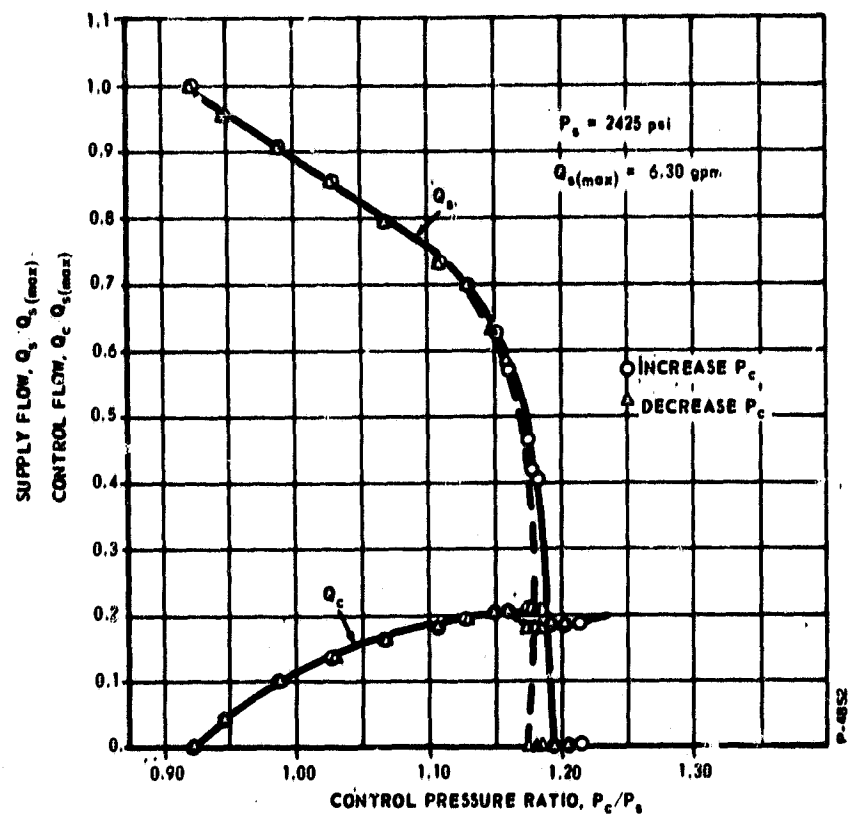

Figure 12 - Vortex Valve Performance - Assembly No. 1; Vortex Valve No. 2

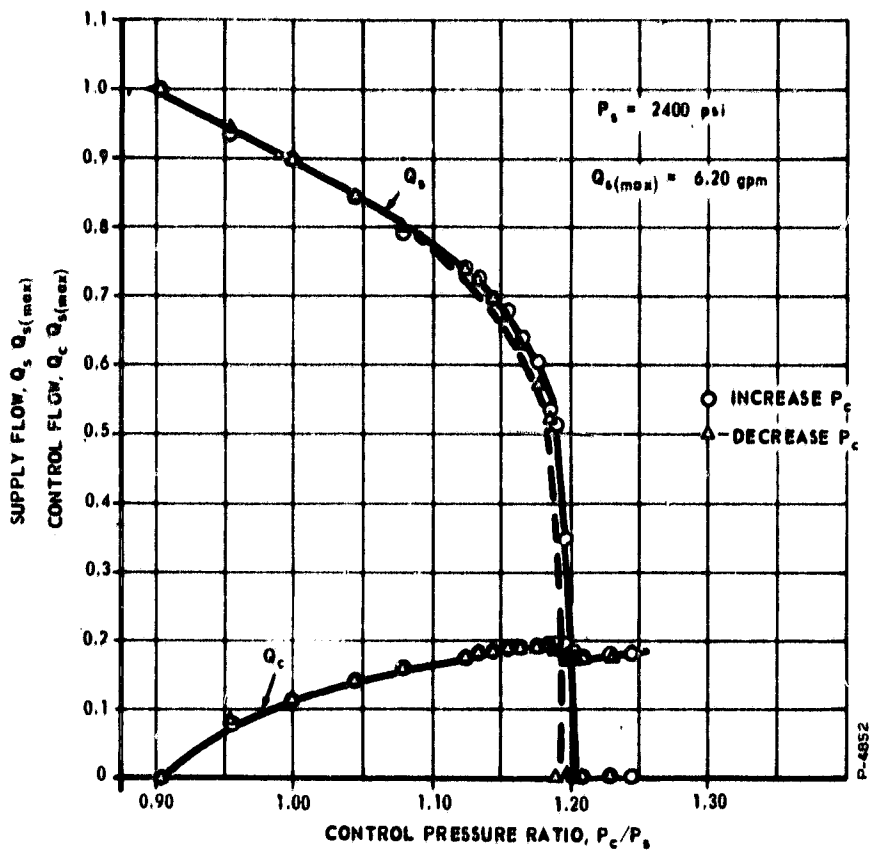

Figure 13 - Vortex Valve Performance - Assembly No. 2; Vortex Valve No. 1

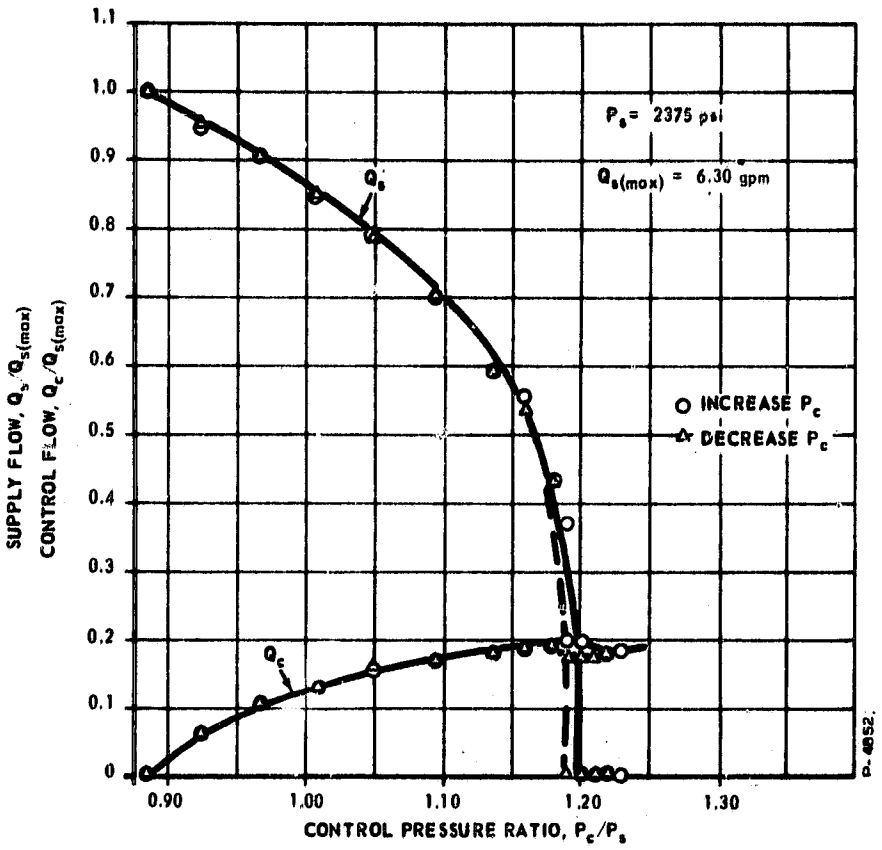

Figure 14 - Vortex Valve Performance - Assembly No. 2; Vortex Valve No. 2

order to provide a more efficient momentum exchange between the control and supply flows. The control to supply momentum ratio, m_c/m_s, was utilized as an evaluation criterion. The momentum ratio is defined as follows:

$$\frac{m_c}{m_s}(\%) = \frac{\sqrt{(P_c/P_s) - 1}}{(Q_{s_{max}}/Q_c)} \times 100 \qquad (1)$$

where

P_c/P_s = control pressure ratio at full turndown

$Q_{s_{max}}/Q_c$ = turndown ratio

Lower values of momentum ratio indicate a more efficient mixing of the supply and control flows. As shown in Table 1, the measured control port flow coefficient is very nearly equal to unity and the momentum ratio is 8% or less for the final design.

Initial testing of the pilot stage was begun after the spring rate of the auxiliary cantilever spring was predicted from the turn-down data. Severe flapper oscillations occurred during the testing. Detailed analyses and experimental determination of flapper forces, torque motor nonlinearities, and component resonances did not result in a stable design. It was concluded that further pilot stage design recommendations such as increased torque-motor power and nozzle shaping must be based on a complete analytical model of the reversed-flow flapper-nozzle system.

Servovalve load-flow data were taken using the hydraulic vortex servovalve power stage and a simulated pilot stage as shown schematically in Figure 15. A Bendix servovalve was used to provide a convenient means of pilot stage flow control. The servovalve load was simulated with a needle valve in the line connecting the servovalve cylinder ports. Typical data obtained are shown in Figures 16 and 17 for the two power stage assemblies. As indicated in Figures 16 and 17, the maximum load pressure differential, ΔP_L, is 2100 psi and maximum no-load flow is 8.9 gpm. As can be seen from the data, there is a slight mismatch of performance when the two vortex valves are operated in the push-pull circuit. This may be due to slight manufacturing differences in the vortex valves or, more likely, may be caused by minor dissymmetries in adjustment of the pilot stage.

After completion of the power stage load-flow tests, the power stage and simulated pilot stage were mounted on the NASA-supplied actuator as shown in Figure 18 and 19. By manual variation of the input differential current to the Bendix servovalve, the actuator could be smoothly stroked to any desired position and held there by closing the feedback loop. At

Table I - Summary of Power Stage Performance Test Data

	SERVOVALVE #1	
ITEM	VORTEX VALVE #1	VORTEX VALVE #2
MAX FLOW, $Q_{S\ MAX}$ (in^3/ sec)	24.0	24.4
TURNDOWN RATIO, Q_S/Q_C	5.15	5.70
CONTROL PRESS.RATIO, P_C/P_S	1.17	1.18
CONTROL MOM.RATIO, M_C/M_S (%)	8.0	7.45
OUTLET HOLE FLOW COEFF., C_{DO}	0.870	0.875
TANGENTIAL HOLE, C_D	1.08	0.96

P-4257

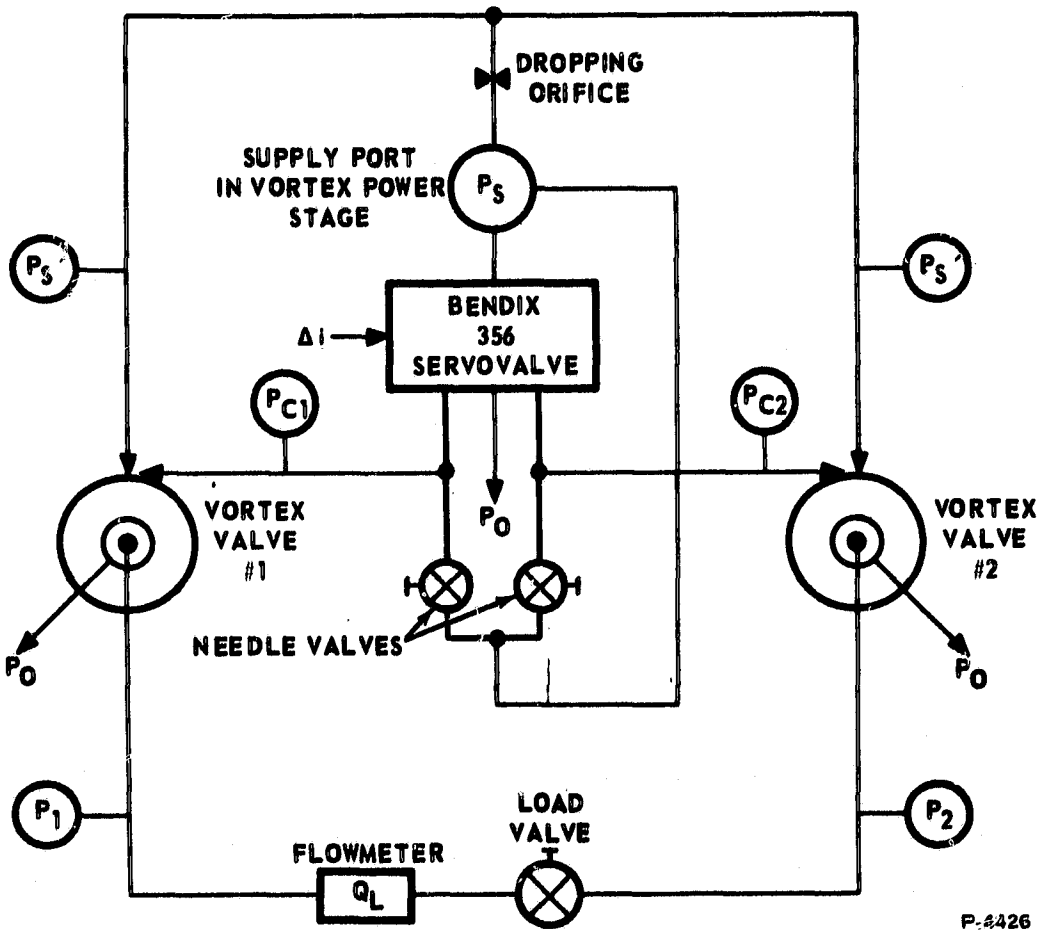

Figure 15 - Hydraulic Circuit for Vortex Servovalve Load-Flow Tests

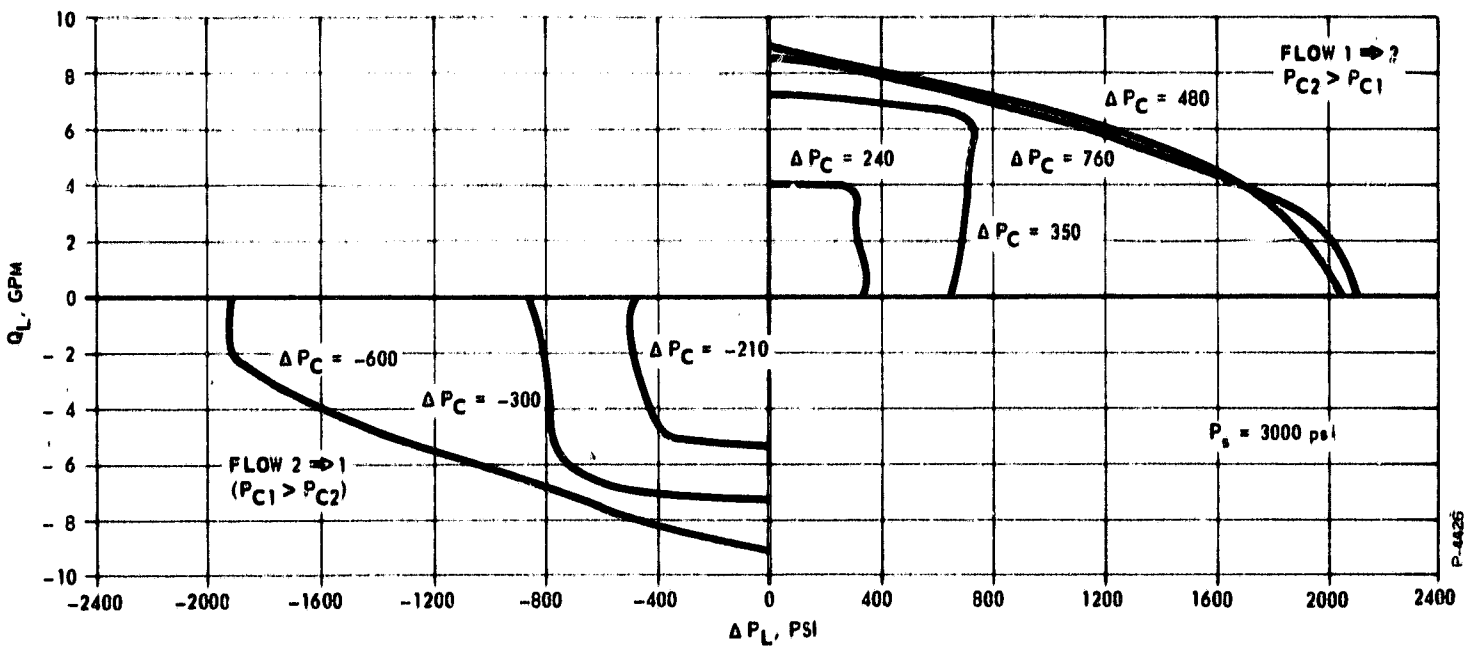

Figure 16 - Load Flow Curves - Assembly No. 1

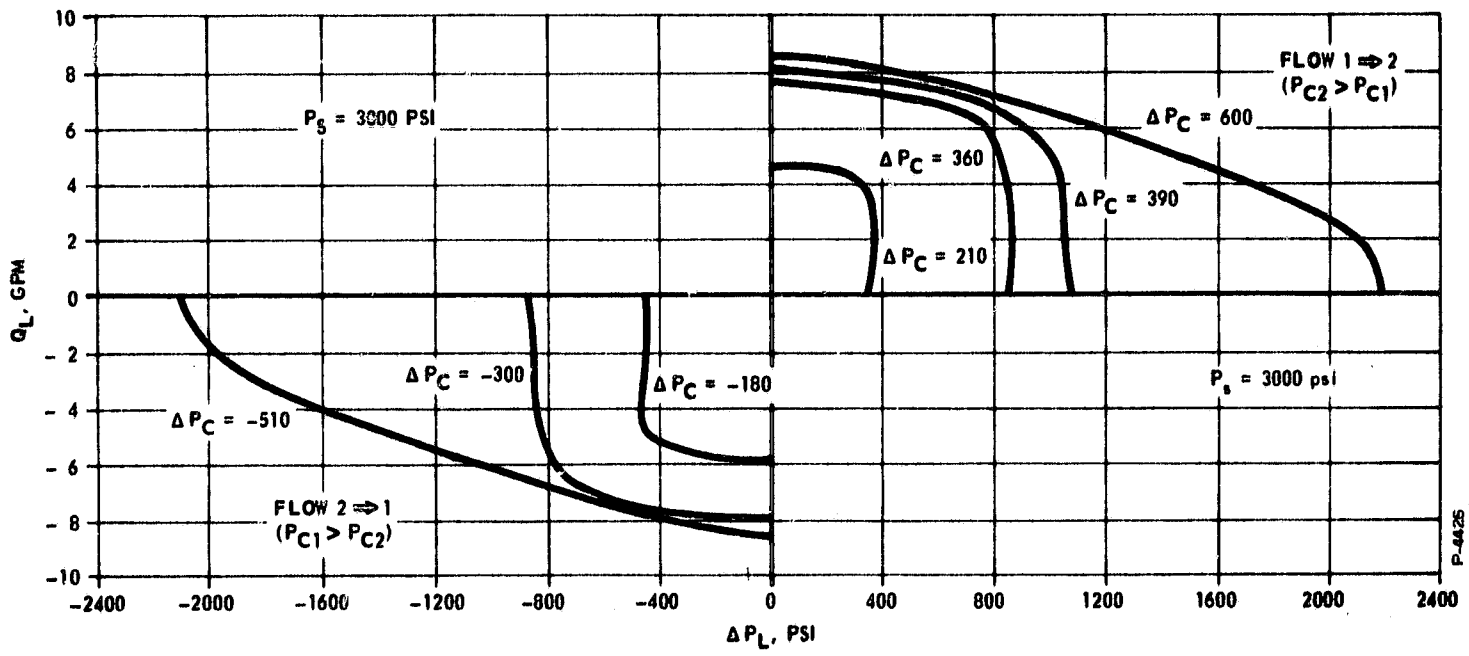

Figure 17 - Load Flow Curves - Assembly No. 2

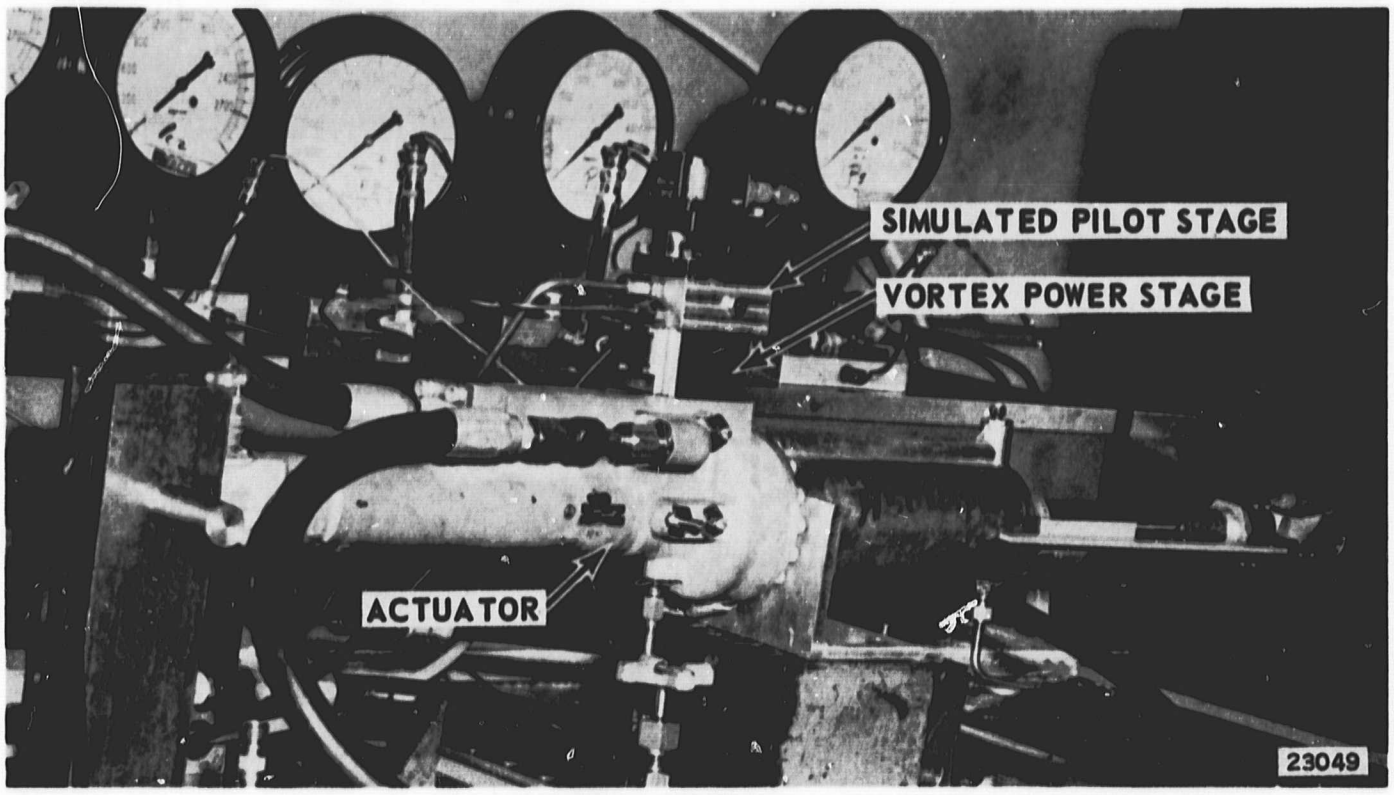

Figure 18 - Hydraulic Vortex Servovalve Power Stage During Tests with the NASA-Supplied Saturn Engine Gimbaling Actuator

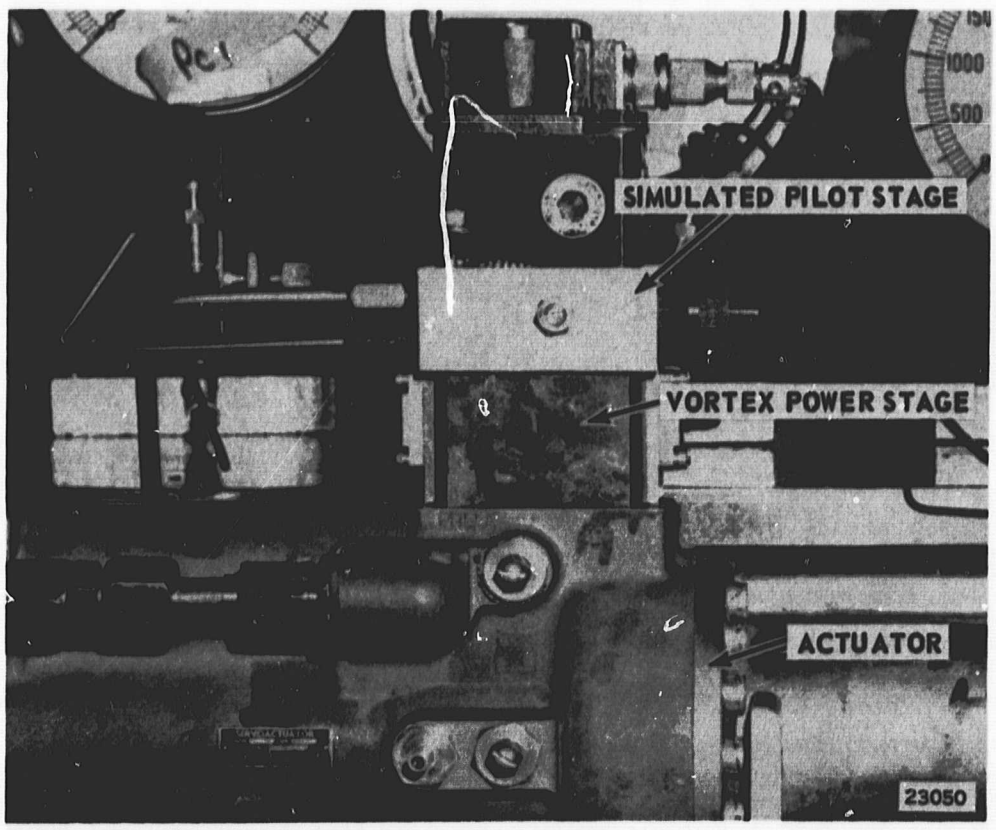

Figure 19 - Hydraulic Vortex Servovalve and Simulated Pilot Stage

either end-of-stroke position, the measured cylinder pressure was 2000 psi. This value was consistent with the blocked-port pressure obtained during the load-flow tests.

After establishing that the actuator could be controlled by the vortex power stage, a function generator was connected to the servo-amplifier driving the Bendix servovalve. The feedback loop was closed and a sinusoidal input was applied to the pilot stage torque motor. The amplitude of the input command signal was adjusted to give an indicated output of $\pm$0.4 degree (0.191 in.) at an input signal frequency of 0.5 cps. (Under these conditions, the input and output signals were considered to be unattenuated.) The exact magnitude of the input command signal amplitude used is of little meaning, since the power requirements of the Bendix servovalve and the final hydraulic vortex servovalve torque motor were not identical. Figures 20 through 26 show traces of the actuator position for different sinusoidal input frequencies, ranging from 0.5 to 30 cps. Actuator position is referenced to degrees since the actuator used was a Saturn SI-B engine gimbaling actuator which was equipped with an external scale calibrated in degrees of rocket engine position. This scale was utilized to determine actuator stroke during the frequency response tests. The conversion factor from degrees to inches of stroke is 0.478 inch/degree.

The traces indicate that the actuator stroked smoothly over the frequency range. At frequencies below 0.5 cps, the output curve indicated some noise as seen in Figures 20 and 27. The remainder of the traces indicate the decrease in output amplitude and increase in phase lag with frequency. The volume under compression in the manifold block between the Bendix 356 servovalve and the hydraulic vortex servovalve power stage was excessive compared to the final design, and affected the response of the test circuit.

Figure 27 shows a trace of the actuator position with no input signal applied to the torque motor. This trace shows that there is some "hunting" of the actuator, but that it is apparently random and of small magnitude (0.020 degree).

The vortex valve principle has been shown to be an effective means of flow control for the hydraulic servovalve application. The present developmental program has resulted in an optimum configuration for the power stage vortex valves. A more thorough understanding of the pilot stage problem areas has been acquired and recommendations have been made for their solution. For a complete description of the development of the servovalve design, see the following two sections of this report.

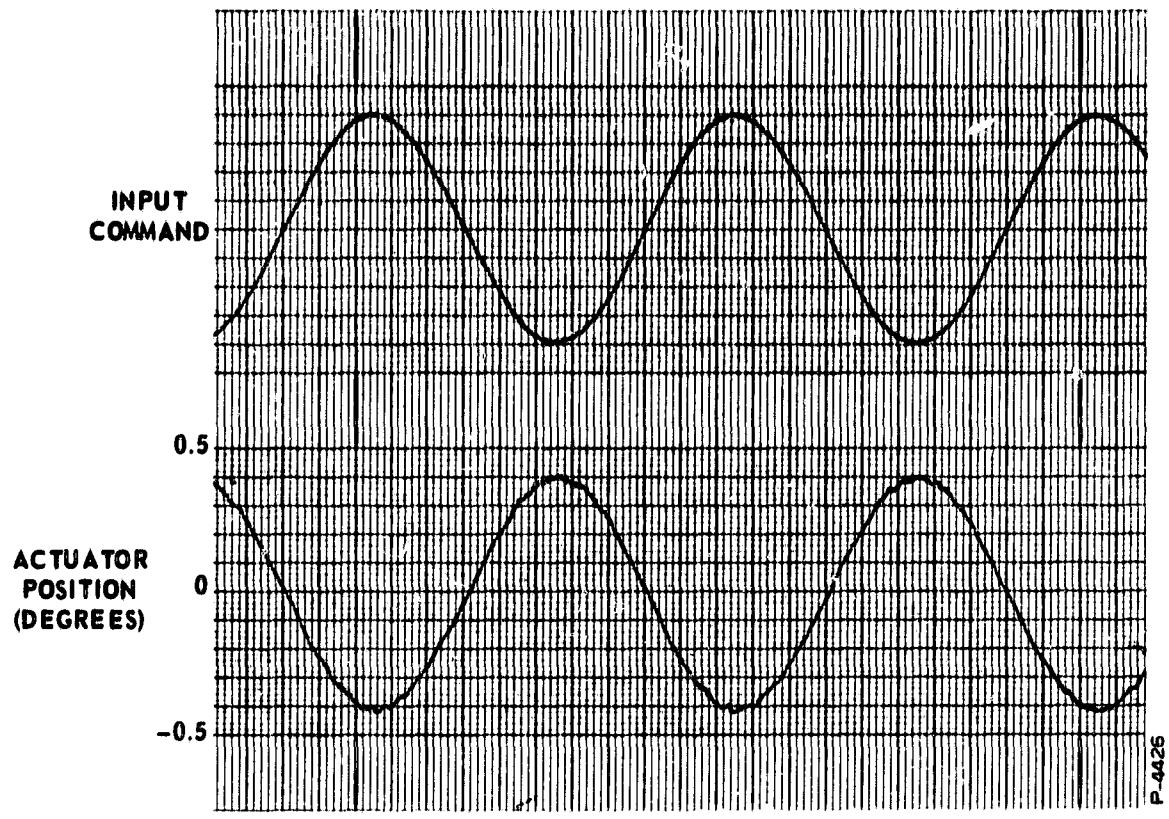

Figure 20 - Trace of Actuator Position for Input Frequency of 0.5 cps
(Chart Speed = 25 mm/sec)

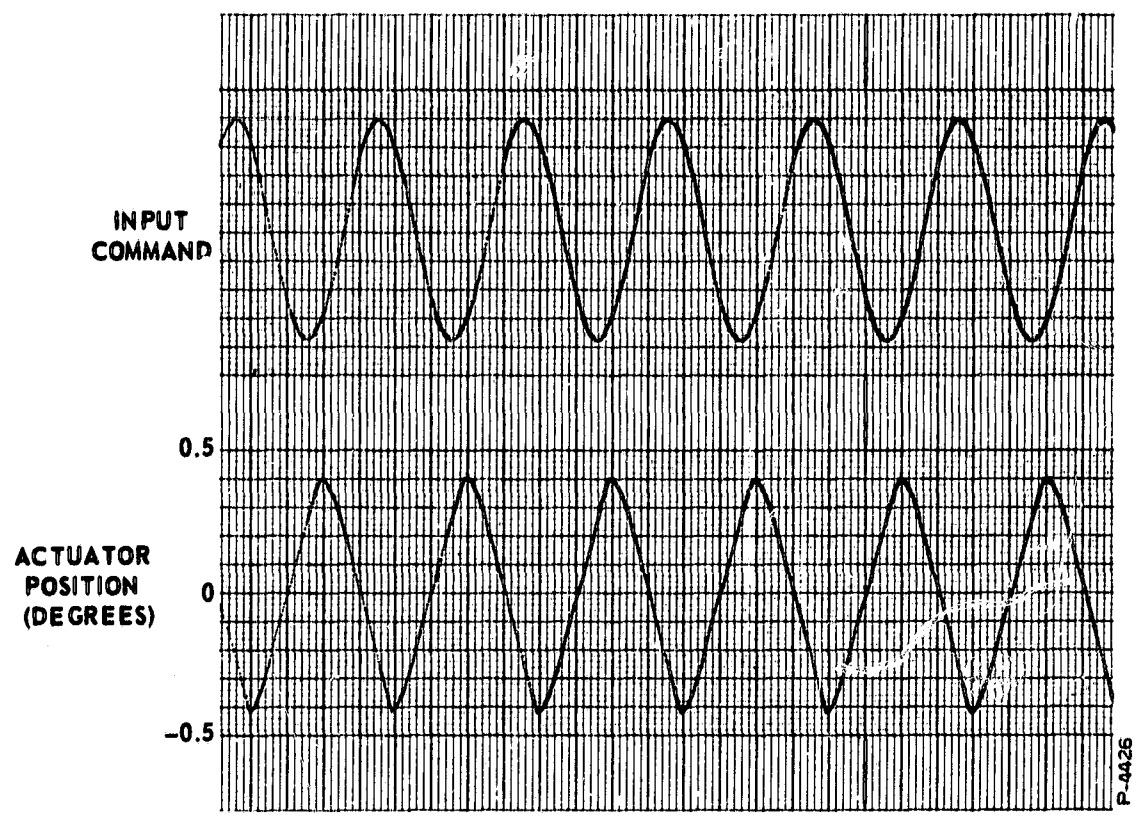

Figure 21 - Trace of Actuator Position for Input Frequency of 5 cps
(Chart Speed = 100 mm/sec)

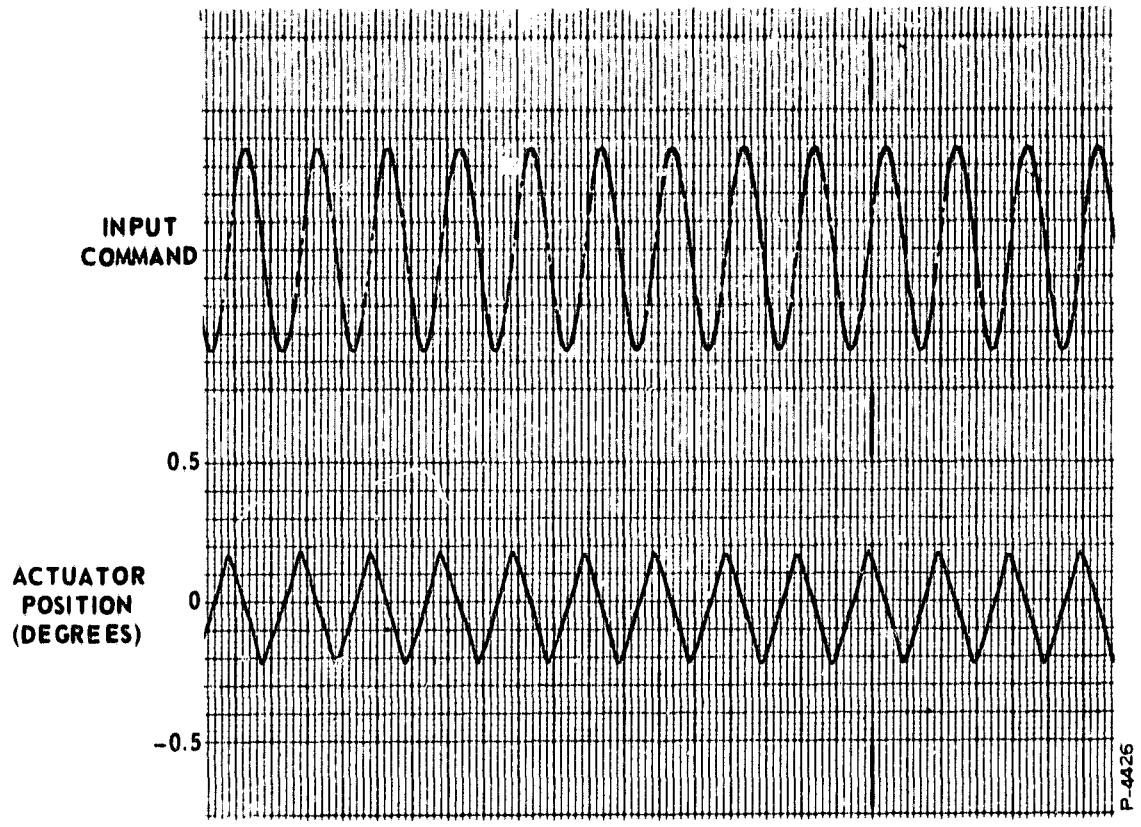

Figure 22 - Trace of Actuator Position for Input Frequency of 10 cps
(Chart Speed = 100 mm/sec)

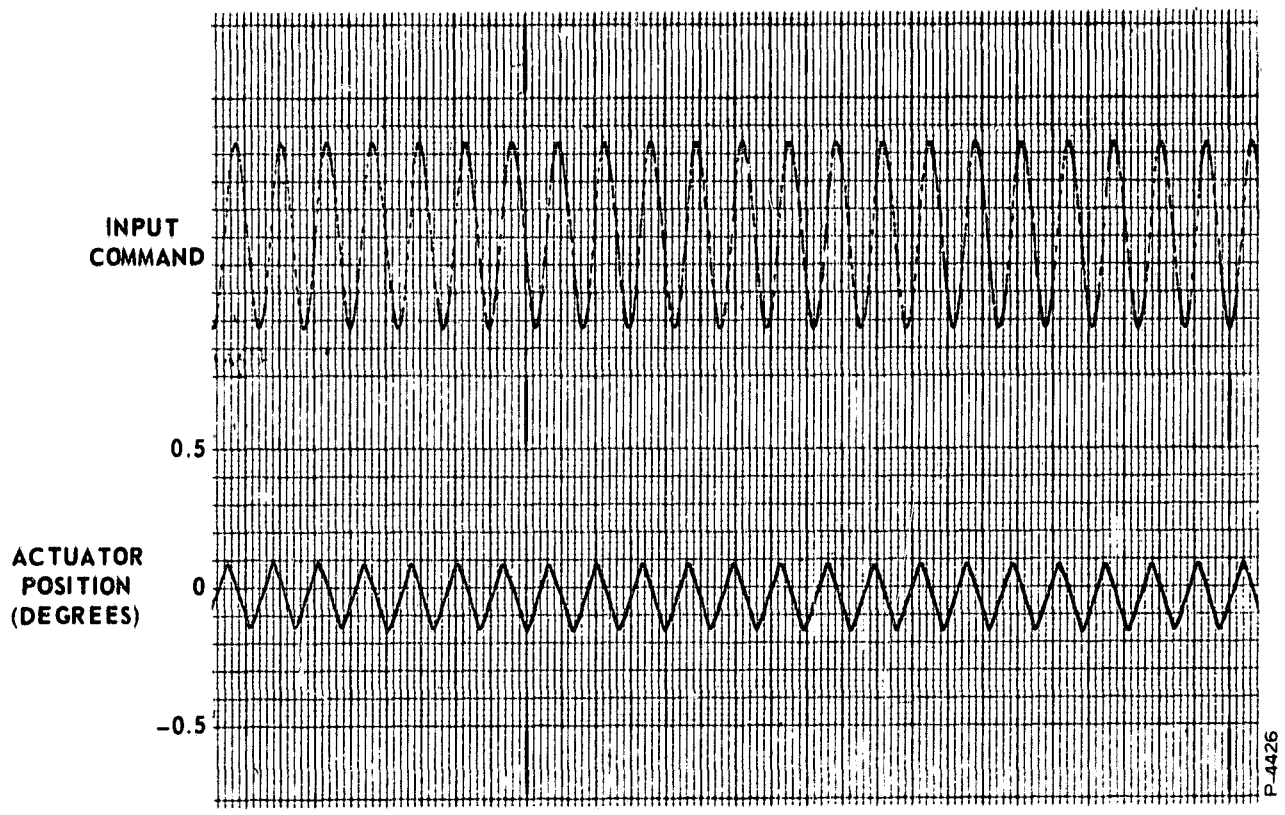

Figure 23 - Trace of Actuator Position for Input Frequency of 15 cps
(Chart Speed = 100 mm/sec)

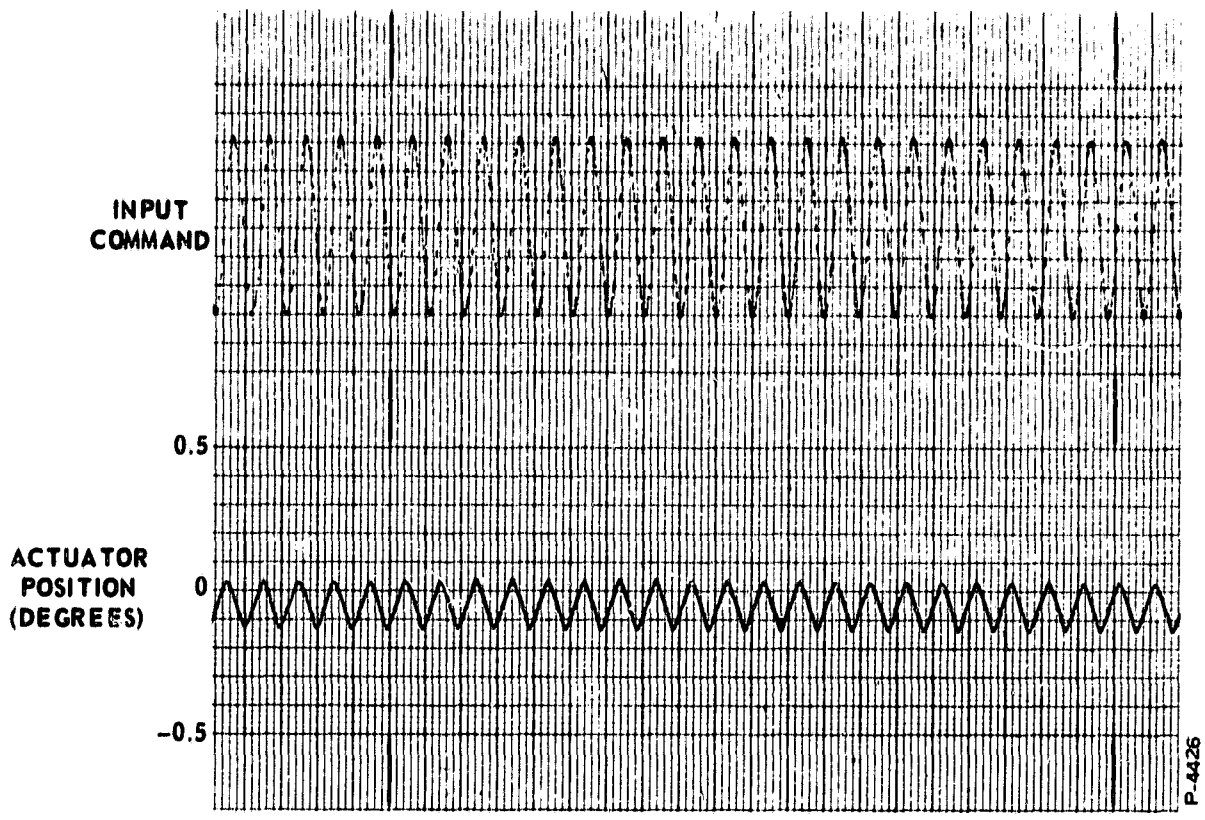

Figure 24 - Trace of Actuator Position for Input Frequency of 20 cps
(Chart Speed = 100 mm/sec)

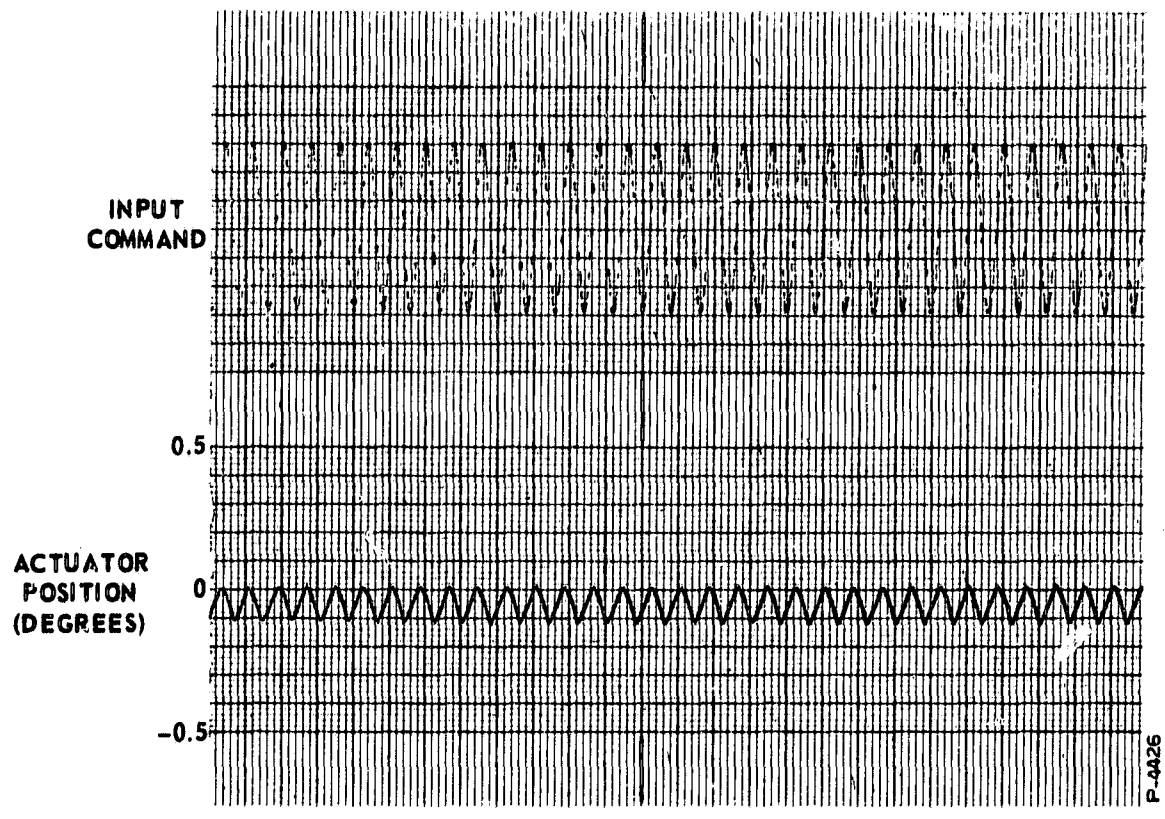

Figure 25 - Trace of Actuator Position for Input Frequency of 25 cps
(Chart Speed = 100 mm/sec)

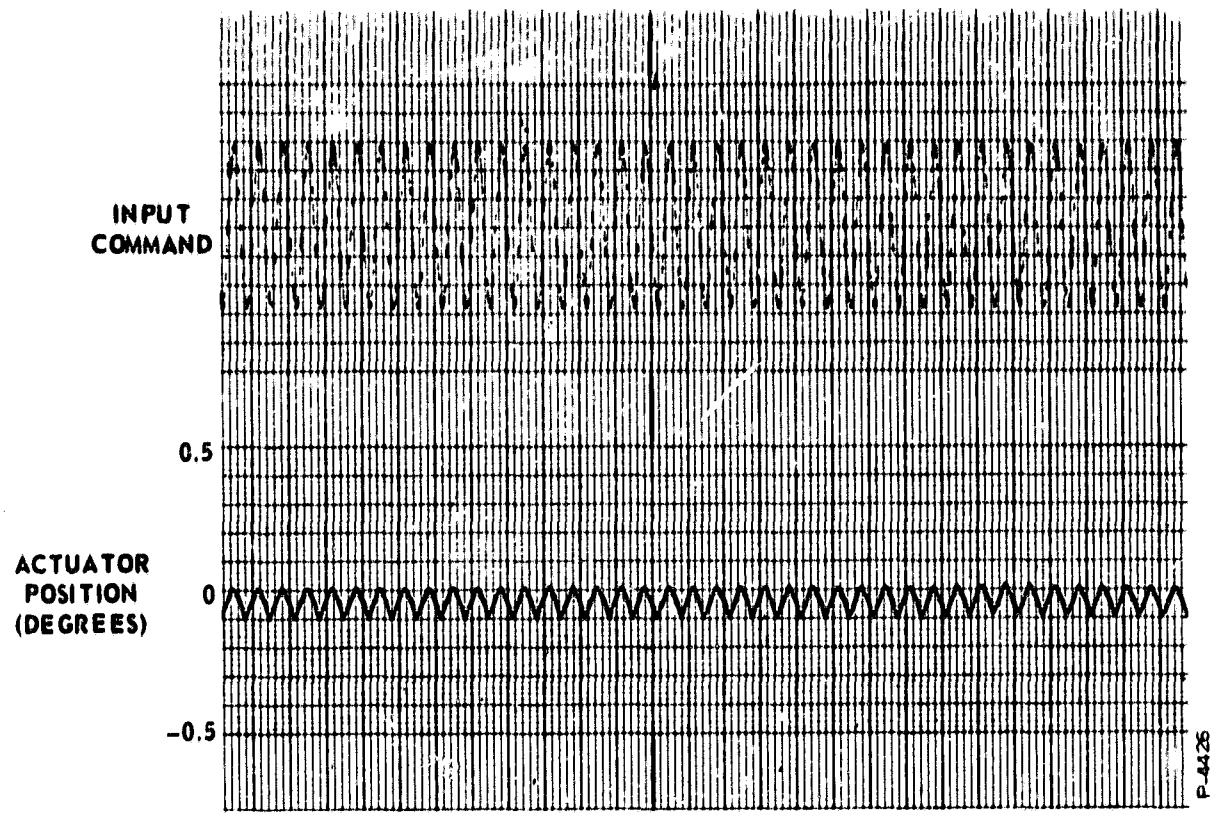

Figure 26 - Trace of Actuator Position for Input Frequency of 30 cps
(Chart Speed = 100 mm/sec)

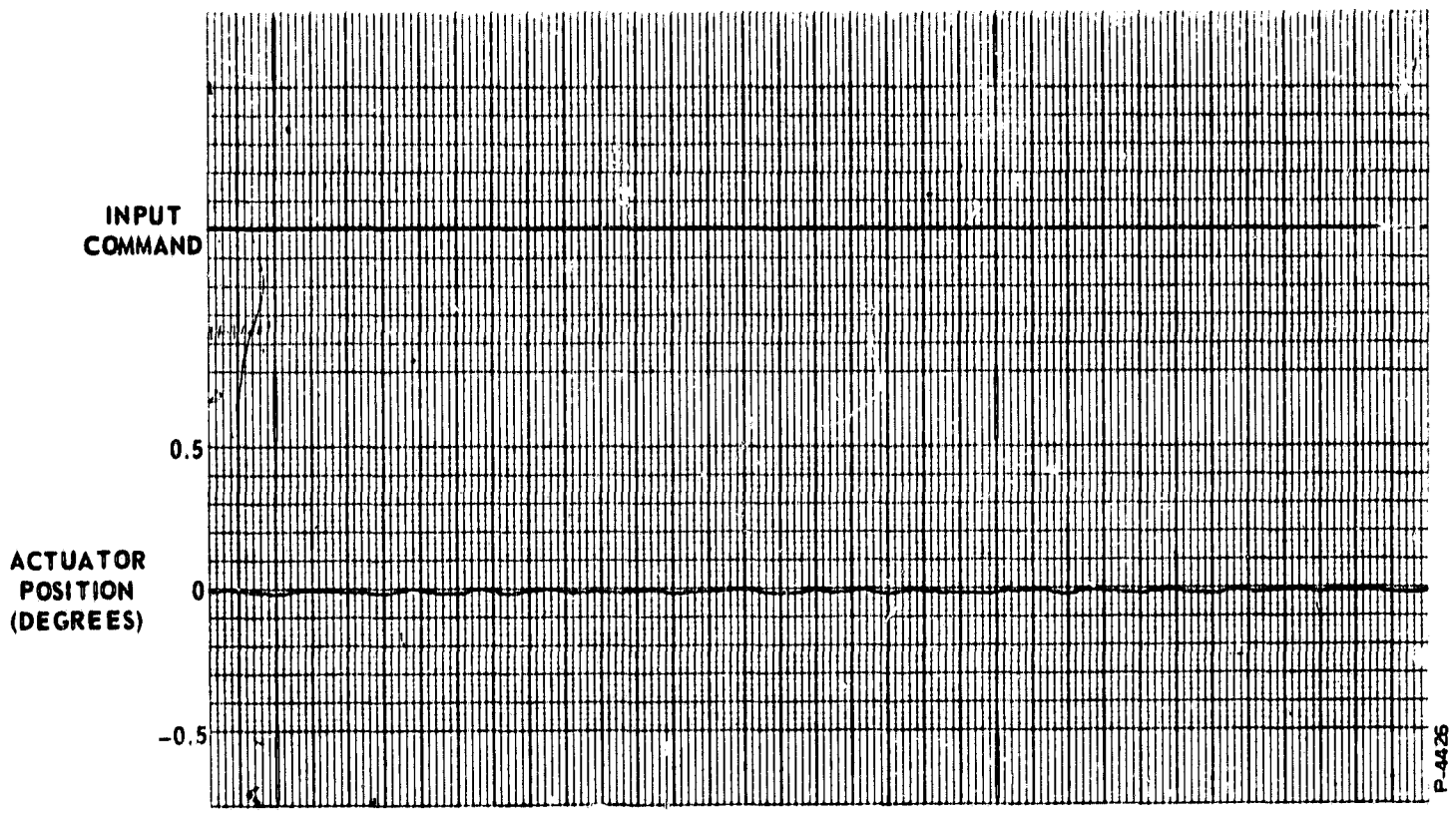

Figure 27 - Trace of Actuator Position for Zero Input Command

SERVOVALVE COMPONENT DEVELOPMENT

Preliminary Hydraulic Circuit Analysis

One of the first tasks undertaken in the development of the hydraulic-vortex servovalve was an analysis of the effects of the vortex valve flow receiver configuration on the servoactuator performance characteristics. The Moog 17-150 servoactuator supplied by NASA-MSFC for Bendix servovalve development had the load-flow requirements shown in Figure 28. Note that only the full stroke (12 ma) curve has been shown. The problem was to approach this performance with a vortex servovalve utilizing the flow receiver.

Considering only the vortex valves which drive the actuator, and examining the power portion of the circuit, it is seen that all the cylinder flow must pass through the vortex valve flow receivers. The vortex valve which is receiving the cylinder return flow will require a significant pressure drop across the flow receiver because it appears as an orifice in the circuit, very near in size to the vortex power valve outlet hole. Since the pressure drop across the power valve outlet hole at zero vorticity is almost full system pressure, it follows that the pressure drop across the backflowing flow receiver must be high. Increasing the flow receiver internal diameter will reduce the pressure drop across the flow receiver. However, this will reduce the pressure recovery of the flow receiver when it is functioning as a receiver. Selection of the flow receiver diameter is a compromise between back pressure, pressure recovery, and flow recovery.

Based on various parametric tests of hydraulic vortex valves with flow receivers, the following load-flow characteristics were established. The general load-flow performance of a vortex valve with a flow receiver is seen in Figure 29(a). The flow receiver internal diameter was the same as the vortex valve outlet hole. Curve P_1 is the flow-pressure characteristic of the vortex valve when the flow receiver is functioning as a receiver. Curve P_2 is the flow-pressure characteristic when the flow is out of the receiver. Examination of the small schematic in Figure 29(a) will indicate the flow direction. The intersection of curve P_1 and P_2 will be the operating point of the system when the cylinder is unloaded and traveling at maximum velocity. If the cylinder is loaded (generating some output force), the cylinder velocity will be reduced. The reduced velocity will allow a pressure differential to be generated across the cylinder and the difference in curve P_1 and P_2 is that pressure differential. Note that the zero flow intersection of curve P_1 is approximately at 0.95 P_s. The maximum pressure differential available to drive the cylinder is therefore 0.95 P_s.

The information in Figure 29(a) was replotted into a more conventional display of Flow versus ΔP as seen in Figure 29(b). This information was used as the basis for comparison for determining the flow receiver to outlet hole ratio best suited for this application.

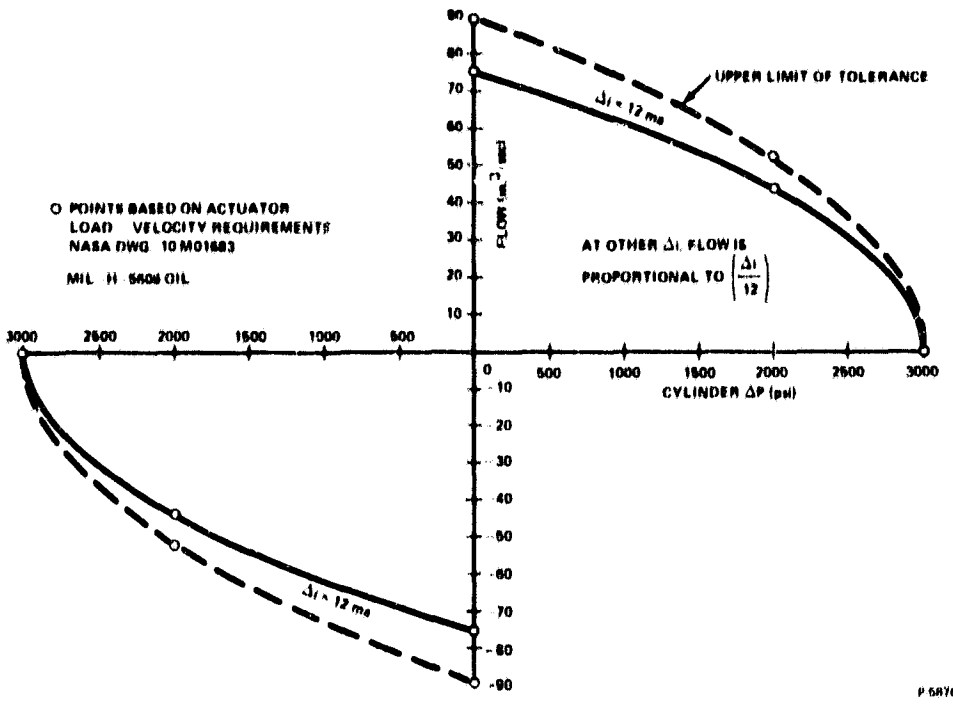

Figure 28 - Load-Flow Requirements of Hydraulic Vortex Servovalve

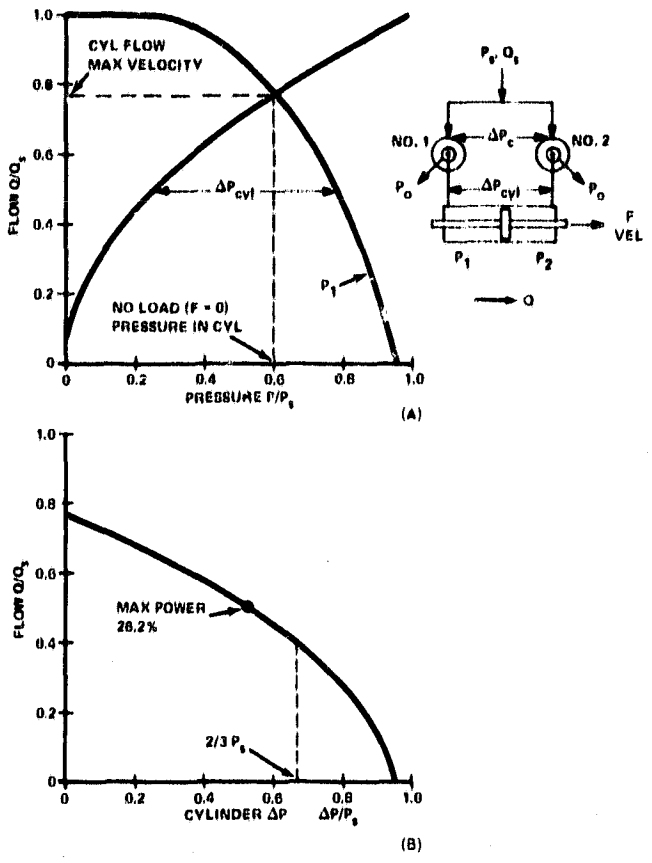

Figure 29 - Load-Flow Characteristics for $D_R/D_o = 1.0$

The performance characteristics of the vortex valve when the flow receiver internal diameter equals the vortex valve outlet hole diameter are shown in Figure 29(a) and 29(b). The variation in cylinder pressure P_1 and P_2, seen in Figure 29(a), is for various loads or flows. Note that for zero cylinder output force (maximum velocity), the cylinder flow is 0.77 of the flow through the number one vortex valve. The blocked actuator maximum ΔP is 0.95 of supply pressure to the vortex valve. Checking the curve of Figure 29(b), the maximum power point is found at $Q/Q_s = 0.50$ and $\Delta P/P_s = 0.53$ which results in a power output of 26.2%.

With a flow receiver diameter ratio of 1.5 to 1, the back pressure effect of the probe is reduced. Note in Figure 30(a), that curve P_2 is more vertical and intersects curve P_1 considerably higher than the previous case. Replotting Figure 30(a) into the more conventional form, produces the results in Figure 30(b). The maximum flow is 1.10 of Q_s which is possible because of entrainment of the fluid surrounding the outlet hole jet. Additional fluid is therefore driven into the receiver tube and is available to drive an actuator or load. This phenomena occurs only if the additional fluid may be drawn from the exhaust line and reservoir. If fluid cannot be drawn from the exhaust lines, the effect is to cut off the curve at a constant Q/Q_s of 1.0 and not affect the remainder of the curve. Note that maximum ΔP is 0.95 and that maximum power is 45%. However, the supply pressure to the valve is not system (3000 psi) pressure. It is necessary to reduce the vortex valve supply pressure to provide a control pressure level greater than the vortex valve supply.

Assuming a flow receiver diameter of two times the outlet hole, it is seen in Figure 31(a) that the back pressure is greatly reduced. However, the maximum $\Delta P/P_s$ is reduced to approximately 0.70 as shown by the intersection of the P_1 curve with the abscissa or zero flow axis. Note the high entrainment flow as shown by the intersection of the P_1 curve and the ordinate. Replotting as before, the load-flow curve of the system is shown in Figure 31(b). The rather low pressure recovery of 0.70 $\Delta P/P_s$ most likely would eliminate this diameter ratio from further consideration. In addition, the maximum power point has decreased to 36.8%. It appears that the 2:1 diameter ratio is larger than the optimum.

It was concluded from this analysis that a flow receiver diameter 1.5 times the outlet hole diameter is the best compromise between pressure and flow recovery, power recovery, and flow receiver back pressure.

After the initial estimate of the vortex valve flow receiver proportions was completed, several hydraulic-circuits were conceived for the servovalve. All of the circuits included implementation of a dynamic pressure feedback system. However, since preliminary circuit evaluation was on a steady-state basis, the dynamic pressure feedback system was not considered in the analysis.

The three circuits which evolved from this analysis all utilized a power stage consisting of two vortex amplifiers operating in a push-pull

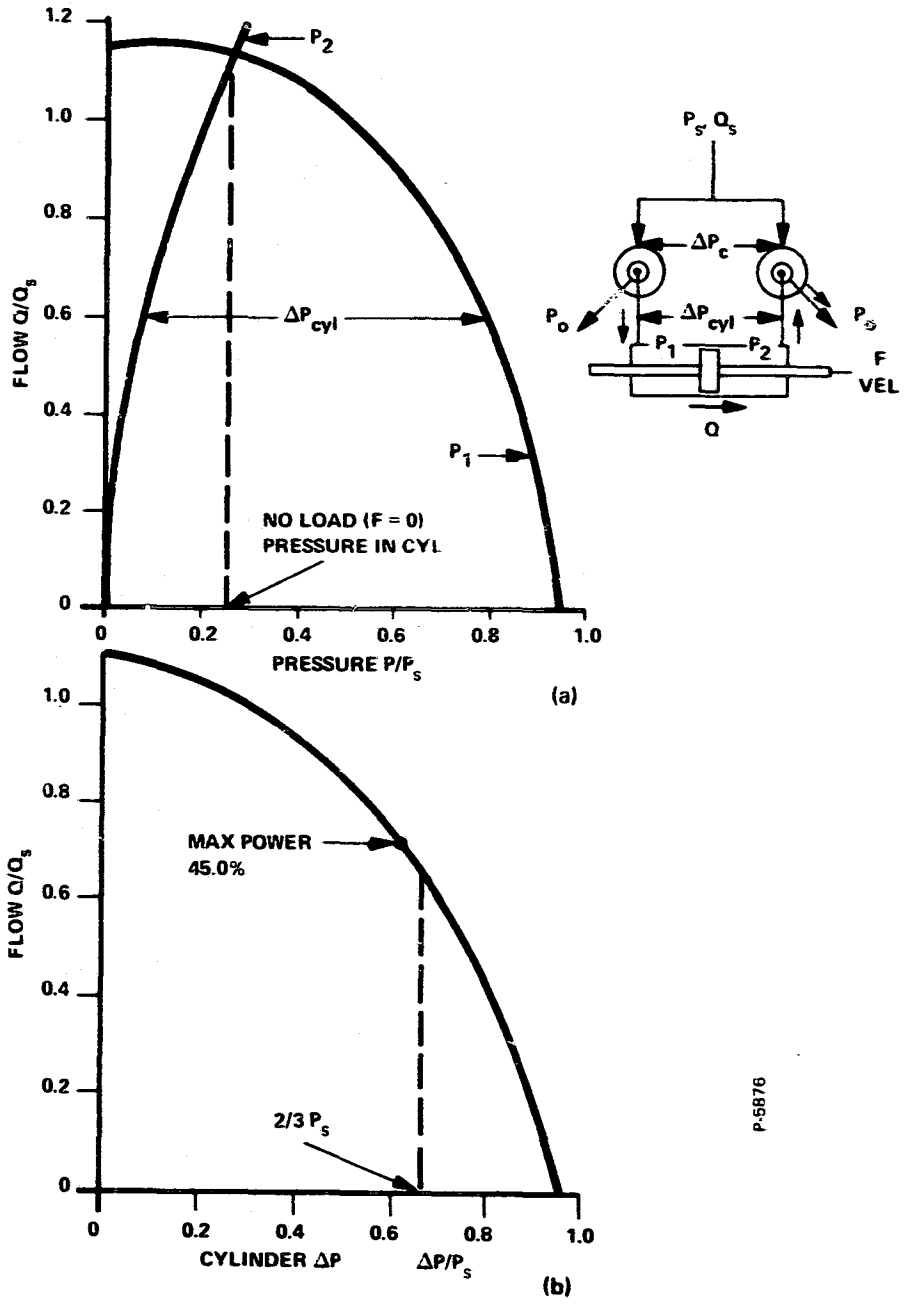

Figure 30 - Load-Flow Characteristics for $D_R/D_o = 1.5$

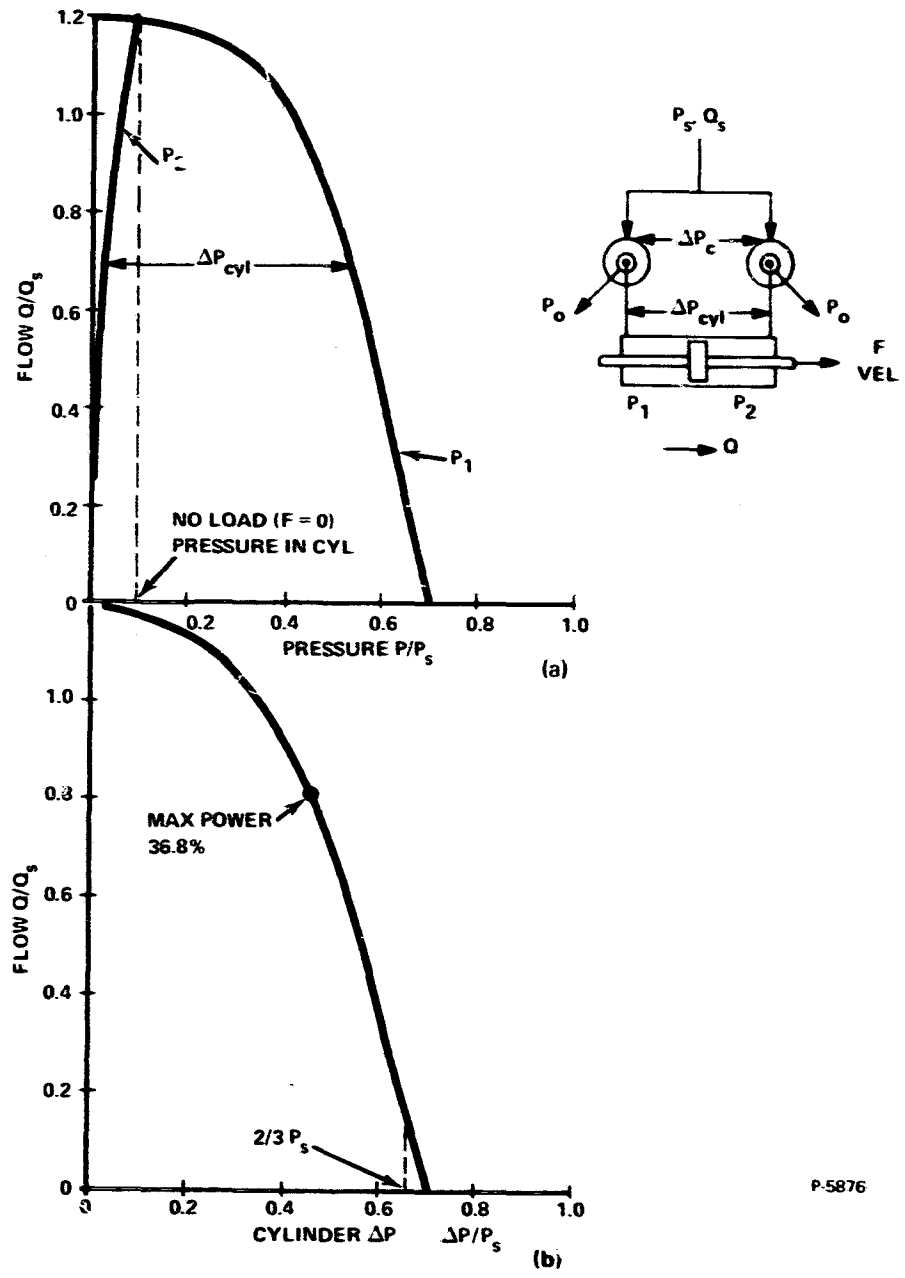

Figure 31 - Load-Flow Characteristics for $D_R/D_o = 2.0$

configuration but differed in the pilot stage arrangement. The first concept consisted of a torque motor-driven, flapper-nozzle pilot stage which provided control flow to the power stage vortex valves. The second concept consisted of a jet-pipe pilot stage in which control flow was ported directly to the vortex valves. The third concept also utilized the jet-pipe pilot stage, but an additional stage of amplification was inserted between the jet pipe output and the vortex valve control ports. In the following paragraphs, the three hydraulic circuit concepts are described in detail.

Concept No. 1.- Steady-state performance of the first circuit is shown in Figure 32. The various pressures and flows which would exist in each channel in the circuit are shown adjacent to the channel. The upper number in the bracket is the pressure while the lower number is the flow. Relative size of the various orifices is shown by the numbers in parentheses. The power stage vortex valve was arbitrarily assigned an area of 100 units and all other orifices were based on that size. Actual orifice size may be computed by determining the pressure drop and flow across any particular orifice. The circuit was analyzed at full stroke conditions. Appropriate performance curves, included in Appendix A, were used to determine the various pressures and flows. Some optimization was performed by varying the size of orifices and vortex valves, until a reasonable compromise of cylinder pressure and total flow input was obtained.

Note in Figure 32, that a relief valve was included in the line from the servovalve supply point to the vortex valves supply point. This relief valve was necessary in order to reduce the vortex valve supply pressure sufficiently to provide a control pressure high enough to inject the required flow into the vortex chamber. (It was possible during testing of the servovalve to eliminate this relief valve and replace it with a fixed orifice since the total impedance of the two vortex power valves did not vary significantly during operation from null to full stroke.)

The maximum theoretical blocked cylinder pressure differential available was approximately 1890 psi. The system was sized to provide 75 cu. in/sec unloaded cylinder flow and required an input flow of 134 cu. in/sec to the valve supply port. This does not include the effect of the dynamic pressure feedback unit on flow and pressure.

Concept No. 2.- Steady-state performance of the second concept is shown in Figure 33, and is quite similar to the previous concept. At full stroke conditions, this concept is only slightly less efficient than the flapper-nozzle concept. Note the check valves in the control pressure lines between the jet pipe receivers and the control ports in the power stage vortex valves. These check valves prevent back flow from the vortex valve in the zero vorticity condition. Since the control port area was large compared to the outlet hole in the vortex valve, the back flow in the control circuit would be appreciable. As in the previous concept, a relief valve is included in order to provide the necessary drop in supply pressure to the vortex valves.

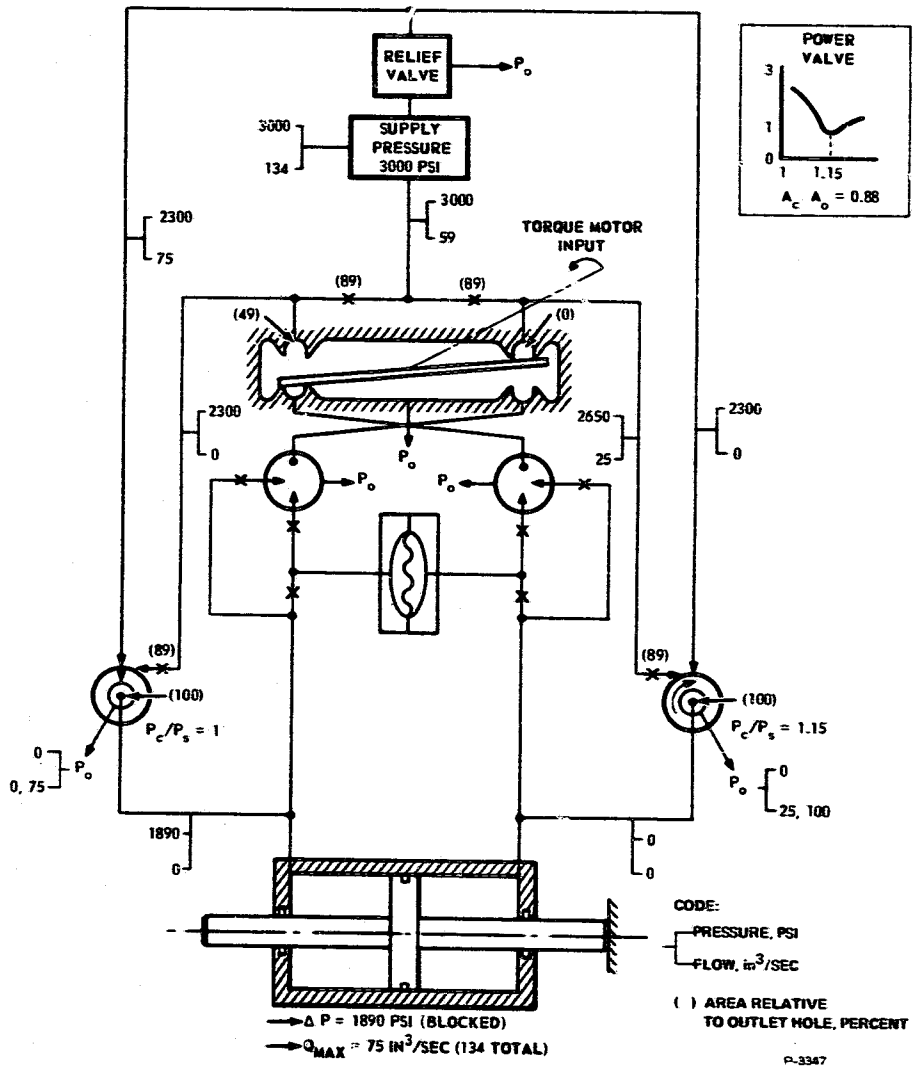

Figure 32 - Concept No. 1

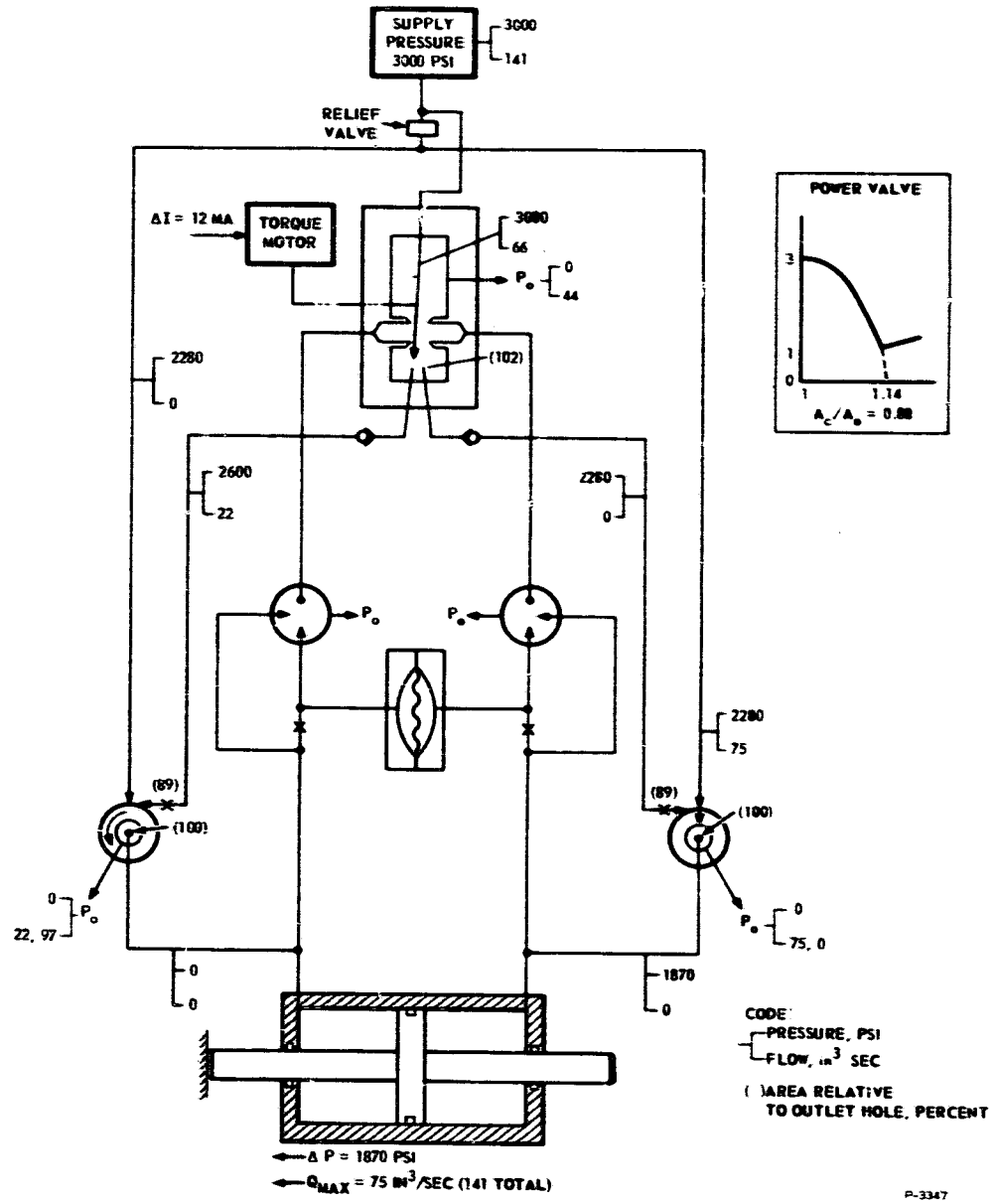

Figure 33 - Concept No. 2

The performance calculations of this system resulted in a blocked cylinder pressure differential of 1870 psi. An input flow of 141 cu.in/sec is required to provide an unloaded cylinder flow of 75 cu.in/sec.

Concept No. 3.- This concept, shown in Figure 34, is the same as Concept No. 2 except that another stage of amplification has been added to the pilot stage in an attempt to reduce the pilot stage flow. A vortex valve without a flow receiver was inserted between the jet pipe pilot stage and the control orifice of the vortex power stage valves. This vortex valve provides a flow modulation function. The circuit analysis revealed that the additional vortex valve requires another relief valve which would further reduce the supply pressure to the power stage vortex valves.

After some optimization, the results indicated that this valve concept was more complex and had poorer performance than the other concepts. The maximum blocked cylinder pressure differential was 1520 psi and the valve required a total flow of 160 cu.in/sec, to provide an unloaded cylinder port flow of 75 cu.in/sec. The added complexity and reduced performance made this concept undersirable for further consideration.

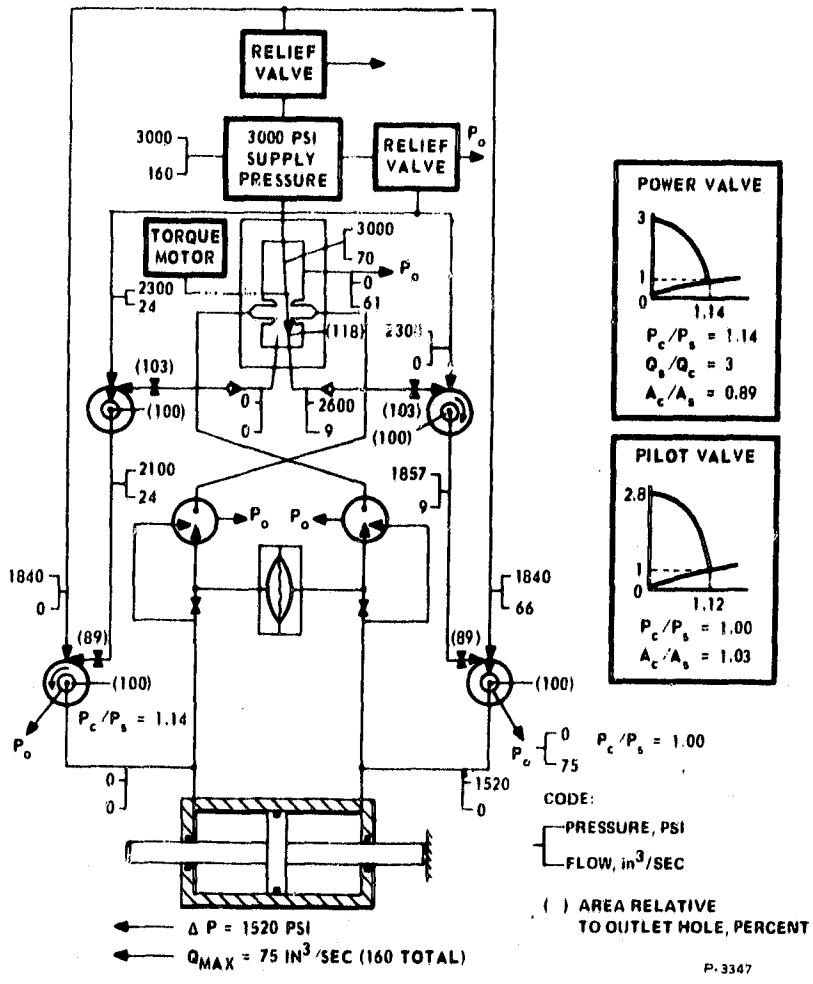

Figure 34 - Concept No. 3

From this preliminary analysis, it was concluded that the flapper-nozzle pilot stage concept (Concept No. 1) resulted in the best overall performance. The flapper-nozzle approach was versatile and more readily accommodated the dynamic pressure feedback system.

Fluidic Component Evaluation

Although Concept No. 1 appeared to have the best characteristics of the circuits considered, the preliminary analysis of the hydraulic circuit also indicated that the output performance of the servovalve would not match the servoactuator load-flow requirements described in NASA-MSFC Specification No. 10M01683. Since the vortex valve control pressure must be greater than the supply pressure, there is a drop in pressure level for every series-connected vortex element encountered in the circuit. In addition, although the various fluidic elements have high blocked port pressure recoveries, the recovered pressure is necessarily reduced when flow occurs in the circuit. Thus, the pressure degradation across each element becomes appreciable, resulting in a reduction of available cylinder driving pressures.

Analysis of the hydraulic circuit also indicated that the large pilot stage flow required an excessively large torque motor. The flow of the flapper-nozzle pilot stage was calculated to be approximately 80% of the maximum flow requirement of the actuator. The torque motor size, then, was essentially only slightly smaller than the torque motor of an equivalent open center single-stage servovalve that would provide the same cylinder flow. The low input power (150 milliwatts) required by the specification makes the torque motor large since electromechanical device size varies inversely with input power. An increase in electrical input power of two orders of magnitude would be required to reduce the torque motor to a reasonable size.

Two possible solutions to the low cylinder pressure problem were realized. First, in order to compensate for the low cylinder pressure differential available, the piston area could have been increased. The force output of the cylinder could then have been increased to an acceptable level. Although this was the most straightforward solution, the NASA actuator to which the servovalve was to be mated had been fixed and a change in bore size appeared unrealistic.

The second solution considered was to increase the vortex valve turndown by improving momentum efficiency. A double outlet vortex valve which had been developed primarily for pneumatic systems had been shown to increase the momentum efficiency of the standard vortex valve significantly. A series of vortex valve tests to improve the efficiency of the vortex valve was undertaken. The configurations tested consisted of the single outlet vortex valve, the double outlet valve, and a radial flow vortex valve.

Single outlet vortex valve.- In order to provide vortex valve data to support the servovalve hydraulic circuit calculations, a series of tests was performed to obtain simultaneous vortex valve turndown and flow receiver characteristics. The single outlet vortex valve fixture shown in Figure 35 was utilized for these tests. Significant vortex valve dimensions, as functions of the outlet hole diameter, D_o, were as follows:

(1) Flow Receiver Diameter, $D_R = 1.5\ D_o$

(2) Flow Receiver Spacing, $L_R = 1\ D_o$ and $2\ D_o$

(3) Vortex Chamber Spacing, $L_1 > 0.5\ D_o$

(4) Vortex Chamber Diameter, $D_{CH} = 4\ D_o$

Tests were performed at two supply pressures - 1000 psi and 2300 psi. The mixing zone annulus area ratio, A_{ANN}/A_o, was 5.0 for these tests. Four control ports were used for all tests and the total control port area was chosen so that, at full turndown, a control pressure ratio P_c/P_s of approximately 1.2 was obtained.

The results of the single outlet vortex valve tests at $P_s = 1000$ psi are shown in Figures 36 through 39. Essential data from these curves are summarized in Table 2.

In order to compare the performance of the vortex valve concepts tested, the control momentum ratio m_c/m_s was defined as follows:

$$\frac{m_c}{m_s}(\%) = \frac{\sqrt{(P_c/P_s) - 1}}{(Q_{s_{max}}/Q_c)} \times 100$$

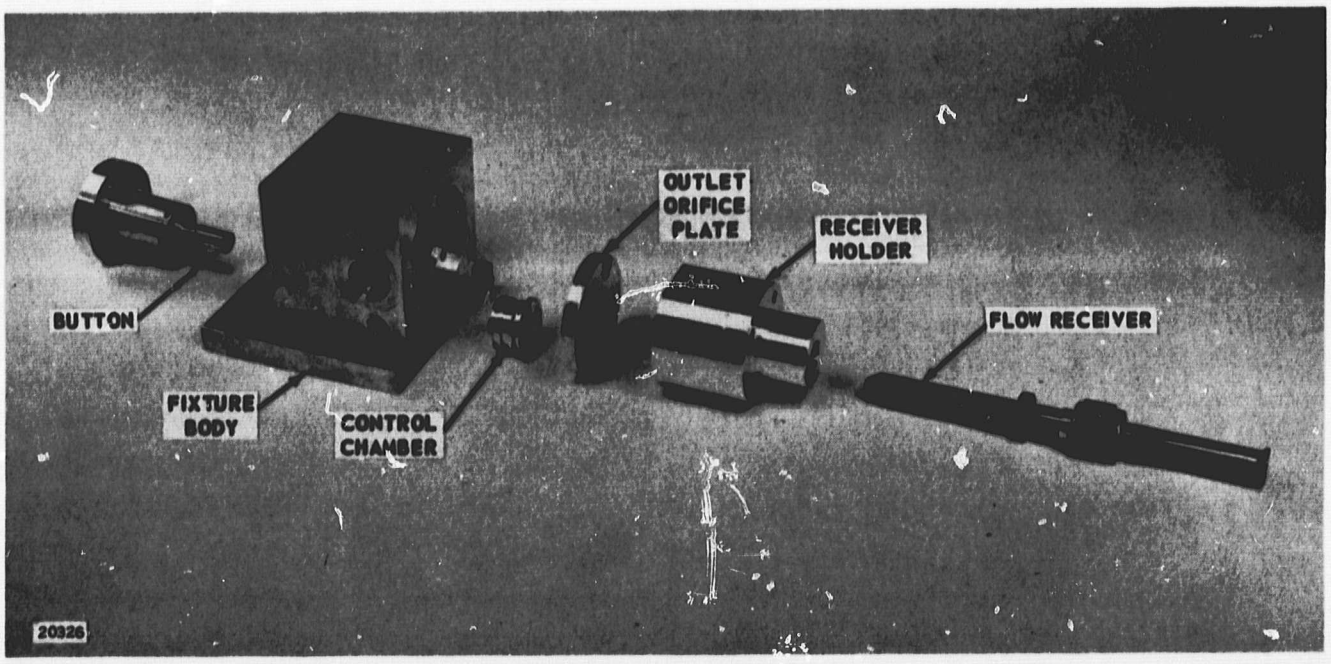

Figure 35 - Single Outlet Vortex Valve Fixture

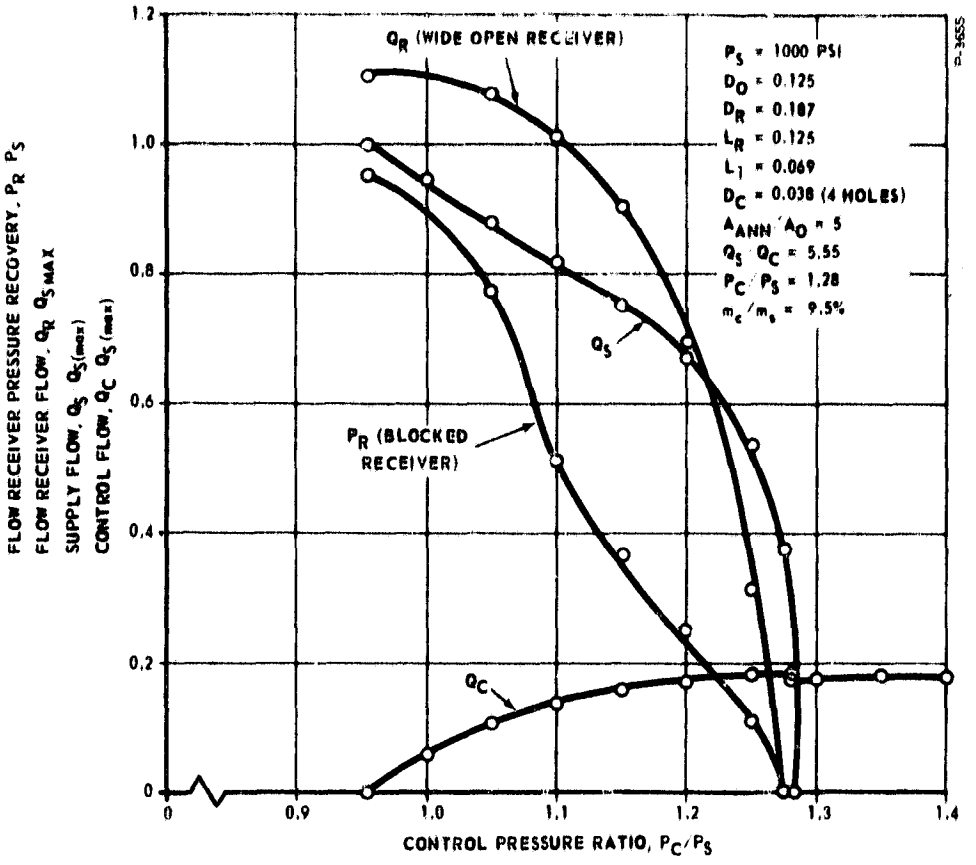

Figure 36 - Single Outlet Vortex Valve Performance Characteristics

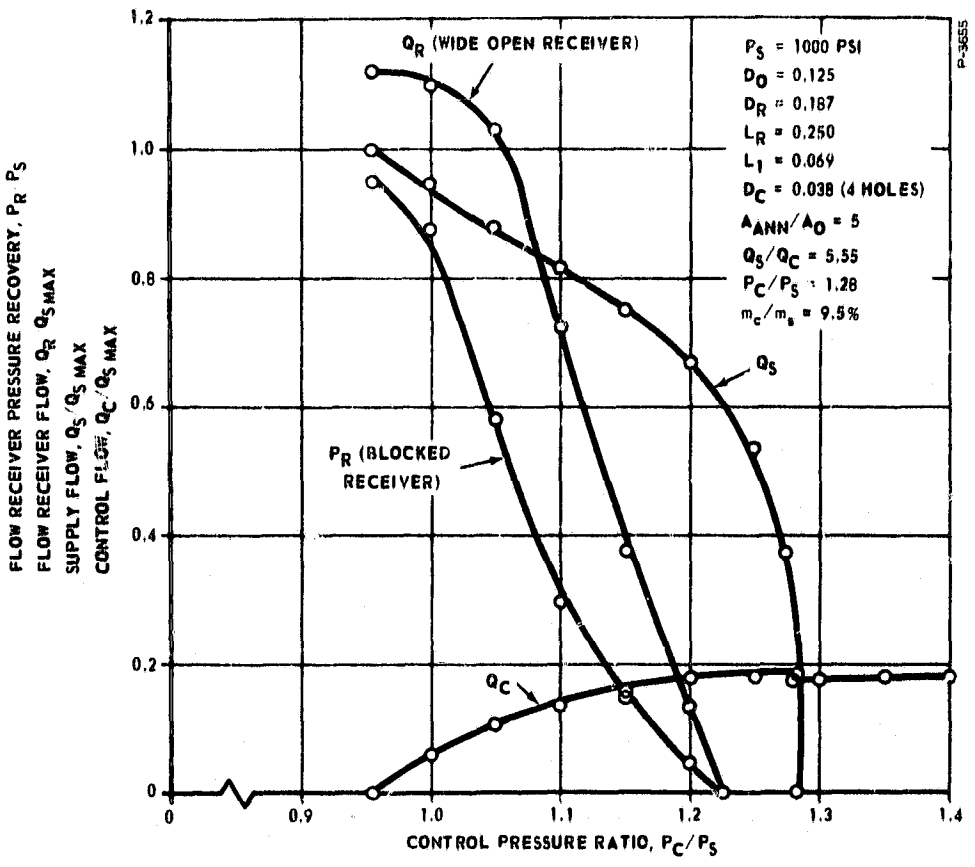

Figure 37 - Single Outlet Vortex Valve Performance Characteristics

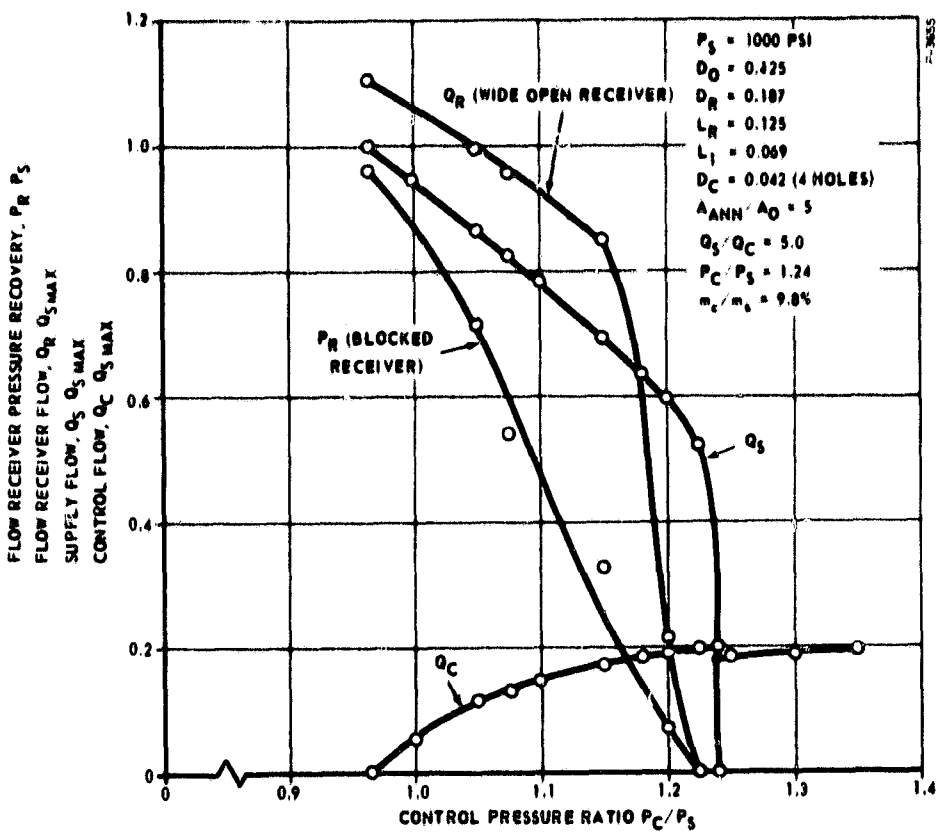

Figure 38 - Single Outlet Vortex Valve Performance Characteristics

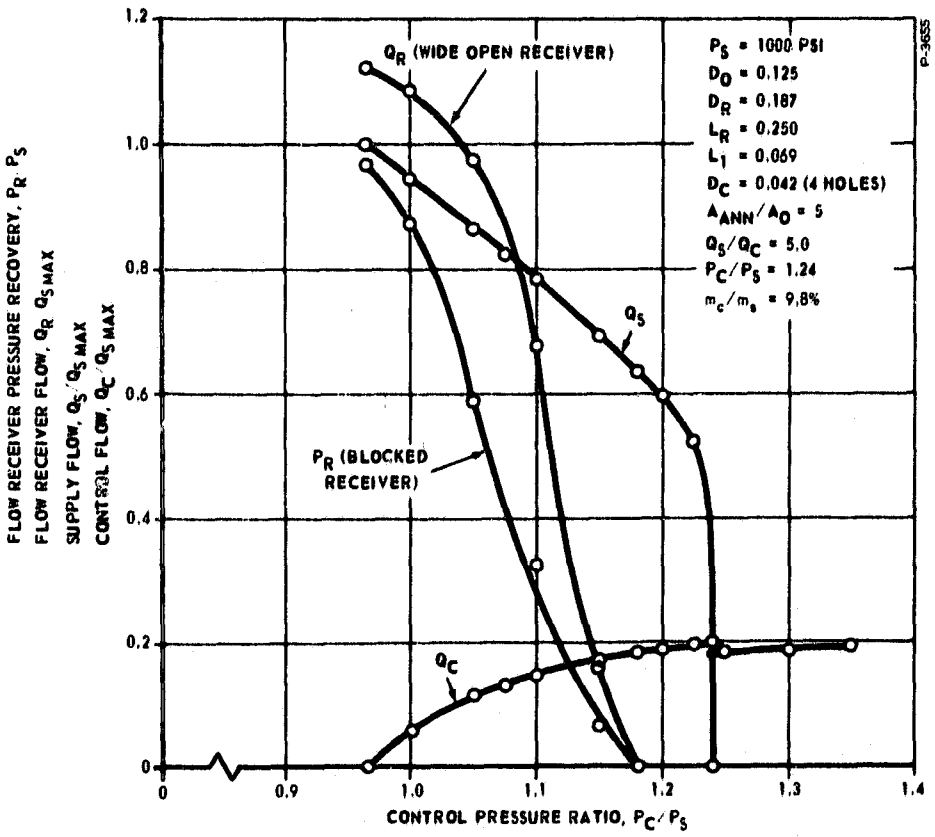

Figure 39 - Single Outlet Vortex Valve Performance Characteristics

Table II - Summary of Single Outlet Vortex Valve Data (P_s = 1000 psi)

	D_c = 0.038	D_c = 0.042
Q_s/Q_c	5.55	5.00
P_c/P_s	1.28	1.24
m_c/m_s (%)	9.50	9.80
$P_{R_{MAX}}/P_S$ ($L_r = D_o$)	0.95	0.96
$Q_{R_{MAX}}/Q_s$ ($L_R = D_o$)	1.11	1.11
$P_{R_{MAX}}/P_s$ ($L_R = 2\ D_o$)	0.95	0.97
$Q_{R_{MAX}}/Q_s$ ($L_R = 2\ D_o$)	1.12	1.12

P-5876

where

P_c/P_s = control pressure ratio at full turndown

$Q_{S_{max}}/Q_c$ = turndown ratio

The momentum ratio thus defined is a measure of the efficiency of the vortex valve since lower values of momentum ratio indicate a more efficient mixing of the control and supply flows.

Vortex valve performance tests were also carried out with MIL-H-5606 hydraulic oil at a constant supply pressure of 2300 psi. This pressure level is the design supply pressure level of the hydraulic fluidic servo-valve. Previous vortex valve tests were performed at 1000 psi supply pressure because the hydraulic stand was flow-limited. A hydraulic test stand capable of delivering 30 gpm at 3000 psi was installed in the Fluid Power Laboratory, allowing comparative tests to be performed at the higher pressure level.

For this series of tests, the vortex valve test fixture was set up with the following proportions:

(1) Outlet Hole Diameter, D_o = 0.125

(2) Flow Receiver Diameter, D_R = 0.125 and 0.187

(3) Flow Receiver Spacing, L_R = 0.125 and 0.250

(4) Control Port Diameter, D_c = 0.042 and 0.045

(5) Number of Control Holes = 4

(6) Vortex Chamber Diameter, D_{ch} = 0.500

(7) Button Diameter, D_B = 0.415

(8) Vortex Chamber Spacing, L_1 = 0.069

The results of the performance tests are shown in Figures 40 through 45. Figures 40 and 41 present performance data for flow receiver spacings of 0.125 and 0.250 inch and diameter of 0.187 inch. Figures 42 and 43 present the performance data for the same flow receiver diameter and spacings but with a control port diameter of 0.045 inch. The data of Figures 44 and 45 were obtained with a smaller diameter receiver (0.125 inch) at spacings of 0.125 inch and 0.250 inch, respectively. (The control port diameter was 0.045 inch for these last tests.)

For a control port diameter of 0.042 inch, a flow turndown, Q_s/Q_c, of 4.97 was obtained at a control pressure ratio, P_c/P_s, of 1.225. This results in a control momentum ratio, m_c/m_s, of 9.5%. For a control port diameter of 0.045 inch, Q_s/Q_c = 4.70 at P_c/P_s = 1.19, resulting in a control momentum ratio of 9.25%.

Flow receiver data for these tests indicate that maximum blocked receiver pressure recovery varies between 92.5 and 98% of supply pressure depending upon receiver diameter spacing. Maximum unloaded receiver flow varies between 86 and 110% of supply flow, again depending upon receiver diameter and spacing. The receiver flow value greater than supply flow results from entrainment of fluid from the vent. Receiver flow and pressure become zero at or prior to complete supply flow cutoff, depending upon control port diameter and receiver diameter and spacing.

The hydraulic vortex servovalve, in which two vortex valves operate in a push-pull circuit, should have the following receiver and control port proportions:

(1) D_R/D_o = 1.5

(2) L_R/D_o = 2.0

(3) Total Control Port Area/Outlet Hole Area, A_c/A_o = 0.53

The servovalve control pressure ratio design limit has been set at 1.2. Test data for a test fixture configuration most nearly matching these servovalve dimensionless design proportions are shown in Figure 43. These data do not take into account any effects of operating two vortex

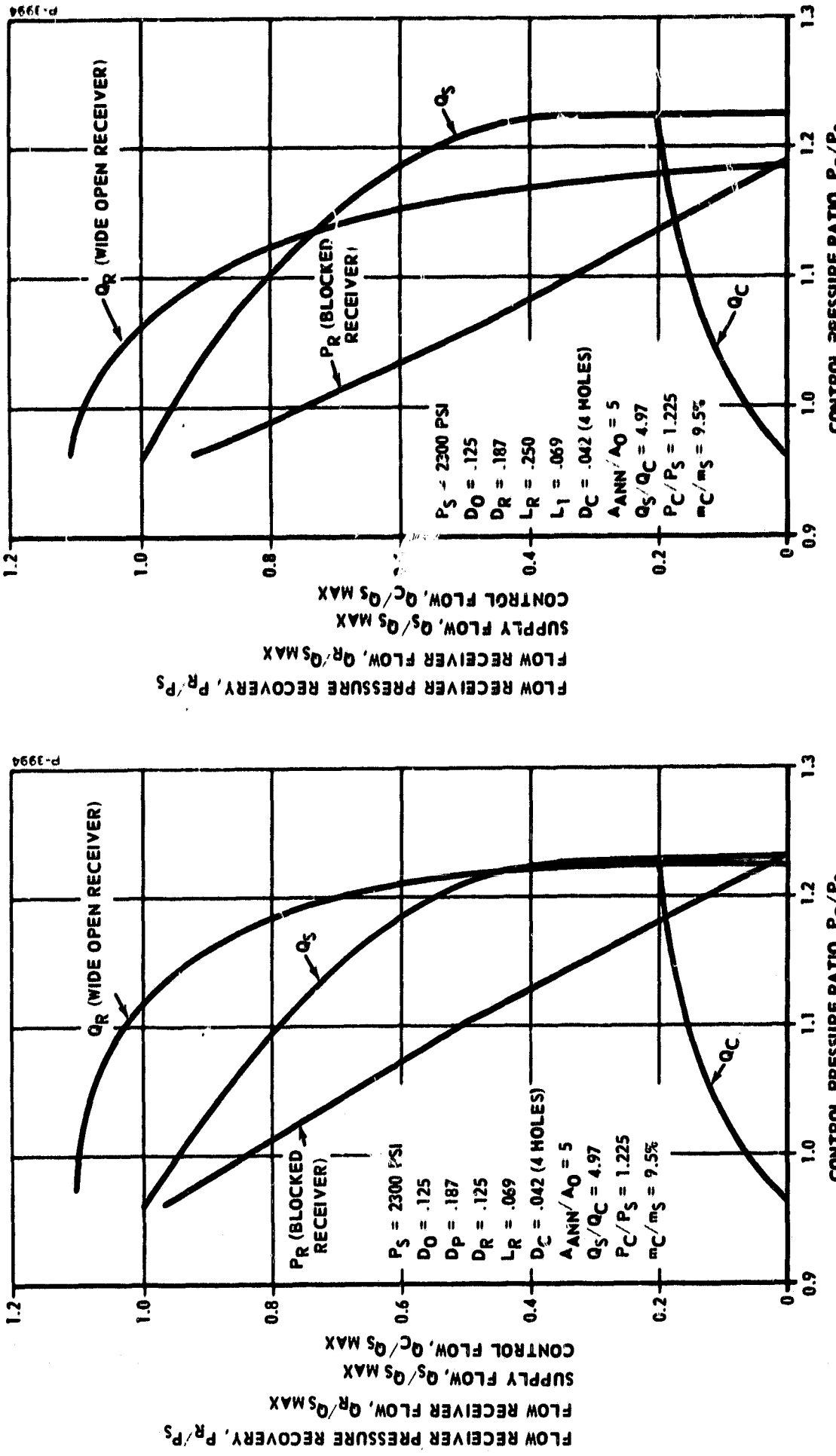

Figure 41 - Single Outlet Vortex Valve Performance Characteristics - Long Spacing

Figure 40 - Single Outlet Vortex Valve Performance Characteristics - Close Spacing

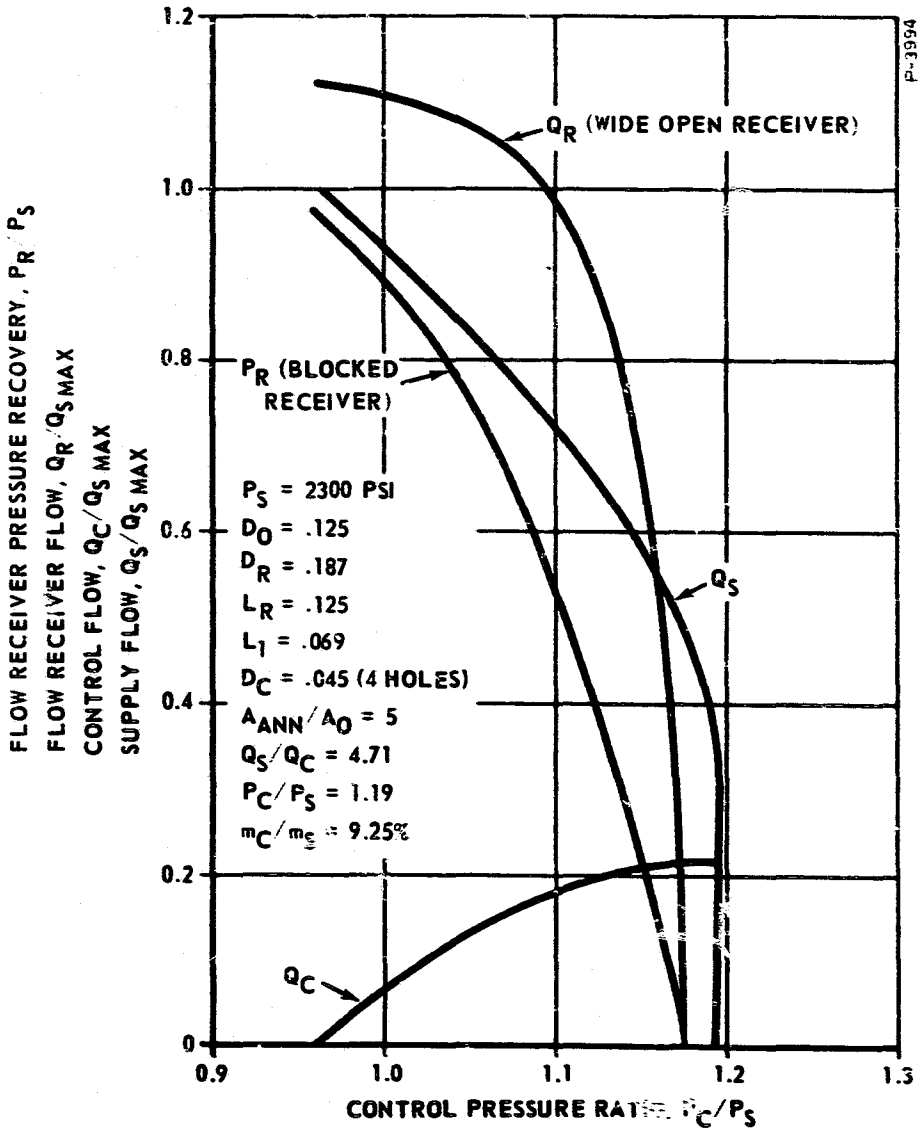

Figure 42 - Single Outlet Vortex Valve Performance Characteristics - Close Spacing

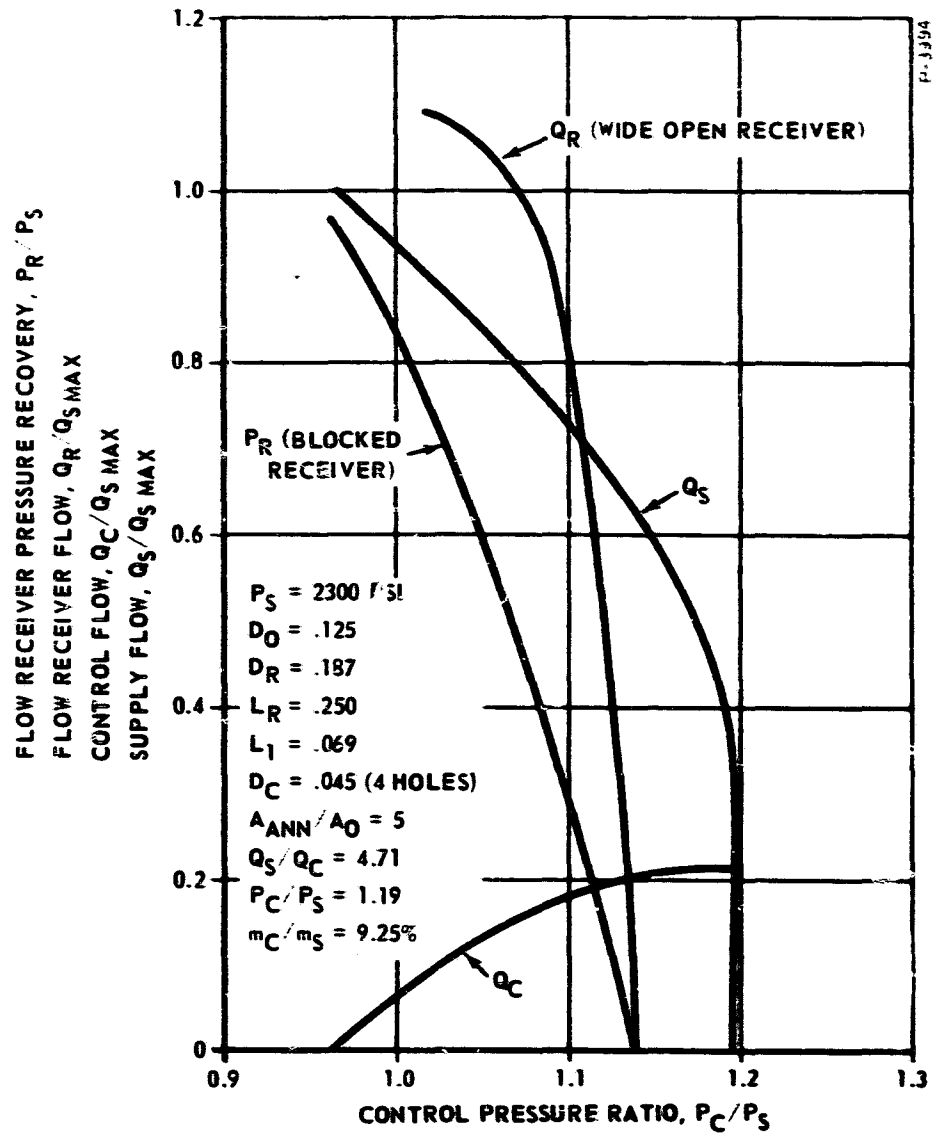

Figure 43 - Single Outlet Vortex Valve Performance Characteristics - Long Spacing

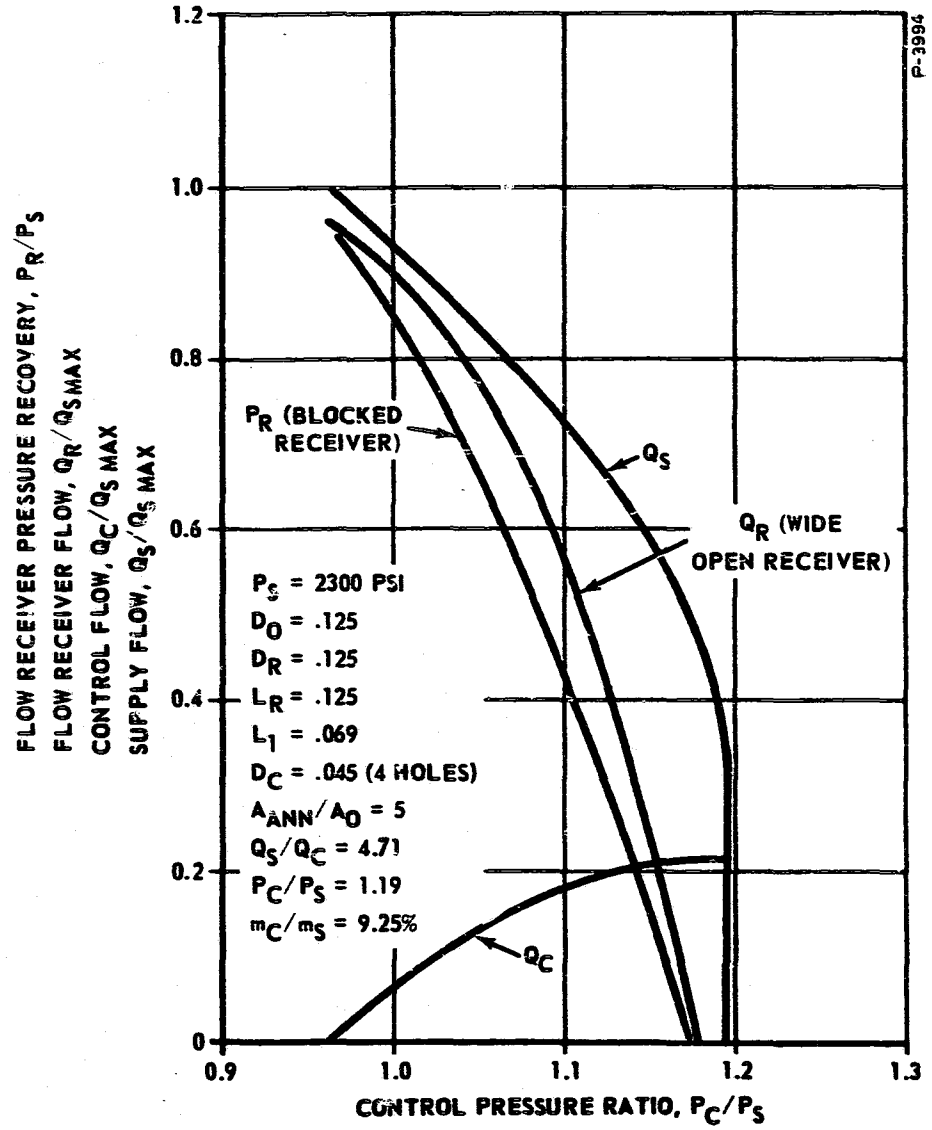

Figure 44 - Single Outlet Vortex Valve Performance Characteristics - Close Spacing

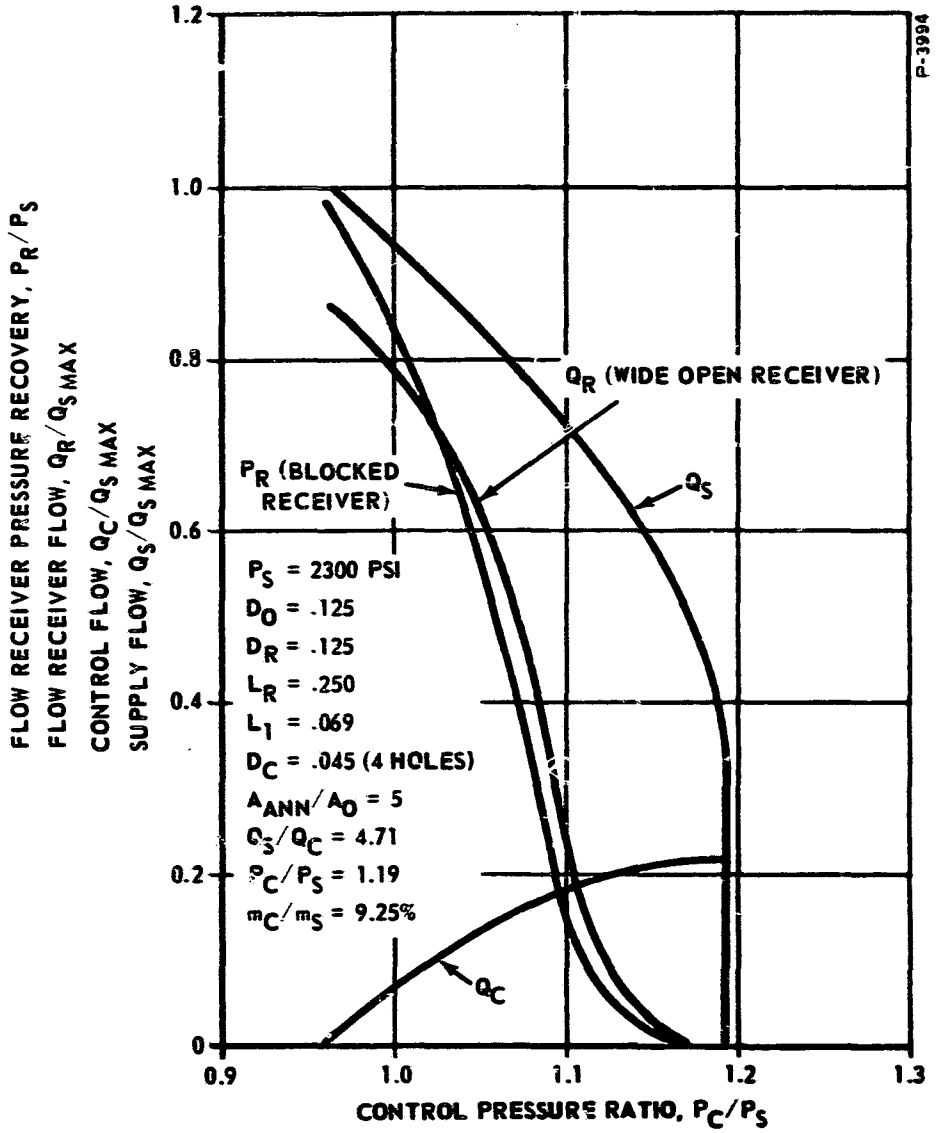

Figure 45 - Single Outlet Vortex Valve Performance Characteristics - Long Spacing

valves in a push-pull arrangement, but they can be used to establish preliminary system performance.

Double outlet vortex valve-button type.- Since the preliminary hydraulic circuit calculations indicated a need for improved flow efficiency of the servovalve, an investigation of the double outlet vortex valve was initiated. The double outlet vortex valve has potential for improved control momentum efficiency and this improvement in the fluidic servovalve circuit would result in reduced pilot stage flow. The double outlet concept had been proven in pneumatic applications but the hydraulic counterpart had previously been unexamined.

Two different series of tests were performed with the device. The first series of tests was aimed at optimization of the vortex valve geometry without consideration of the flow receiver performance (which would be eventually required for a power transfer application). The second series of tests was performed with a double outlet vortex valve using a flow receiver, and the optimum geometry was determined from the first series of tests. The goal of the second series of tests was to evaluate the flow receiver performance of the device.

Basic optimization tests of the double outlet vortex valve were performed with the fixture shown in Figure 46. The effect of valve proportions on the control momentum ratio, m_c/m_s, was determined from the following tests:

(1) Variation of button spacing with a single row of control holes - secondary outlet hole blocked.

(2) Variation of button spacing with a double row of control holes - secondary outlet hole blocked.

(3) Variation of secondary outlet hole diameters with single row of control holes.

Since the control chamber sleeve as shown in Figure 46 did not provide a constant annulus over the button spacing range of interest, another control chamber sleeve was manufactured and assembled in the test fixture as shown in Figure 47. Tests were performed with this sleeve to optimize button spacing, secondary outlet hole diameter, and supply annulus area. The test hardware is shown in Figures 48 and 49.

Another configuration, Figure 50, was also tested. The control chamber sleeve and one vortex valve button were reworked so that the supply flow would be fed into the vortex chamber over only one of the buttons. Optimization of the secondary outlet hole diameter and button spacing was performed.

The results of the tests are as follows:

(1) Variation of button spacing - single row control holes - secondary outlet hole blocked. - The double outlet vortex valve fixture was first set up with a single row of four (4) tangential 0.038-inch diameter control holes, centrally located between the buttons. The

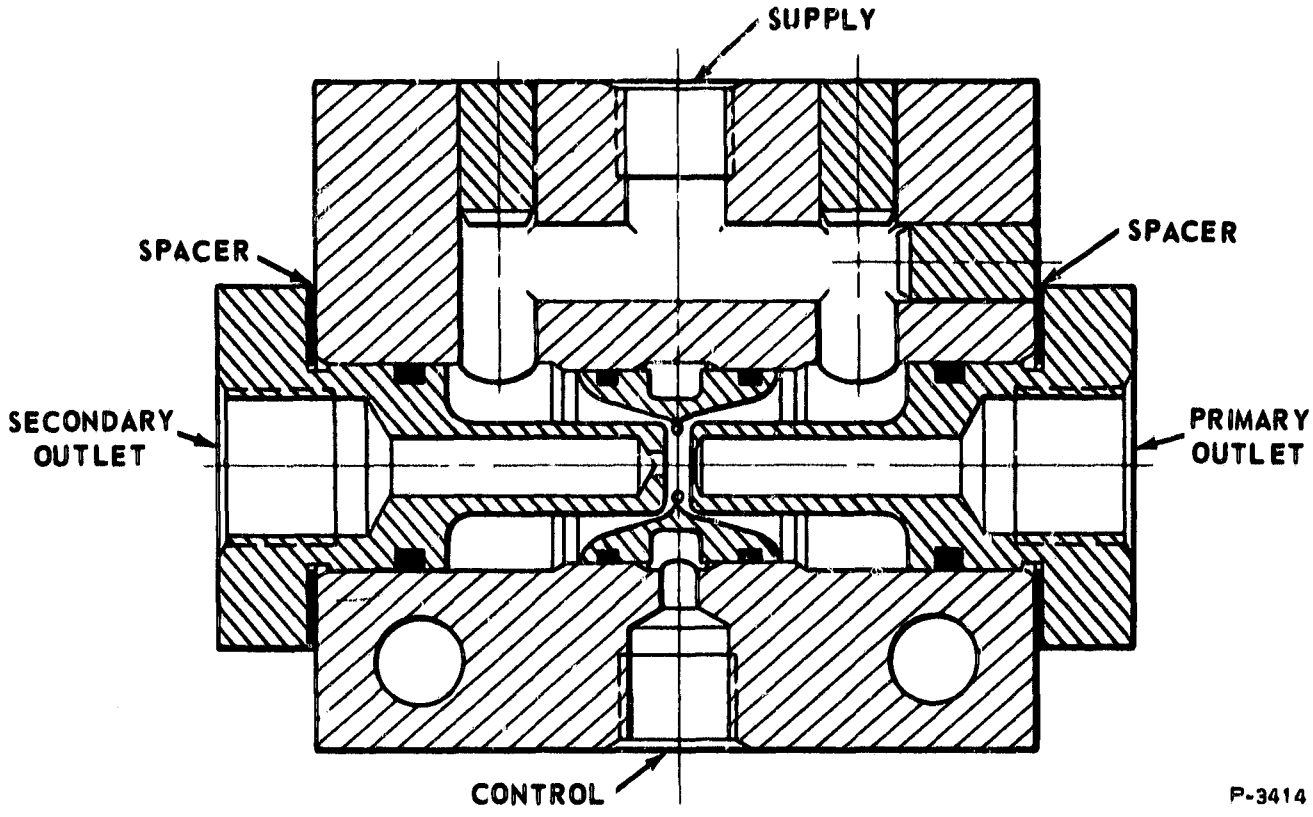

Figure 46 - Double Outlet Vortex Valve (Variable Supply Annulus)

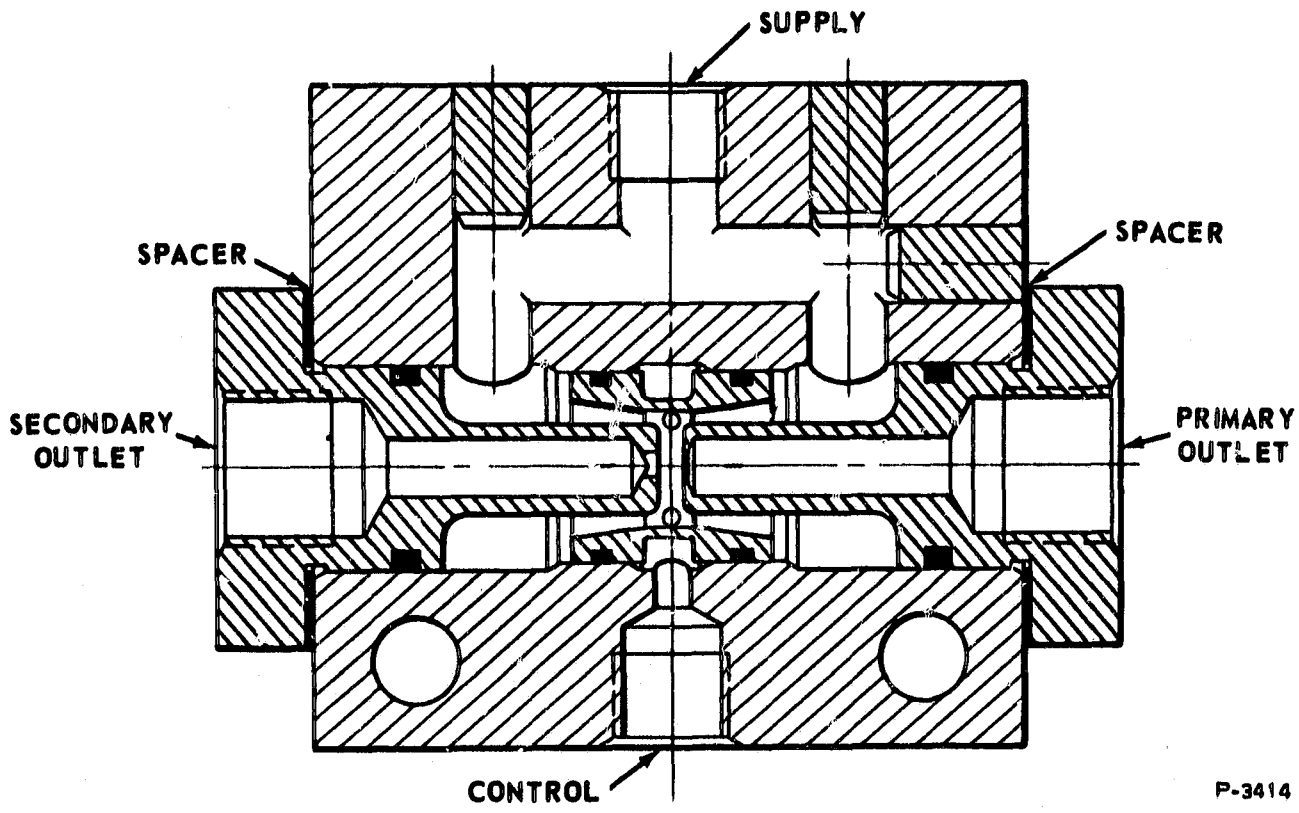

Figure 47 - Double Outlet Vortex Valve (Constant Area Supply Annulus)

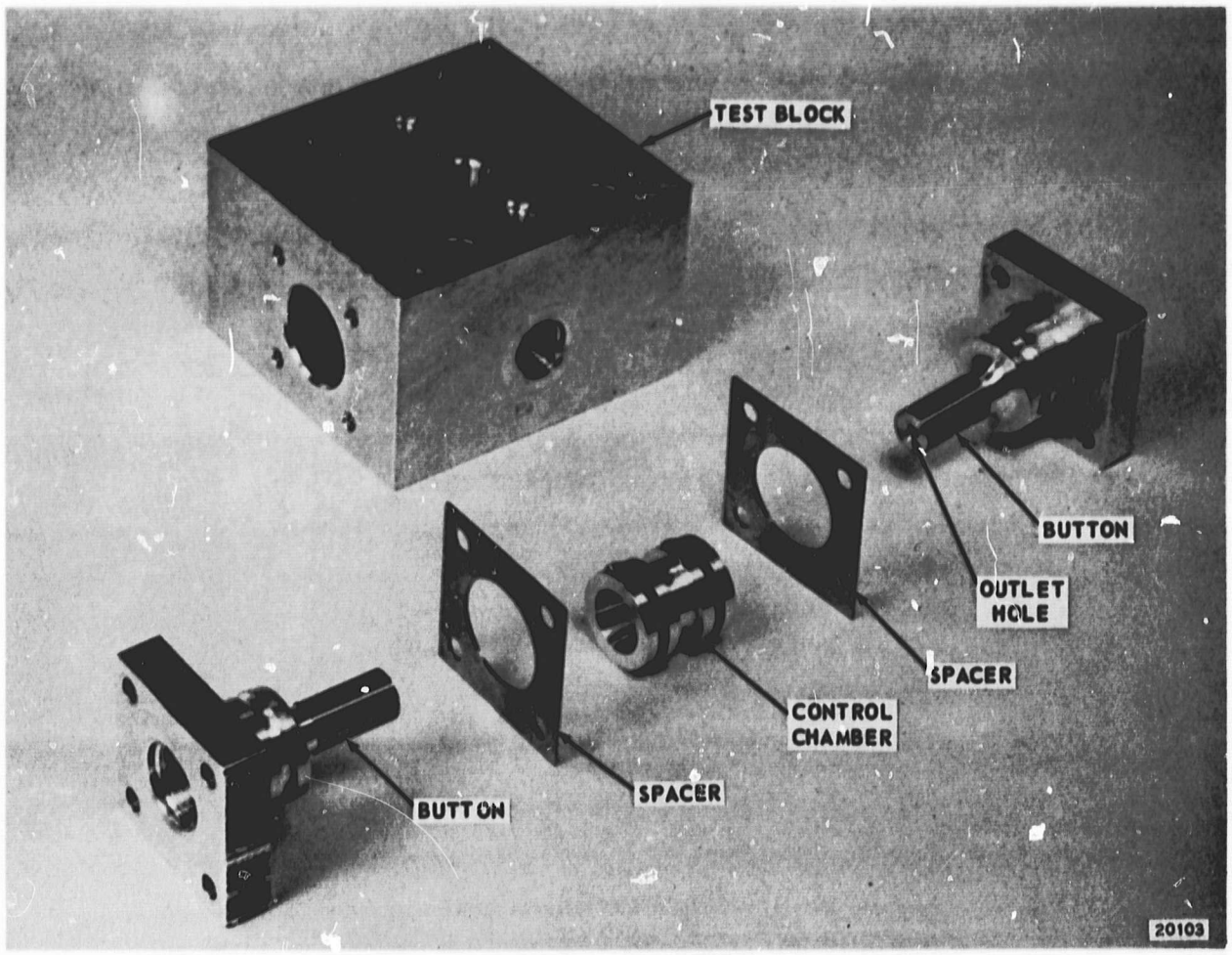

Figure 48 - Double Outlet Vortex Valve Assembly

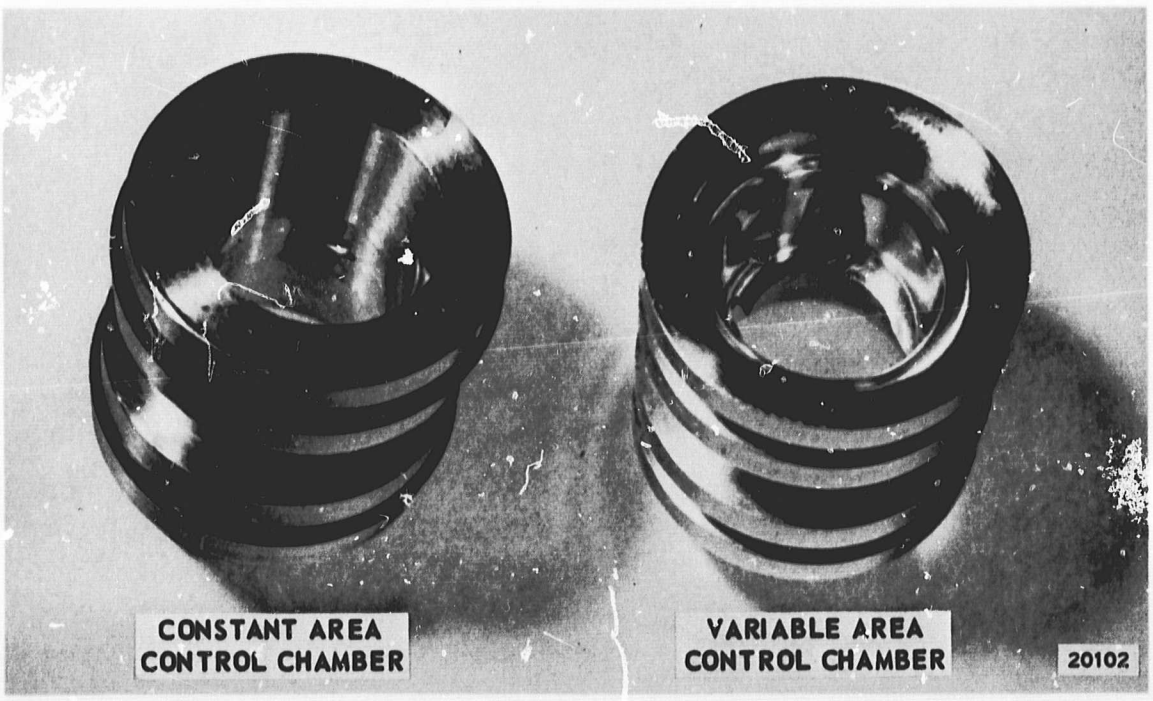

Figure 49 - Double Outlet Vortex Valve Control Chambers

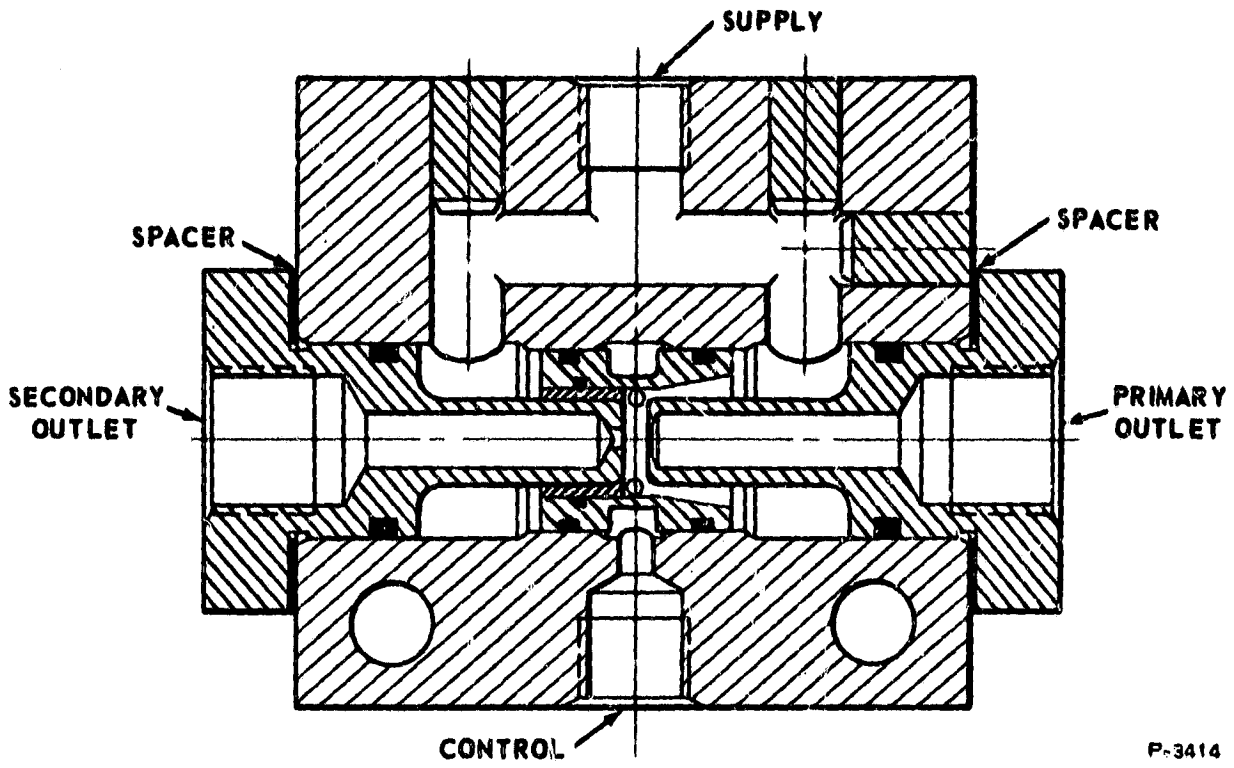

Figure 50 - Double Outlet Vortex Valve (One Supply Annulus Blocked)

primary outlet hole diameter was 0.120, giving a control port to outlet hole area ratio, A_C/A_O, of 0.4. The secondary outlet hole was blocked and the button spacing was varied from 0.018 inch to 0.120 inch. The supply annulus area ratio, A_{ANN}/A_O, was approximately 5:1, but due to the variable internal diameter of the control chamber sleeve (Figure 46), the exact value could not be determined.

Figure 51 presents the momentum ratio for the above configuration as a function of button spacing. The minimum momentum ratio of 9.6% was obtained at a button spacing of 0.034 inch. The corresponding value of flow turndown, Q_S/Q_C, was approximately 5.1.

(2) Variation of button spacing - double row of control holes - secondary outlet hole blocked. - These tests were performed with a second control chamber sleeve containing two (2) rows of control holes. Each row, consisting of four (4) tangential 0.026-inch diameter holes located at 0.100 inch from the center line between buttons, was varied from 0.018 inch to 0.300 inch.

Figure 52 is a plot of the momentum ratio for this configuration. The minimum momentum ratio of 16.2% occurs at a button spacing of 0.060 inch. Maximum flow turndown in this case was 4.16.

(3) Variation of secondary outlet hole diameter - single row of control holes. - Since the minimum momentum ratio of the vortex valve with the blocked secondary hole was obtained utilizing the single

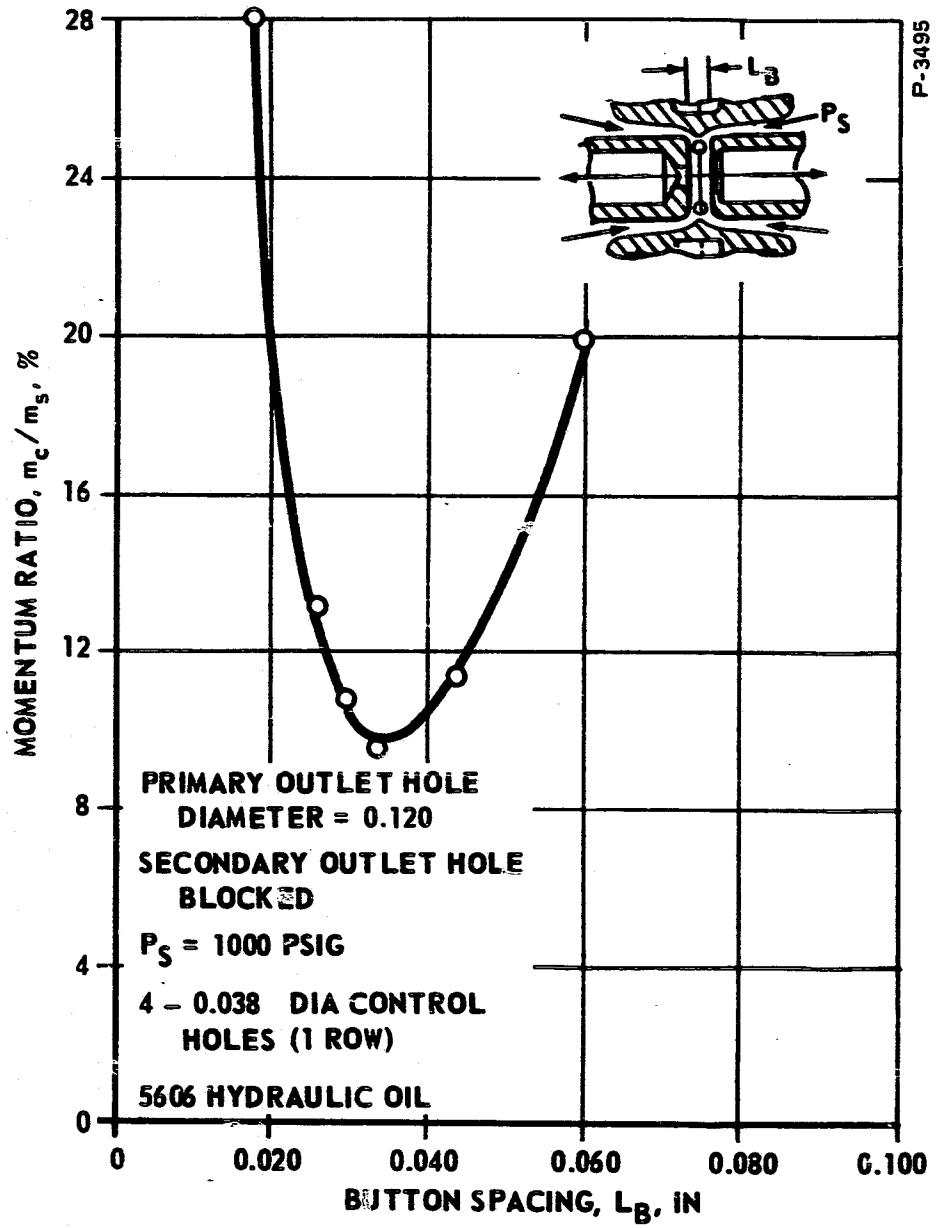

Figure 51 - Momentum Ratio Versus Button Spacing for Double Outlet Vortex Valve - One Row of Control Holes

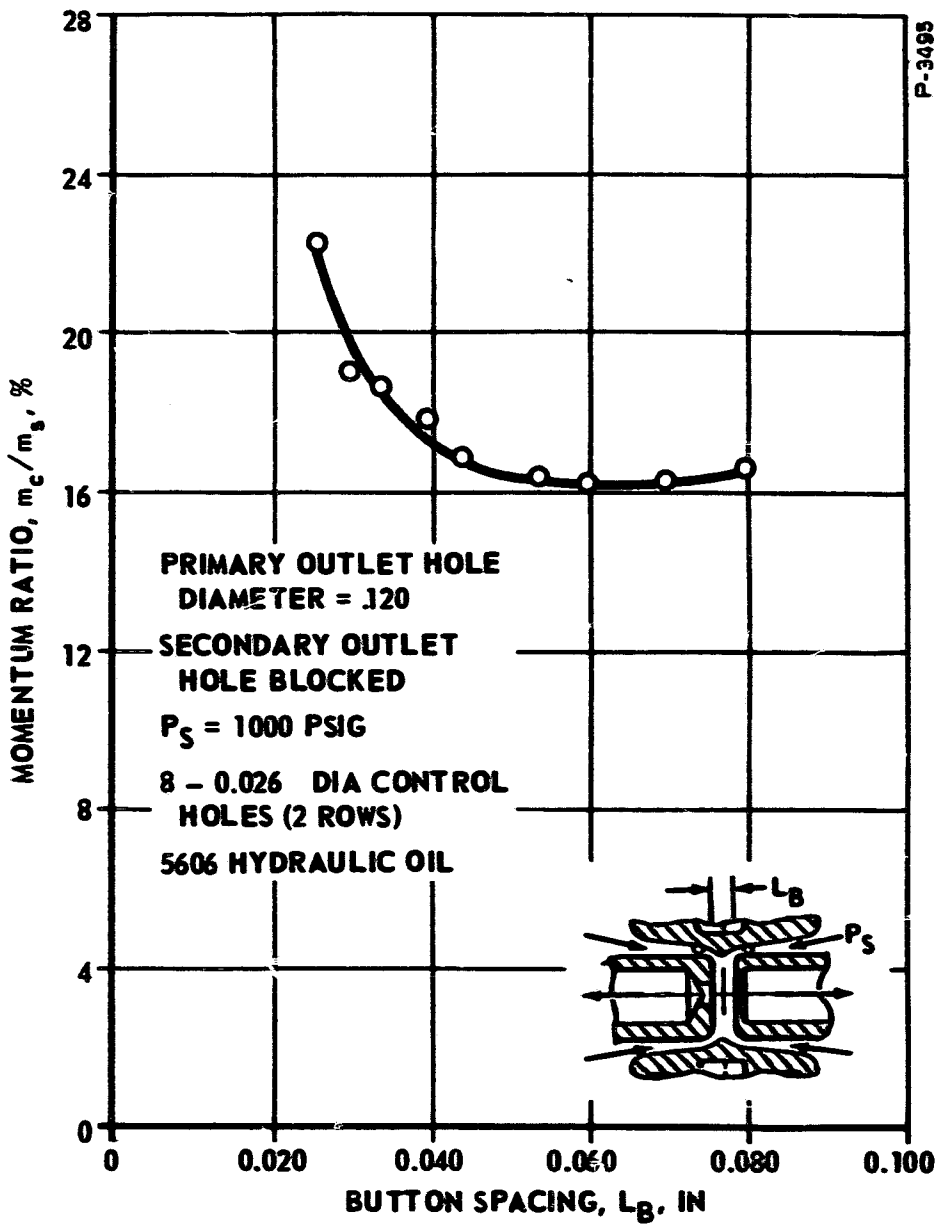

Figure 52 - Momentum Ratio Versus Button Spacing for Double Outlet Vortex Valve - Two Rows of Control Holes

row of control holes, the vortex valve fixture was reassembled with the single row of control holes, and the secondary outlet hole diameter was varied from 0.038 inch to 0.120 inch. The button spacing was held at 0.034 inch. The results of these tests are shown in Figure 53. The minimum momentum ratio calculated from the test data was 8.05% at a secondary outlet hole diameter of 0.088 inch. The corresponding flow turndown was 5.83.

(4) Optimization of button spacing and secondary outlet hole diameter - constant area control chamber - single row of control holes. - The control chamber sleeve was changed to have a constant internal diameter of 0.48 inch for a distance of 0.125 inch on both sides of the center line between buttons. The supply annulus area ratio was held constant at 5:1. The single row of four 0.038-inch diameter control holes was retained. The button spacing was varied from 0.010 inch to 0.100 inch and the secondary outlet hole diameter was varied from 0 inch to 0.120 inch. Results of these tests are shown in Figure 54. The minimum momentum ratio was approximately 7% at a button spacing of approximately 0.060 inch. This ratio was obtained for secondary outlet hole diameters of 0.088 inch to 0.120 inch as shown in Figure 54. The corresponding flow turndown was approximately 7:1 and varied slightly with outlet hole diameter.

In an attempt to improve the momentum ratio further, a 0.030-inch radius was added to the upstream side of the 0.120-inch diameter secondary outlet hole. The flow turndown was increased to 8:1, but since the control pressure ratio simultaneously increased, the resulting momentum ratio did not change significantly.

(5) Optimization of annulus area - constant area control chamber sleeve - single row of control holes. - For these tests, the vortex valve button diameter was increased by the addition of pressed-on-sleeves. By grinding the outside diameter of the sleeve, a variety of annulus area ratios could be obtained. The actual range used was from 0.5 to 2.0. Based on the data from previous tests, both outlet hole diameters were made 0.120 inch and the button spacing was varied from 0.010 inch to 0.100 inch.

Figure 55 presents the results of these tests. The minimum momentum ratio obtained was 5.77% at an annulus area ratio of 1.25:1 and at a spacing of 0.080 inch. The corresponding maximum flow turndown was 7.75:1 at a P_c/P_s ratio of 1.20. Figure 56 shows the minimum momentum ratio as a function of the annulus area ratio. This curve again shows that the optimum area ratio is 1.25:1.

(6) Optimization of outlet hole diameter and button spacing - one supply annulus blocked - single row of control holes. - These tests were performed with the configuration shown in Figure 50. The annulus area ratio was approximately 4:1 and four 0.038-inch diameter control holes were utilized. The button spacing was varied from 0.020 inch

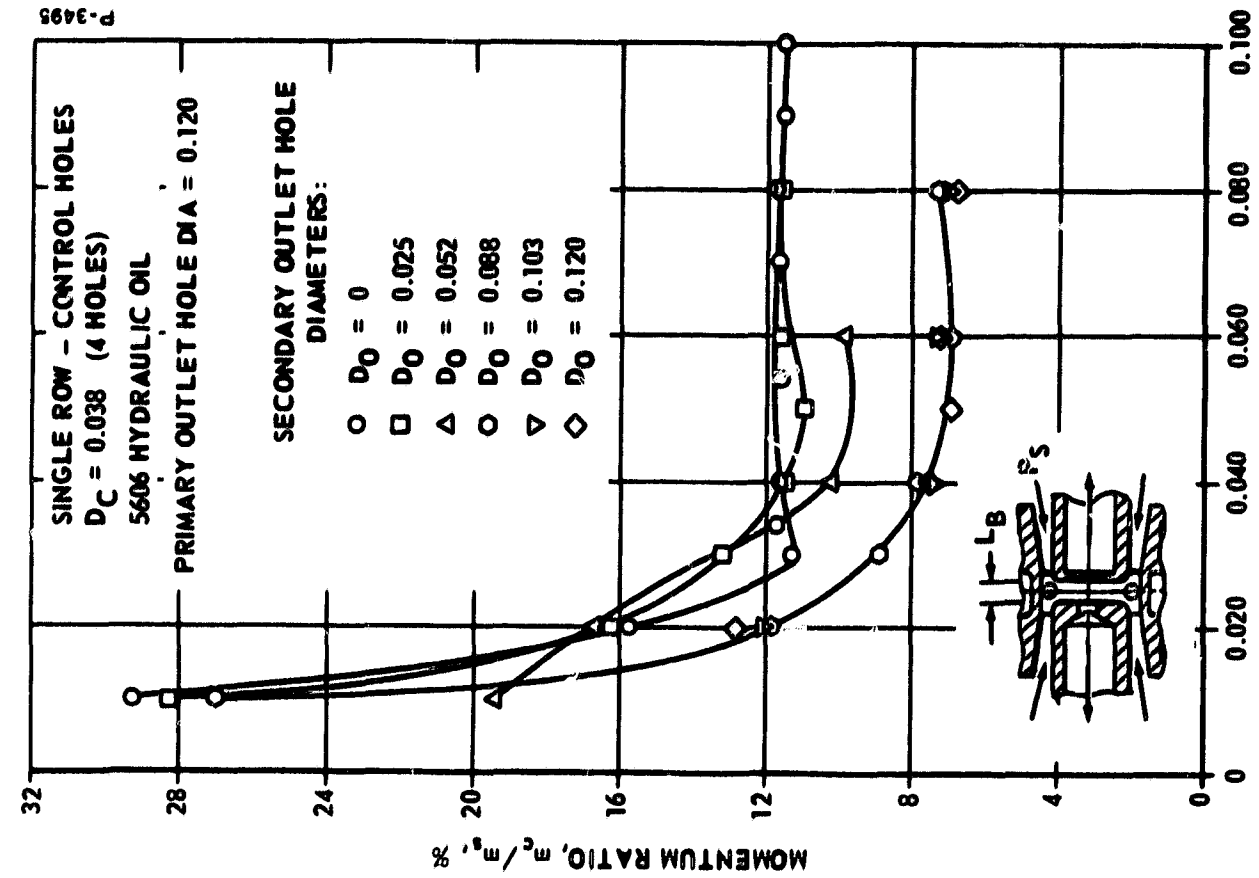

Figure 54 – Momentum Ratio Versus Button Spacing for Double Outlet Vortex Valve – Constant Area Supply Annulus

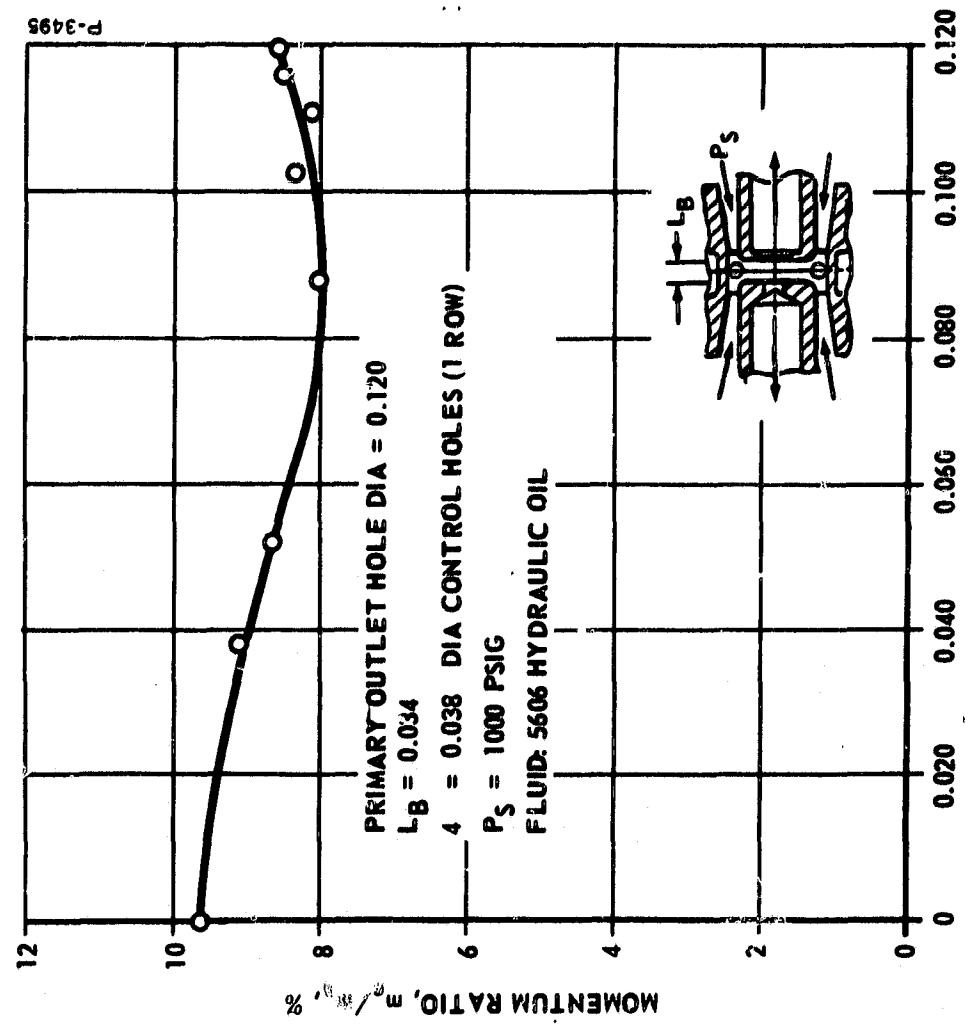

Figure 53 – Momentum Ratio Versus Secondary Outlet Hole Diameter for Double Outlet Vortex Valve

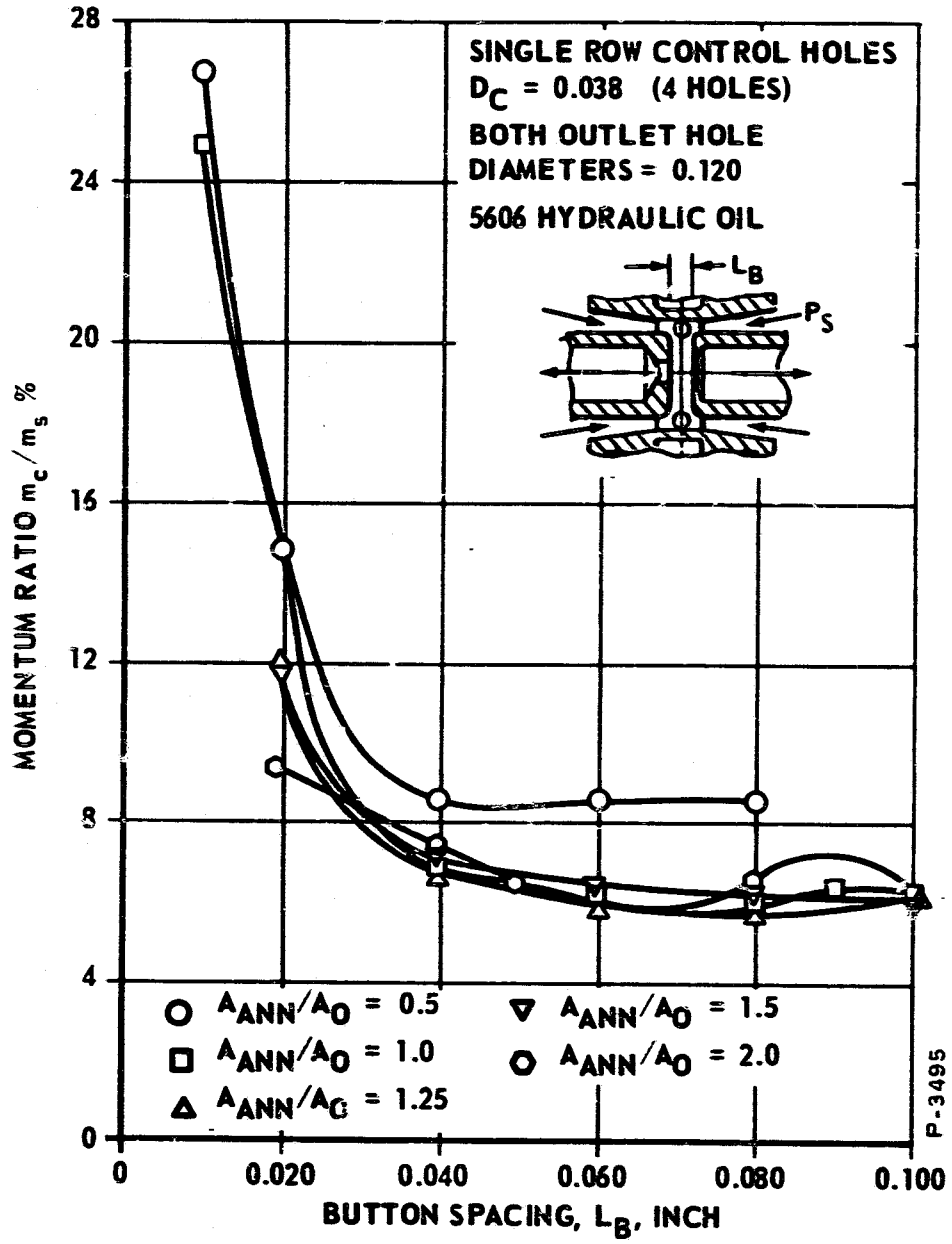

Figure 55 - Momentum Ratio Versus Button Spacing for Double Outlet Vortex Valve - Variable Area Supply Annulus

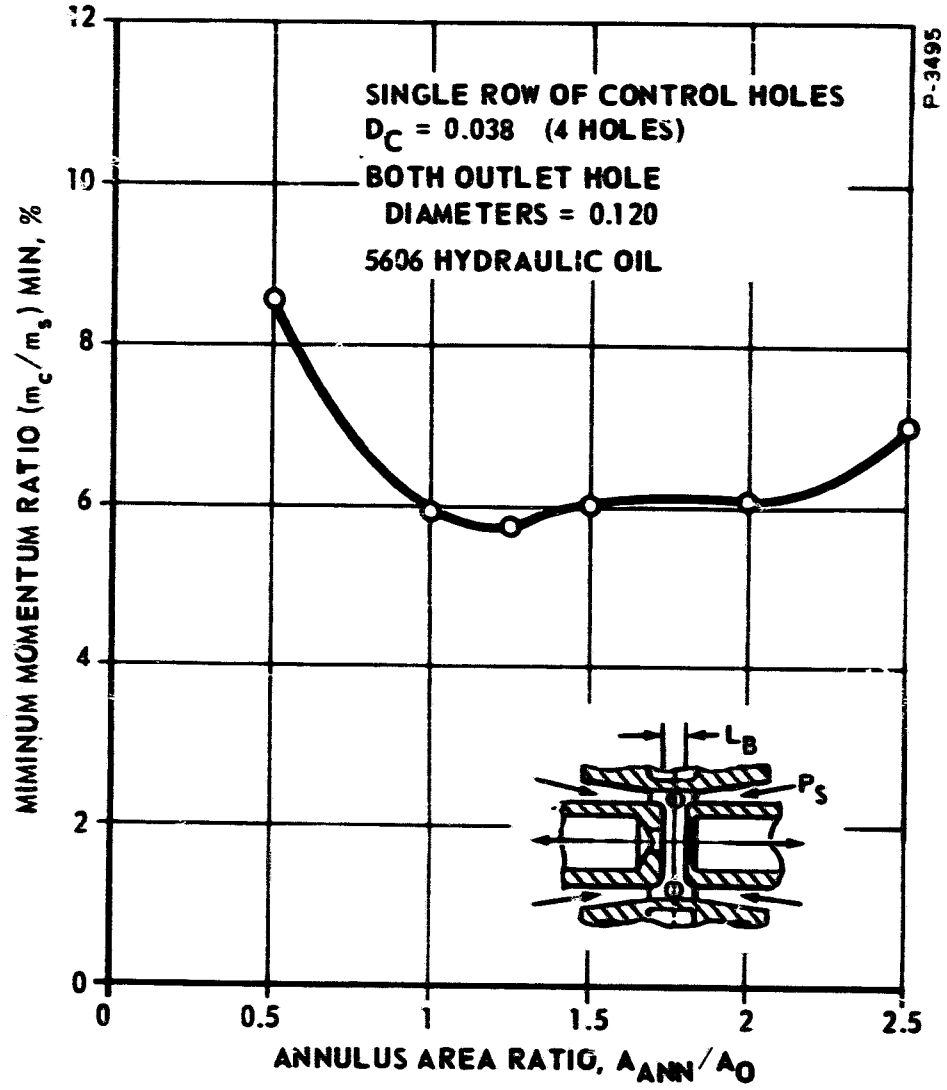

Figure 56 - Minimum Momentum Ratio Versus Annulus Area Ratio for Double Outlet Vortex Valve

to 0.080 inch and the secondary outlet hole was varied from zero to 0.120 inch. Data resulting from these tests are shown in Figure 57. The minimum momentum ratiowas 6.9% at a spacing of 0.040 inch. The maximum flow turndown obtained under these conditions was 7.3:1. Between secondary outlet hole diameters of 0.088 inch and 0.120 inch, there was little difference in performance for the button spacings tested.

Based on the tests performed above, the double outlet vortex valve can be an effective means for improving the efficiency (or control momentum ratio, m_c/m_s) of the conventional single outlet vortex valve. It can be concluded that, with the basic configuration as shown in Figure 47, the following geometrical proportions should be used for optimum performance:

(1) Primary Outlet Hole Diameter = 0.120 inch

(2) Secondary Outlet Hole Diameter = 0.120 inch

(3) Vortex Chamber Diameter = 0.480 inch

(4) Button Spacing = 0.060 to 0.080 inch

(5) Single Row of Four Tangential Control Holes. (Control hole diameter for these tests was 0.038 inch.)

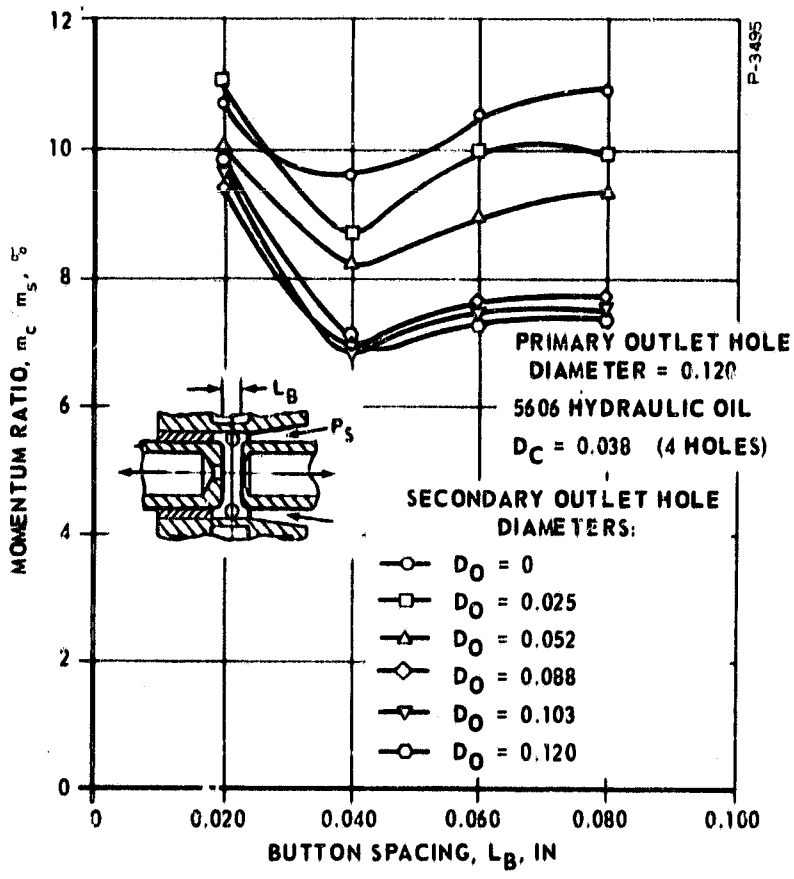

Figure 57 - Momentum Ratio Versus Button Spacing for Double Outlet Vortex Valve - One Supply Annulus Blocked

In ratio form, the proportions are:

	Item	Ratio
(1)	Outlet Hole - primary and secondary D_o	1
(2)	Vortex Chamber Diameter D_{ch}	4 D_o
(3)	Vortex Chamber Length L_b	0.50 to 0.66 D_o
(4)	Total Annulus Area/Total Outlet Hole Area	1.25

After the basic double outlet vortex valve optimization tests were completed, a series of tests was performed to obtain simultaneous vortex valve turndown and flow receiver characteristics. The double outlet vortex valve fixture, Figures 58 and 59, was reworked to include flow receivers for these tests. The fixture was set up with the same basic vortex valve proportions as used in the single outlet vortex valve tests. Two valves of annulus area ratio, 1.25 and 3.00, were investigated and the total control port area was chosen to obtain a control pressure ratio of 1.2 at full turndown. The results of the double outlet tests are shown in Figures 60 through 63. The essential data from these curves are summarized in Table III.

Examination of the performance data shows that the minimum momentum ratio was obtained with the double outlet vortex valve with an annulus area ratio of 1.25. However, the maximum blocked receiver pressure with this configuration was lower than any of the other configurations tested. Since the series orifice combination formed by the "mixing zone" annulus and the outlet hole resulted in a pressure upstream of the outlet hole of only 60% of supply, the maximum blocked receiver pressure, in turn, could only be 50% of the available supply pressure. The blocked receiver pressure was increased to 90% of supply by increasing the annulus area ratio to three (3). This increased the momentum ratio to 8.2%, as indicated in Figure 62 and 63. The control pressure ratio also increased beyond the value of 1.2 thought to be consistent with the overall servovalve circuit performance requirements.

Double outlet vortex valve - radial type. - A radial inlet double outlet vortex valve was also briefly investigated. This concept offered simplicity of design and potential for reduction of size over the double outlet devices described previously. This results primarily from elimination of the button in the vortex chamber and utilizing a cylindrical chamber which is supplied at the outer periphery as shown in Figure 64. The control ports are angle-drilled into the chamber end-walls. All of the vortex action takes places between the point of control flow injection and the outlet holes. As shown in Figures 64 and 65, all the vortex valve parts are simply machined cylindrical pieces. The test fixture is larger than would be required because of the geometrical variations and porting required for the testing.

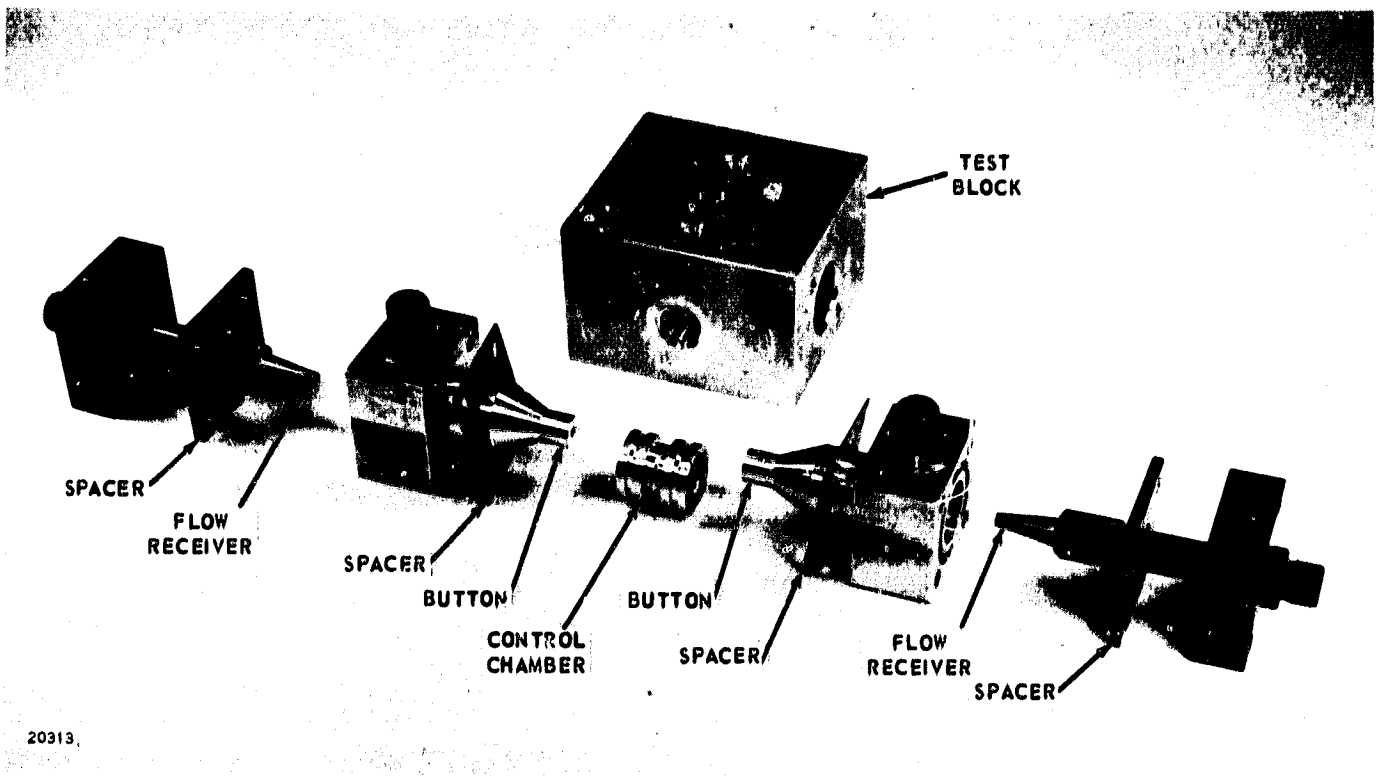

Figure 58 - Double Outlet Vortex Valve Fixture

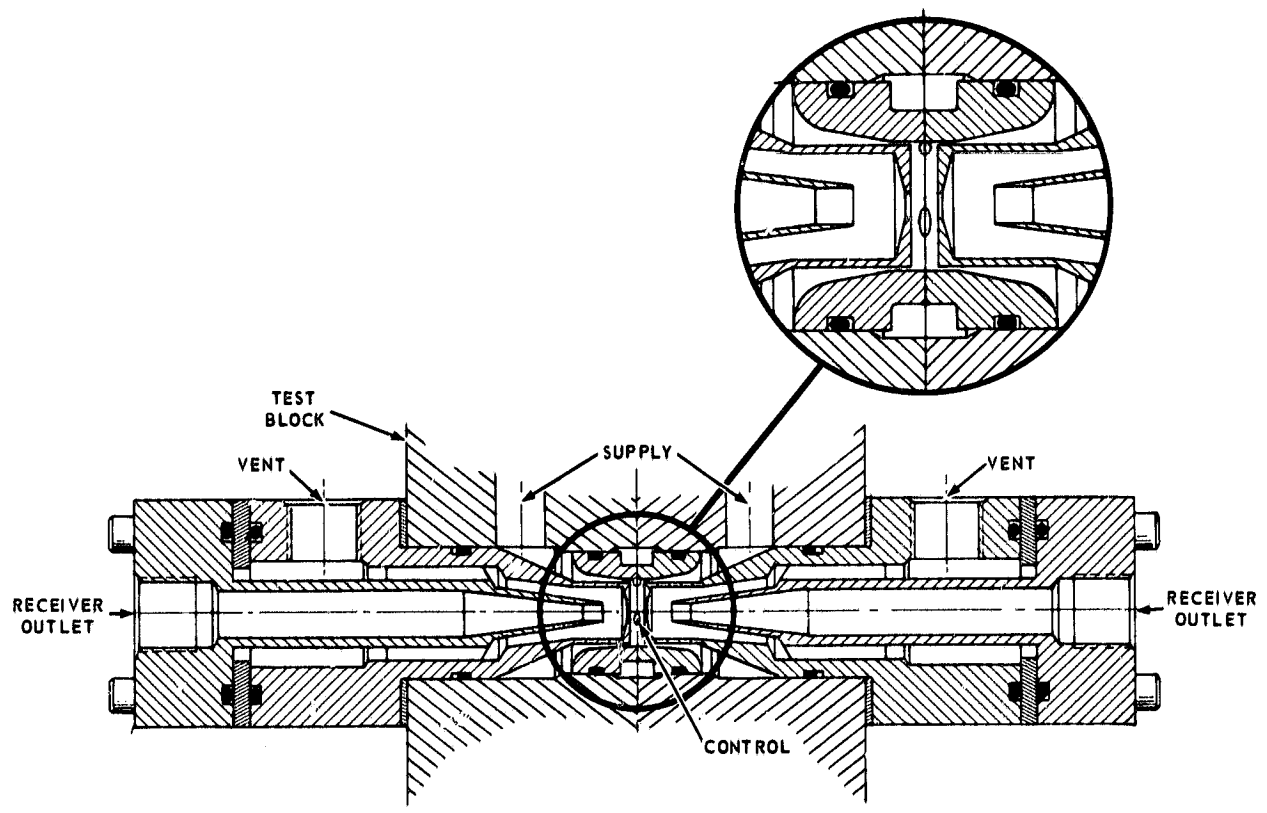

Figure 59 - Double Outlet Vortex Valve Performance Characteristics

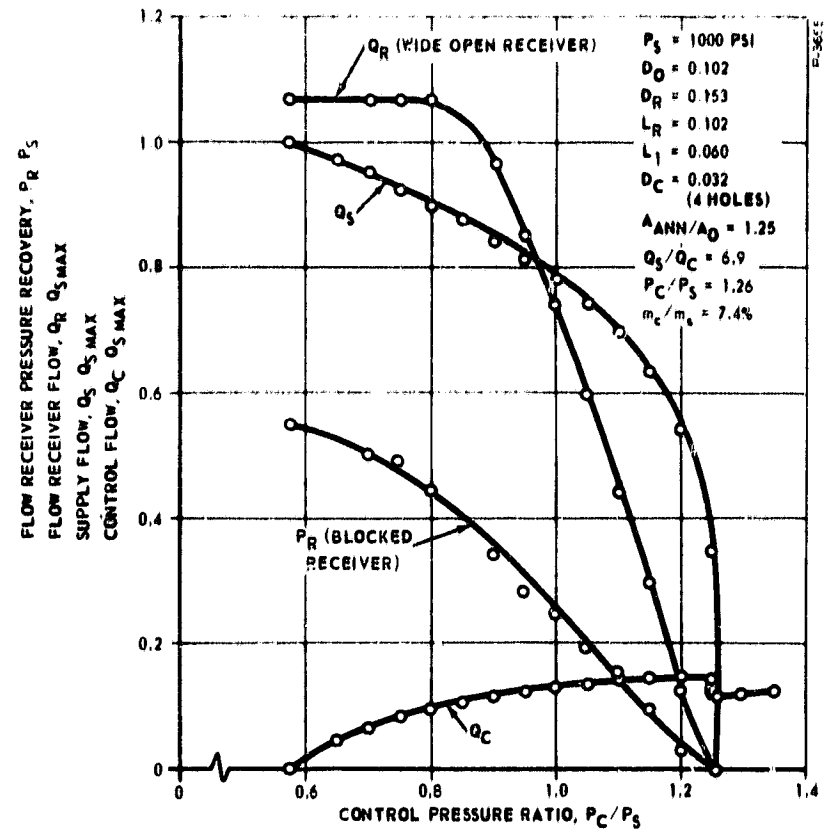

Figure 60 - Double Outlet Vortex Valve Performance Characteristics

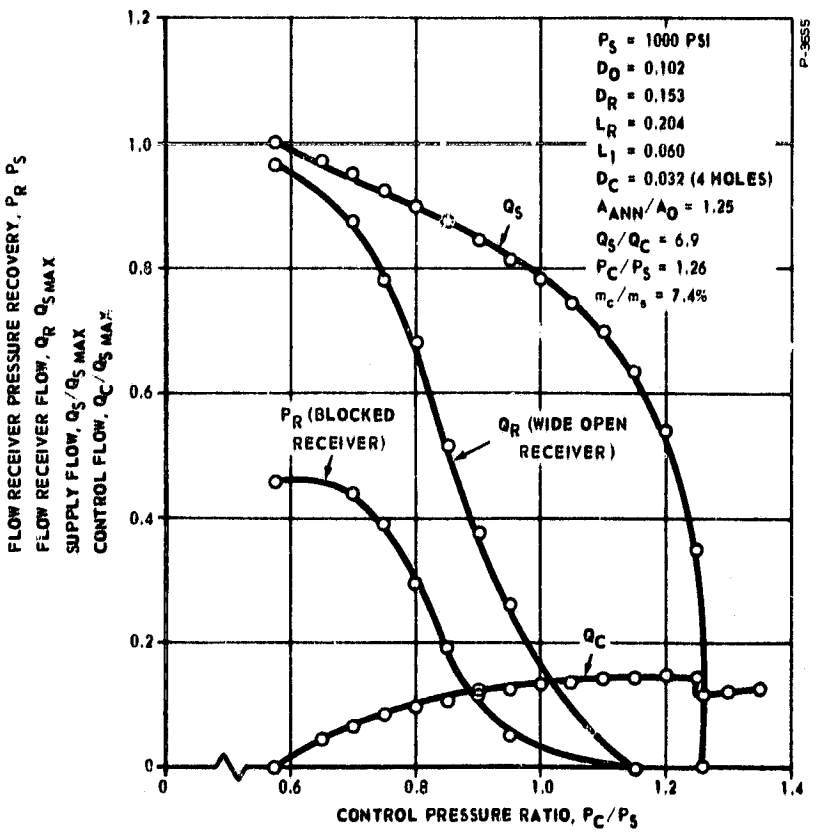

Figure 61 - Double Outlet Vortex Valve Performance Characteristics

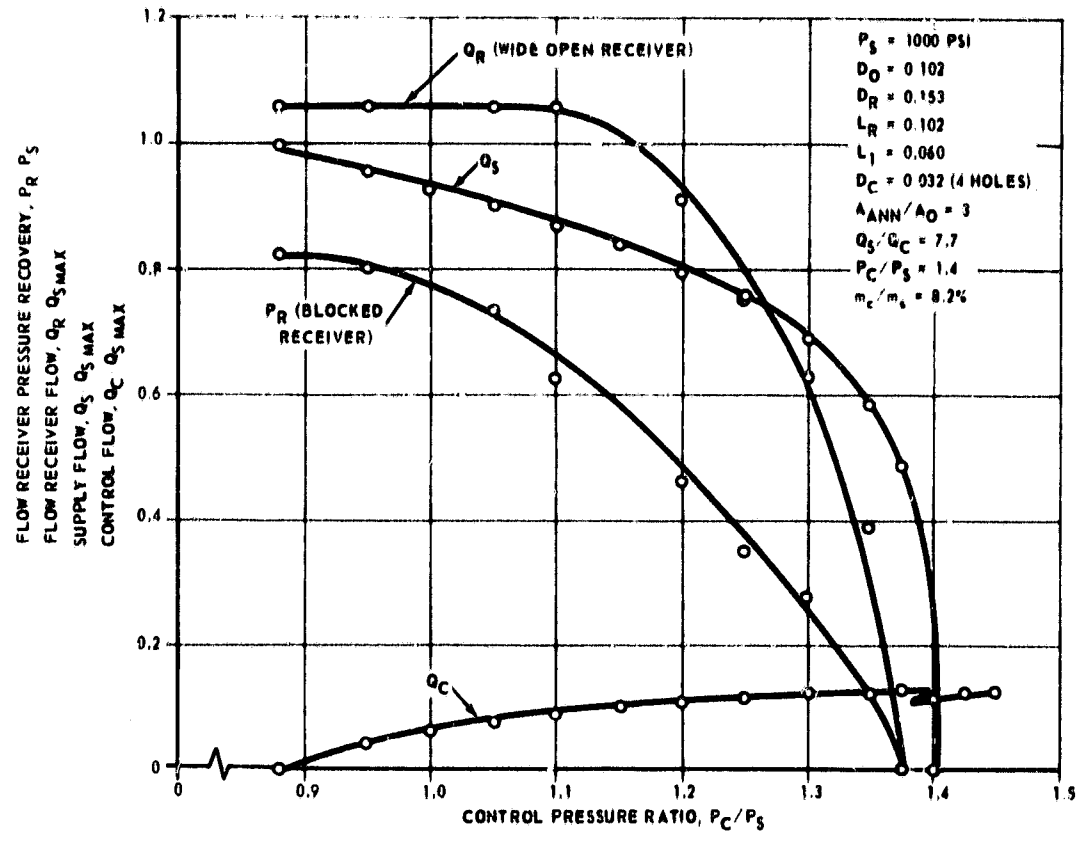

Figure 62 - Double Outlet Vortex Valve Performance Characteristics

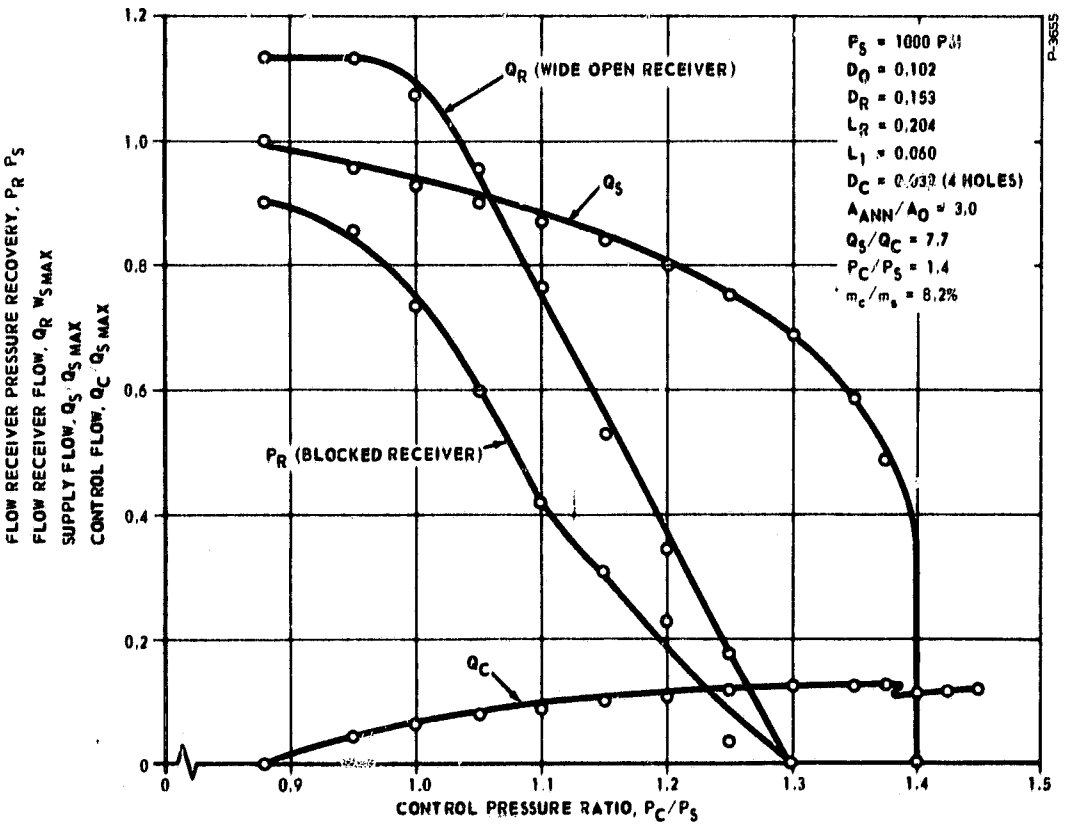

Figure 63 - Double Outlet Vortex Valve Performance Characteristics

Table III - Summary of Double Outlet Vortex Valve Test Data

	A_{ANN}/A_o = 1.25	A_{ANN}/A_o = 3
Q_s/Q_c	6.90	7.70
P_c/P_s	1.26	1.40
m_c/m_s (%)	7.40	8.20
$P_{R_{MAX}}/P_s$ ($L_R = D_o$)	0.55	0.825
$Q_{R_{MAX}}/Q_s$ ($L_R = D_o$)	1.07	1.06
$P_{R_{MAX}}/P_s$ ($L_R = 2\ D_o$)	0.46	0.90
$Q_{R_{MAX}}/Q_s$ ($L_R = 2\ D_o$)	0.965	1.13

P-5876

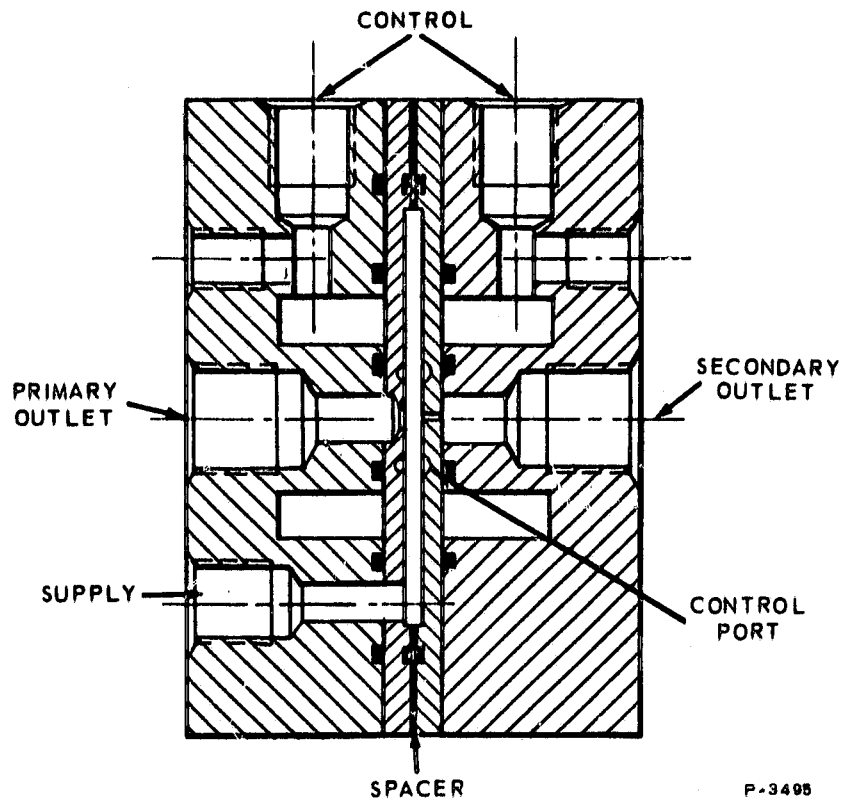

Figure 64 - Radial Inlet - Double Outlet Vortex Valve

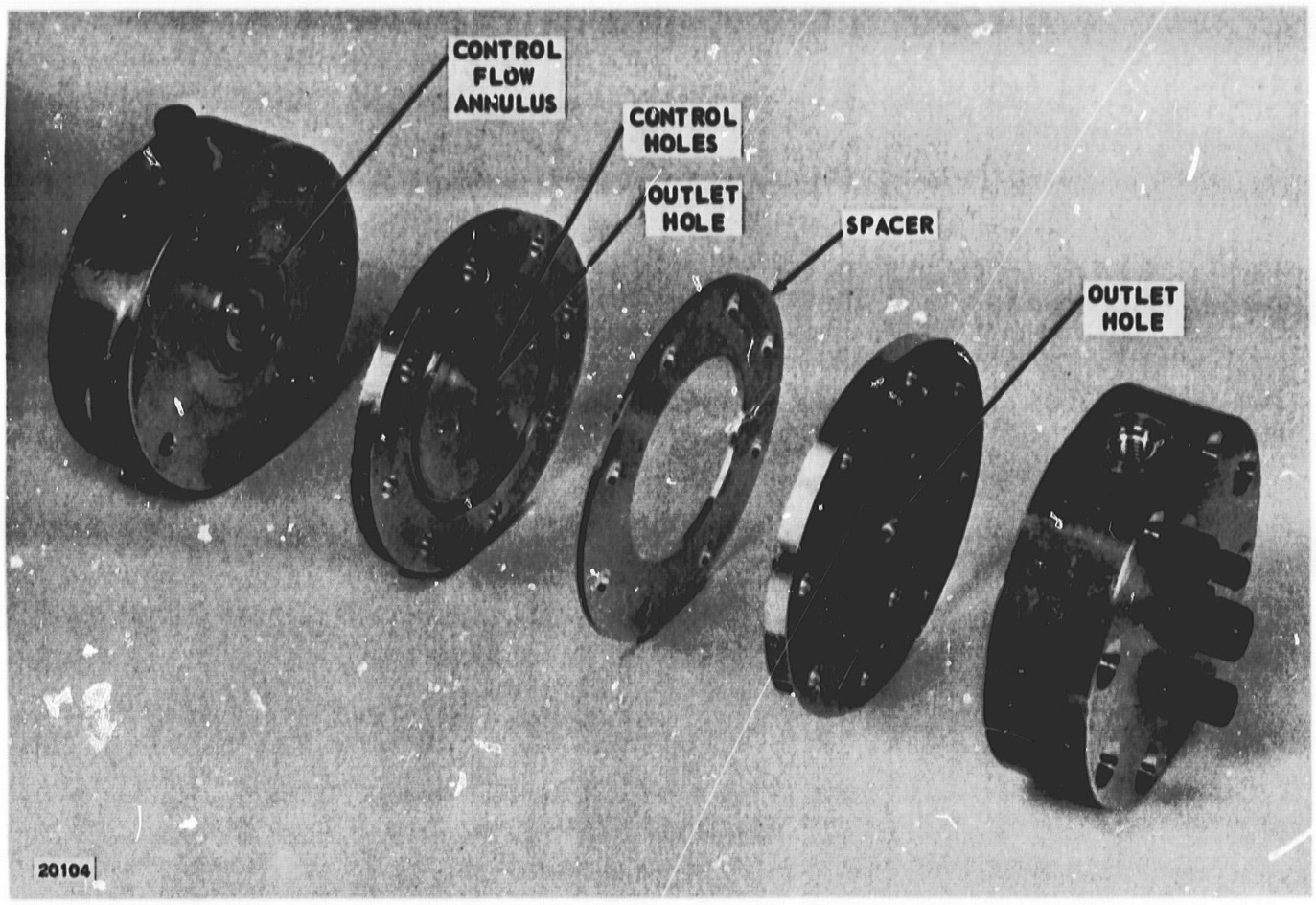

Figure 65 - Radial Inlet - Double Outlet Vortex Valve

The results of the radial inlet double outlet vortex valve tests are shown in Figures 66 and 67. Figure 66 presents the control-to-supply momentum ratio, m_c/m_s, as a function of vortex chamber spacing for various secondary outlet hole diameters. Eight 0.020 diameter control holes were utilized. The minimum momentum ratio of 9% was obtained with two 0.090 diameter outlet holes at a spacing of 0.038 inch. The control pressure ratio, P_c/P_s, was 1.40. Figure 67 shows the momentum ratio as a function of vortex chamber spacing when the outlet holes are enlarged to 0.120 inch. The minimum momentum ratio obtained was 8.5% at a vortex chamber spacing of 0.038 inch. The control pressure ratio was decreased to 1.24 by enlarging the control holes and, as Figure 67 shows, the momentum ratio was not changed significantly.

This brief test of the radial inlet vortex valve indicated performance as good as for the double outlet vortex valves discussed previously. Further optimization of the radial inlet concept was not carried out because of a decision not to utilize the double outlet vortex valve because of design problems in the final servoactuator package.

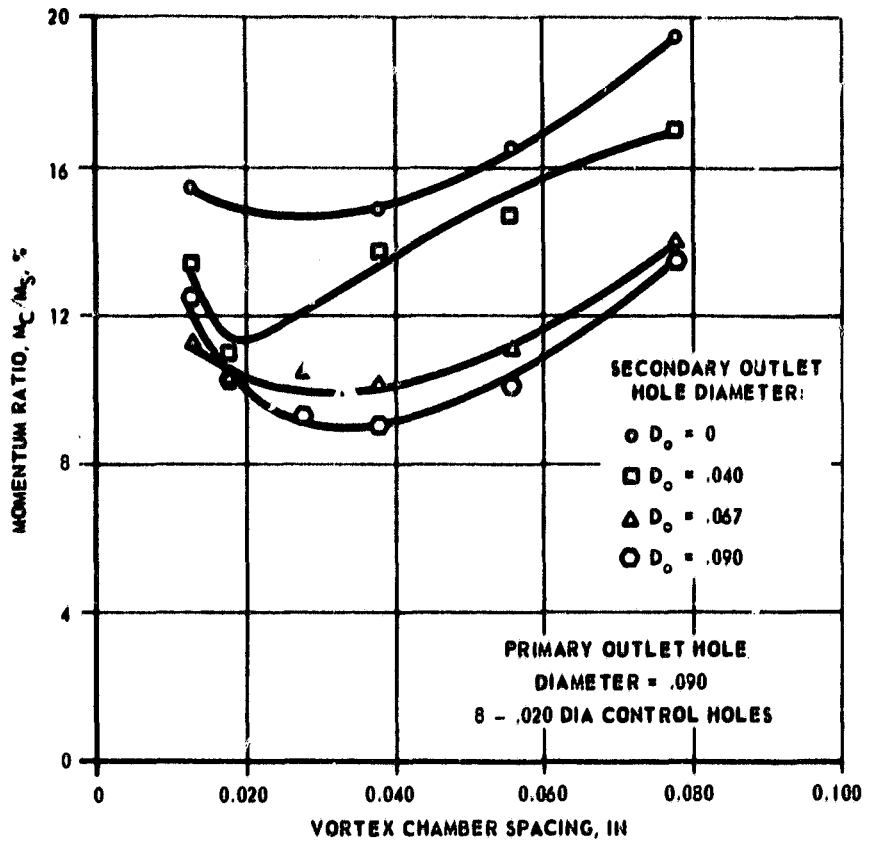

Figure 66 - Momentum Ratio Versus Vortex Chamber Spacing for Radial Inlet - Double Outlet Vortex Valve

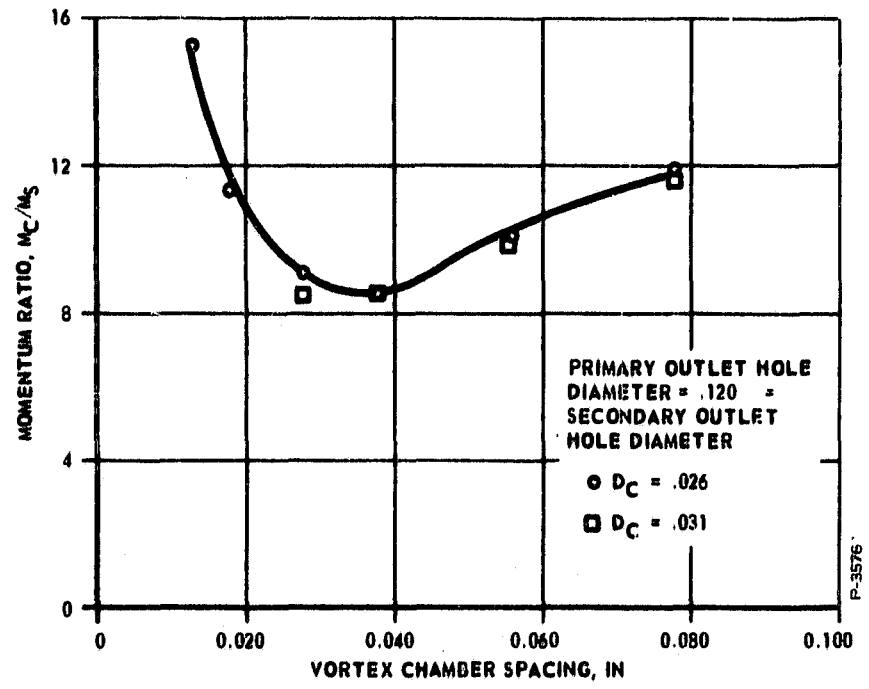

Figure 67 - Momentum Ratio Versus Vortex Chamber Spacing for Radial Inlet - Double Outlet Vortex Valve

Circular jet-on-jet amplifier. - The dynamic pressure feedback system concept utilized a circular jet-on-jet fluidic amplifier as a signal amplifier. Little data existed for this device at the start of the project. The preliminary work accomplished indicated adequate performance. In order to determine the performance characteristics of the dynamic pressure feedback system, actual jet-on-jet amplifier data were required.

A series of performance tests was performed using the jet-on-jet test fixture shown in Figure 68. The supply and control nozzles were maintained fixed in the test body and an adjustable receiver was provided. For these tests, the supply, control, and receiver nozzles were the same diameter (0.063 inch). The spacing between the receiver and the supply nozzle was varied over a L/D ratio range of 2 to 6, where L is the receiver spacing and D is the supply nozzle diameter. Blocked receiver pressure for L/D's of 2, 4, and 6 are shown in Figure 69. The maximum pressure recovery is 95% of supply pressure for all L/D ratios. The control pressure ratio to fully deflect the supply flow is significantly decreased as the spacing is increased.

For an L/D = 4, the pressure recovery of the jet-on-jet device for various load orifice area ratios is shown in Figure 70. When the area ratio is varied from zero (blocked receiver) to one (1), the maximum pressure recovery is seen to change from 0.95 P_s to 0.64 P_s and is similarly decreased throughout the control pressure range of the test.

An additional control nozzle test was performed to calibrate flow and to investigate any flow interference as a result of the receiver position. Figure 71 shows the calibration data for L/D's of 2 and 6 when the supply pressure is zero and 2000 psig. These values represent the maximum and minimum conditions of the performance tests. For L/D = 6, there is no interference effect and the normal orifice calibration curve is obtained for both supply levels. For the close spacing, there is a marked effect when the supply pressure is increased. However, since the performance tests indicate that the optimum pressure recovery occurs at the wider spacings, the interference effect will not be of consequence for the present application.

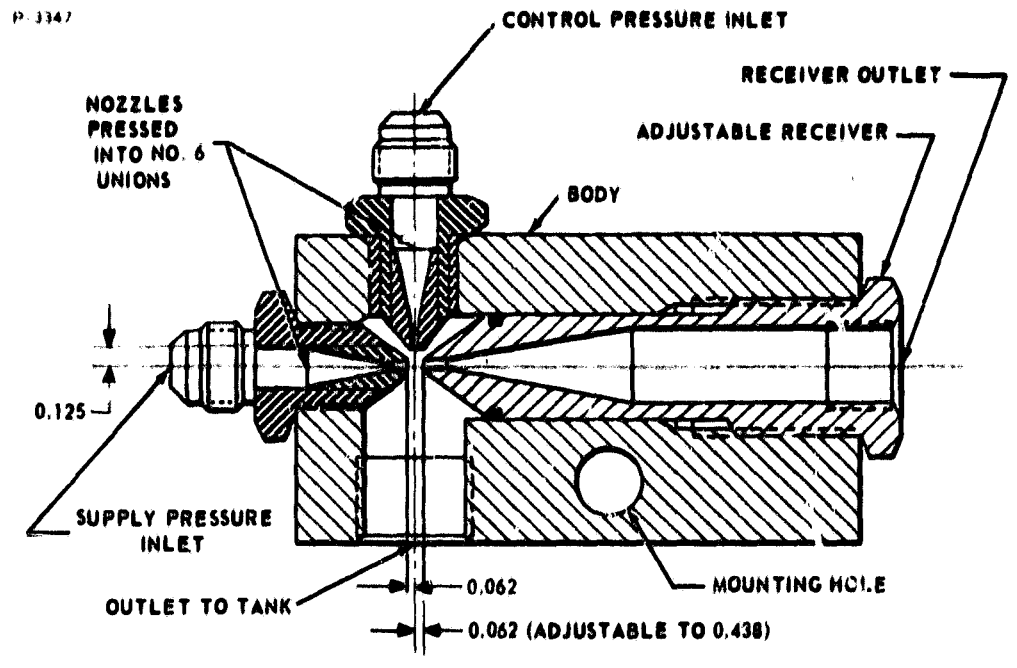

Figure 68 - Jet-on-Jet Amplifier

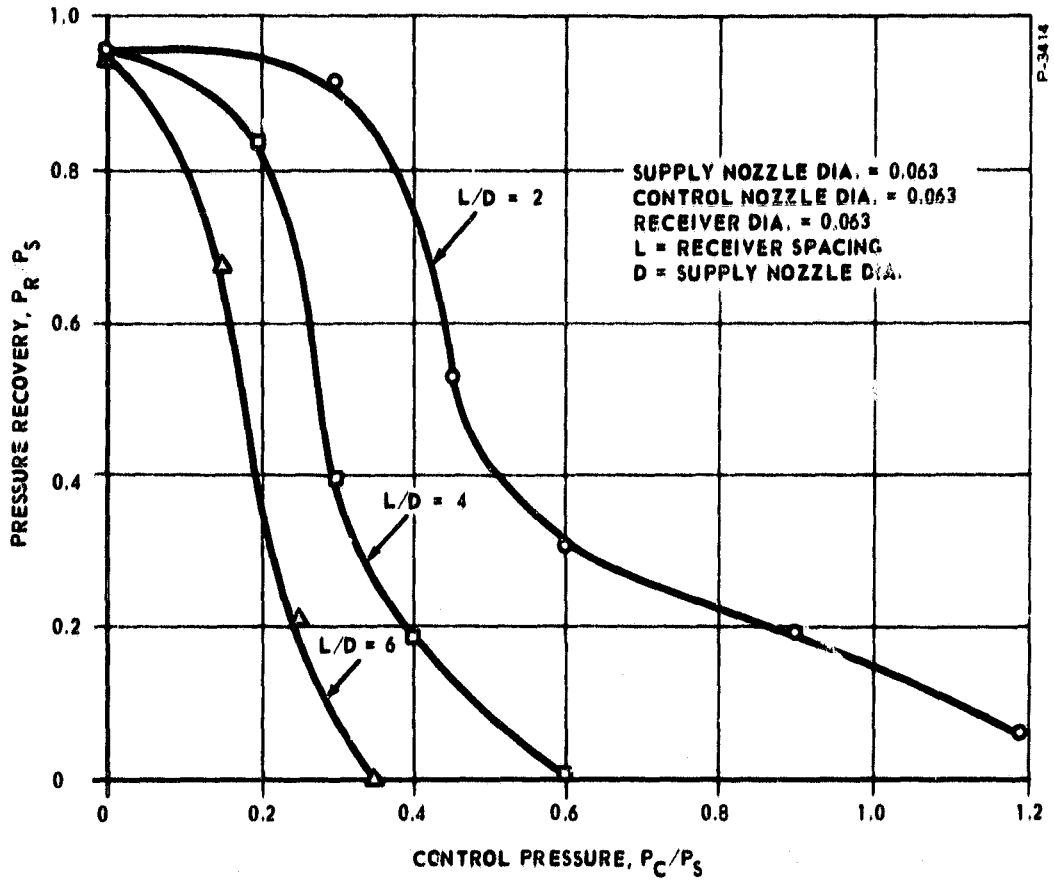

Figure 69 - Pressure Recovery of Circular Jet-on-Jet Device (Blocked Receiver)

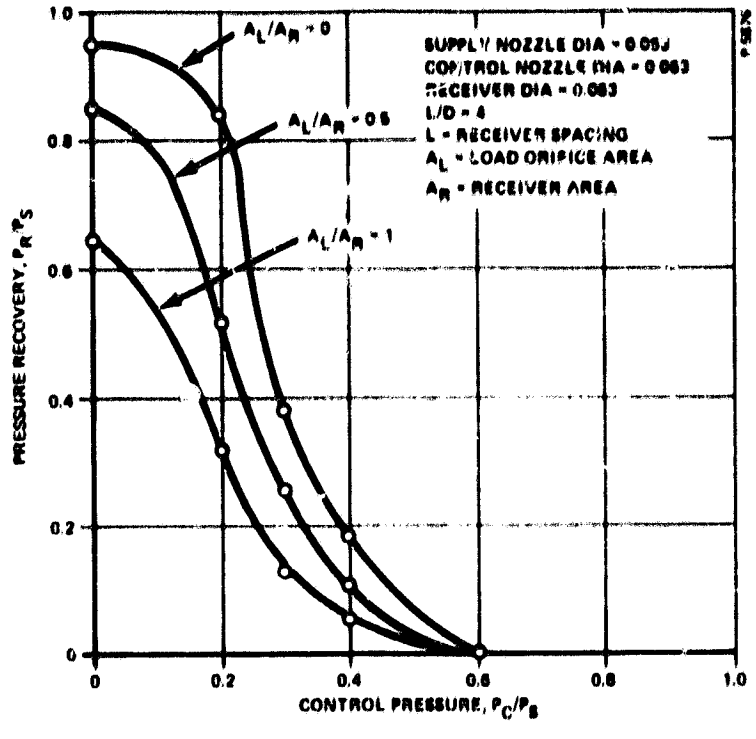

Figure 70 - Pressure Recovery of Circular Jet-on-Jet Device

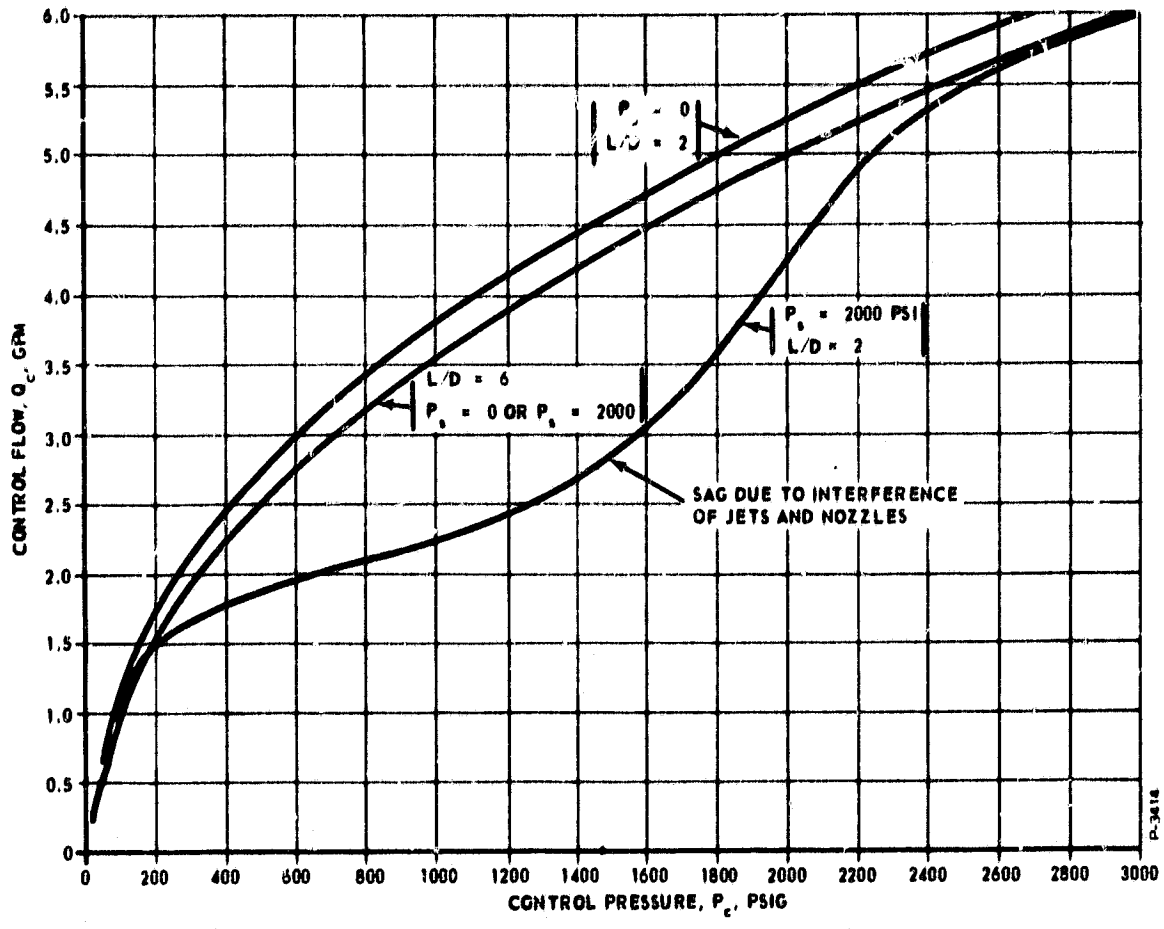

Figure 71 - Control Flow Versus Control Pressure for Jet-on-Jet Amplifier

SERVOVALVE DESIGN AND DEVELOPMENT

Hydraulic Circuit

The hydraulic fluidic servovalve design was begun with a redefinition of the hydraulic circuit. As discussed in the previous sections, the preliminary hydraulic circuit analyses indicated that the flow efficiency of the servovalve was lower than anticipated. In order to alleviate this problem, the double outlet vortex valve was designed and tested. This effort resulted in a more efficient vortex valve concept which, when utilized in the power stage of the servovalve, would result in some reduction of pilot stage flow. A further reduction in pilot stage flow and in torque motor size was desirable, however, and a reversed-flow flapper-nozzle pilot stage concept was devised.

The pilot stage for the first servovalve circuit concepts consisted of a fixed upstream orifice and a flapper-nozzle downstream orifice. The pressure between these orifices was the control pressure to the vortex valves. Flow through the flapper-nozzle orifice was exhausted to the reservoir and represented a loss of energy. The flow direction was out of the nozzles.

The reversed-flow flapper-nozzle circuit concept is shown in Figure 72. This circuit deletes the dynamic pressure feedback system for clarity.

The reversed-flow flapper-nozzle system operates with the flapper-nozzle cavity at the supply pressure level. The flapper nozzle then becomes the variable upstream orifice of the pilot stage. Note that the flow direction in the nozzles is the opposite of the conventional flapper-nozzle flow. This concept was advantageous for this application for the following reasons:

(1) All the pilot stage flow enters the vortex valves and none is bled off to the reservoir.

(2) The pressure in the nozzles varies with flapper position in such a way that the force on the flapper acts like a negative rate spring. By balancing this negative hydraulic spring with the positive mechanical spring rate of the torque motor and feedback device, potentially, a much smaller torque motor is required.

(3) The vortex valves may be readily turned down any desired amount by appropriately setting the null nozzle flapper clearance. Thus, quiescent flow may be greatly reduced, thereby reducing pump flow requirements and energy dissipation as heat.

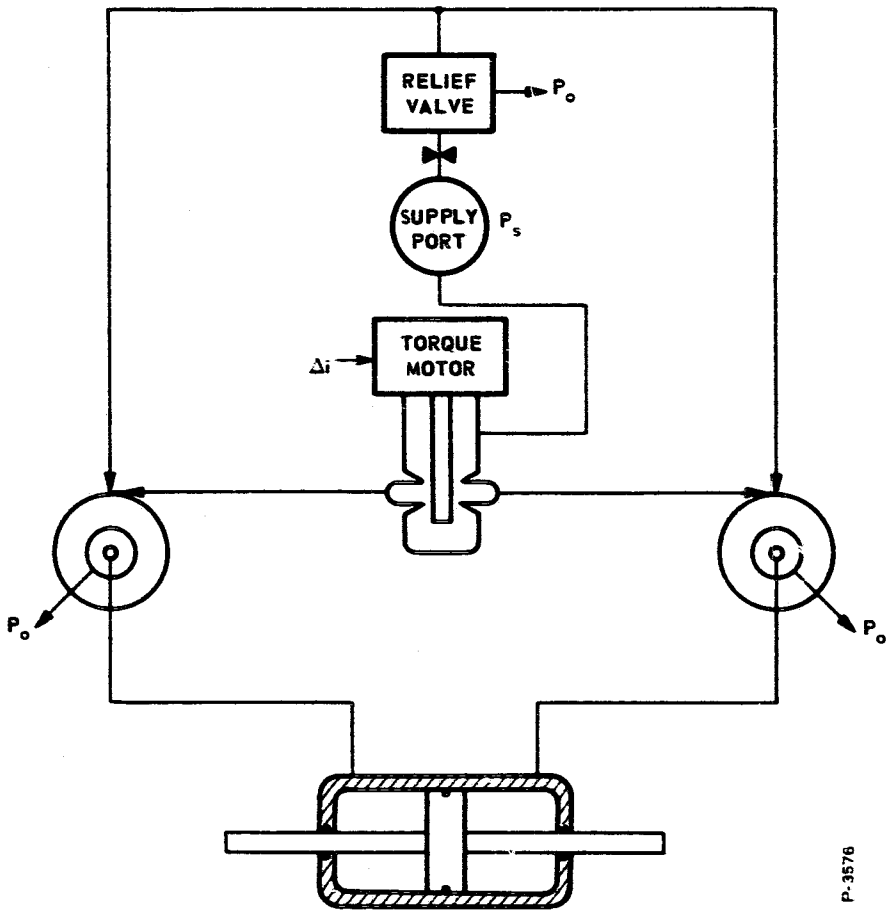

Figure 72 - Reversed-Flow Flapper-Nozzle Pilot Stage Concept Applied to Vortex Valve Power Stage

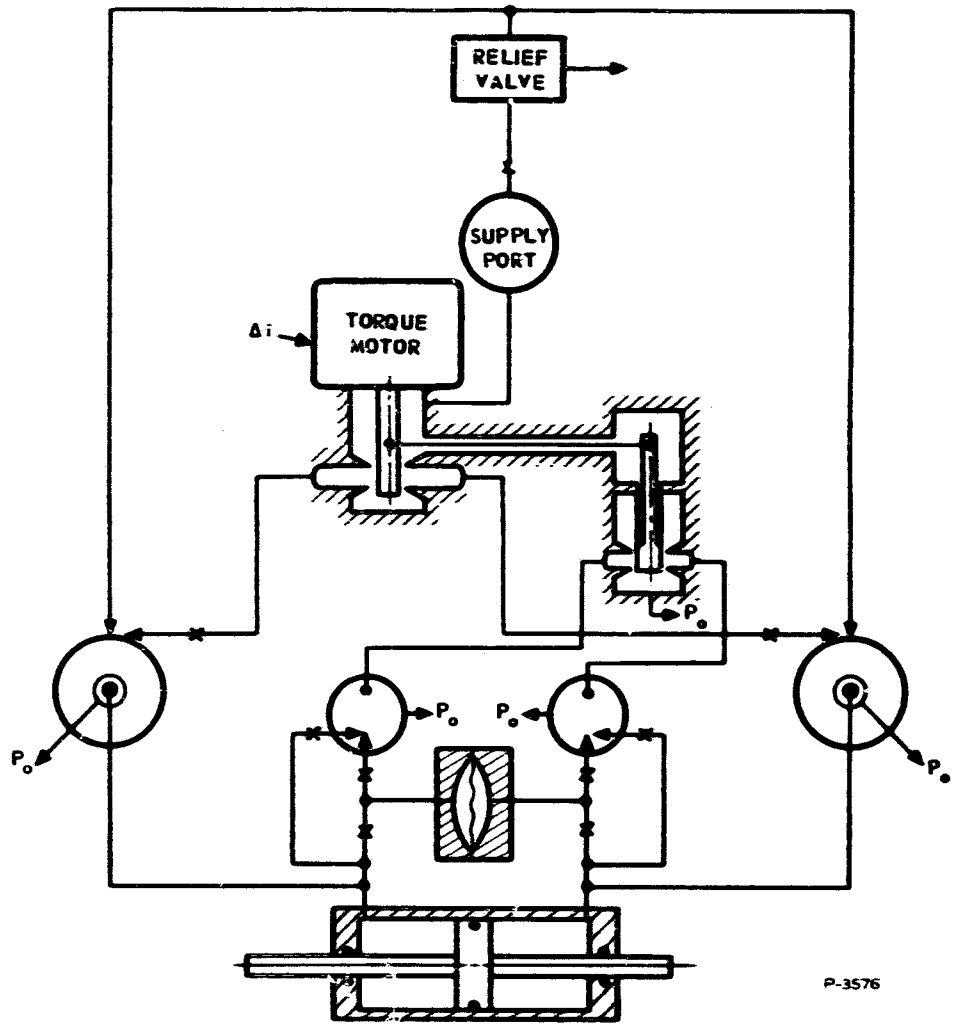

Figure 73 - Complete Servovalve Circuit Schematic

The complete servovalve hydraulic circuit is shown in Figure 73. The dynamic pressure feedback circuit is the same as for the previous concept. However, since the pilot stage flapper-nozzle cavity is at supply pressure instead of exhaust pressure, it is necessary to remove the feedback nozzles from the flapper-nozzle cavity. This is accomplished as indicated in Figure 73 by use of a tubular high pressure seal and a center rod for transmitting motion through the seal member. This spring seal tube concept has been used by Bendix in many applications and is a common torque motor armature suspension system. The method of transmitting the feedback motion and force to the flapper is shown in Figure 74. Note the spring tube seal of the feedback device. This tube must withstand system supply pressure and function as a cantilever spring. The feedback fork is normally fitted about 0.0001 inch, loose on the pilot stage flapper shaft and appears to be essentially a frictionless joint for the motions involved. The positive spring rate of the feedback spring tube will be set to essentially cancel out the negative spring rate of the pilot stage flapper nozzle.

Based on the new schematic circuit, a preliminary pressure-flow map indicated an increase in performance over the original concept. The vortex valve performance used for this calculation is shown in Figure 75, which was estimated and felt to be realistic. The pressure and flow distribution around the circuit is shown in Figures 76 and 77 for null and full stroke, respectively. Note that the maximum flow into the supply port is 35 cu.in./sec, while the maximum flow across the load is 25 cu.in./sec. A blocked cylinder pressure differential of 2000 psi appears attainable. Note also at null that the vortex valves are turned down considerably, since P_c/P_s equals 2700/2300 or 1.175. In Figure 78 is shown the present servoactuator performance and the flight data boundary. The present servoactuator is obviously ample to handle the flight conditions observed to date. The fluidic servoactuator performance is shown for comparison. While it is less effective than the spool valve controlled actuator, the fluidic servovalve has adequate performance to readily surround the flight loading conditions. This performance is based on using the present hydraulic pump installation.

Servovalve Configuration

Dynamic pressure feedback system - A dynamic analysis of the hydraulic vortex servovalve and actuator system was performed. This analysis, shown in detail in Appendix B, led to the elimination of the dynamic pressure feedback unit in the servoactuator system.

In brief, the results are as follows. When vortex valves are used in a push-pull configuration to drive an actuator, cylinder motion pumps oil out of one vortex valve probe and the pressure rise is a function of piston velocity and not displacement. Therefore, the system will exhibit high damping and low stiffness as compared to a conventional spool valve driven actuator which normally exhibits high stiffness and low damping.

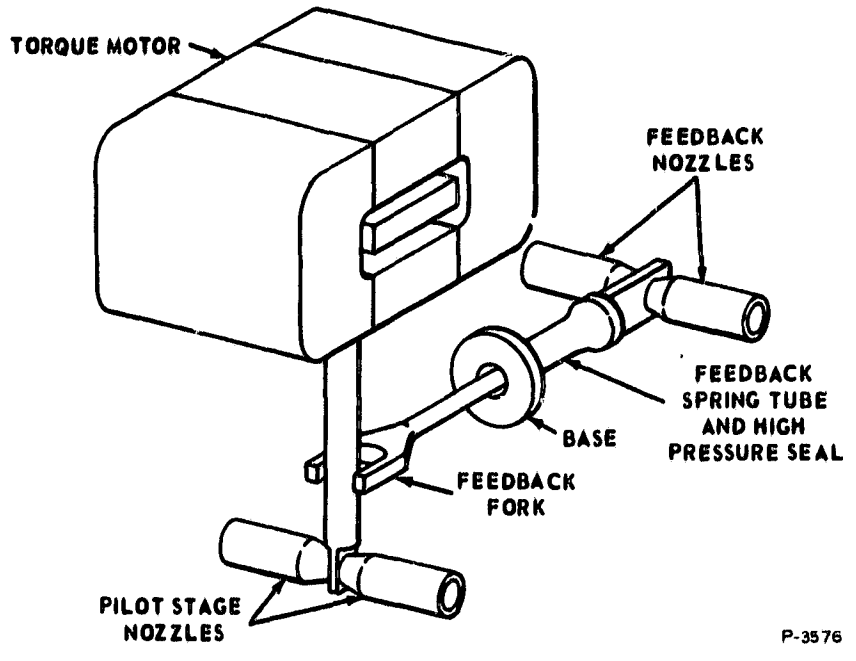

Figure 74 - Feedback Device Method of Implementation

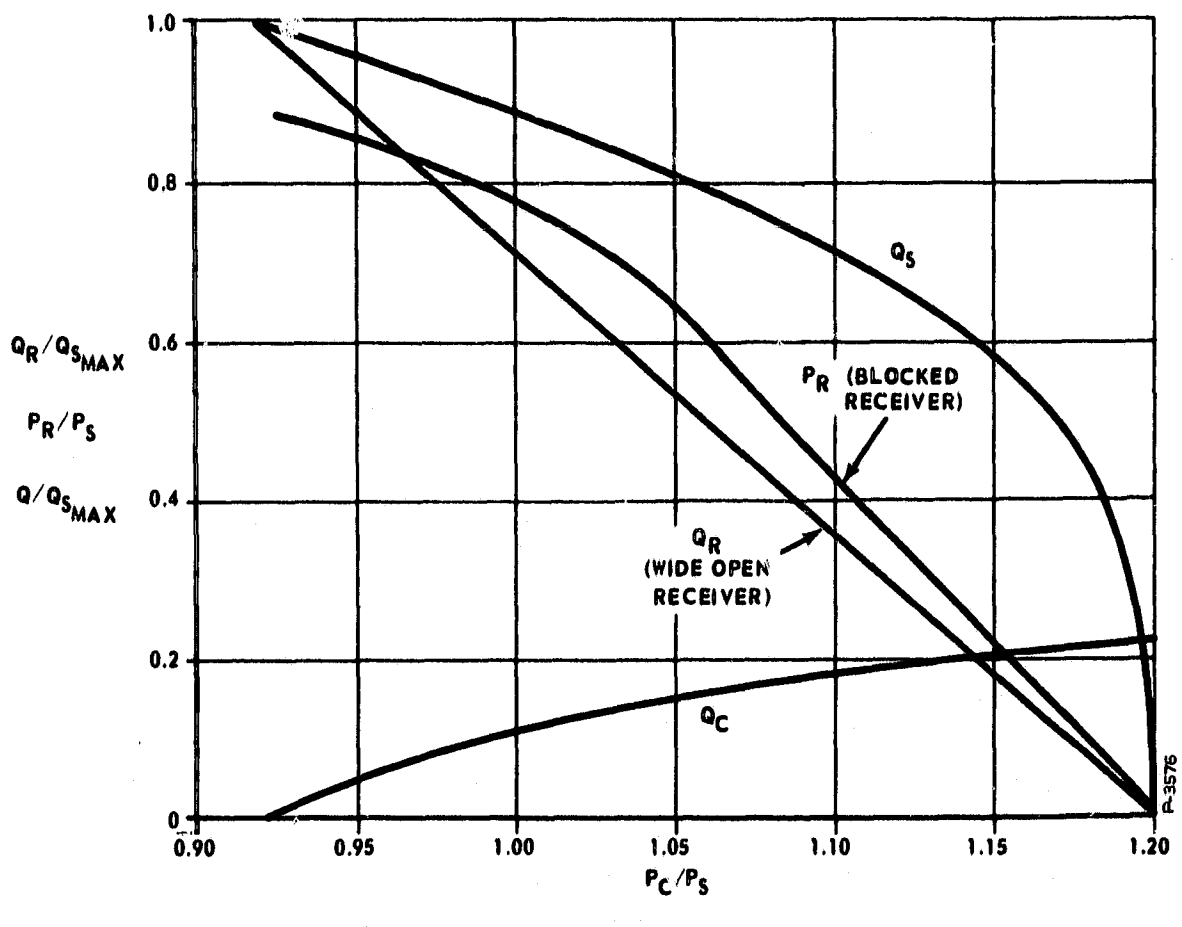

Figure 75 - Estimated Vortex Valve and Probe Performance Characteristics

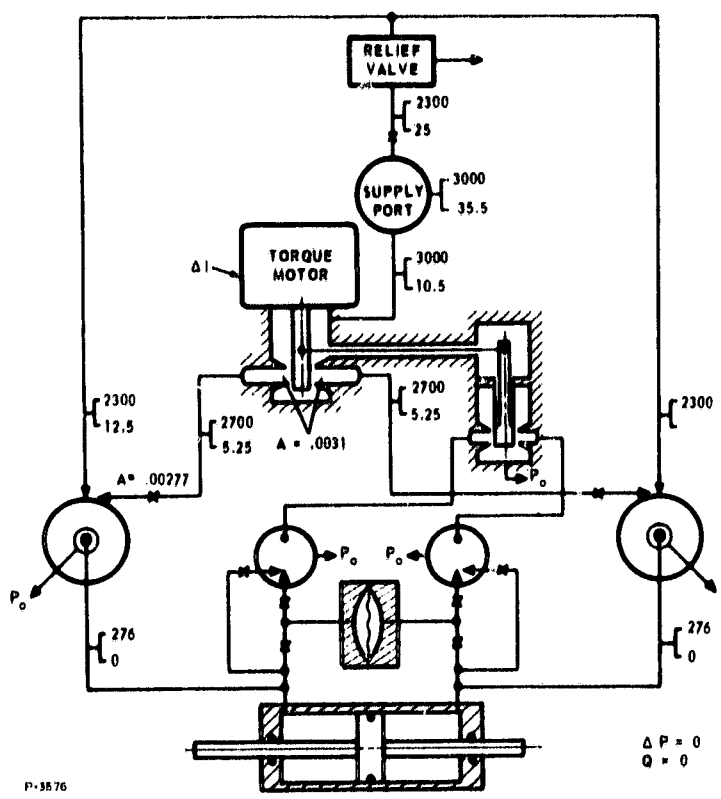

Figure 76 - Pressure-Flow Map at Null

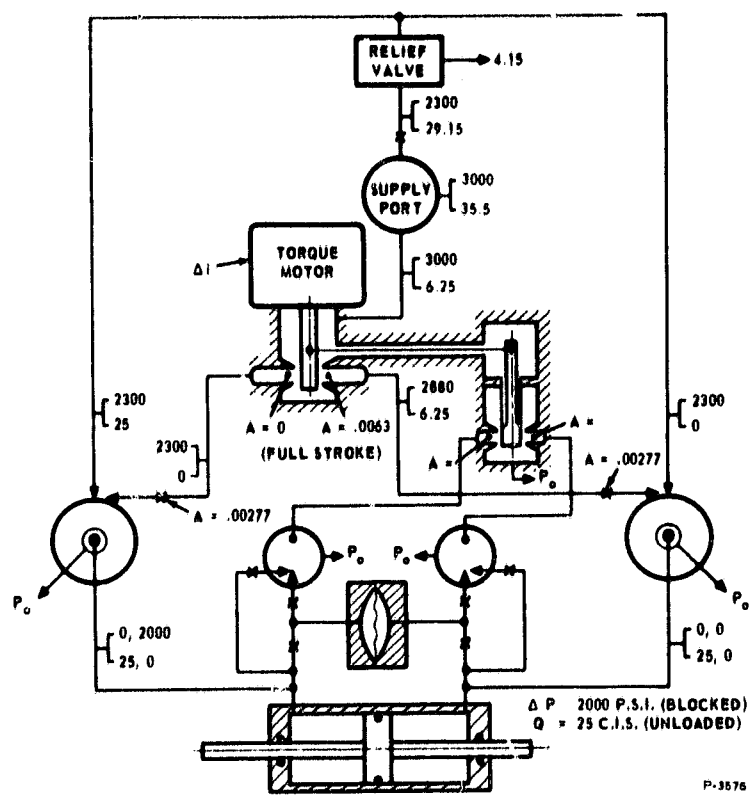

Figure 77 - Pressure-Flow Map at Full Stroke

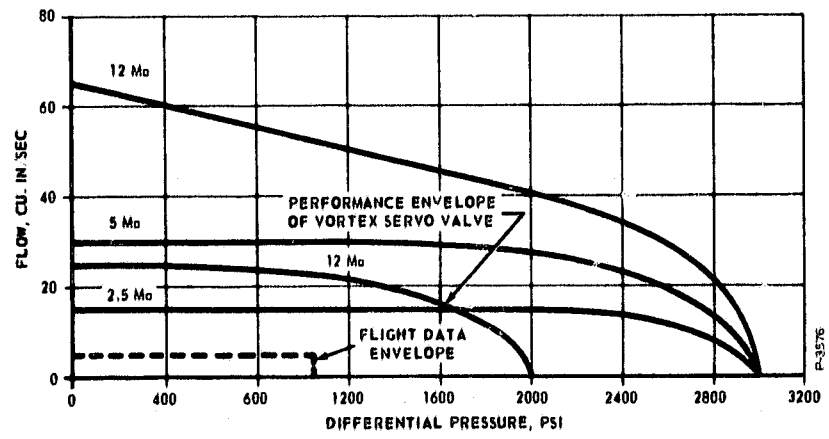

Figure 78 - Comparison of Flight Data and Vortex Servovalve Performance

The dynamic analysis indicated that the frequency response requirements of the servoactuator could be met but with reduced stiffness. The natural damping characteristics and the increased simplicity gained by elimination of the dynamic pressure feedback unit were significant advantages of the hydraulic vortex servovalve.

Reversed-flow flapper-nozzle pilot stage. - It was decided that the servovalve design would incorporate the reversed-flow flapper-nozzle pilot stage. The high power gain of this approach was required to permit the use of torque motors of reasonable size. However, even with this approach, it was necessary that the torque motors be adjusted by the manufacturer to a very high gain. This is evident by the nonlinearity of the delivered torque motors. The net effective spring rate of the torque motor was minimized to provide the most output power possible commensurate with static stability. With the elimination of dynamic pressure feedback and its associated hardware, a means of providing a positive spring rate between the flapper and ground was required. The method selected was to use a circular cross section cantilever spring attached to the pilot stage body and fitted to the flapper. The spring used a spherically-shaped end which was closely fitted into a slot in the flapper. The relative motion between the spherical surface and the slot was believed to be small and no hysteresis effects were expected. The spring rate of the cantilever spring had to be matched to the net effective rate of the torque motor and the negative rate of the particular valve nozzle setting under test. Subsequent experience indicated that null adjustment was difficult with this system. A better approach would have provided the positive spring integral with the torque motor assembly. The method of implementing the auxiliary spring is shown in Figure 79.

Single outlet vortex valve power stage. - After reviewing the various vortex valve test results and comparing various preliminary power stage layouts, it was concluded that the single outlet vortex valve was the best solution to the total design problem. The double outlet valve gave slightly better performance but implementation of this technique was not practical. As shown in Figure 80, a large body and a very complicated porting arrangement is required for the double outlet valve. The flight data load-flow requirements could be met with two single outlet vortex valves and it was decided that this was the best approach.

Referring to Figure 79, it can be seen that the servovalve assembly is made up of two subassemblies — a reversed-flow flapper-nozzle pilot stage (including torque motor) and a vortex valve power stage. The torque motor, provided per Specification DS-735 (see Appendix C), had provisions for attachment of the cantilever spring device to the flapper. The pressure differential across the flapper varies with stroke in such a way that the resultant force on the flapper is in the direction of flapper motion. The positive spring rate of the cantilever spring device combines with this negative hydraulic spring rate to provide a small net positive rate which the torque motor must drive. Supply pressure is communicated to the flapper-nozzle cavity and the pressure downstream of the two nozzles is the control pressure to the vortex valves.

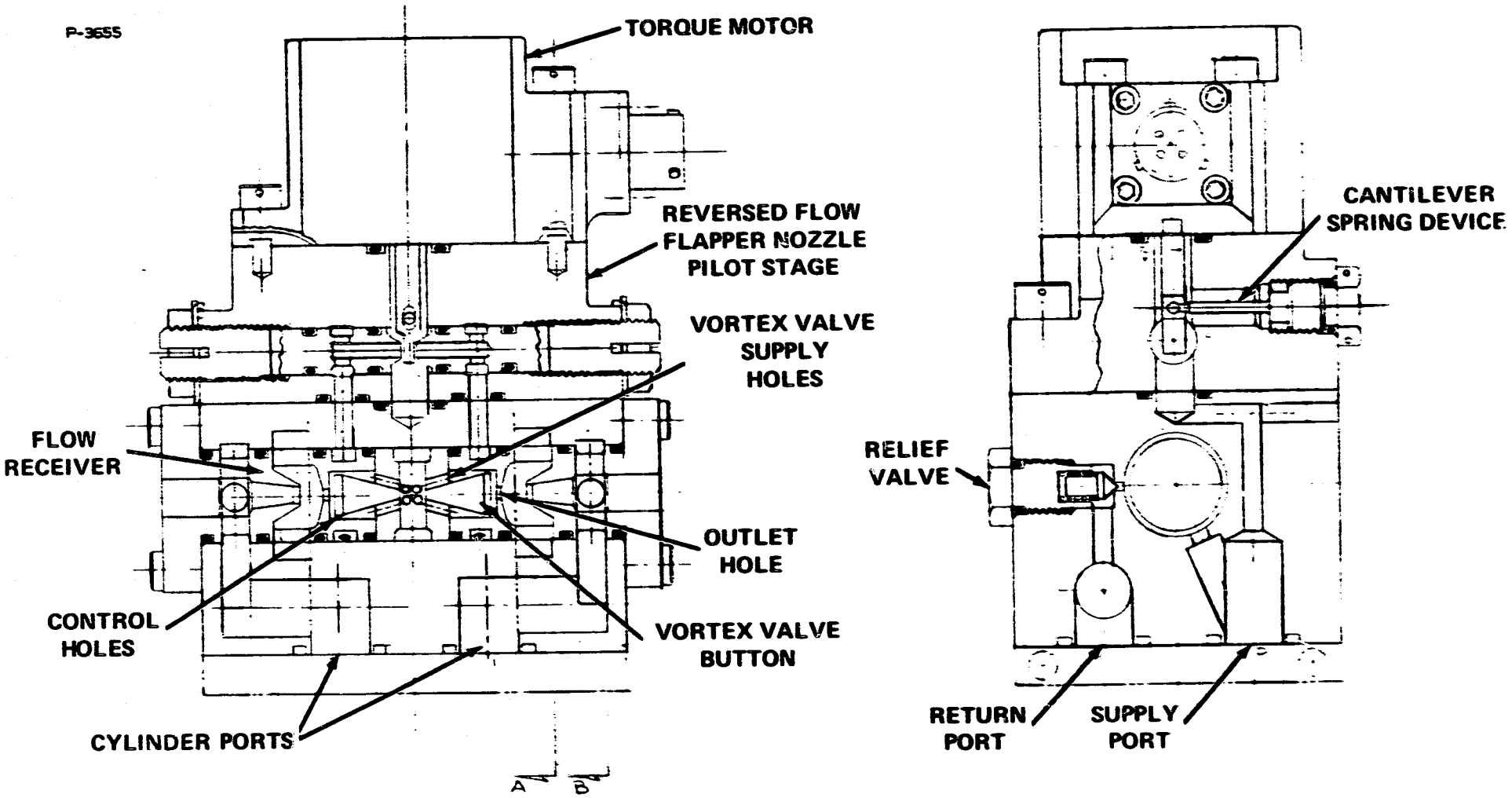

Figure 79 - Hydraulic Fluidic Servovalve

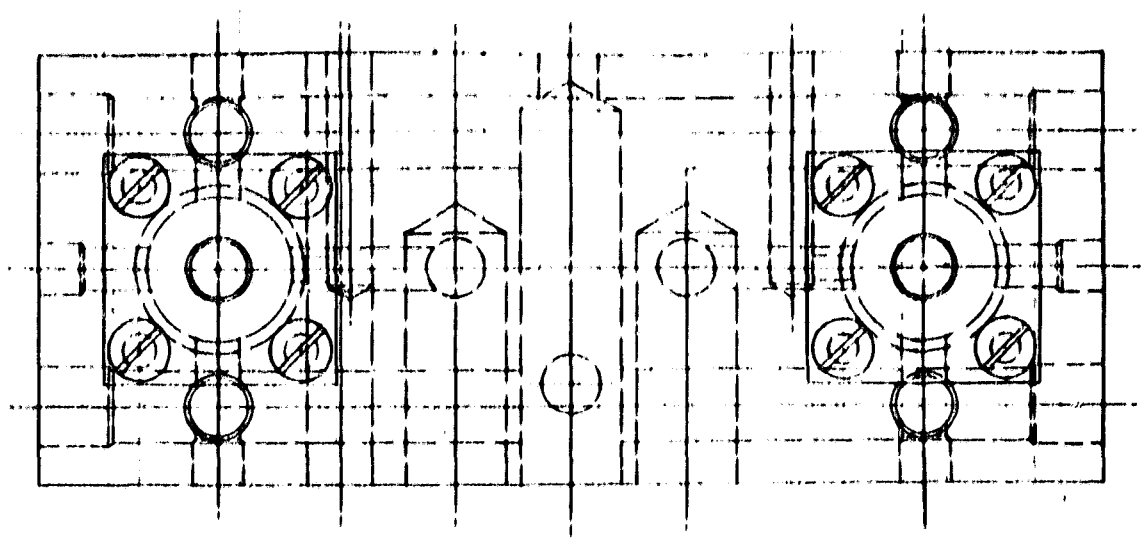

Figure 80 - Fluidic Servovalve Power Stage with Double Outlet Vortex Valves

The power stage consists of two single outlet vortex valves which are end-to-end in the servovalve body. Supply flow enters each vortex valve through six drilled passages connecting the vortex chamber to a centrally located supply annulus. After passing over the vortex valve button, where control flow is admitted through four tangential holes, the hydraulic fluid exits through the outlet hole. Depending upon the amount of control flow, a portion of the flow enters a flow receiver with the remainder being ported to exhaust. The receiver flow is then channeled to the two cylinder ports which connect to the NASA-supplied actuator.

The hydraulic vortex servovalve hardware is shown in Figures 81 through 84. Figure 81 is a photograph of the complete servovalve assembly. As shown, the pilot and power stages are individual "modules" which can be tested and modified before final assembly and testing of the complete servovalve. Figure 82 is an exploded view of the pilot stage showing the adjustable pilot stage nozzles with integral locking devices. The cantilever spring used to counteract the negative hydraulic spring rate of the reversed-flow flapper-nozzle pilot stage is also shown in Figure 82. Figure 83 is an exploded view of the power stage showing the two vortex valve assemblies and the relief valve. Figure 84 is a close-up view of the two vortex valve assemblies showing the vortex valve buttons, chambers, and flow receivers.

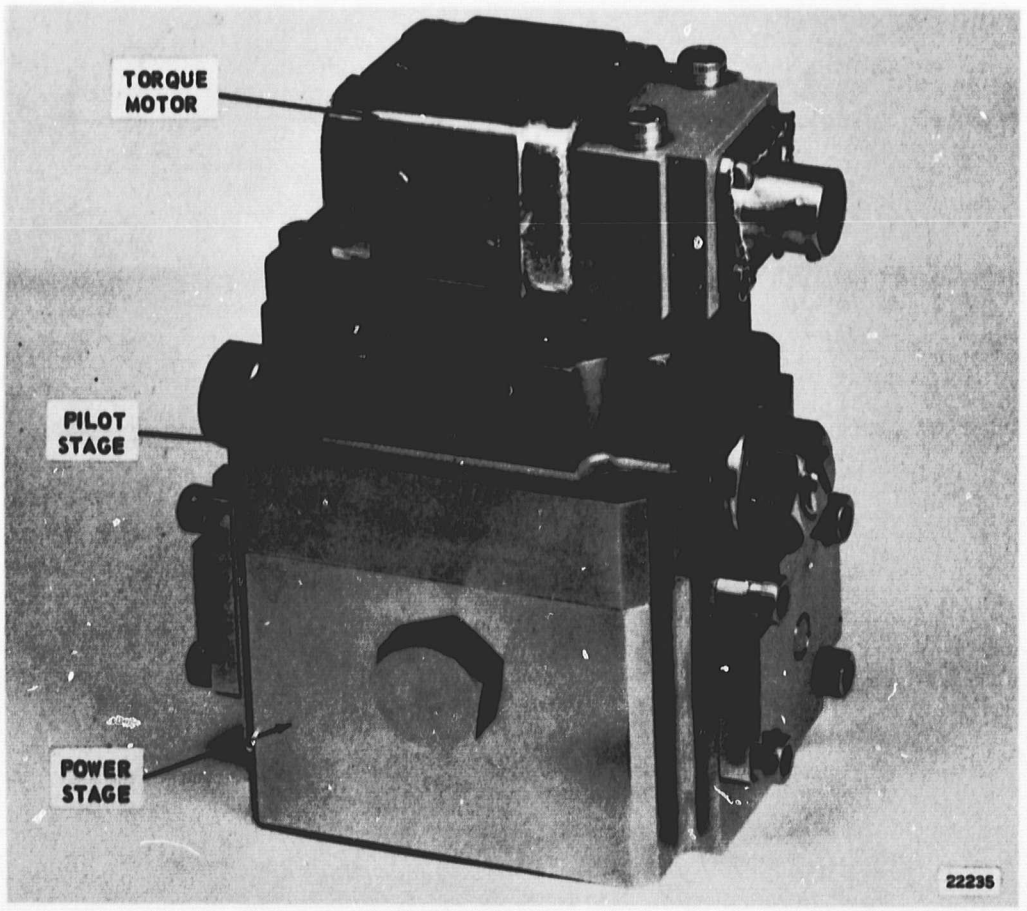

Figure 81 - Hydraulic Vortex Servovalve

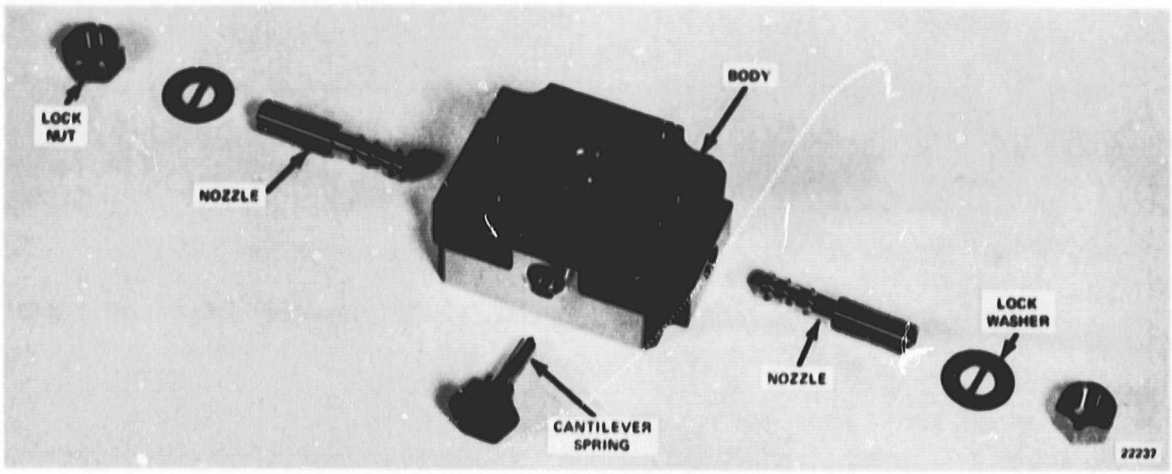

Figure 82 - Pilot Stage - Hydraulic Vortex Servovalve

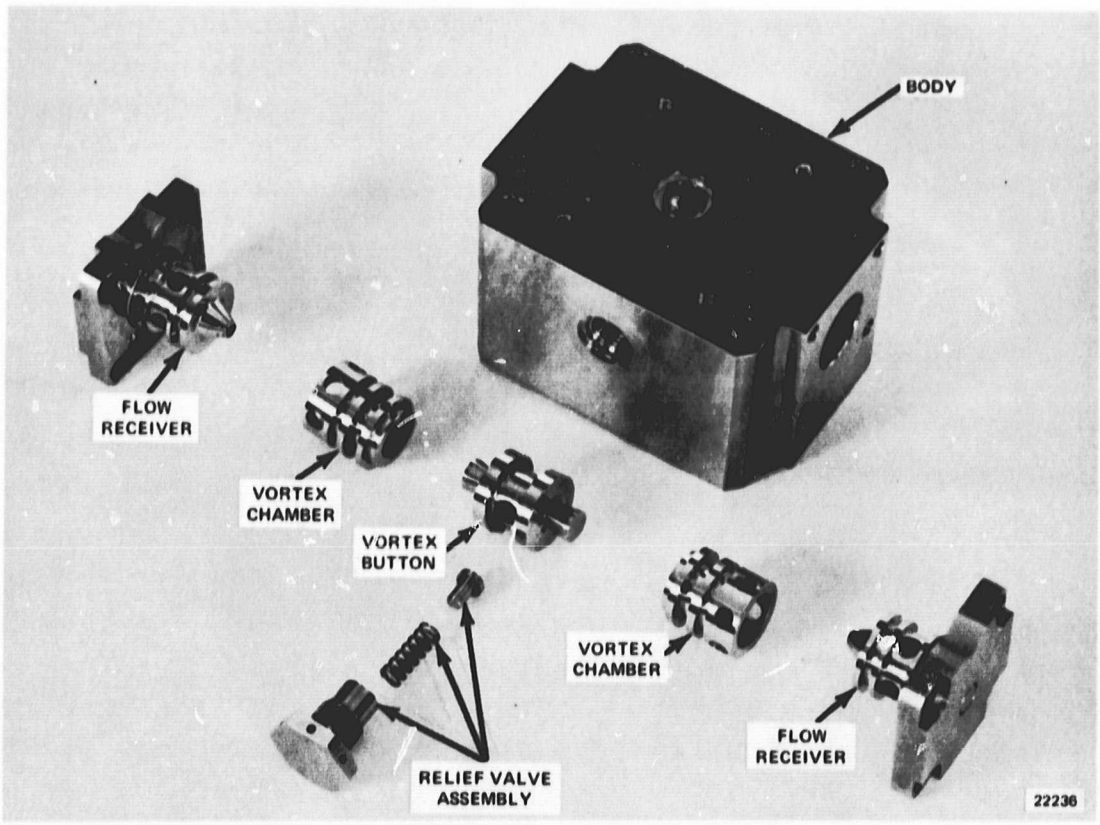

Figure 83 - Power Stage - Hydraulic Vortex Servovalve

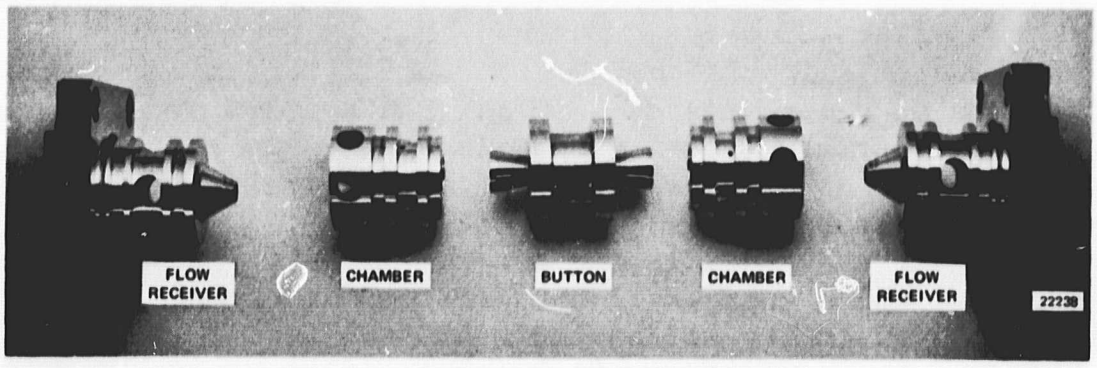

Figure 84 - Power Stage Vortex Valves

Servovalve Performance Tests

Power stage vortex valve static performance - After fabrication of the servovalve was completed, power stage testing was initiated. The two vortex valves of each power stage were individually tested to determine turndown and flow receiver load-flow performance. This data was required to determine the actual pilot stage pressure and flow requirements prior to adjusting the torque motor and pilot stage nozzles.

The initial data recorded for the power stage vortex valves indicated that all of the units had closely matched performance. However, the turndown ratio, Q_s/Q_c obtained was only 3.70 at a control pressure ratio of 1.5. (A turndown ratio of approximately 5.00 at a control pressure ratio of 1.20 was desired.) The maximum vortex valve supply flow of 5.25 gpm, was considerably less than the design flow of 6.50 gpm (25 cu. in/sec). In addition, the control flow for full turndown was higher than anticipated. The flow receiver performance data indicated that the blocked receiver pressure recovery was 91% of supply pressure. Maximum receiver flow was 116% of supply flow indicating that flow was entrained from the vent cavity surrounding the flow receiver.

In order to determine the cause of the reduction of flow through the vortex valve under zero vorticity conditions, the outlet hole flow coefficient was determined without the vortex button in place. The flow coefficient as determined by this test was found to be 0.750 rather than the 0.850 expected. In addition, with the button in place, the pressure just upstream of the outlet hole was reduced to approximately 91% of supply pressure by the mixing zone annulus area restriction. Both of these factors contributed to the low flow recorded during the initial performance tests. The maximum vortex valve flow was brought to the design level by increasing the outlet hole upstream radius and by decreasing the vortex valve button diameter.

The combination of low control pressure and high control flow for full turndown presented a somewhat different problem. The results of the tests indicated that the control port area was too large. By simply decreasing this area, some improvement in performance would have been realized. An analysis was performed to determine the effect of control port orifice coefficient on overall vortex valve performance. The results of the analysis, shown in detail in Appendix D, indicate that the tangential control port orifice coefficient should be high and as close as possible to unity. From practical considerations, the tangential orifice diameters should be fabricated slightly smaller than that predicted and the holes should be lapped to the size necessary to give the desired P_c/P_s ratio at full vortex valve turndown. The underlying theory is that the fluid in the tangential holes is accelerated to maximum velocity and momentum in the vena contracta and should be injected into the supply stream in that condition. If the fluid in the tangential holes is allowed to re-expand to fill the hole, which happens if the orifice coefficient is significantly less than one, the velocity and momentum of the fluid are reduced. Thus, only a portion of the maximum momentum available is actually efficiently mixed with the supply flow.

Rework of the vortex chambers was performed as shown in Figure 85 to maximize the orifice coefficient and to provide lapping material in the tangential holes. The results of testing the reworked vortex valves are shown in Table IV. Note the relatively high orifice coefficients obtained for the tangential holes. The value of 1.08 shown is not feasible, of course, and is the result of slight instrument recording and reading errors. The orifice area used in the calculation is four times the area of one hole and a slight error in measuring the hole diameter is reflected in an error in the total area. It is apparent, however, that the orifice coefficient was high and approaching unity.

Based on the performance of the vortex valves, a spring rate was predicted for the auxiliary cantilever spring. The spring proportions necessary to give the desired rate, deflection, and stress level were calculated. The spring blanks were finished to the dimensions shown in Figure 86.

Pilot stage tests - flapper force measurements. - Initial testing of the reversed-flow flapper-nozzle pilot stage indicated a higher null control pressure level than anticipated and evidence that severe flapper oscillations had occurred. The flapper-nozzle orifice area was reduced by decreasing the flapper-nozzle clearance. This reduced the null control pressure to the level determined by the power stage tests. With this change, a new cantilever spring was required. The new spring rate was predicted to be 1485 lb/in and a new spring blank was finished, ground to the proper proportions.

In order to obtain data on the frequency and amplitude of the torque-motor flapper oscillations, the torque motor was reassembled on the pilot stage body. With no differential current applied to the torque motor, the control pressure fluctuations were recorded on an oscilloscope. At a control pressure level of 1000 psi, the frequency and peak-to-peak amplitude of the oscillations were 14,000 cps and 150 psi, respectively. At a control pressure level of 1500 psi, the pilot stage became extremely unstable and the peak-to-peak amplitude of the oscillations approached 2000 psi, with a frequency of approximately 2500 cps. Higher pressure levels were not applied in an attempt to prevent torque-motor failure and nozzle damage.

An analysis of the flapper forces was performed to determine the cause of the instability. A linearized force summation computation on the flapper leads to four conclusions:

(1) The negative hydraulic spring rate is greater than originally estimated.

(2) The negative hydraulic spring rate can be quite nonlinear.

Table IV - Summary of Power Stage Performance Test Data

Item	Servovalve No. 1	
	Vortex Valve No. 1	Vortex Valve No. 2
Max. Flow, $Q_{S\ MAX}$ (in^3/sec)	24.0	24.4
Turndown Ratio, Q_S/Q_C	5.15	5.70
Control Pressure Ratio, P_C/P_S	1.17	1.18
Control Momentum Ratio, M_C/M_S(%)	8.0	7.45
Outlet Hole Flow Coefficient, C_{DO}	0.870	0.875
Tangential Hole, C_D	1.08	0.96

P-5876

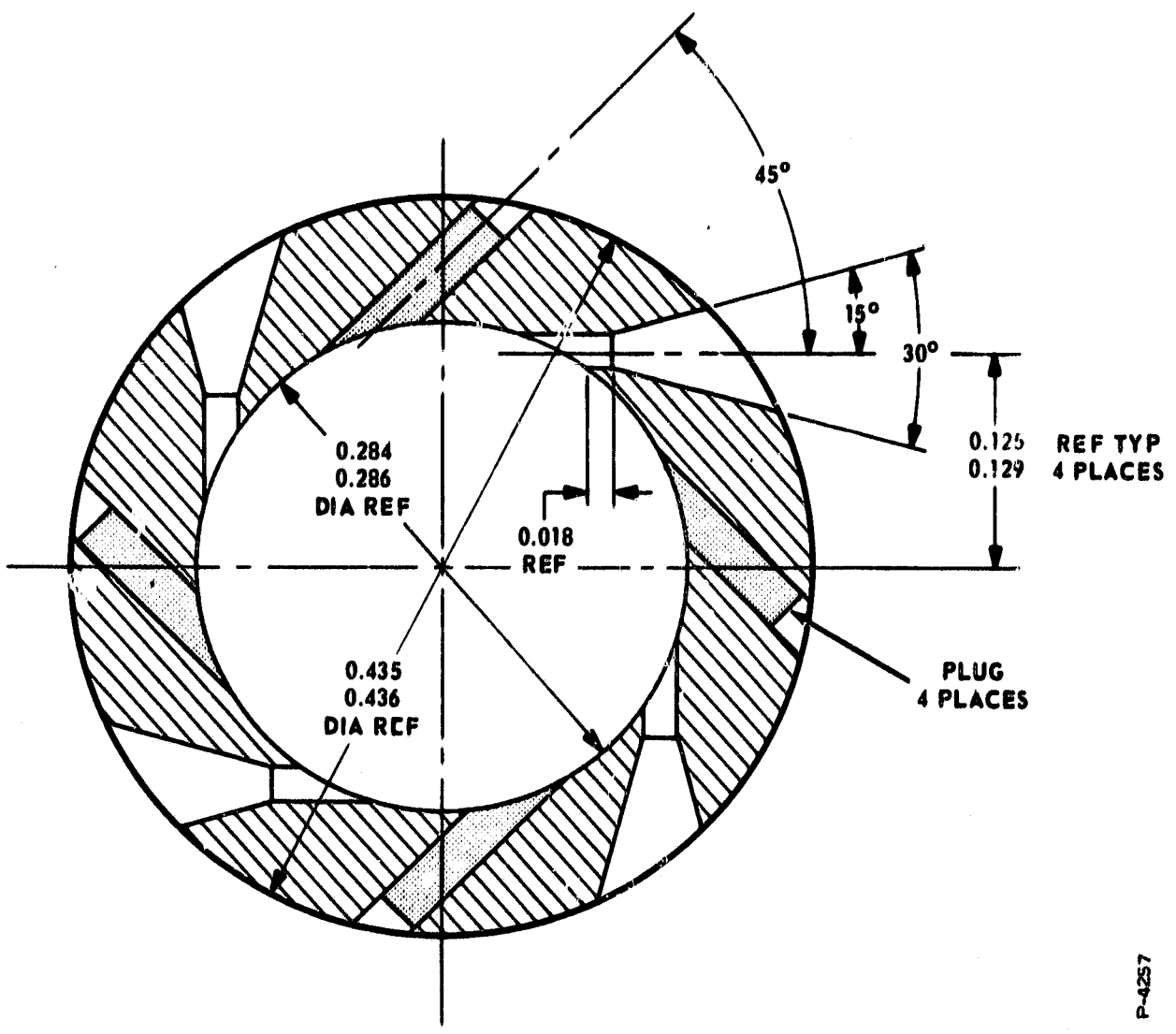

P-4257

Figure 85 - Tangential Hole Rework Method for the Hardened Vortex Chamber Steel Sleeves

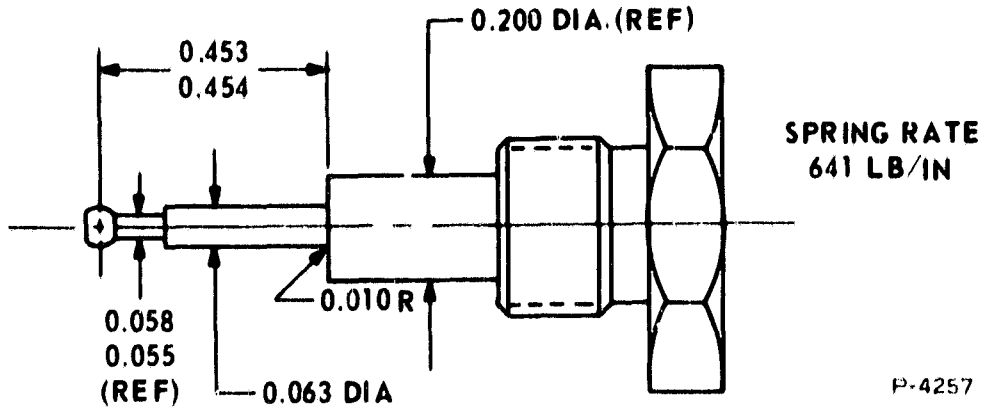

Figure 86 - Cantilever Spring Dimensions

(3) The negative hydraulic spring rate can reverse and become positive at very small flapper-nozzle clearances such as occur at full stroke.

(4) The calculated supply pressure at which the flapper becomes statically unstable appears to correlate well with the observed supply pressure at which heavy oscillation occurs.

Since the analysis used several simplifying assumptions, it was desirable to experimentally determine the total flapper force as a function of flapper stroke, supply pressure, and null clearance. From the data, the cantilever spring rate could be accurately specified. In order to perform these tests, the test fixture shown in Figure 87 was fabricated.

As shown, the fixture was essentially the same configuration as the pilot stage body, except that a very rigid cantilever beam replaced the torque-motor output flapper. The nozzles were adjustable to provide relative changes in null clearances. The cantilever beam was instrumented with two strain gages calibrated to indicate the bending force acting on the beam. The use of two strain gages on opposite sides of the beam provided temperature compensation and reduces the effects of any axial loading. The strain gages were mounted in the bore of cantilever, as shown, in order to eliminate sealing problems and possible failure of the strain gage by direct exposure to the high pressure oil. An externally-mounted micrometer was used to determine the flapper position between the nozzles. The flapper force measurement fixture was mounted on the hydraulic vortex servovalve power stage so that the actual pilot stage loading (control port areas) existed.

Data resulting from the tests are presented in Figures 88 through 93. Figures 88, 89 and 90 present force data for a flapper width of 0.340 inch and nozzle spacings of 0.012 inch, 0.015 inch, and 0.020 inch, respectively. Figures 91, 92 and 93 present data for the same nozzle spacings but with a flapper width of 0.156 inch, which was identical to the actual flapper used in the pilot stage. Supply pressures of 1000, 2000, and 3000 psi were used for these tests. The data indicated that the flapper force was not as extreme a nonlinear function of stroke as computed. The flapper forces were found to be very nearly proportional to supply pressure

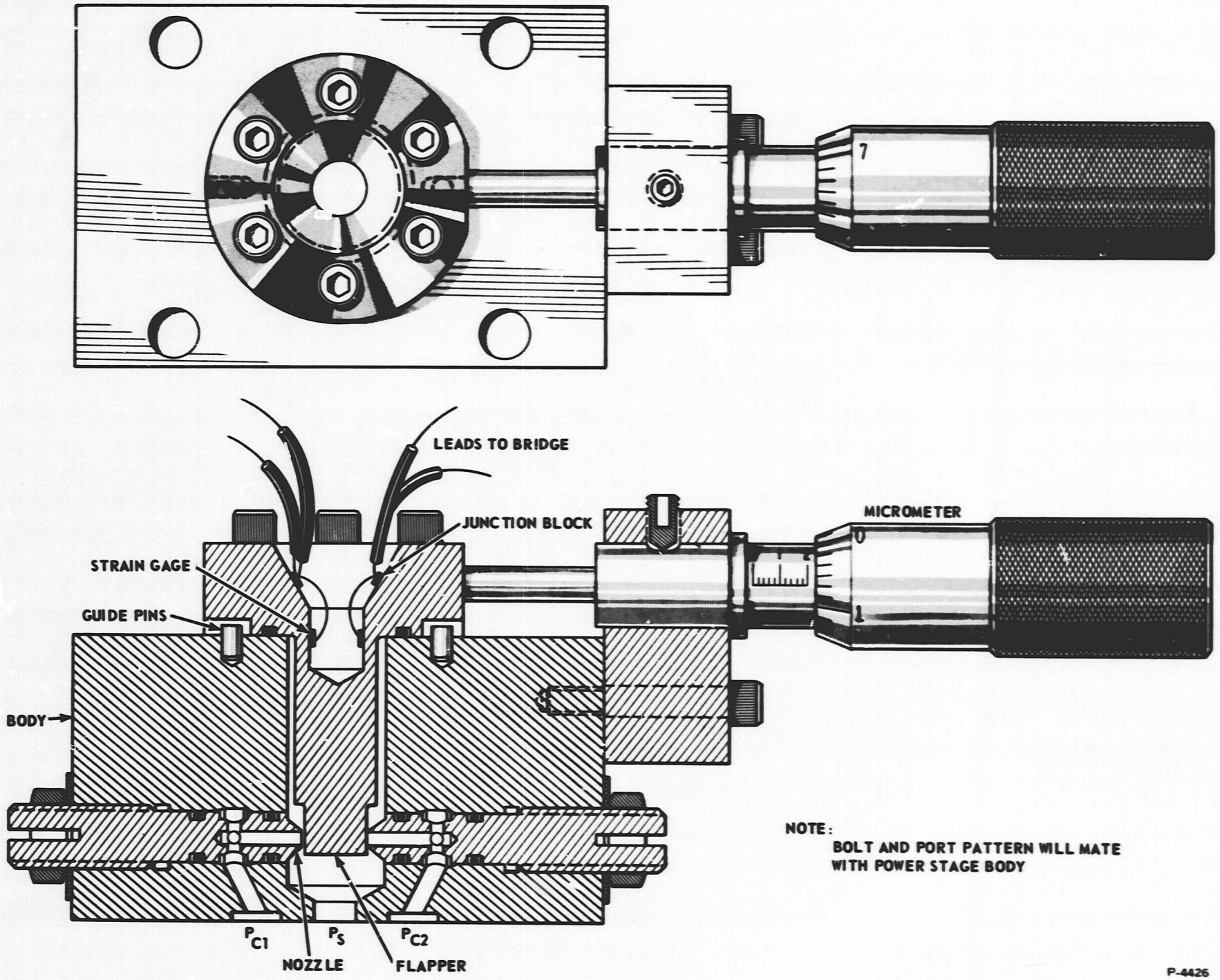

Figure 87 - Flapper Force Measurement Fixture

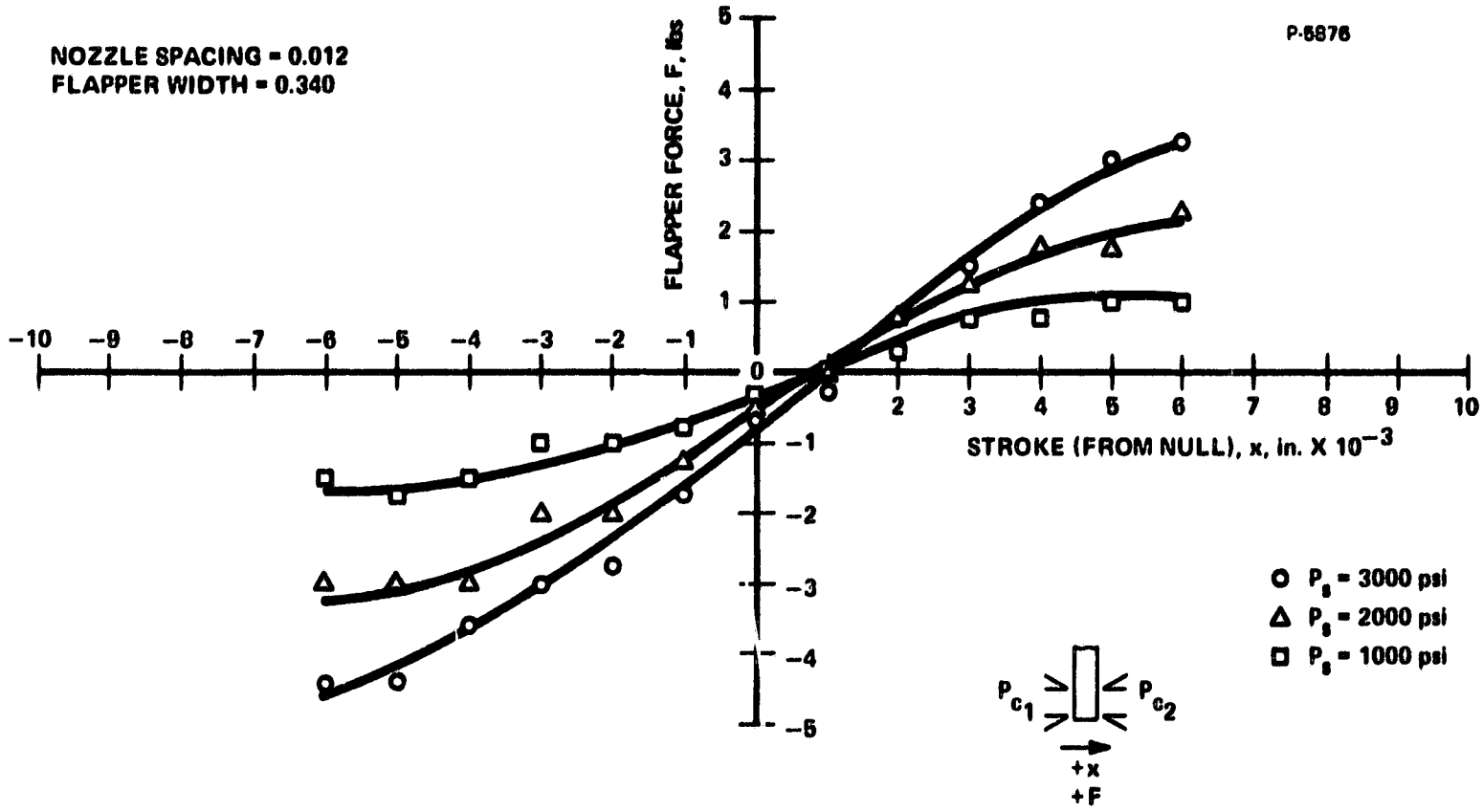

Figure 88 - Flapper Force Versus Stroke for Reversed-Flow Flapper-Nozzle Pilot Stage (Nozzle Spacing = 0.012, Flapper Width = 0.340)

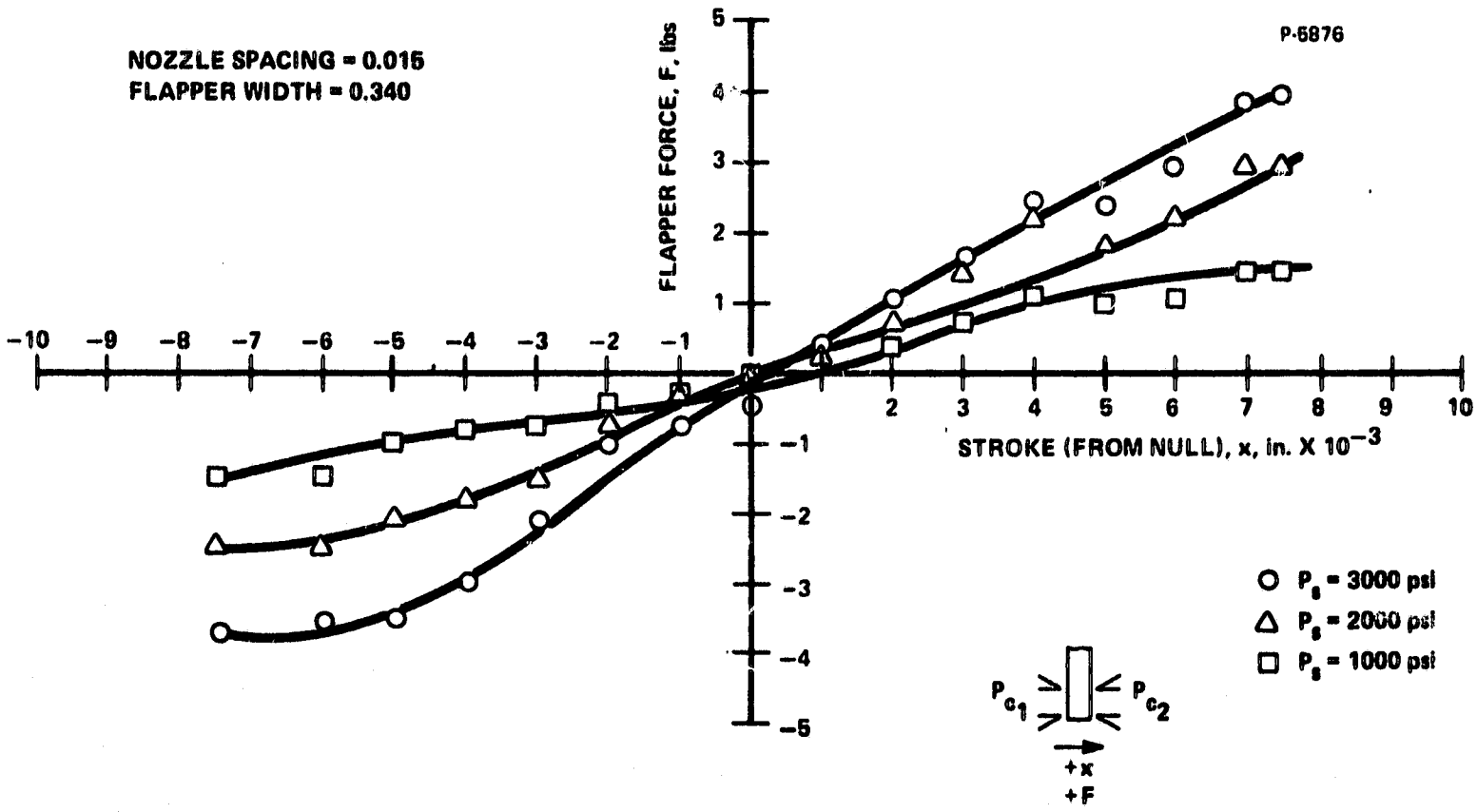

Figure 89 - Flapper Force Versus Stroke for Reversed-Flow Flapper-Nozzle Pilot Stage (Nozzle Spacing = 0.015, Flapper Width = 0.340)

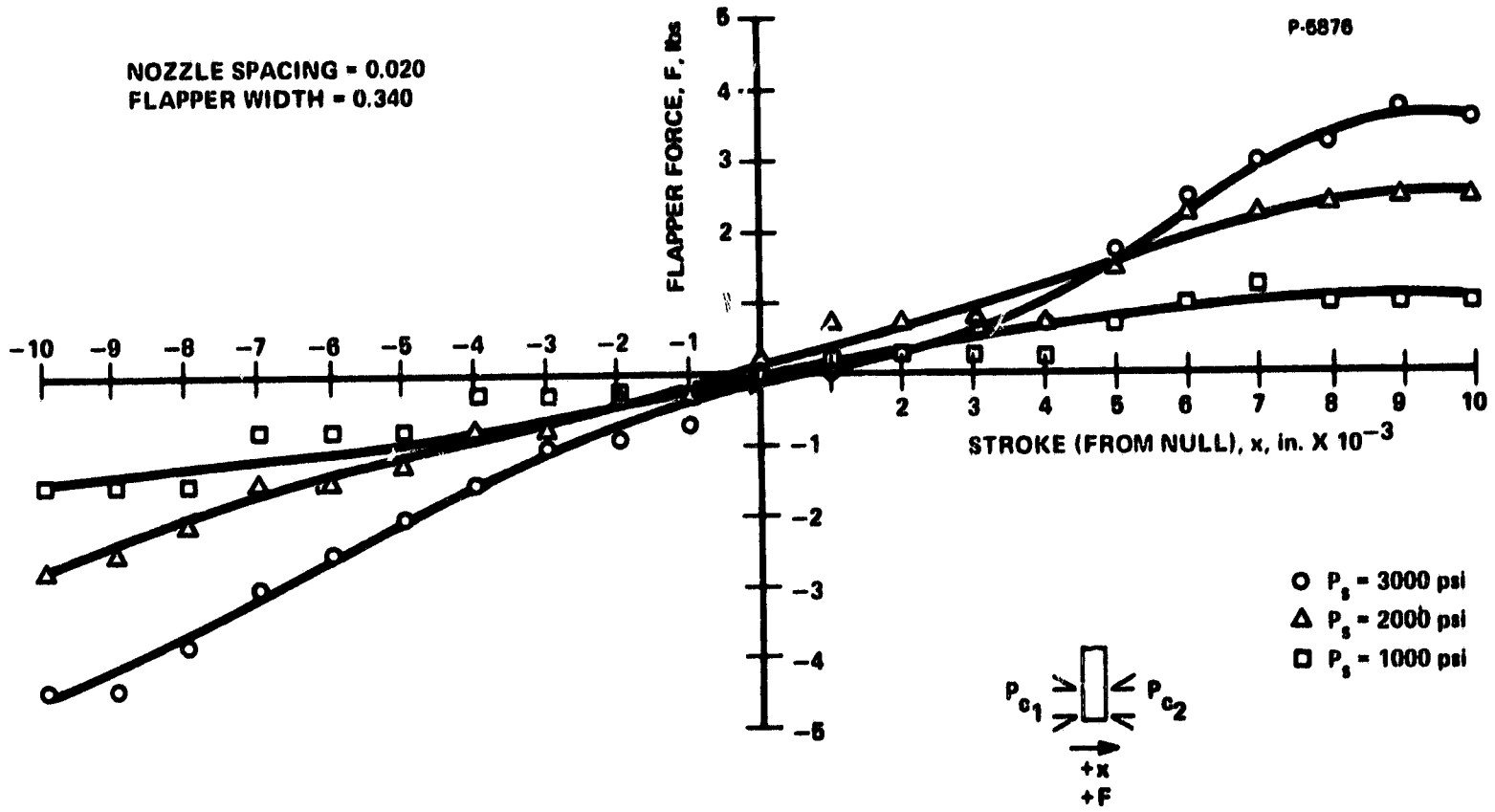

Figure 90 - Flapper Force Versus Stroke for Reversed-Flow Flapper-Nozzle Pilot Stage (Nozzle Spacing = 0.020, Flapper Width = 0.340)

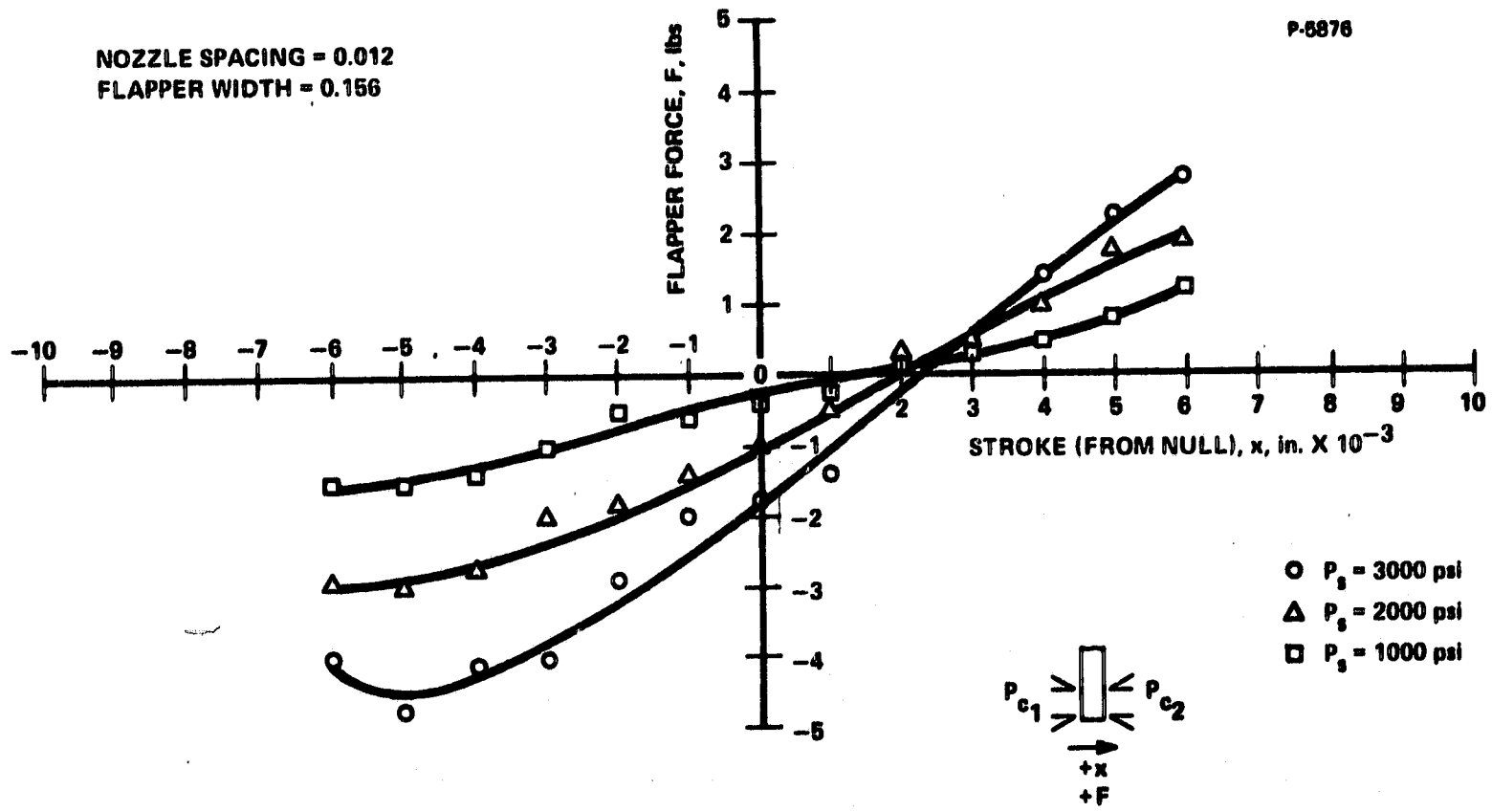

Figure 91 - Flapper Force Versus Stroke for Reversed-Flow Flapper-Nozzle Pilot Stage (Nozzle Spacing = 0.012, Flapper Width = 0.156)

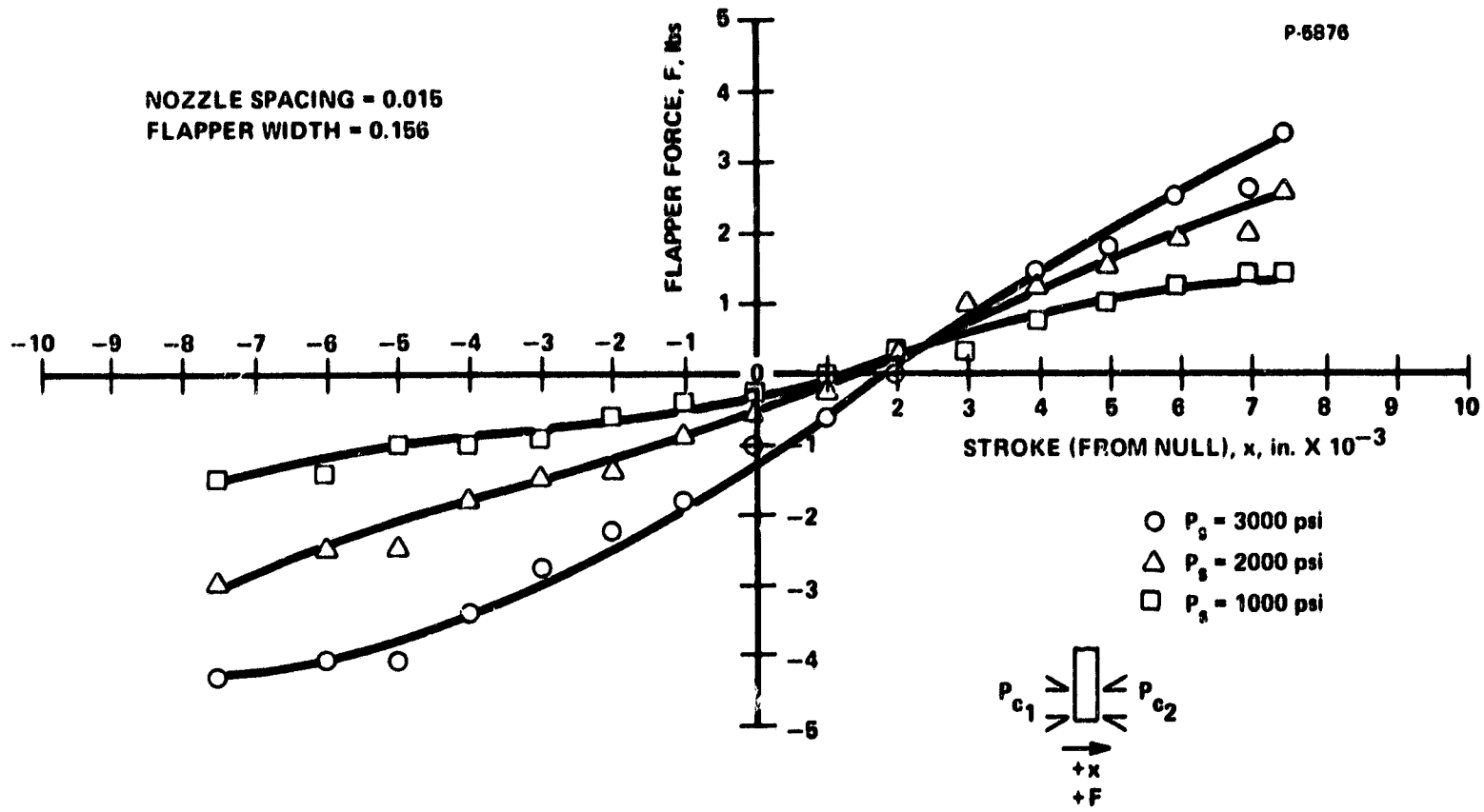

Figure 92 - Flapper Force Versus Stroke for Reversed-Flow Flapper-Nozzle Pilot Stage (Nozzle Spacing = 0.015, Flapper Width = 0.156)

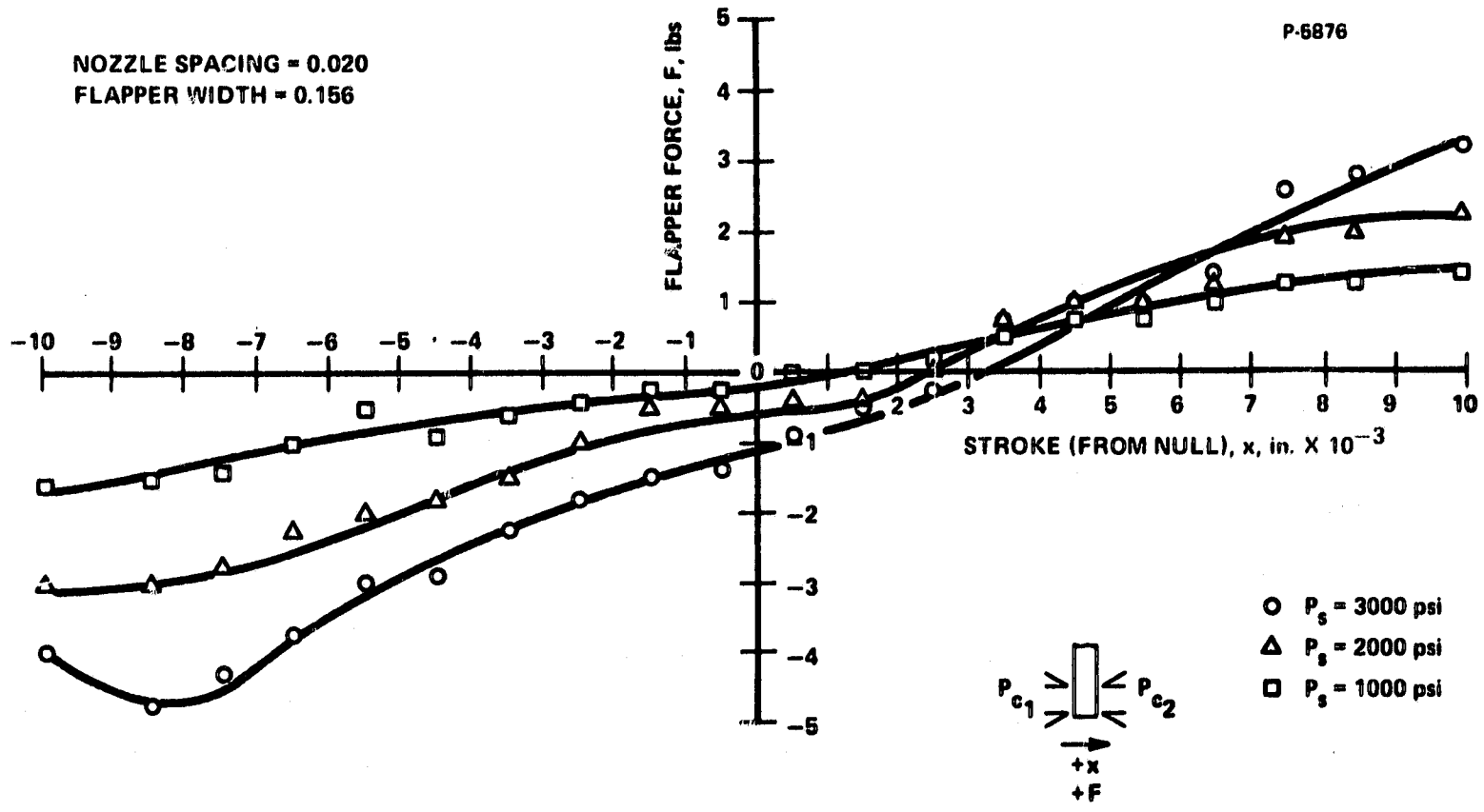

Figure 93 - Flapper Force Versus Stroke for Reversed-Flow Flapper-Nozzle Pilot Stage (Nozzle Spacing = 0.020, Flapper Width = 0.156)

and were not appreciably altered by the nozzle spacing. In some instances, it was found that the null position (x = 0) force was not equal to zero as would be expected. This was probably due to the fact that the control hole impedances were not identical to the two vortex valves which constitute the power stage. This produces a control pressure unbalance at null, which results in a net force on the flapper. In addition, the strain readings recorded are in the 1-microinch range which is near the lower limit of strain gage usefulness.

In order to improve the force readings, particularly near null, additional data were taken, using selected sleeves with more nearly matched control ports. These data are shown in Figure 94 for a flapper width and nozzle spacing of 0.156 inch and 0.012 inch, respectively. These dimensions are representative of the actual pilot stage dimensions. Supply pressure was maintained at 3000 psi.

The data of Figure 94 were used to re-size the cantilever spring used to negate the hydraulic forces acting on the flapper. The required spring rate was determined as follows: The slope of the force-stroke curve through the zero force axis was transferred to the origin, as shown by the solid straight line of Figure 94. The torque motor force of 1.5 pounds at 0.006 inch (full stroke) was then added to the full-stroke hydraulic force. The resulting straight line (dashed line of Figure 94) was then the required force-deflection curve of the cantilever spring. The spring rate calculated from this data was 1000 lb/in. This value would be the spring rate if the spring were located at the nozzle position. Since this was not the case, the spring rate was altered by consideration of the spring position from the pivot point of the torque-motor armature. The required spring rate was calculated to be 1800 lb/in.

The cantilever spring was machined to obtain a spring rate of approximately 3000 lb/in. This allowed successive grinding operations to be performed and, at each new spring rate, a functional test of the pilot stage was performed. The final spring rate would be obtained when the desired stroke and control pressure specifications were met. Table V lists the spring diameters and spring rates used for these tests. The spring length was held constant at 0.363 inch. During the last test performed (spring rate of 1990 lb/in), the torque motor flapper went "hard-over" against one of the nozzles and could not be driven off the nozzle by increasing the differential current in the opposite direction. Upon disassembly of the pilot stage, the torque motor was found to be very unsymmetrical. It could not be determined whether pilot stage instability or torque motor asymmetry (caused by slippage of the torque motor gain screws) was the cause of the "hard-over" condition.

Pilot stage tests - torque motor tests. - The torque motor was partially disassembled to inspect the air gaps between the armature and pole pieces. The air gaps were found to be unequal on one end of the torque motor, producing a high gain when the output flapper was stroked toward this end. This condition was alleviated somewhat by shimming the torque motor between the base plate and the pole piece assembly at

Table V - Cantilever Spring Rates
(Effective Spring Length = 0.363 Inch)

Spring Diameter (Inch)	Spring Rate (lb/in)
0.087	2970
0.084	2780
0.081	2225
0.078	2020
0.076	1990

P-5876

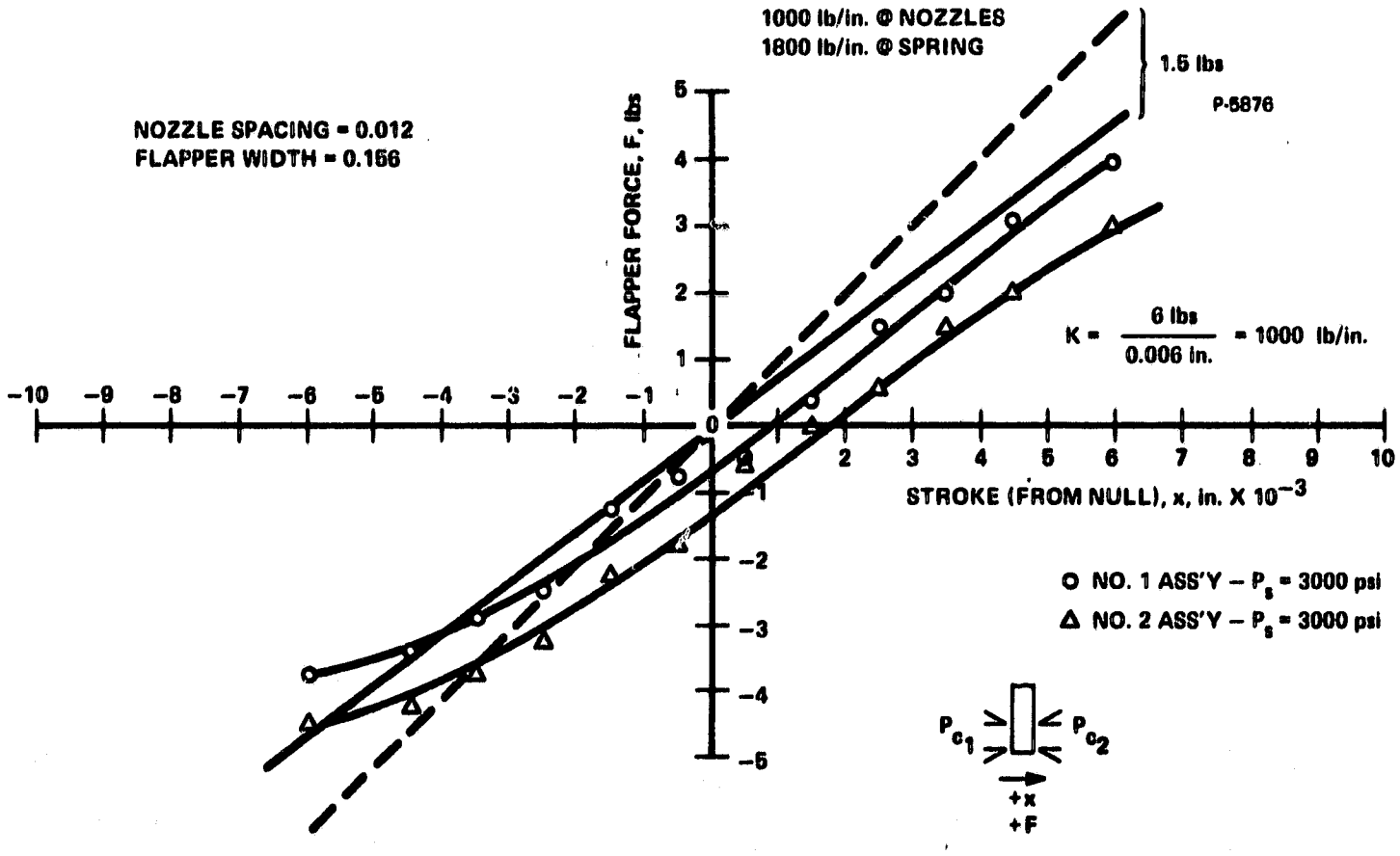

Figure 94 - Flapper Force Versus Stroke for Reversed-Flow Flapper-Nozzle Pilot Stage (Nozzle Spacing = 0.012, Flapper Width = 0.156)

the unsymmetrical end only. Torque-motor stop and gain adjustments were then made, resulting in the stroke-differential current data shown in Figure 95. A high-gain region is still indicated in Figure 95, but is not as severe as the nearly vertical operation obtained previously. Figure 96 shows the stroke-differential current data for a second torque motor obtained from the manufacturer. The curve clearly shows the high-gain region at the connector end of the torque motor. This is built into the torque motor design, in order to match the load requirements of Bendix Specification DS-735.

In order to determine whether this high-gain characteristic was detrimental to pilot stage performance, the torque motor whose stroke-differential current curve is shown in Figure 95, was assembled on the pilot stage body. A new cantilever spring with a rate of 2620 lb/in was used for these tests. This rate was approximately 800 lb/in greater than required and would permit trimming to the correct rate. The pilot stage nozzles were adjusted to the proper distance. The supply pressure was set at 3000 psi. The differential current to the torque motor was increased until the pilot stage became unstable. To stop the oscillation, the supply pressure had to be reduced. Increasing the differential current in the opposite direction did not have any effect. Subsequent attempts to bring the supply pressure up to the 3000 psi level (with $\Delta i = 0$) resulted in an unstable condition at $P_s = 2750$ psi. During the last test, the cantilever spring fractured, due to a high stress concentration at the point where the spring is "necked down" to provide the desired rate. The progressive fatigue failure of the spring at this point could have lowered the rate of the spring throughout the duration of these tests, contributing to the unstable condition. For subsequent tests the radius at the "necked down" point was increased to reduce the stress concentation.

At the completion of the above series of tests, a viscous shear damping device was designed and added to the pilot stage assembly. This device was positioned along an axis perpendicular to the center line of the pilot stage nozzles. An adjustable pad and a machined flat on the side of the torque-motor flapper were utilized. As the flapper moved between the nozzles, the oil film between the pad and flapper would provide some viscous damping. The degree of damping would be dependent upon the clearance between the pad and flapper, the flapper velocity, and the oil viscosity.

A series of tests was performed with a clearance between the pad and flapper set at 0.001 inch. A new cantilever spring was assembled in the pilot stage body. Additionally, prior to final pilot stage assembly, torque motor gain and stop adjustments were made to provide linear operation with flapper stroke limited to $\pm$0.006 inch from null. Stroke-differential current data are shown in Figure 97 for various loads. After assembly of the pilot and power stages, supply pressure to the servovalve was slowly increased to 3000 psi and the control pressures were adjusted to the proper level. The pilot stage remained in a stable condition with no differential current applied to the torque motor, although the control

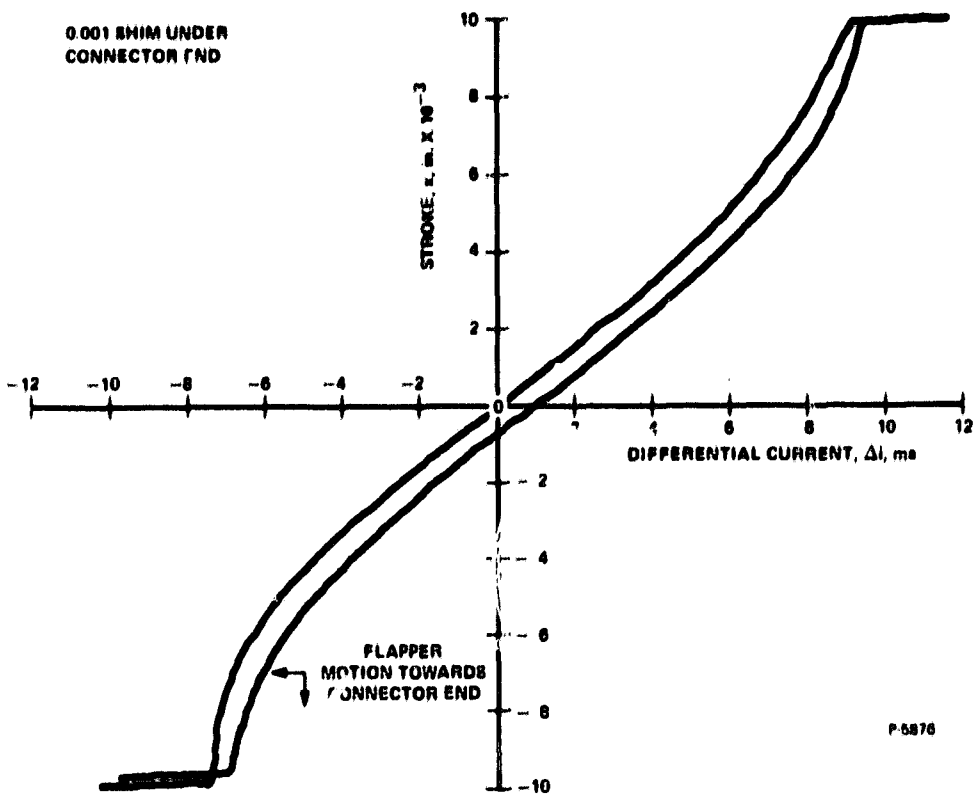

Figure 95 - Stroke Versus Current Data for Torque Motor No. 8206 (0.001 Shim Under Connector End)

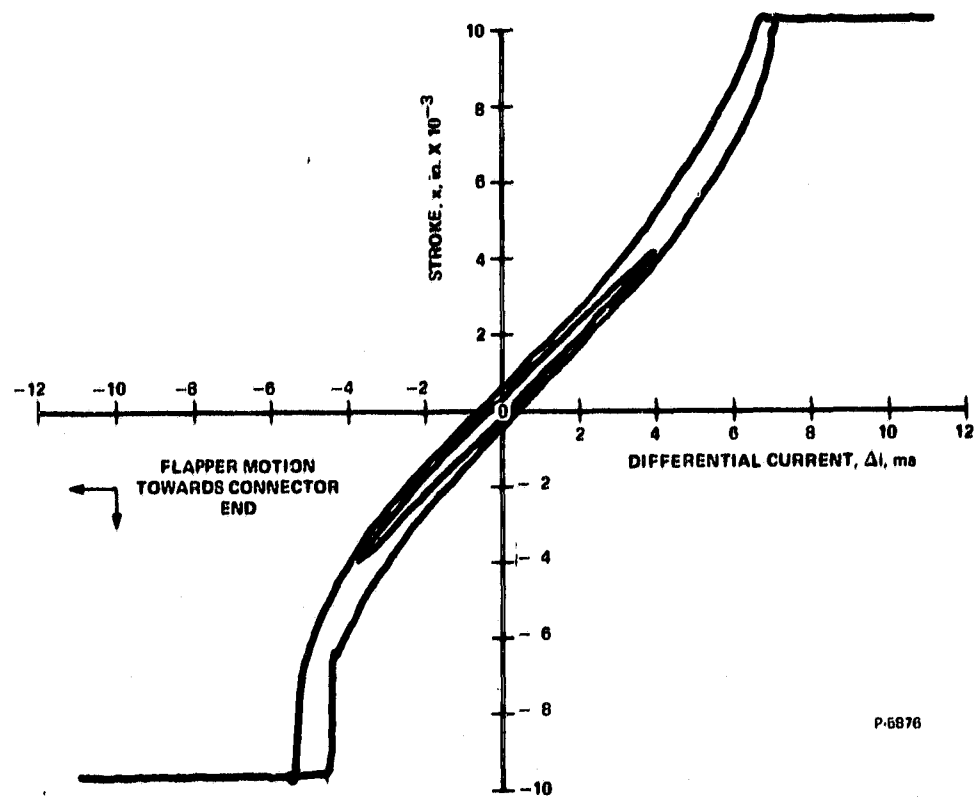

Figure 96 - Stroke Versus Current Data for Torque Motor No. 8205

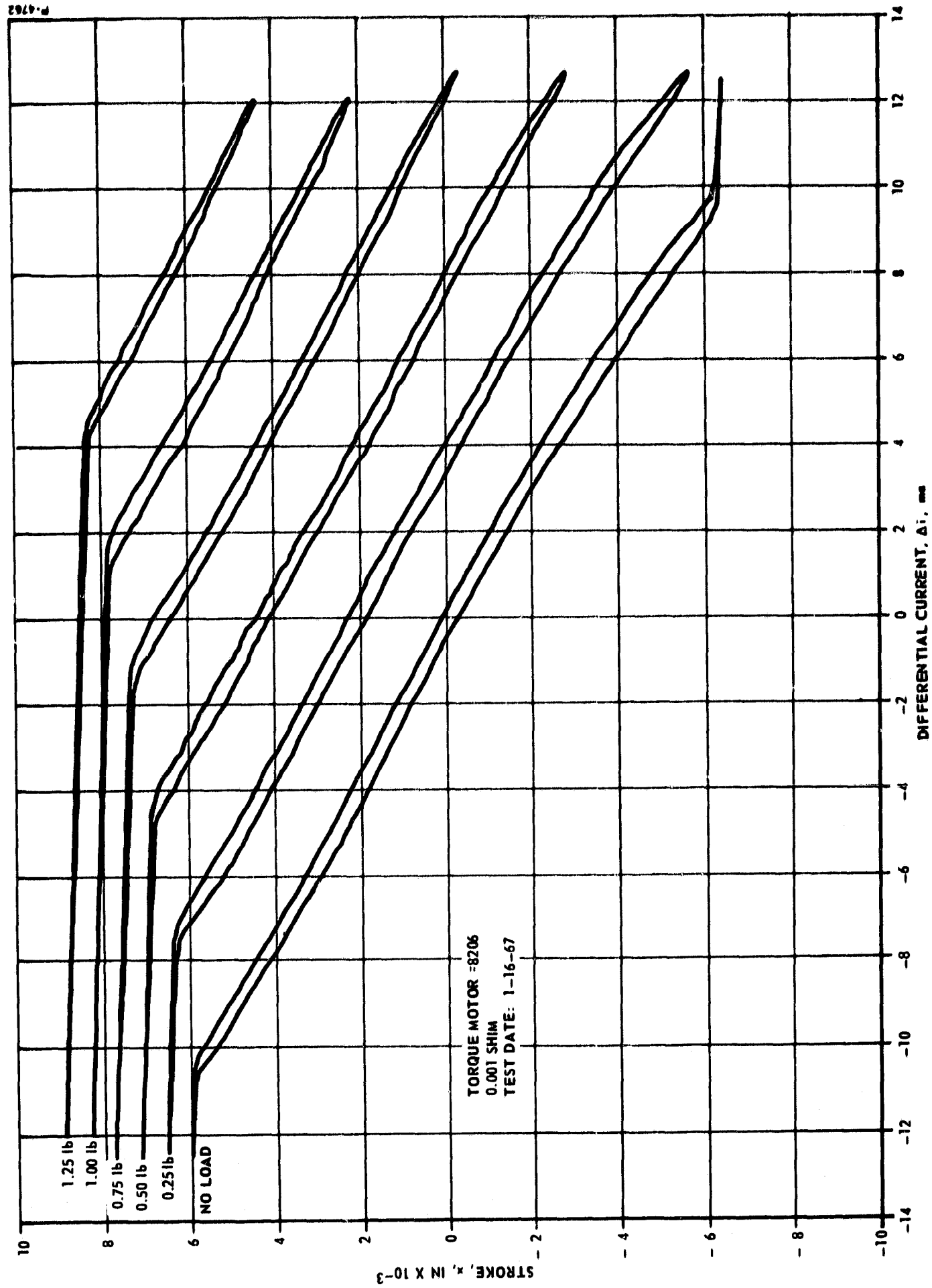

Figure 97 - Stroke Versus Current Data for Torque Motor No. 8206

pressures fluctuated slightly. The pilot stage was then stroked in both directions. No unstable condition was apparent. Since the cantilever spring rate was high, full stroke was not attained. The cantilever spring was removed from the assembly and machined to provide a lower spring rate. After reassembling the pilot stage and adjusting the control pressure level, differential current to the torque motor was increased. The pilot stage became unstable and oscillated as the torque motor was stroked in the direction opposite the connector end of the motor (negative Δi). Adjustment of the damper had no effect on this unstable condition. The torque motor was removed from the assembly and the gain curve was checked. These data agreed with the data of Figure 97, thereby eliminating the torque motor as the source of the instability. In order to determine if the unstable condition was supply-pressure sensitive, a cantilever spring with a much lower spring rate was assembled in the pilot stage and a supply pressure of 2000 psi was utilized. The pilot stage was stable but stroke was limited. When the supply pressure was increased so that full stroke could be obtained, the pilot stage again became unstable.

As supply pressure is increased to the servovalve, the total spring rate of the pilot stage reduces from a high positive rate to zero and can become a negative rate or statically unstable. It appears that as the pilot stage total spring rate goes down with increasing supply pressure, the flapper stroke increases. Before the flapper can be driven to full stroke, however, the system becomes dynamically unstable and only by lowering supply pressure can the oscillation be stopped.

Pilot stage tests - vortex valve hysteresis. - Power stage vortex valve performance was checked experimentally to determine the amount of hysteresis in the turndown curve. A significant "hysteresis loop" could result in rapid variations of control flow and pressure as the vortex valves are turned down during servovalve operation. The results of the performance tests are shown in Figures 98 through 101 for the four vortex valves which are contained in the two servovalve assemblies. Data points are shown for increasing and decreasing values of control pressure, P_c. The curves indicate a small amount of hysteresis near full turndown, but this was not considered to be the order of magnitude required to produce the pilot stage instability

To further verify the results of the above tests, pilot stage tests were performed without the power stage assembly. As supply pressure was increased to 3000 psi, an oscillatory condition was encountered as in previous testing. The pilot stage instability, therefore, could not be attributed to the power stage.

Pilot stage tests - frequency analysis and measurements. - A preliminary investigation of the natural frequencies of critical pilot stage components was undertaken. Analysis and test were used to study potential sources of the dynamic instability of the reversed-flow flapper-nozzle system. The natural frequency of the torque-motor flapper was calculated, first, by assuming that the flapper could be represented by a fixed-free

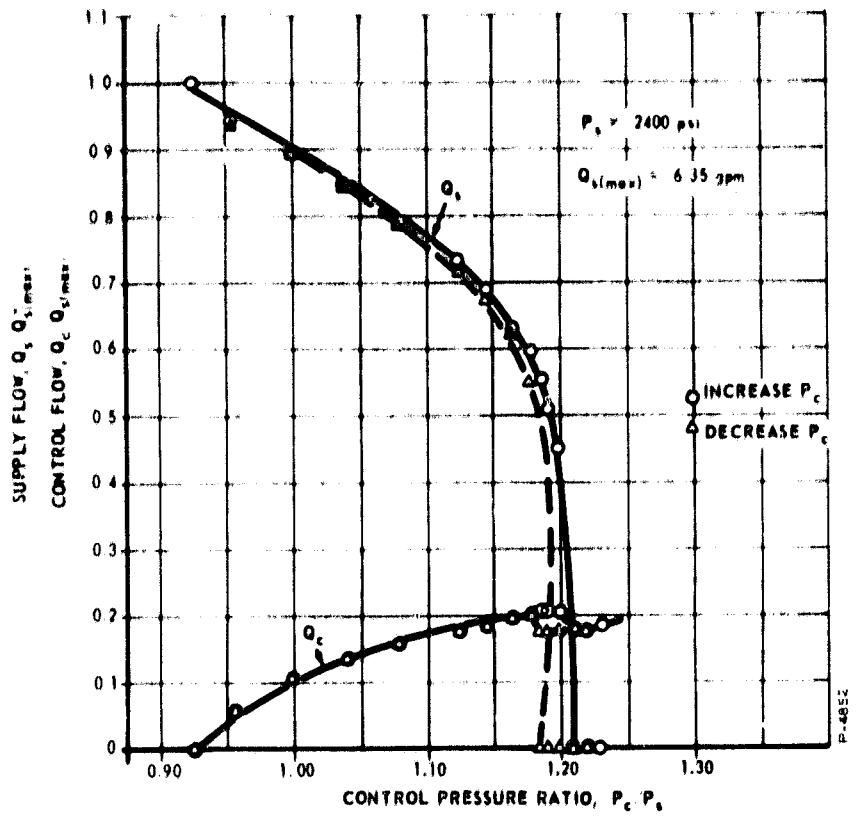

Figure 98 - Vortex Valve Performance - Assembly No. 1; Vortex Valve No. 1

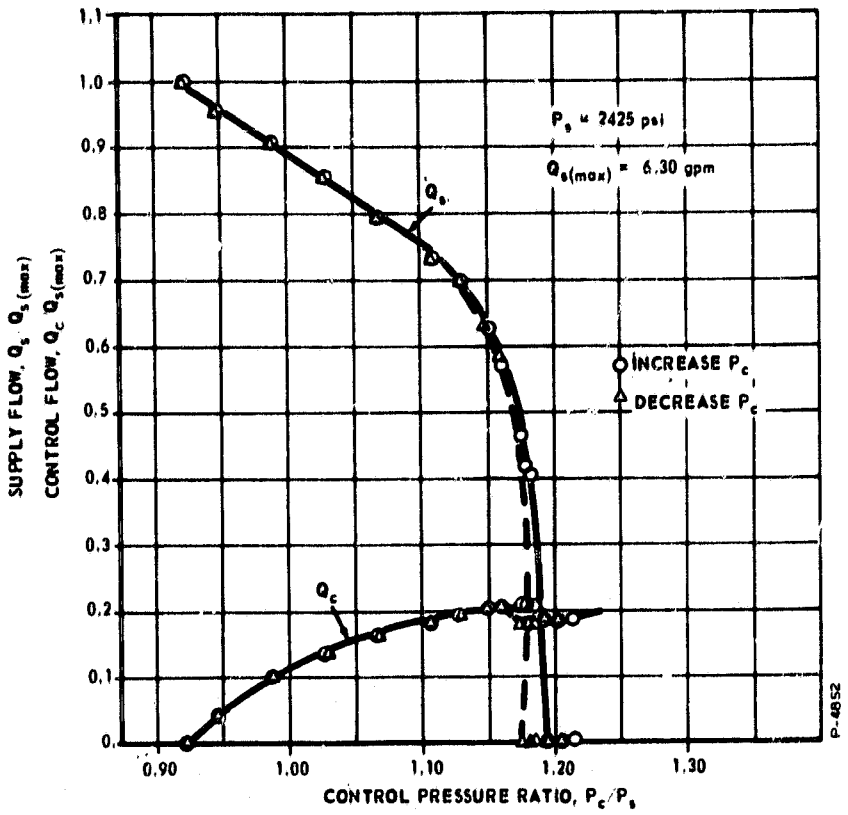

Figure 99 - Vortex Valve Performance - Assembly No. 1; Vortex Valve No. 2

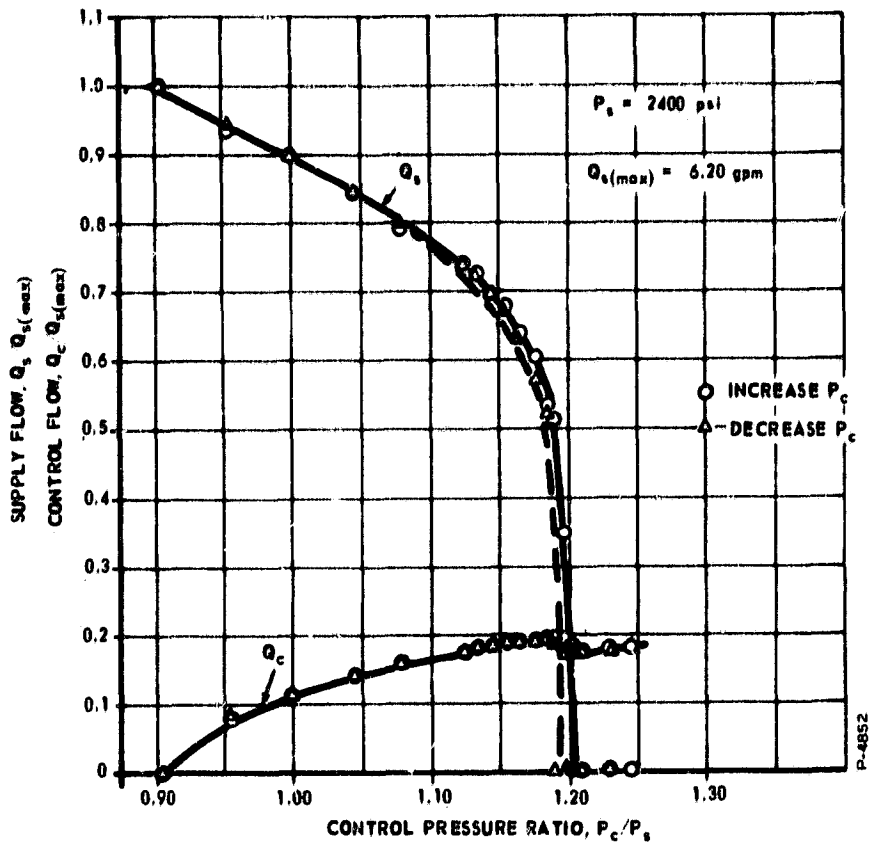

Figure 100 - Vortex Valve Performance - Assembly No. 2; Vortex No. 1

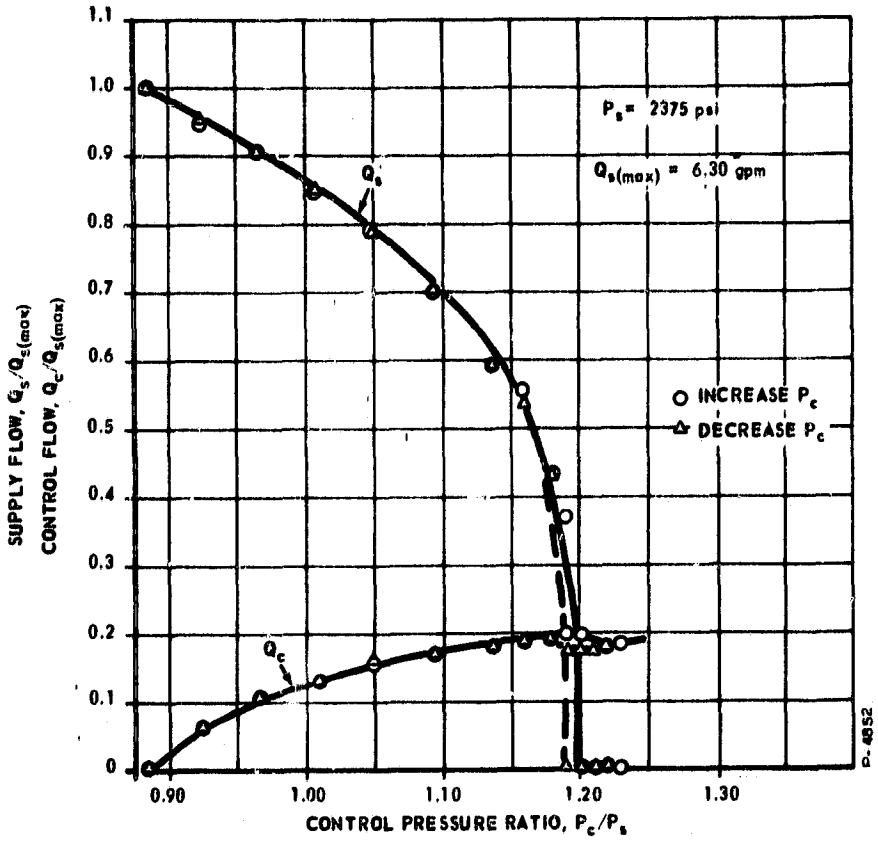

Figure 101 - Vortex Valve Performance - Assembly No. 2; Vortex Valve No. 2

(cantilever) beam and secondly, by assuming that it is a hinged-free beam. The true natural frequency of the output flapper can be considered to be somewhere between these two limiting cases. The following frequencies were calculated for the flapper:

	Fixed-Free Beam	Hinged-Free Beam
f_1	2,640 cps	0
f_2	16,500 cps	11,500 cps

where f_1 and f_2 are the fundamental and second natural frequencies of the beam, respectively. In order to determine if some forcing function could be present in the system which could act in conjunction with the torque-motor flapper system to produce the re-occurring instability, the resonant frequency of an oil column of length equal to that in the pilot stage nozzle was calculated. Assuming a bulk modulus for Mil-H-5606 oil to be 75,000 psi, the resonant frequency of the oil column was found to be 16,800 cps. This is the same order of magnitude as the second natural frequency of the flapper system and is also of the same order as the measured frequency of control pressure fluctuations (12,000 cps). Under the resonant conditions, then, it was possible that flapper oscillations, which are ordinarily small, could be significantly amplified, resulting in the pilot stage instability. To "de-tune" the system, the nozzle outlet hole volume can be increased by lengthening the oil column or by increasing the diameter of the outlet hole a short distance from the nozzle entrance. With the hardware design, the simplest change was to drill the nozzle hole deeper.

Before these tests, the pilot stage nozzles were machined to remove any nicks and burrs which might affect performance. Brass shims were soldered to the torque-motor flapper to provide a smooth flapper surface in the nozzle area and to facilitate the repair of the surface if the flapper is marked by the nozzles during subsequent testing. The pilot stage was then assembled, adjusted, and mounted on the hydraulic test fixture. The control pressure oscillations were measured with a pressure transducer mounted as close as possible to the servovalve test manifold. The output of the transducer was recorded on a Brüel & Kjaer (B&K) Audio Frequency Spectrometer. The filter system and voltmeter of the Audio Frequency Spectrometer allows convenient determination of the relative amplitudes of the harmonics of a complex waveform.

The first test was performed at 3000 psi supply pressure with the original nozzle design having a nozzle depth of 0.500 inch. For this depth, the calculated resonant frequency of the oil column is 16,800 cps. For two subsequent tests, the nozzle depth was increased to 0.850 inch and 1.00 inch to reduce the calculated resonant frequency of the oil column to 9900 cps and 8400 cps, respectively. For each nozzle depth, the control pressure and torque-motor back emf oscillation spectra were

scanned with the B&K equipment. Table VI lists representative data recorded during these tests. The control pressure frequency shown is the frequency at which the largest amplitude signal was recorded. This frequency changed slightly with the first change in the oil column length, but the pilot stage was unstable for all of the tests as soon as the differential current to the torque motor was increased. Table VI also lists the predominant frequency of the back emf generated by the motion of the torque-motor armature. This frequency remained unchanged with changes in the oil column length. Lengthening of the oil column, then, did not significantly alter the pilot stage instability.

The oil column could not be shortened less than 0.500 inch because of interference with the cross-drilled holes cummunicating the control pressure to the vortex valves in the power stage body. Reducing the length of the oil column or adding an adjustable volume to the column would have required extensive rework of the pilot stage nozzles. It was not considered feasibile to investigate these effects during the present contract.

Another consideration which contributes to the instability of the reversed-flow flapper-nozzle pilot stage is the high pilot stage power gain. A high gain was necessary to handle the high pilot stage flow and to be compatible with the low input electrical power requirements. As shown in Table VII, the power gain for the present pilot stage is essentially four (4) times greater than the servovalve it replaces and is more than twice that of other conventional designs. Stability of the system can only be assured, then, if the excessive power gain of the pilot stage is reduced, or if improved designs are formulated for matching the requirements.

Table VI - Comparison of Calculated and Measured Resonant Frequencies

Oil Column Length	Calculated Natural Frequency of Oil Column	Dominant Frequency of Control Pressure Oscillation	Dominant Frequency of T/M Back EMF
(in.)	(cps)	(cps)	(cps)
0.500	16800	700	1600
0.850	9900	200	1700
1.000	9400	200	1600

P-5876

Table VII - Summary of Conventional Hydraulic Servovalve Pilot Stage Gain

Item \ Servovalve	Moog Series 31 and 32	SIB (Moog)	Bendix Electro-dynamics Division	Vortex Hydraulic Servovalve
Input Elect. Power (watts)	0.040	0.150	0.0304 at null	0.150
Pilot Stage Flow (in^3/sec)	0.3	0.75	0.19	10.5
Pilot Stage ΔP (psi)	1000 (assumed)	1000 (assumed)	1500	300
Pilot Stage Power (watts)	500	1260	478	5,300
Pilot Stage Power Ratio $\left(\frac{W_{out}}{W_{in}}\right)$	12,500	8,400	15,700	35,000

P-5876

$$\text{Input Power (watts)} = 2\left(\frac{\Delta i_{max}}{2}\right)^2 \times (\text{resistance/coil})$$

$$= 2\,(\text{quiescent current})^2\,(\text{resistance/coil})$$

$$\text{Pilot Stage Power (watts)} = (1.678)\,(\Delta P)\,Q$$

In order to resolve the pilot stage instability problem, it was concluded that the following should be accomplished:

(1) Develop a complete analytical model of the reversed-flow flapper-nozzle system

(2) Experimentally determine the present torque-motor dynamics for verification and correlation with the mathematical model of Item 1

(3) Procure larger torque motors with increased input power based on the results of Item 1.

Of the tasks outlined, Item 1 is the most important, since further changes in the pilot stage design depend on a thorough understanding of the dynamics of the system and the effects of changes in the system parameters. It is believed that only in this manner can specific design recommendations such as increased torque-motor power and pilot stage nozzle shaping be made.

Power Stage Actuator Tests

Static tests. - Servovalve load-flow data were taken, using the hydraulic vortex servovalve power stage and a simulated pilot stage as shown schematically in Figure 102. A Bendix servovalve was used to provide a convenient means of pilot stage flow control. The servovalve is connected to the control ports of the two power stage vortex valves. The needle valves shown in the schematic may be adjusted to provide a wide range of vortex valve null control pressure level. The vortex valve flow receivers and cylinder ports are connected together through a flowmeter and load valve. To obtain the load-flow data, the Bendix servovalve is stroked to obtain the desired ΔP_c to the vortex valves and the load valve is varied from the full open no-load condition to the blocked condition. Typical data obtained during these tests are shown in Figures 103 and 104 for the two power stage assemblies. For plotting purposes, load flow, Q_L, was taken to be positive when its direction was from Vortex Valve No. 1 to Vortex Valve No. 2. Under these conditions, P_{c2} is greater than P_{c1} and, therefore, ΔP_c was defined as $(P_{c2} - P_{c1})$. As indicated in Figures 103 and 104, the maximum load pressure differential,

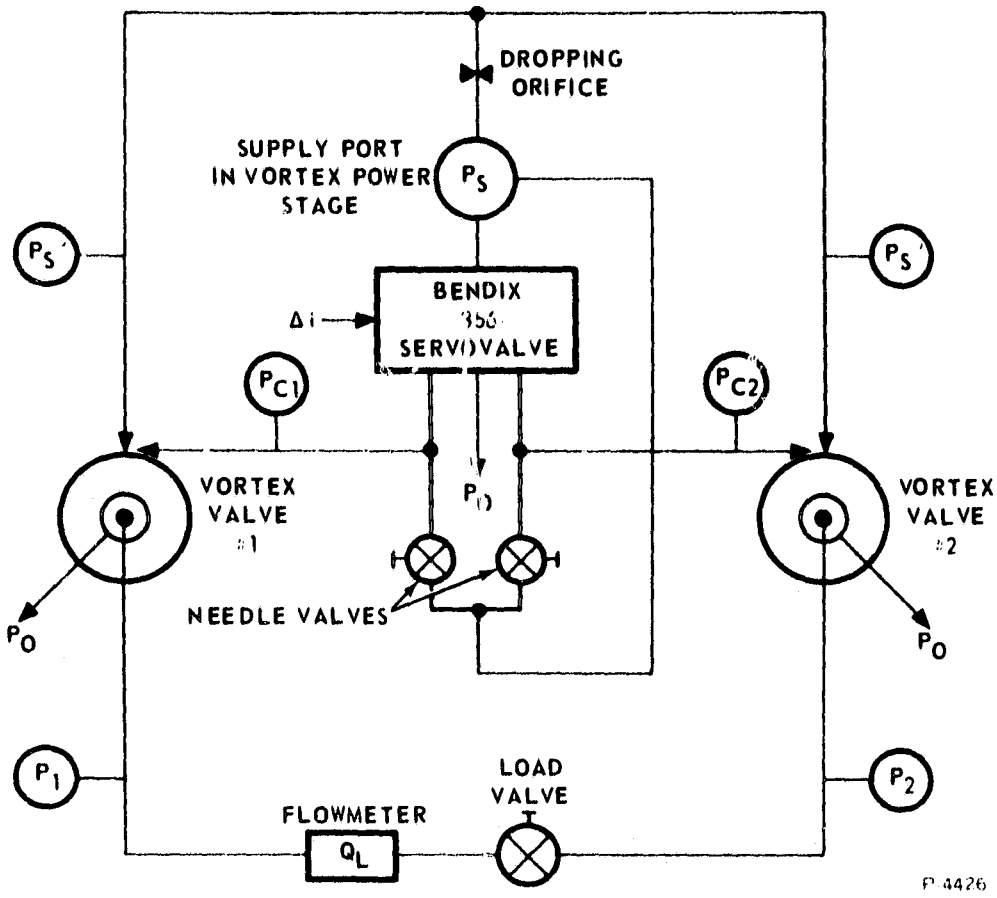

Figure 102 - Hydraulic Circuit for Vortex Servovalve Load-Flow Tests

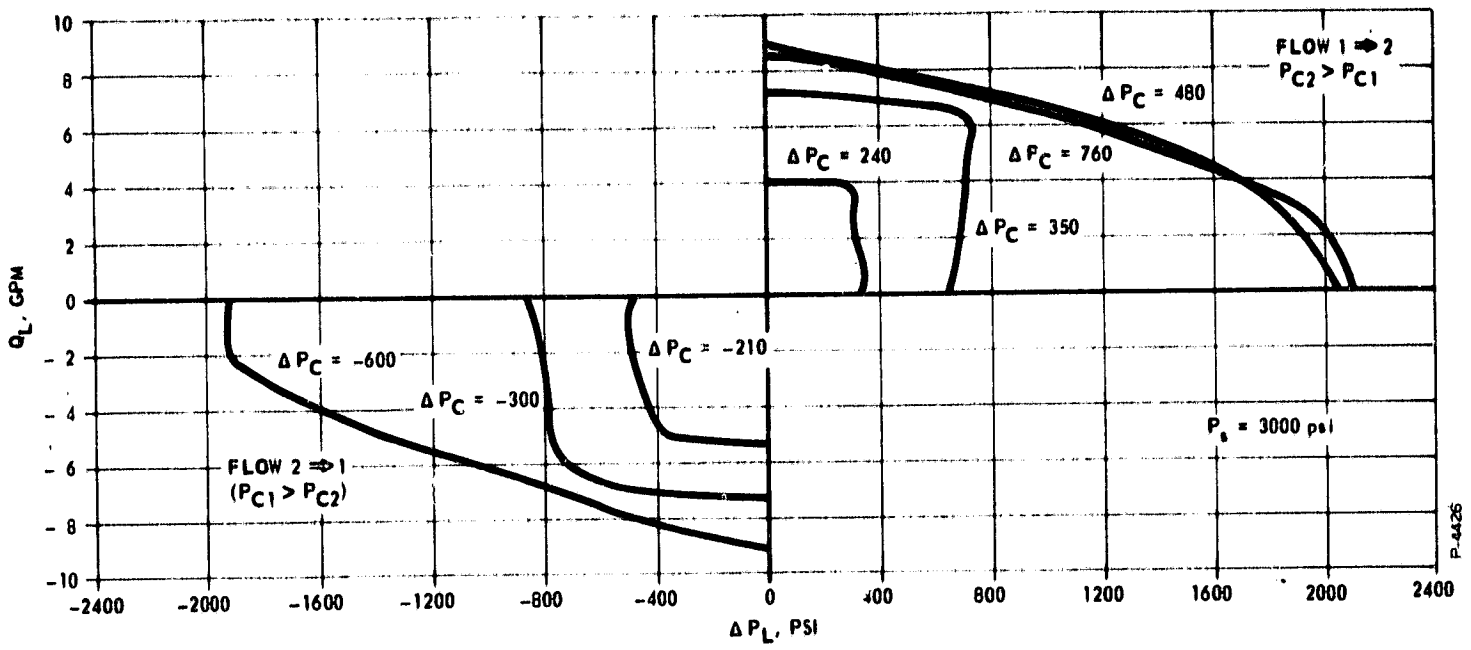

Figure 103 - Load-Flow Curves - Assembly No. 1

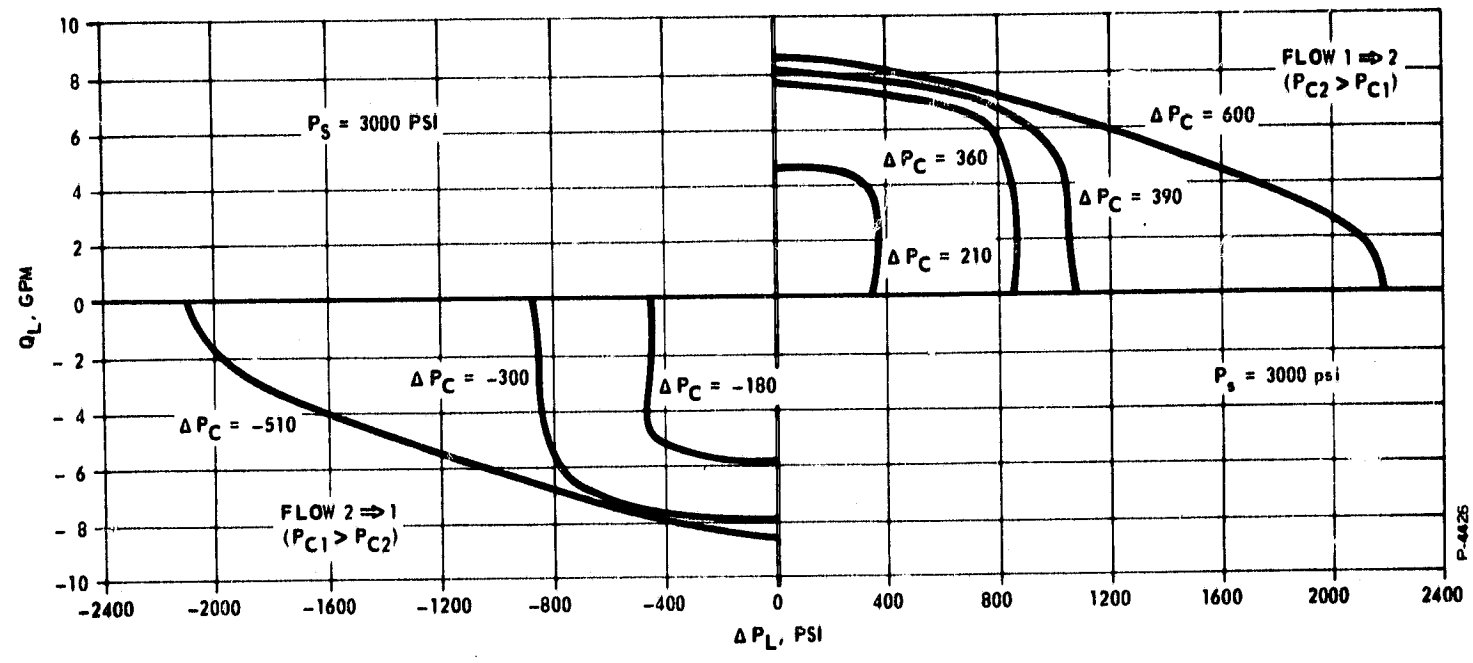

Figure 104 - Load-Flow Curves - Assembly No. 2

ΔP_L, is 2100 psi and maximum no-load flow is 8.9 gpm. The curves shown are characteristic of the vortex valve probe data measured during vortex valve developmental tests performed in the early phases of the present program. As can be seen from the data, however, there is a slight mismatch of performance when the two vortex valves are operated in the push-pull circuit. This may be due to slight manufacturing differences in the vortex valves or, more likely, may be caused by minor errors in adjustment of the simulated pilot stage.

After completion of the servovalve power stage load-flow tests, the power stage and simulated pilot stage were mounted on the NASA-supplied actuator (Moog 17-150 S/N 35), as shown in Figures 105 and 106. A series of functional tests was performed on the unloaded actuator with and without position feedback. By manual variation of the input differential current to the Bendix servovalve, the piston could be smoothly stroked to any desired position and held in this position by closing the feedback loop. At either end-of-stroke position, the measured cylinder pressure was 2000 psi. This value was consistent with the blocked port pressure obtained during the load-flow tests.

Dynamic tests. - After establishing that the actuator could be driven by the two vortex valves operating in a push-pull circuit, a function generator was connected to the input of the servoamplifier used to drive the Bendix servovalve. The feedback loop was closed and a sinusoidal input was applied to the pilot stage torque motor. The amplitude of the input command signal was adjusted to give an indicated output of $\pm$0.4 degree (0.191 inch) at an input signal frequency of 0.5 cps. (Under these conditions, the input and output signals are considered to be unattenuated.) The exact magnitude of the input command signal amplitude used was of little meaning, since the power requirements of the Model 356 Servovalve and the final hydraulic vortex servovalve were not identical. Figures 107 through 113 show traces of the actuator position for different sinusoidal input frequencies, ranging from 0.5 to 30 cps. Actuator position is referenced to degrees since the actuator used was a Saturn-IB engine gimbaling actuator which was equipped with an external scale calibrated in degrees of rocket engine position. This scale was utilized to determine actuator stroke during the frequency response tests. The conversion factor from degrees to inches of stroke is 0.478 inch/degree.

The traces indicate that the actuator stroked smoothly over the frequency range. At frequencies below 0.5 cps the output curve indicated some noise, as seen in Figures 107 and 114.

The remainder of the traces indicate the decrease in output amplitude and increase in phase lag with frequency. The volume under compression in the manifold block between the Bendix servovalve and the hydraulic vortex servovalve power stage was excessive, compared to the final design, and affected the response of the test circuit. These effects would not be apparent in the final servovalve, since the rated input differential current (12 ma) will be utilized and the feedback loop will be closed through the NASA servodriver rather than through a servoamplifier built for a completely different application.

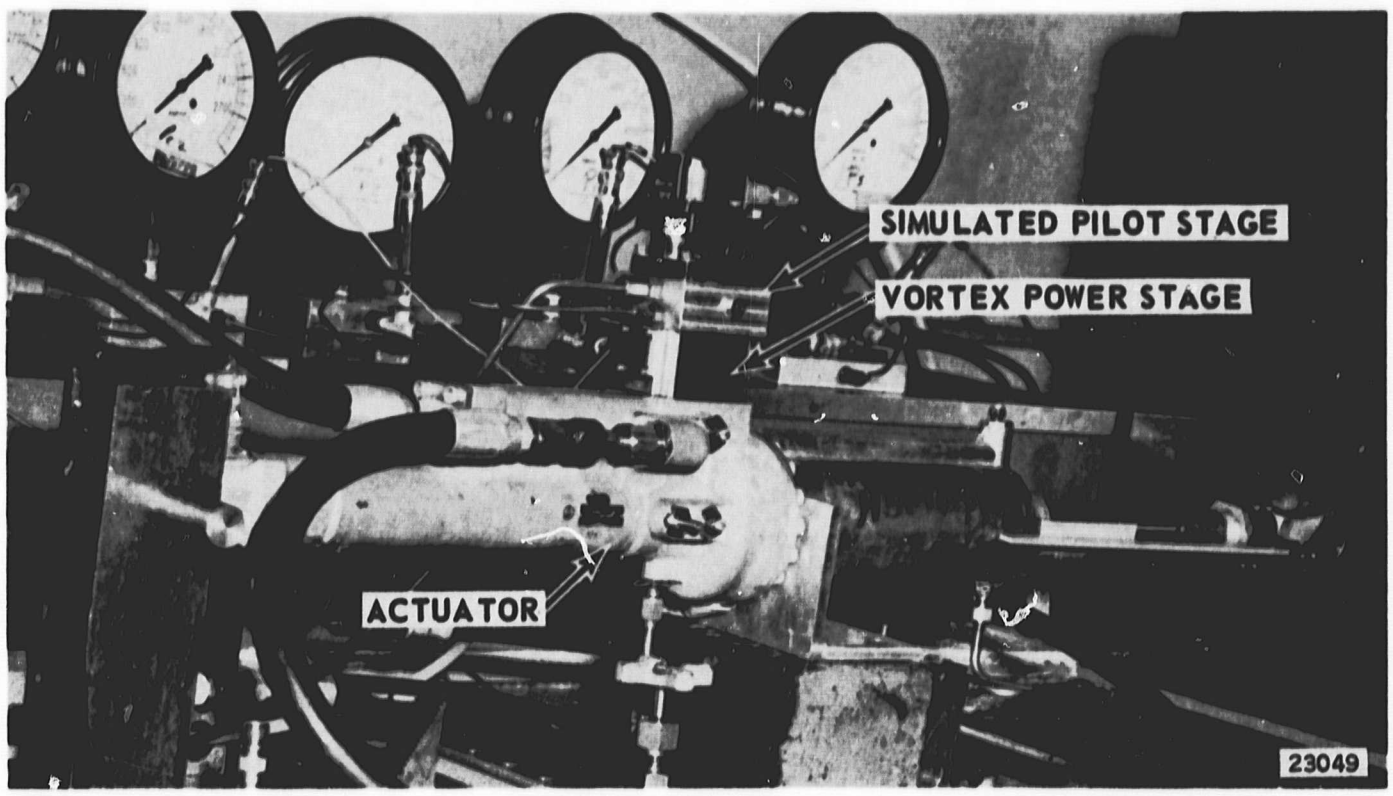

Figure 105 - Hydraulic Vortex Servovalve Power Stage During Tests with the NASA-Supplied Saturn Engine Gimbaling Actuator

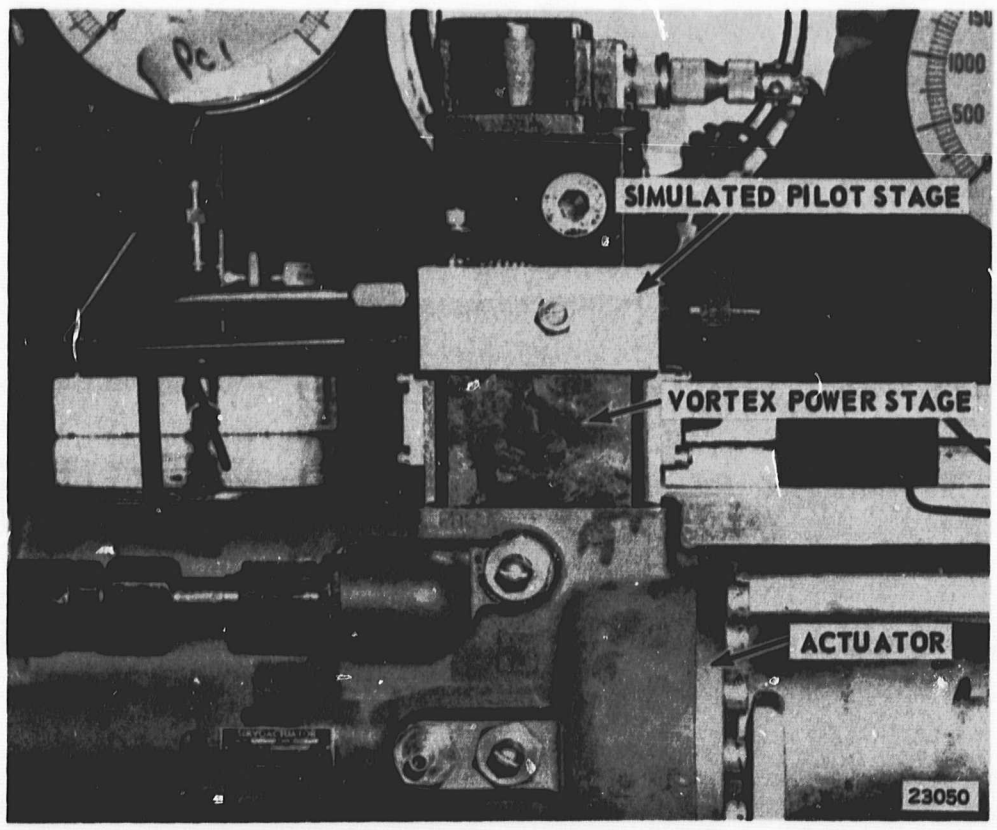

Figure 106 - Hydraulic Vortex Servovalve and Simulated Pilot Stage

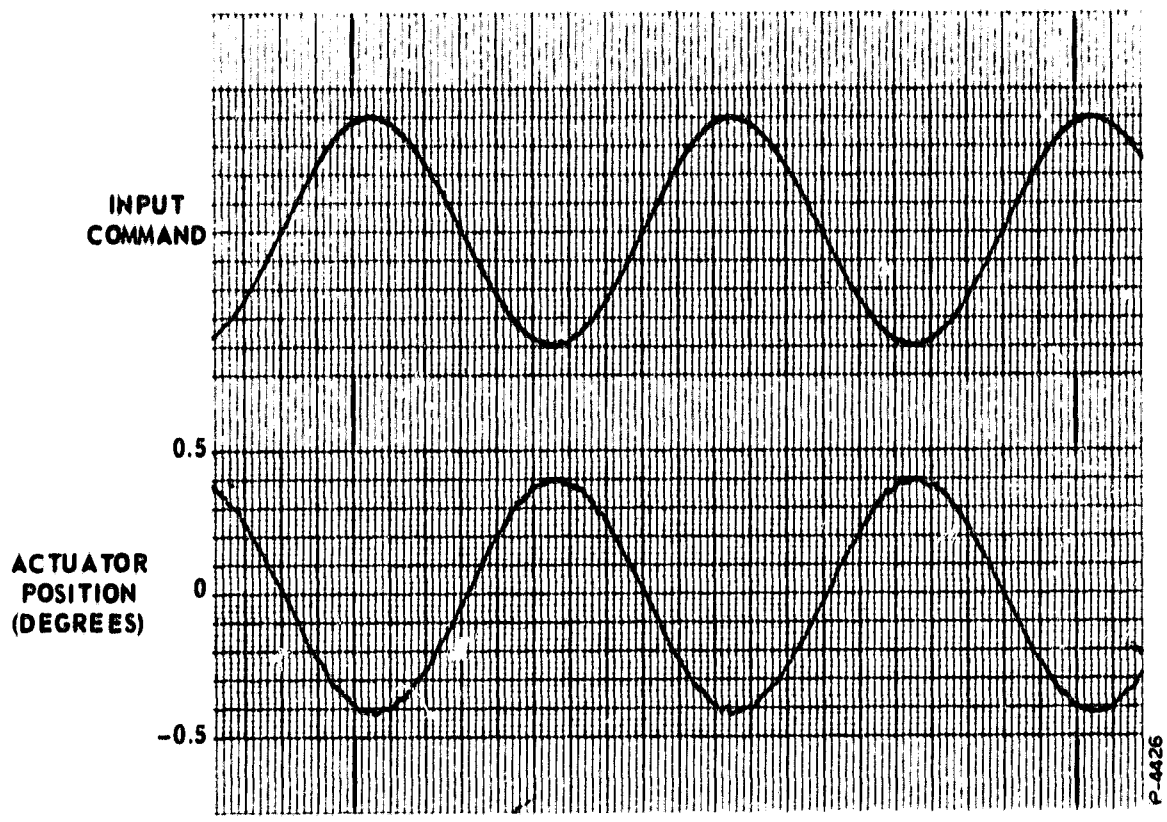

Figure 107 - Trace of Actuator Position for Input Frequency of 0.5 cps (Chart Speed = 25 mm/sec)

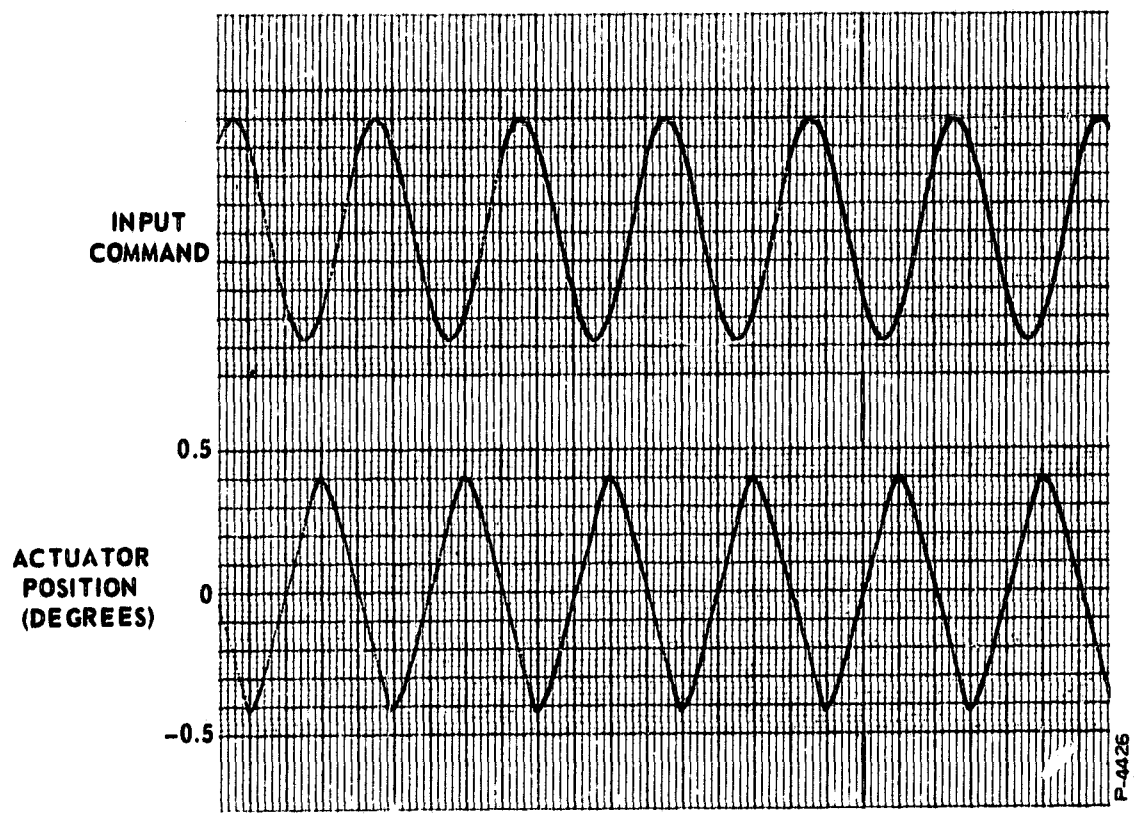

Figure 108 - Trace of Actuator Position for Input Frequency of 5. cps (Chart Speed = 100 mm/sec)

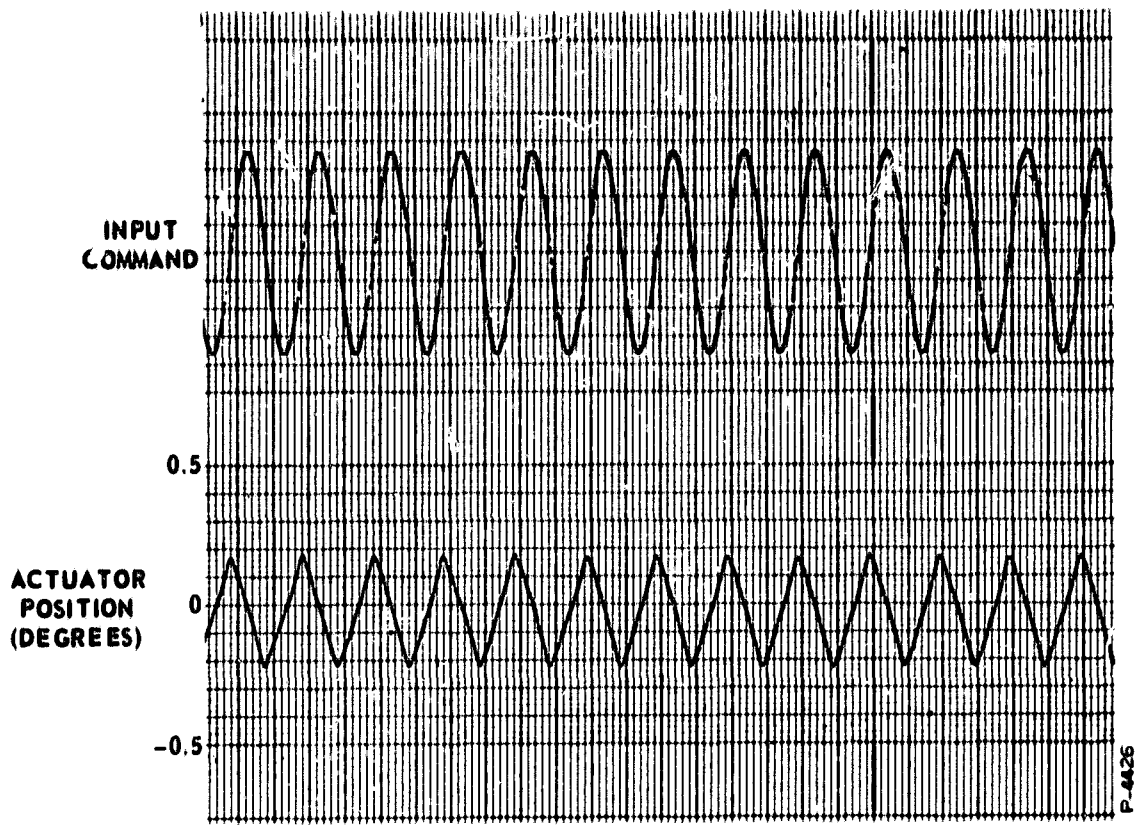

Figure 109 - Trace of Actuator Position for Input Frequency of 10 cps (Chart Speed = 100 mm/sec)

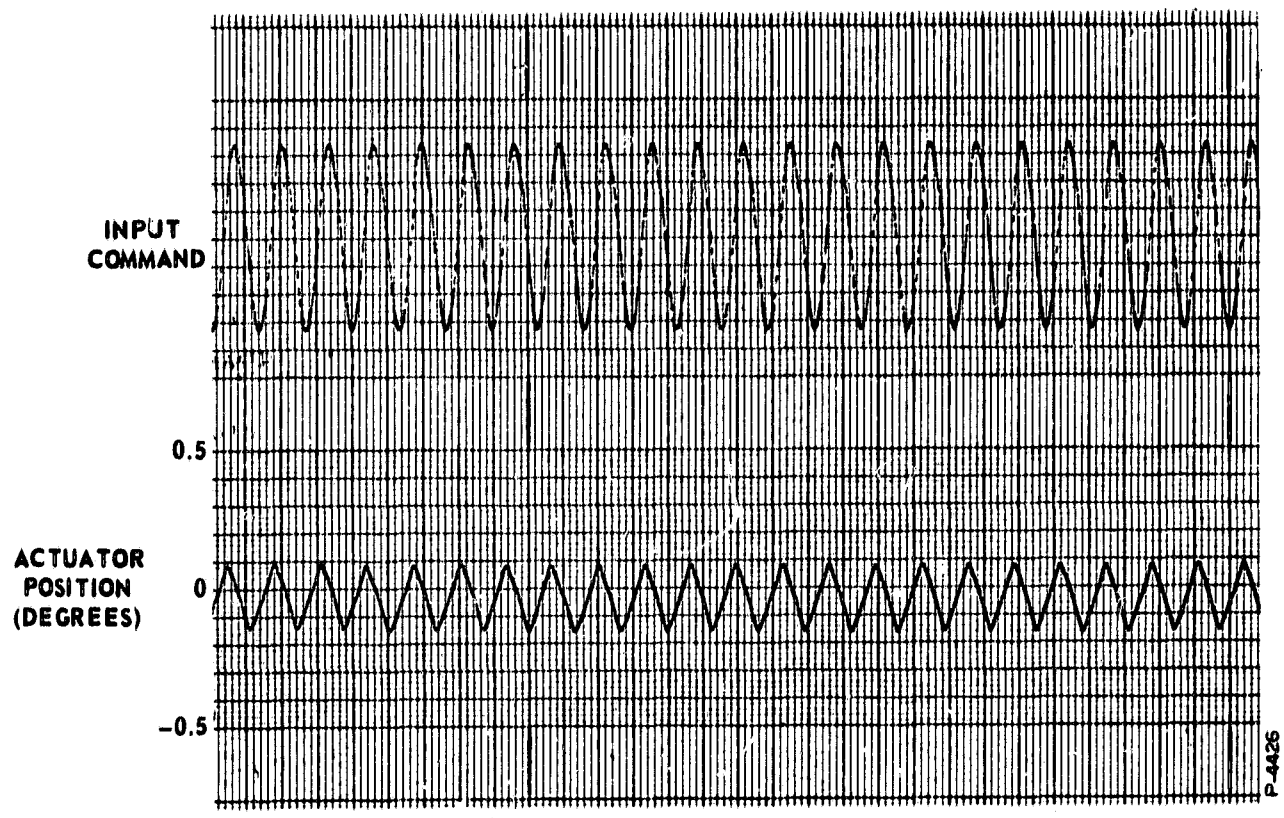

Figure 110 - Trace of Actuator Position for Input Frequency of 15 cps (Chart Speed = 100 mm/sec)

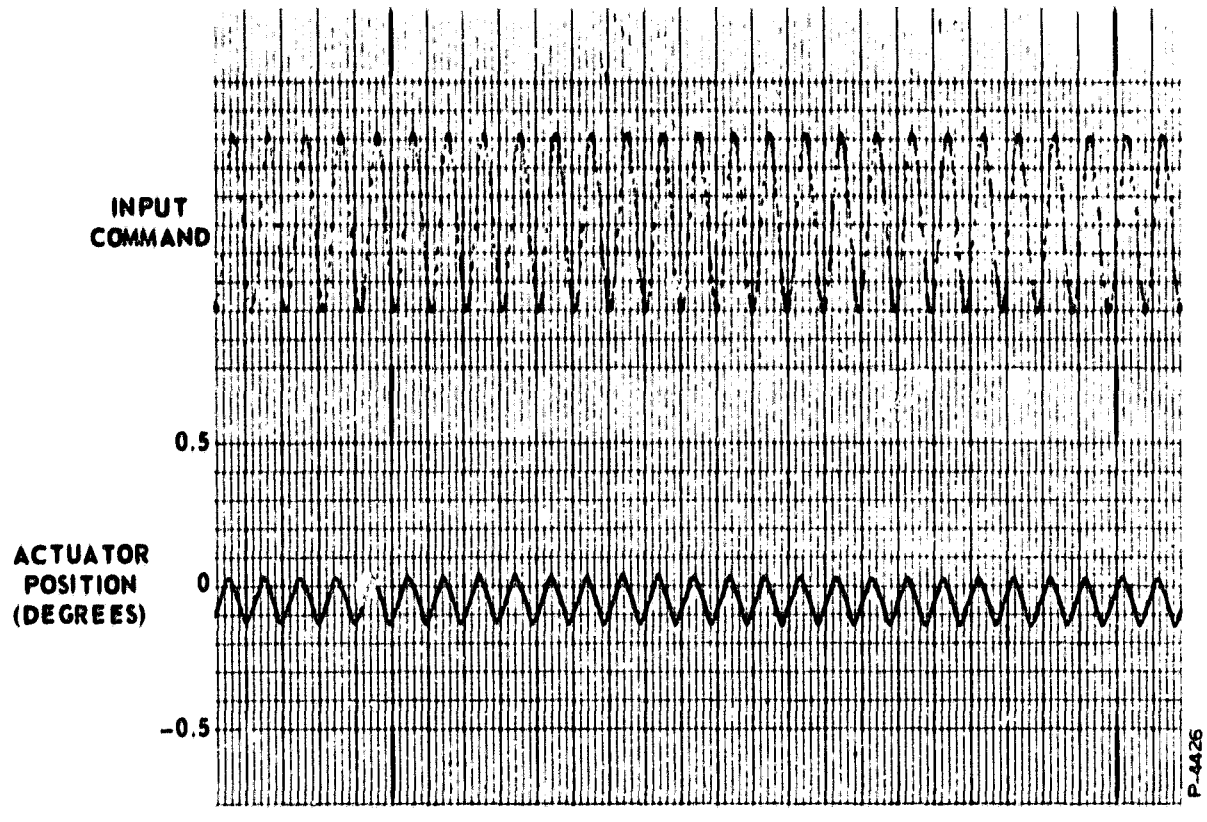

Figure 111 - Trace of Actuator Position for Input Frequency of 20 cps (Chart Speed = 100 mm/sec)

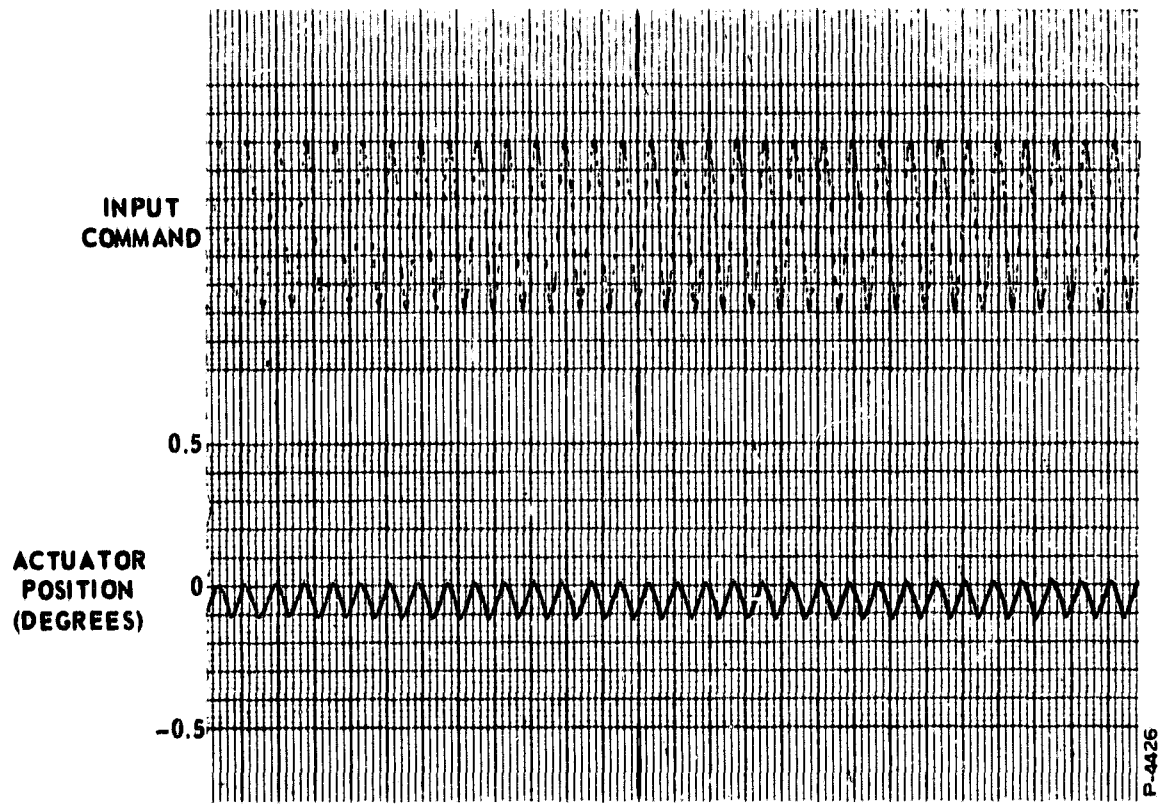

Figure 112 - Trace of Actuator Position for Input Frequency of 25 cps (Chart Speed = 100 mm/sec)

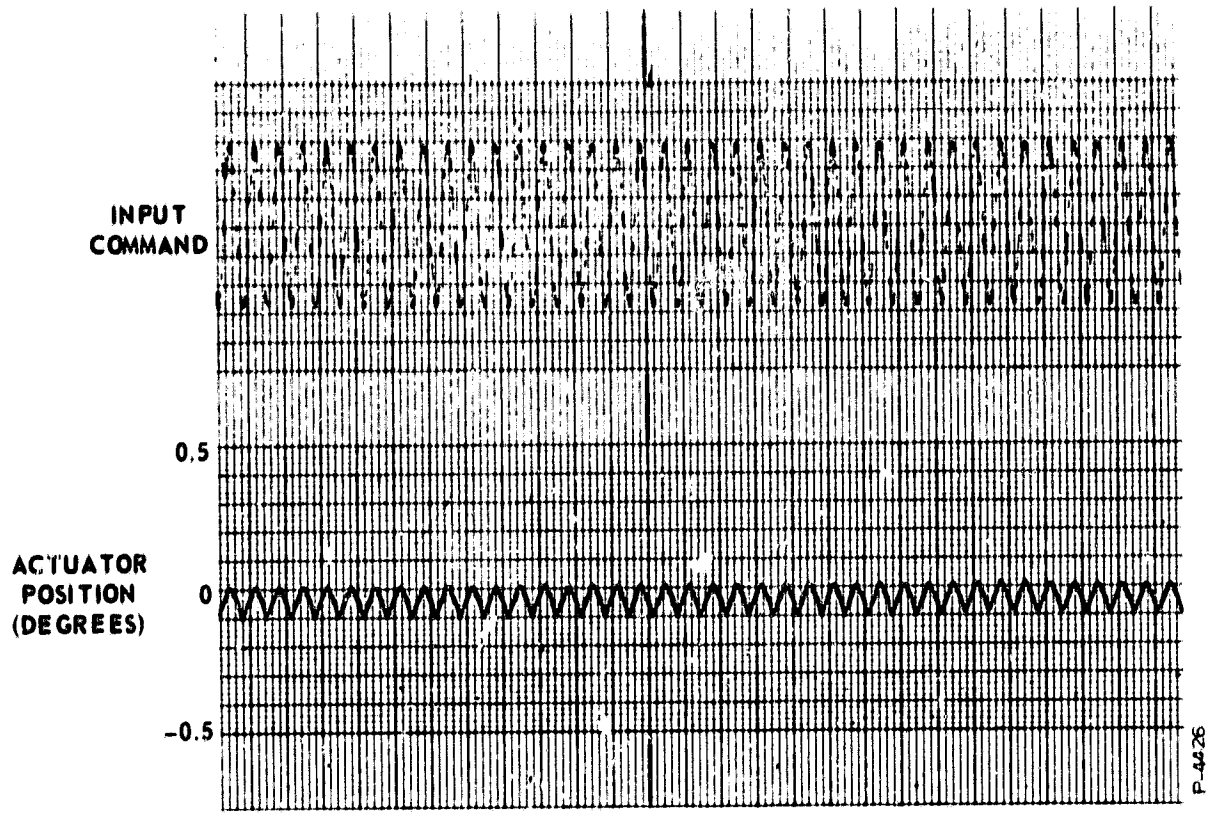

Figure 113 - Trace of Actuator Position for Input Frequency of 30 cps (Chart Speed = 100 mm/sec)

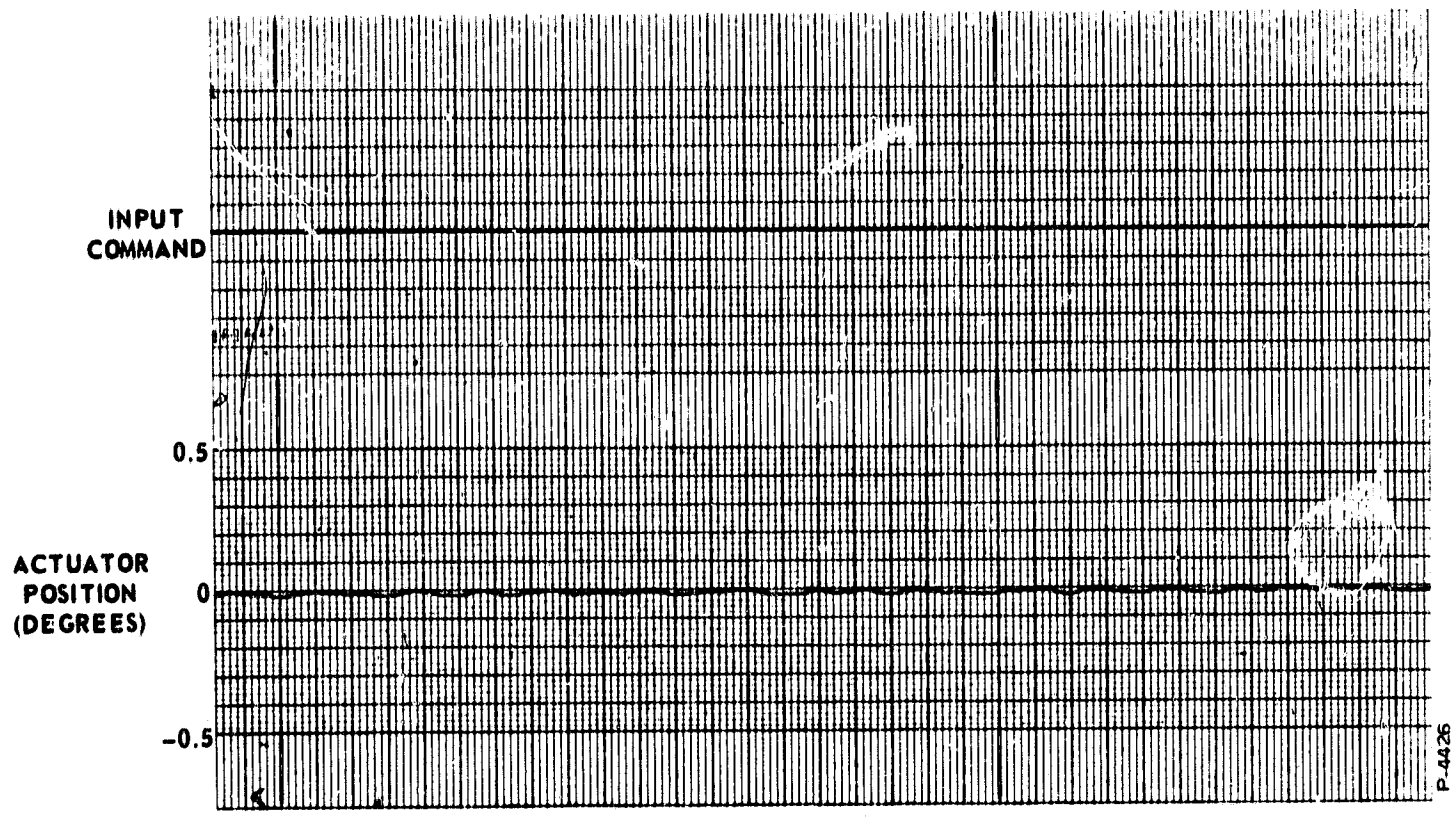

Figure 114 - Trace of Actuator Position for Zero Input Command

Figure 114 shows a trace of the actuator position with no input signal applied to the torque motor. This trace shows that there is some "hunting" of the actuator, but that it is apparently random and of small magnitude (0.020 degree).

This series of tests definitely showed the feasibility of employing two vortex valves in a push-pull configuration to drive this actuator. The vortex valve power stage performed with considerably less audible noise than experienced in the breadboard tests. Further "tuning" of the loop can be performed to optimize the actuator performance to the requirements.

Analysis

A complete analytical model of the reversed-flow flapper-nozzle system is required. The analytical results should be correlated with experimental observations and utilized to formulate new pilot stage design criteria. A preliminary analysis was performed during the course of the present program in order to obtain a "first look" at conditions for stability. Appendix E presents this analysis, along with a mechanical analogy and block diagram of the system which can be used for a preliminary analog computer study.

CONCLUSIONS AND RECOMMENDATIONS

Conclusions

The hydraulic vortex servovalve program has demonstrated the feasibility of utilizing two vortex valves in a push-pull configuration to drive a positive displacement actuator. At the same time, significant technological advances in high pressure (2000-3000 psi) hydraulic fluidic concepts have been made, and techniques have been devised to optimize component and system performance. Single and double outlet vortex valve characteristics have been experimentally determined. Tradeoff studies were made of various circuit concepts to insure that the servovalve performance adequately surrounded the flight data envelope.

Two servovalve assemblies have been fabricated and tested. The selected design incorporated single outlet vortex valves with flow receivers in the power stage, and with control flow and pressure provided by a reversed-flow flapper-nozzle pilot stage. The pilot stage was driven by an electromagnetic torque motor.

Power stage vortex valve tests were performed for optimization and flow-trimming purposes. Tests of the power stage assembly on the Saturn-IB actuator provided additional data to substantiate the design.

The reversed-flow flapper-nozzle pilot stage was utilized in order to meet the high pilot stage flow and low torque-motor power requirements of the servoactuator system. This necessitated an inherently high power gain pilot stage. The pilot stage negative hydraulic spring rate had to be carefully balanced with positive mechanical spring rates in the torque motor-flapper system. In a preliminary analysis of the pilot stage system dynamics, it was determined that system damping, flapper rigidity, and nozzle oil column resonance influence system stability.

Recommendations

Based on the results of the recent developmental program, the following recommendations are made:

(1) A complete mathematical model of the servovalve should be formulated in order to obtain a thorough understanding of the system dynamics and to evaluate the effects of changes in the system parameters. An analog computer should be utilized for this analysis. Correlation of the analytical results with test observations could then be made and the requirements for stable operation of the pilot stage defined.

(2) The hydraulic vortex servovalve concept should be evaluated for application to a servoactuator system such as the

Saturn-IC gimbaling system in which fuel (RP-1) is used as the hydraulic fluid. The corrosion and contamination problems of this system would be alleviated with a no-moving-part device. Design simplicity, reduced cost, and increased reliability would be distinct advantages of the fluidic servovalve.

A higher input electrical power to the servoactuator should aid in developing a stable pilot stage configuration. The problem of rejecting the heat generated in a high flow system is eliminated since the flow from the actuator is returned to the large volume fuel system rather than to a closed-loop hydraulic system reservoir.

Once the feasibility of the servovalve concept is firmly established, it is recommended that a complete servoactuator package be developed. This would consist of an integrated servovalve, actuator and potentially a fluidic position feedback. Only in this way can individual component matching be made to achieve desired overall system performance.

APPENDIX A

DESIGN CURVES

The following performance curves of various hydraulic devices were compiled to permit analysis of the various hydraulic circuit concepts discussed in the program.

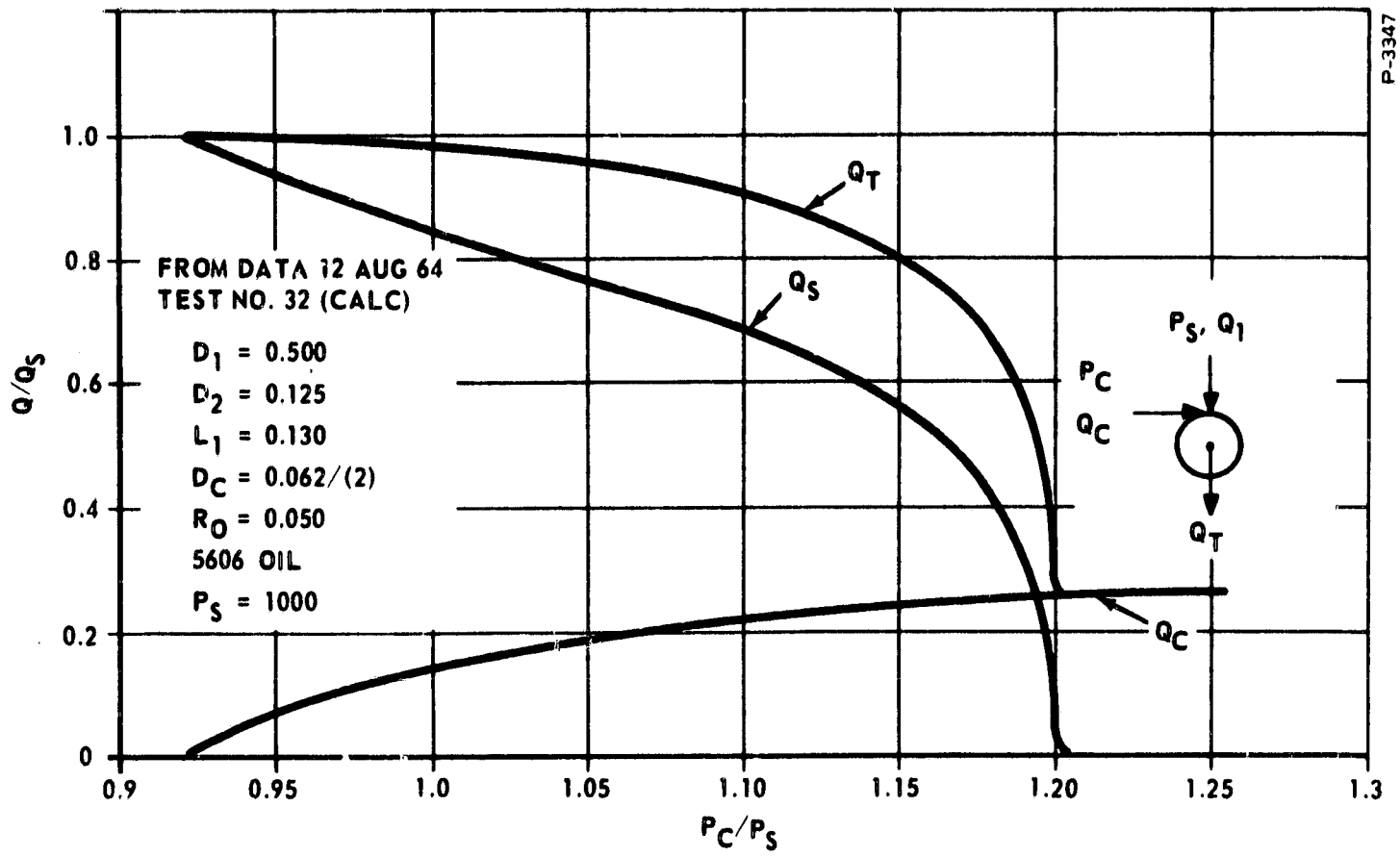

Figure 115 - Flow Turndown Data for a Hydraulic Vortex Valve

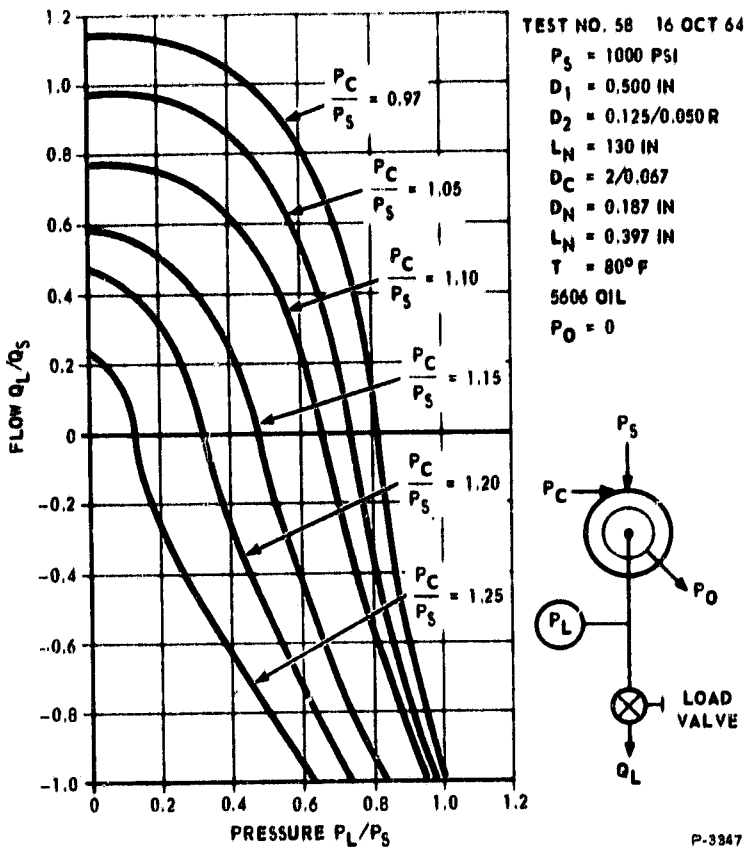

Figure 116 - Two Quadrant Load-Flow Data for a Vortex Valve

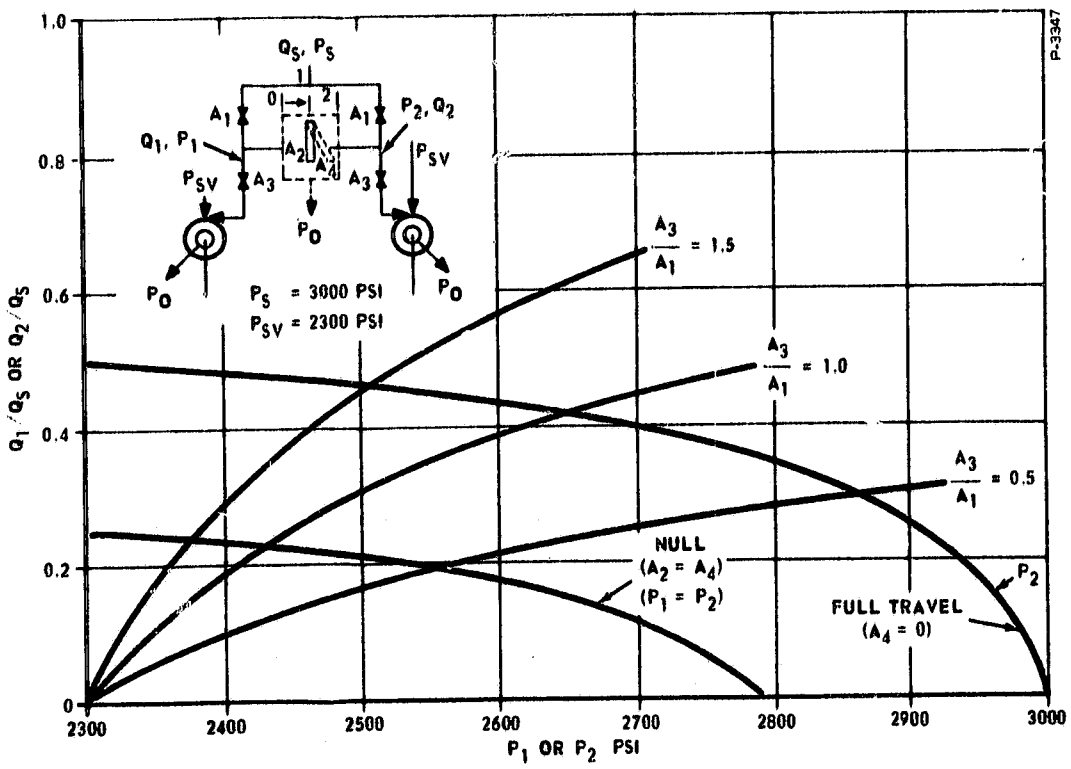

Figure 117 - Flapper Valve Characteristics

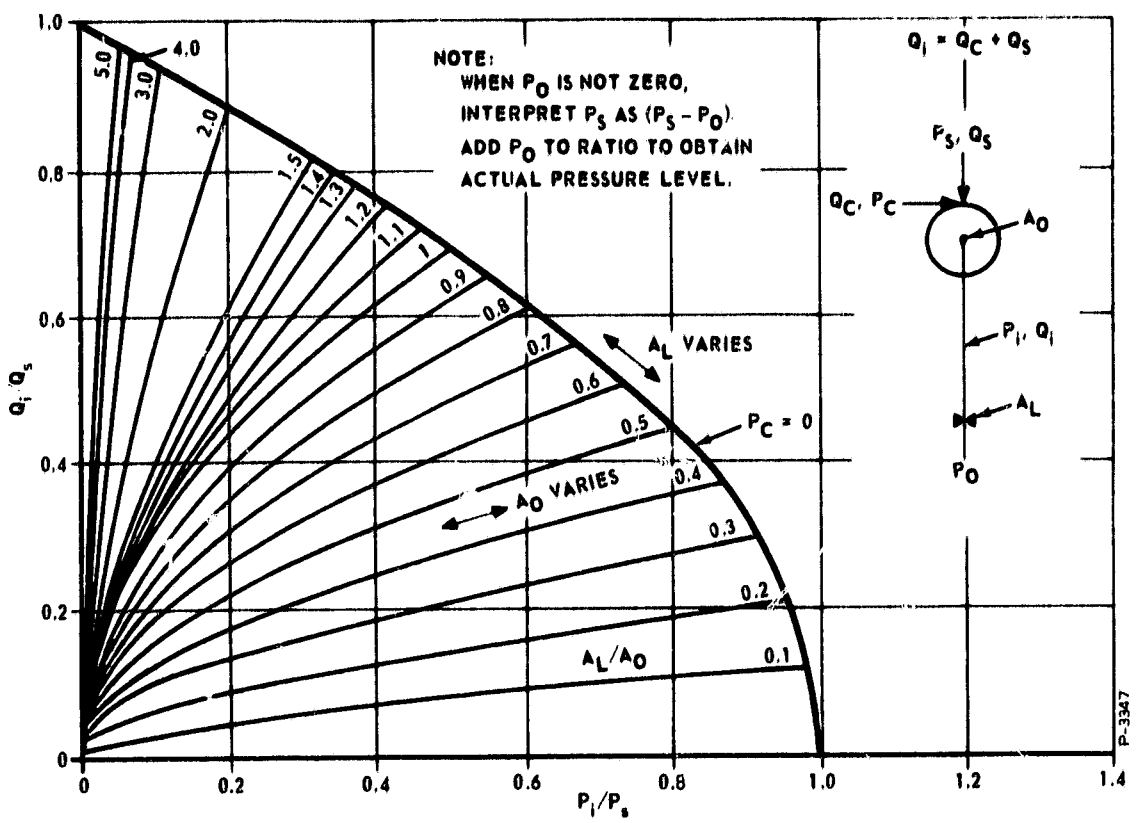

Figure 118 - Intermediate Pressure Between a Vortex Valve and a Load Orifice at Various A_L/A_O Ratios

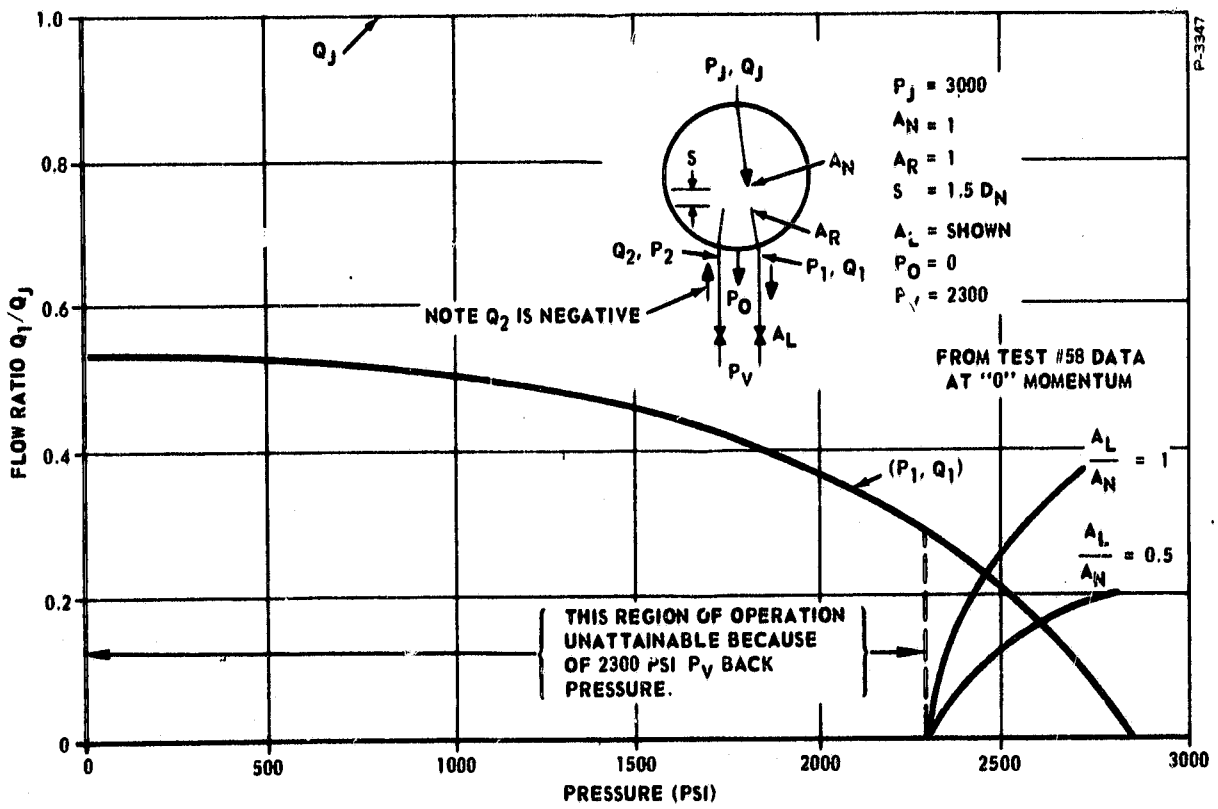

Figure 119 - Load-Flow Characteristics of a Jet Pipe Valve Driving Individual Loads

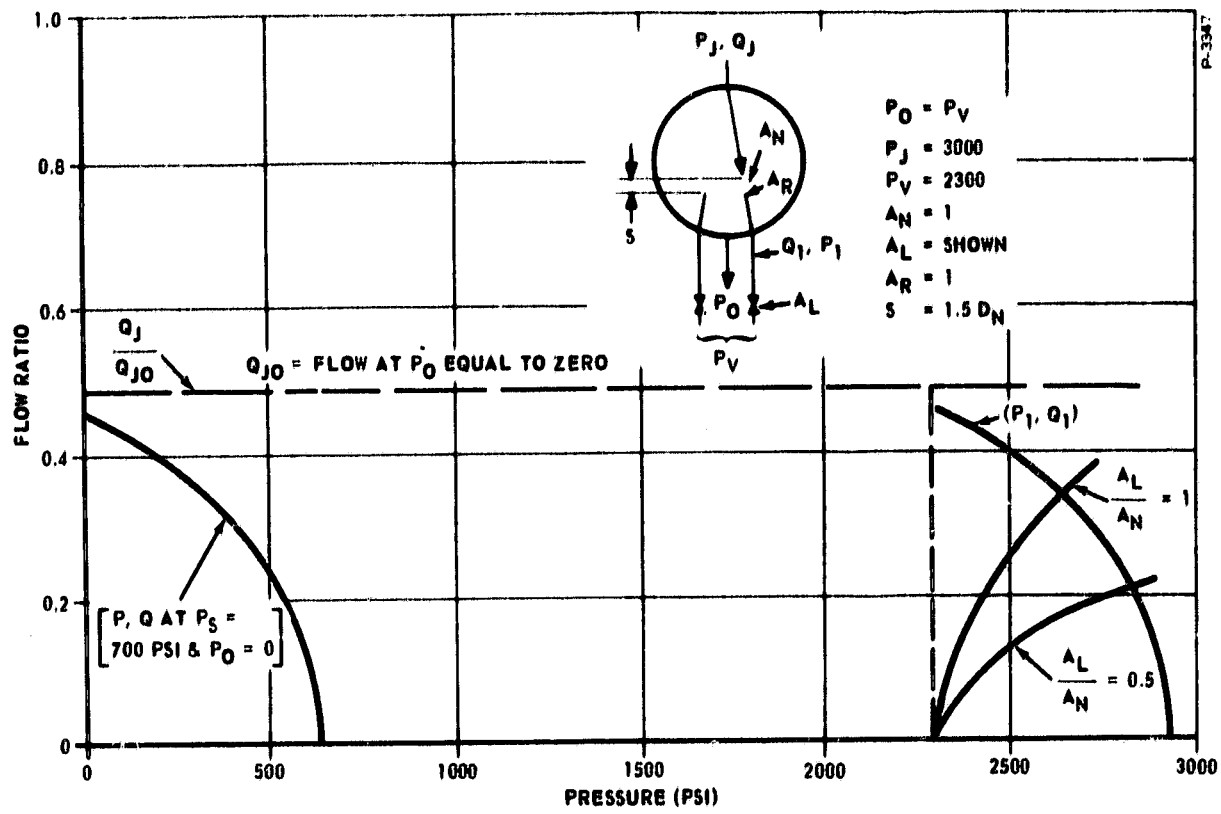

Figure 120 - Load-Flow Characteristics of a Jet Pipe With a Receiver Cavity at High Pressure

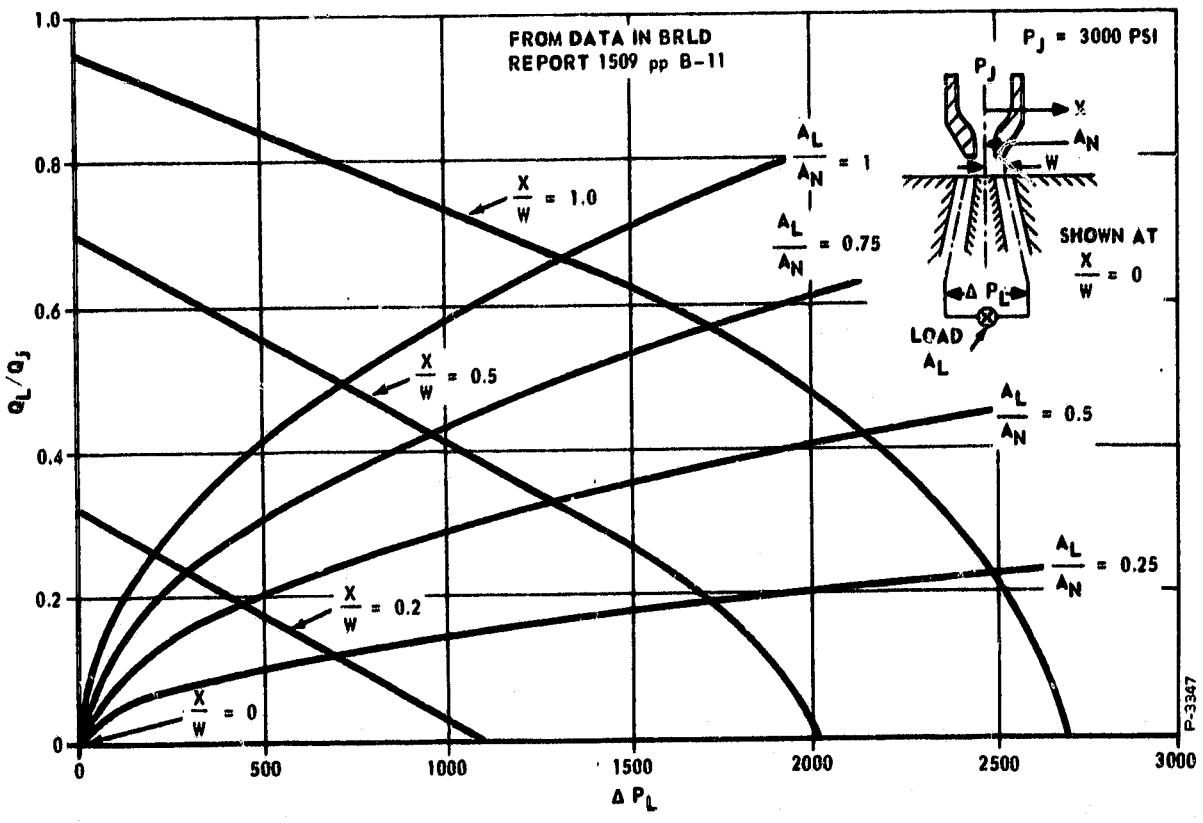

Figure 121 - Load-Flow Characteristics of a Jet Pipe Device Driving a Communicated Load

APPENDIX B

THRUST VECTORING SYSTEM PERFORMANCE USING THE FLUIDIC SERVOVALVE WITHOUT LOAD PRESSURE FEEDBACK

References

(1) Specification for a Hybrid, Fluid Interaction, Servovalve, Marshall Space Flight Center, Drawing No. 50M35032, 30 September 1964.

(2) Specification for a Thrust Vector Control Actuator, Marshall Space Flight Center, Drawing No. 10M01683, 17 June 1963.

Introduction

The dynamic load-pressure feedback specified in Reference (1) is based on the lightly damped open-loop characteristics of a spool-type (flow control) servovalve, piston actuator, and the spring mass dynamics of the engine, drive members, and mounting structure. The purpose of this analysis is to study the system damping problem when the fluidic servovalve is used without load pressure feedback. A very much simplified model of the system is used, but it is sufficient to show the most significant effects of the fluidic servovalve.

Summary

The fluidic servovalve and piston actuator are best represented as a force source with internal velocity feedback.

The open-loop response of the fluidic servovalve, piston actuator, and load is not lightly damped as in the case of the spool-type valve. With all other parameters fixed, the damping increases as the output pressure of the power stage vortex valves become less dependent on output flow, i.e., as they approach ideal pressure amplifiers.

The system damping can be controlled by selection of the valve blocked port pressure gain, but system stiffness must be traded for damping. When the pressure gain is set at $\Delta P_L/\Delta i = 288$ psi/ma for a system damping ratio $\zeta = 0.5$, the system frequency response specification is satisfied, but the stiffness is only 11,500 lb/deg of engine position error compared with 400,000 lb/deg which is obtained if the valve pressure gain is 10,000 psi/ma as required by Reference (2). If 11,500 lb/deg is an adequate stiffness, no-load pressure feedback is required.

If the fluidic servovalve pressure gain is increased to obtain high static stiffness, the overall system response becomes similar to the

response using a spool valve without load pressure feedback. If the pressure gain for the required stiffness is greater than the gain for minimum allowable damping, additional compensation will be required.

Analysis

Nomenclature.

A - actuator piston area, in^2

D - engine damping coefficient, lb/(in/sec)

E - engine position error, deg

F_A - actuator force, lb

G(s) - frequency dependent part of transfer functions

H - engine angular displacement per inch of actuator travel, deg/in

i - torque motor current, ma

K - spring constant, lb/in

K_F - flapper gain, psi/in

K_P - vortex valve no-flow pressure gain, psi/psi

K_Q - vortex valve parameter - $\left.\frac{\partial P_L}{\partial Q}\right|_{Q = 0}$, psi/($in^3$/sec)

K_{TM} - torque motor gain, in/ma

K_{VA} - valve-actuator-load gain, (in/sec)/in

M_A - actuator mass, lb-sec^2/in

M_L - load mass, lb-sec^2/in

Q - flow, in^3/sec

X_A - actuator position, in.

X_L - effective displacement of the engine, in.

y - torque-motor flapper displacement, in.

β_c engine position command, deg

β_e engine position

$\Delta(\ )$ discrete change in ( )

System Dynamics Using a Spool Valve.

Neglecting the servovalve and amplifier dynamics and removing the load pressure feedback in Figure III of Reference (1) produces the simplified system in part (a) of Figure 122; part (b) shows that the closed-loop poles on the loci between the poles and zeros of $G_\chi(s)$ are approximately cancelled by the closed-loop zeros for all values of loop gain; part (c) shows the poles of the overall system transfer function $\beta_e(s)/\beta_c(s)$ which include the lightly damped poles of $G_c(s)$. The important point here is that, when the spool valve is used, the system damping can not be increased by dropping loop gain because the valve, piston actuator, and load are hydraulically stiff and lightly damped for any loop gain.

The dynamic load pressure feedback method provides the necessary system damping without loss of the high static stiffness capability of the spool value.

Valve-Actuator-Load Model.

The simplified model (Figure 123) assumes the following:

(1) The actuator is stationary

(2) The equation of motion for the load mass is given by the transfer function $G_c(s)$ in Figure III of Reference (1)

(3) The actuator mass M_A is negligible compared with the load mass M_L

(4) Control pressure increments ΔP_{c1}, ΔP_{c2} are proportional to the flapper displacement y

(5) Load pressure increments ΔP_{L1}, ΔP_{L2} are linear combinations of the control pressure increments and the load flow $A\dot{X}_A$

(6) Fluid compressibility is negligible.

Then the control pressure increments are

$$\Delta P_{c1} = K_F y$$

$$\Delta P_{c2} = K_F y \qquad (1)$$

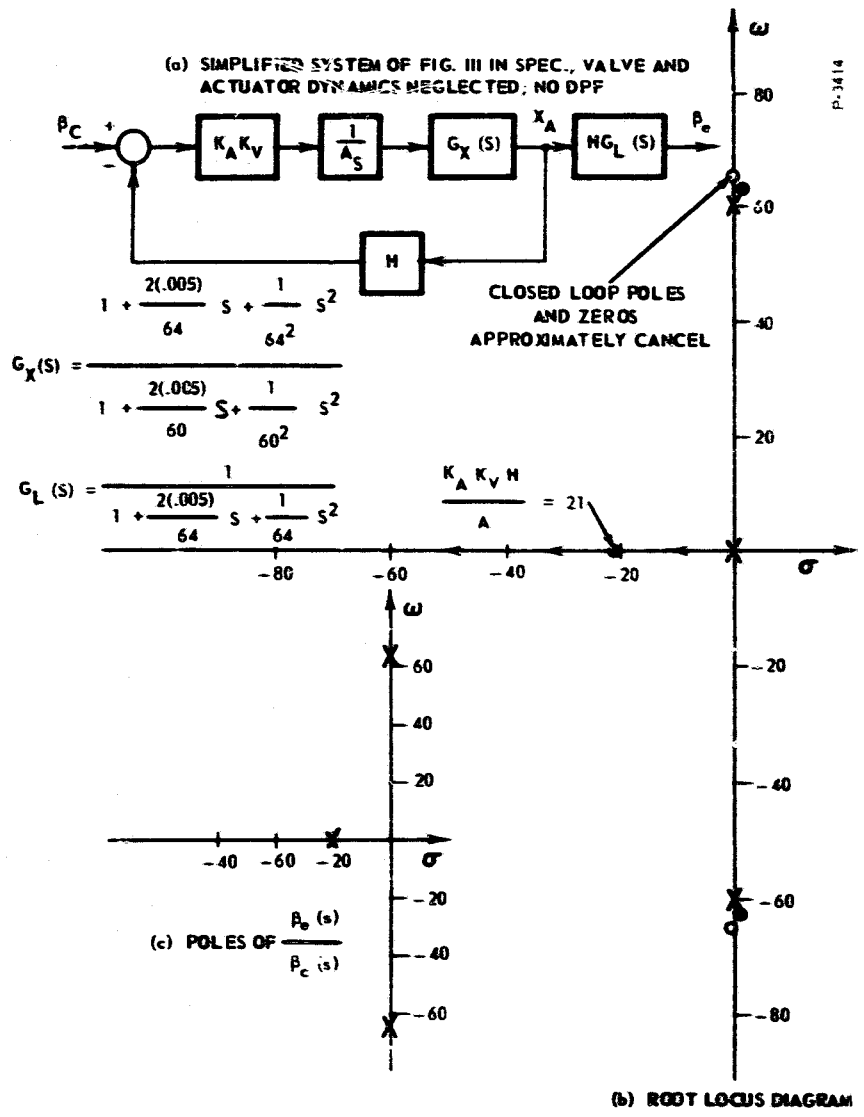

Figure 122 - System Dynamics With Spool Valve (Flow Control) and No DPF

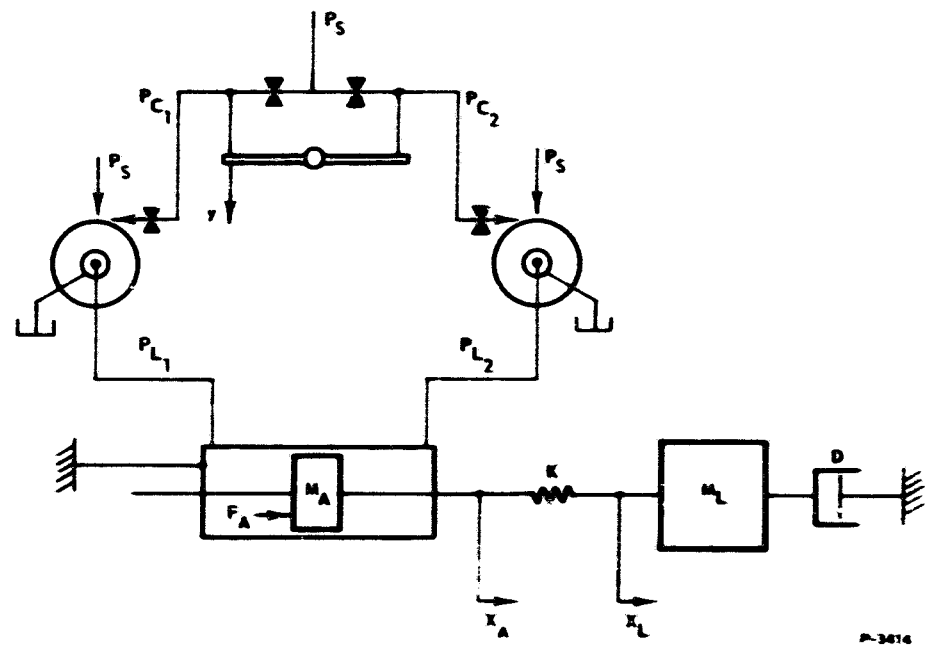

Figure 123 - Valve-Actuator-Load Model

The load pressure increments are

$$\Delta P_{L_1} = -K_P \Delta P_{c_1} - K_Q A\dot{X}_A$$
$$\Delta P_{L_2} = -K_P \Delta P_{c_2} + K_Q A\dot{X}_A \qquad (2)$$

The actuator force is

$$F_A = \Delta P_L A = (\Delta P_{L_1} - \Delta P_{L_2})A \qquad (3)$$

or using equations (1) and (2) in (3)

$$F_A = (2K_{\ } K_F y - 2K_Q A\dot{X}_A)A \qquad (4)$$

The equations of motion for the actuator and load masses are

$$M_A \ddot{X}_A = F_A - K(X_A - X_L)$$
$$M_L \ddot{X}_L = K(X_A - X_L) - D\dot{X}_L \qquad (5)$$

Taking Laplace transforms of equation (5) and solving for the transforms of $\dot{X}_A$ and X_L gives

$$\dot{X}_A(S) = \frac{1}{D} \frac{\frac{M_L}{K} S^2 + \frac{D}{K} S + 1}{\left[\frac{M_A M_L}{KD} S^3 + \frac{M_A}{K} S^2 + \frac{M_A + M_L}{D} S + 1\right]} F_A(S) \qquad (6)$$

$$X_L(S) = \frac{1}{\frac{M_L}{K} S^2 + \frac{D}{K} S + 1} X_A(S) \qquad (7)$$

Equivalent forms for equations (6) and (7) are

$$\dot{X}_A(S) = \frac{1}{D} \frac{(aS^2 + bS + 1)}{(cS^3 + dS^2 + eS + 1)} F_A(S) \triangleq \frac{1}{D} G_F(S) F_A(S) \qquad (6a)$$

$$X_L(S) = \frac{1}{(aS^2 + bS + 1)} X_A(S) \triangleq G_L(S) X_A(S) \qquad (7a)$$

From Figure III of Reference (1),

$$a = 2.41 \times 10^{-4} \text{ sec}^2$$

$$b = 1.55 \times 10^{-4} \text{ sec}$$

$$K = 66{,}300 \text{ lb/in}$$

This implies

$$M_L = 16.1 \frac{\text{lb sec}^2}{\text{in}} = \frac{6200}{386} \frac{\text{lb}}{\text{in/sec}^2}$$

$$D = 10.4 \frac{\text{lb}}{\text{in/sec}}$$

When the actuator mass is neglected,

$$(M_A \to 0),\ c = d = 0 \text{ and } e = 1.55 \text{ sec}$$

A block diagram of the valve, actuator, and load is given in Figure 124 and a root locus diagram for the internal velocity feedback loop is given in Figure 125. When

$$K_Q = 20 \frac{\text{lb/in}^2}{\text{in}^3/\text{sec}}$$

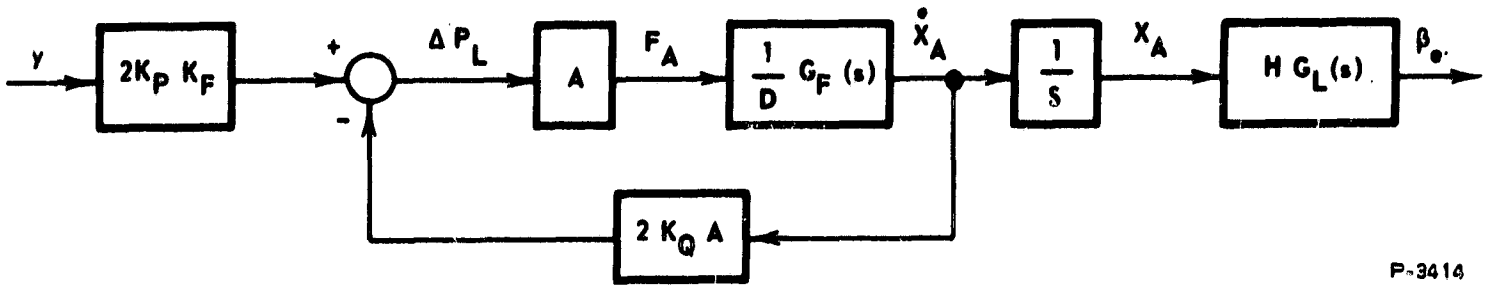

Figure 124 - Valve-Actuator-Load Block Diagram

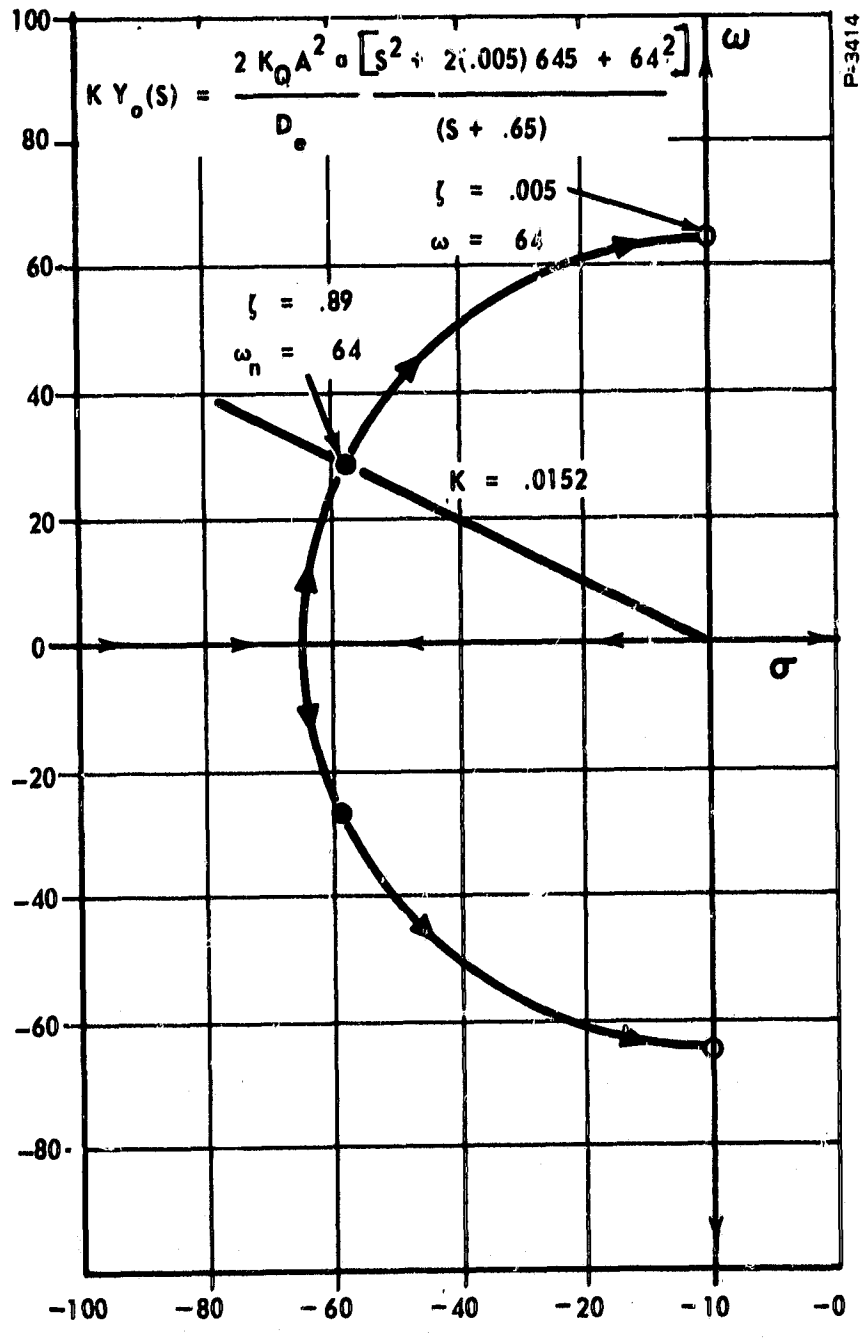

Figure 125 - Root Locus for the Valve Internal Feedback Loop in Figure 124

$$A = 5 \text{ in}^2$$

$$D = 10.4 \frac{\text{lb}}{\text{in/sec}}$$

$$a = 2.41 \times 10^{-4} \text{ sec}^2$$

$$e = 1.55 \text{ sec}$$

the valve, actuator, and load transfer function are

$$\frac{\dot{X}_A(S)}{y(S)} = \frac{2K_P K_F A}{D + 2K_Q A^2} \frac{(aS^2 + bS + 1)}{(fS^2 + g S + 1)} y(S) \triangleq K_{VA} G_{VA}(S)$$

$$\frac{\dot{X}_A(S)}{y(S)} = \frac{K_P K_F}{101} \frac{\left[\frac{1}{64^2} S^2 + \frac{2(0.005)}{64} S + 1\right]}{\left[\frac{1}{64^2} S^2 + \frac{2(0.89)}{64} S + 1\right]} \tag{8}$$

$$\frac{\beta_e(S)}{X_A(S)} = \frac{H}{(aS^2 + bS + 1)} \triangleq H G_L(S)$$

$$\frac{\beta_e(S)}{X_A(S)} = \frac{2.09}{\left[\frac{1}{64} S^2 + \frac{2(0.005)}{64} S + 1\right]} \tag{9}$$

Thrust Vectoring System Performance.

A block diagram for the system using the fluidic servovalve without load-pressure feedback is given in Figure 126, and a root locus diagram for the system is given in Figure 127 for the following component transfer functions:

$$K_A G_A = 8 \text{ ma/deg}$$

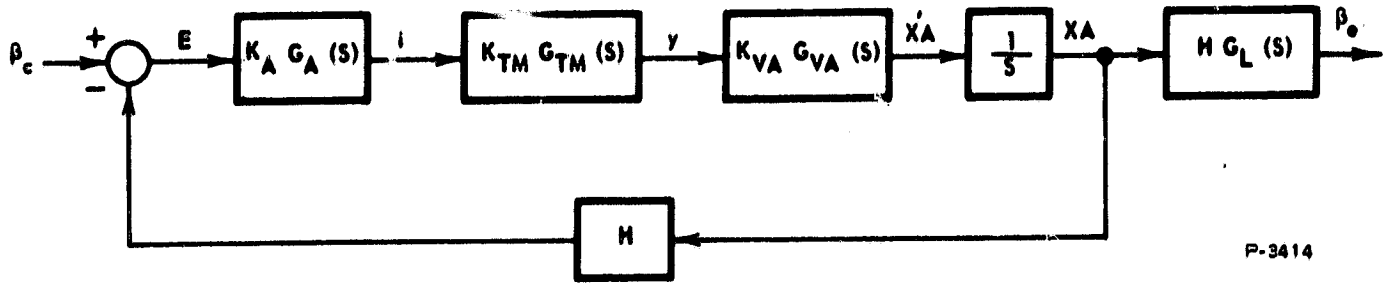

Figure 126 - Thrust Vectoring System Block Diagram

$$K\,y_o(s) = \frac{K_{TM}\,K_P\,K_F}{6} \left[\frac{1}{64^2}\,S^2 + \frac{2(.005)}{64}\,S + 1\right] \Big/ S\left[\frac{1}{64^2}S^2 + \frac{2(.89)}{64}\,S + 1\right]$$

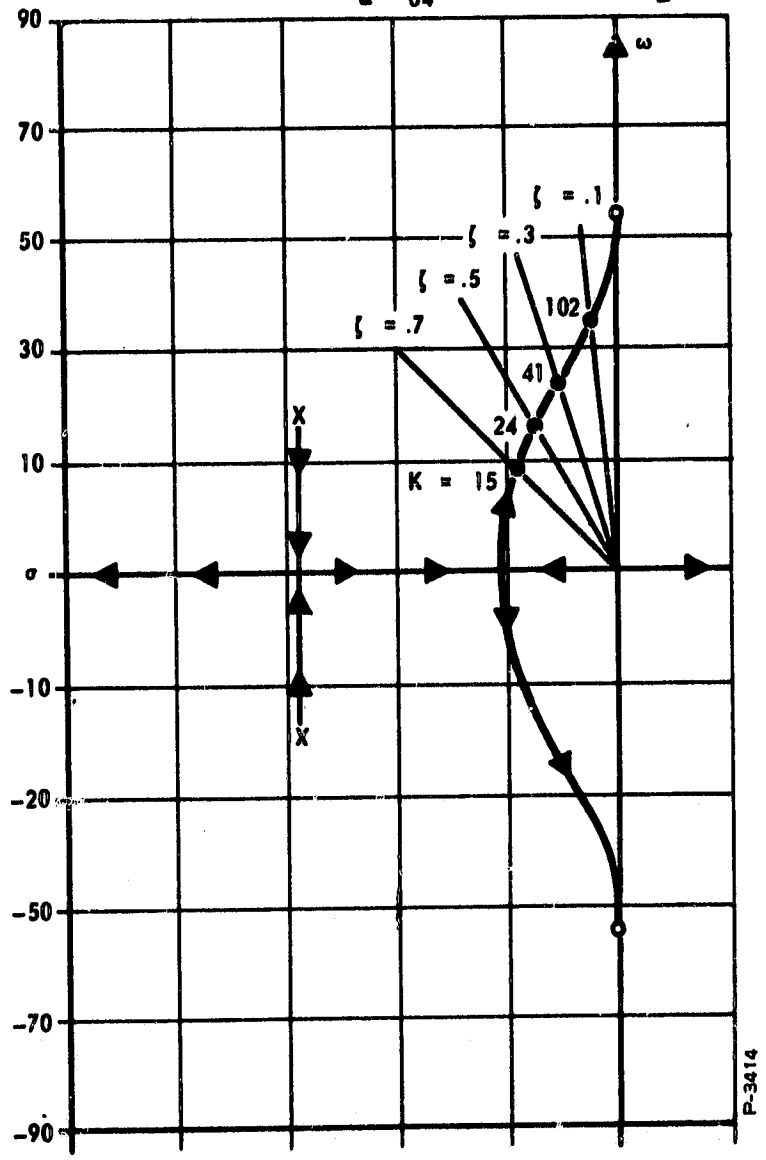

Figure 127 - Root Locus for the Actuator Position Feedback Loop; Fluidic Servovalve Without Load Pressure Feedback

$$K_{TM}\ G_{TM}\ (S) = K_{TM}\ in/ma$$

$$K_{VA}\ G_{VA}\ (S) = \frac{K_P\ K_F}{101}\ \frac{\left[\frac{1}{64^2}\ S^2 + \frac{2(0.005)}{64}\ S + 1\right]}{\left[\frac{1}{64^2}\ S^2 + \frac{2(0.89)}{64}\ S + 1\right]}\ \frac{in/sec}{in}$$

$$H\ G_L(S) = \frac{2.09}{\frac{1}{64^2}\ S^2 + \frac{2(0.005)}{64}\ S + 1}\ \frac{deg}{in}$$

$$H = 2.09\ \frac{deg}{in}$$

The dynamics of the amplifier and torque motor have been neglected.

The closed-loop transfer function $X_A(S)/\beta_c(S)$ has zeros that cancel the poles of $G_L(S)$ so the damping of system transfer functions $\beta_e(S)/\beta_c(S)$ is determined by the gain $K_{TM}\ K_P\ K_F$. When $K_{TM}\ K_P\ K_F = 144$, for a damping ratio $\zeta = 0.5$, the system frequency response requirements are satisfied as shown by Figures 128 and 129.

The system stiffness is

$$\left.\frac{\Delta F_A}{\Delta\ E}\right|_{\dot{X}_A = 0} = K_A\ K_{TM}\ (2K_P\ K_F)\ A\ \frac{lb}{deg}$$

Using $K_A = 8$ ma/deg (the present amplifier gain), $A = 5\ in^2$, and $K_{TM}\ K_P\ K_F = 144$ gives

$$\left.\frac{\Delta F_A}{\Delta\ E}\right|_{\dot{X}_A = 0} = 11{,}500\ \frac{lb}{deg}$$

The blocked port pressure gain of the fluidic servovalve is $2K_{TM}\ K_P\ K_F$ psi/ma. The servovalve pressure gain required in Reference (2) is 10,000 psi/ma; this produces a stiffness of 400,000 lb/deg which is 35 times

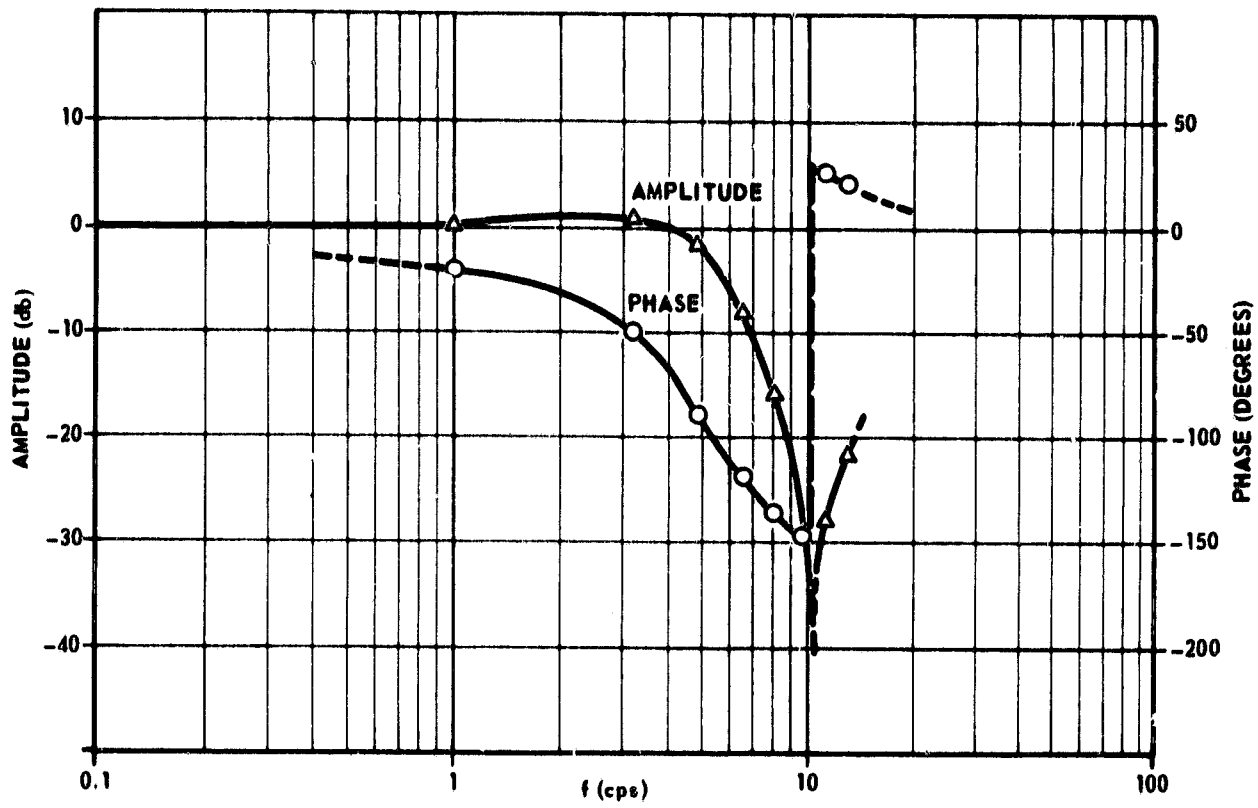

Figure 128 - Frequency Response X_a/β_c; $K_{TM}\ K_F\ K_P$ = 144

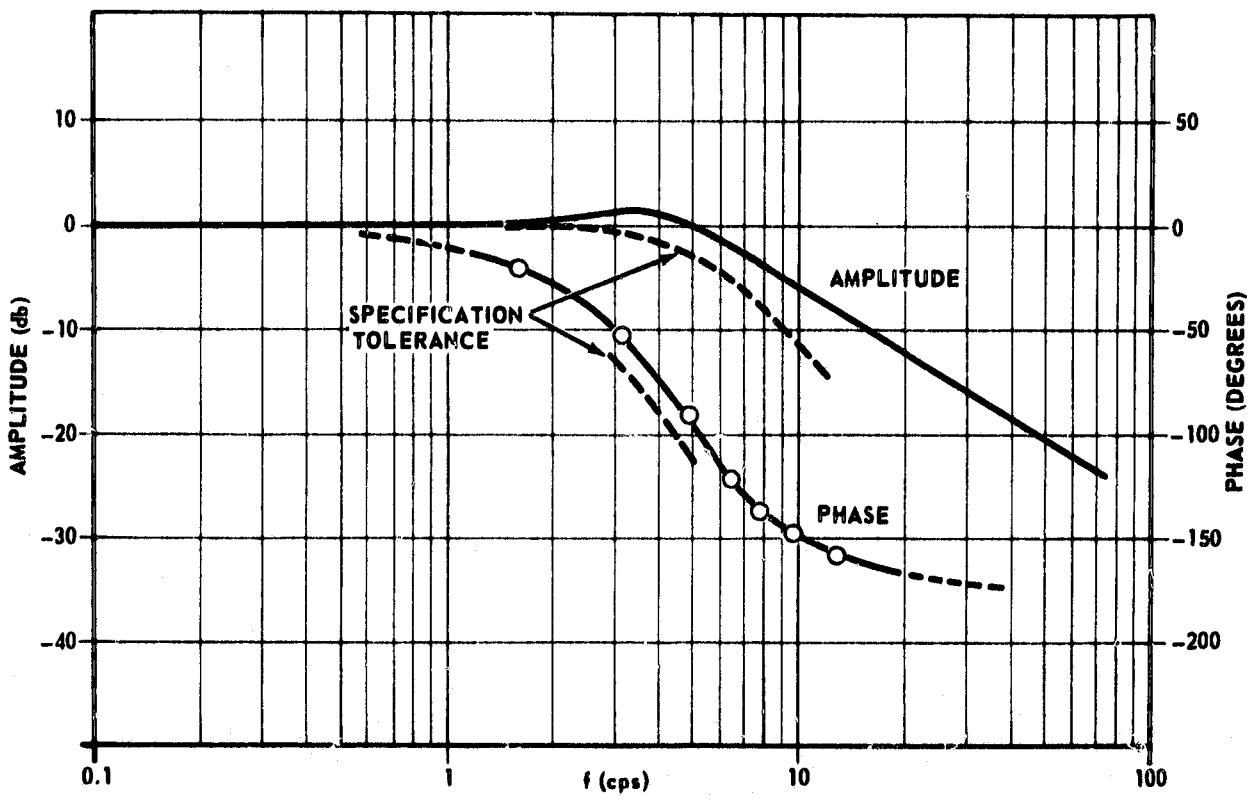

Figure 129 - Frequency Response β_e/β_c; $K_{TM}\ K_P\ K_F$ = 144

the stiffness of the system using a fluidic servovalve with pressure gain $2K_{TM}\ K_P\ K_F$ = 288 psi/ma.

It is clear that increasing the stiffness above 11,500 lb/deg by increasing the valve pressure gain will drive the system damping below ζ = 0.5. Some tradeoff between stiffness and damping can be made, but if the stiffness is doubled the damping will be less than ζ = 0.3.

Conclusions and Recommendations

The system damping problem is inherently different for the spool-type servovalve and proposed fluidic servovalve.

The servovalve would be simplified if no load pressure feedback were required. The minimum stiffness required for the thrust vectoring system should be established with MSFC. If it is less than 11,500 lb/deg, the natural damping characteristics of the fluidic servovalve are a significant performance advantage. The stiffness requirement is probably determined by resolution specifications and the engine gimbal bearing friction. MSFC will probably want as much stiffness as possible, but the elimination of load pressure feedback elements would be worth some sacrifice in stiffness.

APPENDIX C

TORQUE MOTOR SPECIFICATION

PROJECT NO.	THE BENDIX CORPORATION RESEARCH LABORATORIES DIVISION SOUTHFIELD, MICHIGAN	CODE IDENT.	SPECIFICATION NO.	REV.
2834-311		11272	DS-735	X-4

ENGINEERING SPECIFICATION

TITLE	DATE
Specification For An Electromagnetic Torque Motor	15 November 1965

This specification defines the requirements of a torque motor which will be used to drive the servovalve of a high performance hydraulic servo control system. The torque motor is to use construction techniques and materials suitable for use in a flyable primary control system.

1. Design

1.1 Type

The torque motor shall be a dry coil, permanent magnet polarized, two coil type with attached connector.

1.2 Weight

To be determined.

1.3 Installation

The torque motor shall conform to the space envelope, bolt pattern and output member as shown by Figure 1 in this specification.

1.4 Assembly

All threaded assemblies shall be positively locked to prevent loosening under vibration. Non-metallic adhesives shall not be used for assembly of the torque motor parts.

1.5 Connector

A connector shall be provided on the torque motor which will mate with Bendix Pygmy Connector PT06-8-4S.

1.6 Seals

The torque motor must be sealed to the servovalve body with standard MS "O" rings in appropriate grooves.

1.7 Amplifier

The amplifier is GFE and may be considered to be a constant current source.

PREPARED BY	CHECKED BY	APPROVED BY
T. A Phillips		A. Blatter

REVISIONS

PROJECT NO.	THE BENDIX CORPORATION RESEARCH LABORATORIES DIVISION SOUTHFIELD, MICHIGAN	CODE IDENT.	SPECIFICATION NO.	REV.
2834-311		11272	DS-735	X-4

ENGINEERING SPECIFICATION

TITLE	DATE
Specification For An Electromagnetic Torque Motor	15 November 1965

1.8 Coil Resistance

The resistance of each coil shall be 1000 ohms plus or minus 10%.

1.9 Polarity

The polarity of the unit shall be such that when the current in coil A-B is greater than the current in D-C the flapper motion is towards the connector end of the torque motor.

1.10 Coil Insulation

The insulation resistance between all pins connected together and case shall be greater than 50 megohms.

1.11 Coil Dielectric Strength

The coils shall withstand a voltage of 1000 vrms at 60 cps between coils and between coils and case.

1.12 Fluid

The unit shall be compatible with mil-o-5606 hydraulic fluid.

1.13 Internal Sealing

The output flapper of the unit shall contain a flexible seal capable of sealing system pressure of 3000 psi during normal operation.

1.14 Maximum Coil Current

The coil current shall not exceed 16.5 milliamps.

1.15 Quiescent Current

The quiescent current shall be 8.5 ±2 milliamps per coil.

PREPARED BY	CHECKED BY	APPROVED BY

REVISIONS

PROJECT NO.	THE BENDIX CORPORATION RESEARCH LABORATORIES DIVISION SOUTHFIELD, MICHIGAN	CODE IDENT.	SPECIFICATION NO.	REV.
2834-311		11272	DS-735	X-4

ENGINEERING SPECIFICATION

TITLE	DATE
Specification For An Electromagnetic Torque Motor	15 November 1965

2.0 Environmental Conditions

The torque motor mounted to the servovalve will be subjected to the following environmental conditions in any combination and the torque motor shall be designed to meet the requirements of this specification during such exposure.

2.1 Temperature

The torque motor must operate within the specified performance envelope of Figure 2 throughout the temperature range of 0°F to +150°F immediately following a 4 hour soak at the selected temperature.

2.2 Vibration

The torque motor must withstand the vibration schedule of Procedure II of Mil-E-5272 under a non-operating condition with the servovalve filled with oil. All vibration schedule time shall be 60 minutes at 70°F. The torque motor shall meet the performance after being subjected to the above vibration schedule.

In addition, the torque motor will be subjected to a vibration schedule as follows during which a frequency response test of the servovalve will be conducted.

5 cps at 0.5 inch D.A.
10 cps at 0.5 inch D.A.
110 cps at 0.020 inch D.A.
500 cps at 0.012 inch D.A.

2.3 Shock

The torque motor shall operate within the specification performance after being subjected to a 40g shock of 11 millisecond duration in any direction.

PREPARED BY	CHECKED BY	APPROVED BY

REVISIONS

PROJECT NO.	THE BENDIX CORPORATION RESEARCH LABORATORIES DIVISION SOUTHFIELD, MICHIGAN	CODE IDENT.	SPECIFICATION NO.	REV.
2834-311		11272	DS-735	X-4

ENGINEERING SPECIFICATION

TITLE	DATE
Specification For An Electromagnetic Torque Motor	15 November 1965

2.4 Altitude

The torque motor must operate from sea level to 300,000 ft. altitude within the performance specification. All electrical leads, connection, and coil construction shall be designed such that altitude induced electrical leakage will not effect the torque motor performance.

PREPARED BY	CHECKED BY	APPROVED BY

REVISIONS

PROJECT NO.	THE BENDIX CORPORATION RESEARCH LABORATORIES DIVISION SOUTHFIELD, MICHIGAN	CODE IDENT.	SPECIFICATION NO.	REV.
2834-311		11272	DS-735	X-4

ENGINEERING SPECIFICATION

TITLE	DATE
Specification For An Electromagnetic Torque Motor	15 November 1965

3. Performance

Characteristic	Unit	Valve
Stroke	in	±.00975
Mid-position	lb	2.0
End of Stroke	lb	1.0
Hysteresis	%	<2
Resonant Frequency	cps	>100
Differential Current, Δ i (Range)	amp	±.012

Note: Torque motor output force requirements are shown in Figure 2.

PREPARED BY	CHECKED BY	APPROVED BY

REVISIONS

PROJECT NO.	THE BENDIX CORPORATION RESEARCH LABORATORIES DIVISION SOUTHFIELD, MICHIGAN	CODE IDENT.	SPECIFICATION NO.	REV.
2834-311		11272	DS-735	X-4

ENGINEERING SPECIFICATION

TITLE	DATE
SPEC. FOR ELECTROMAGNETIC TORQUE MOTOR	1-28-66

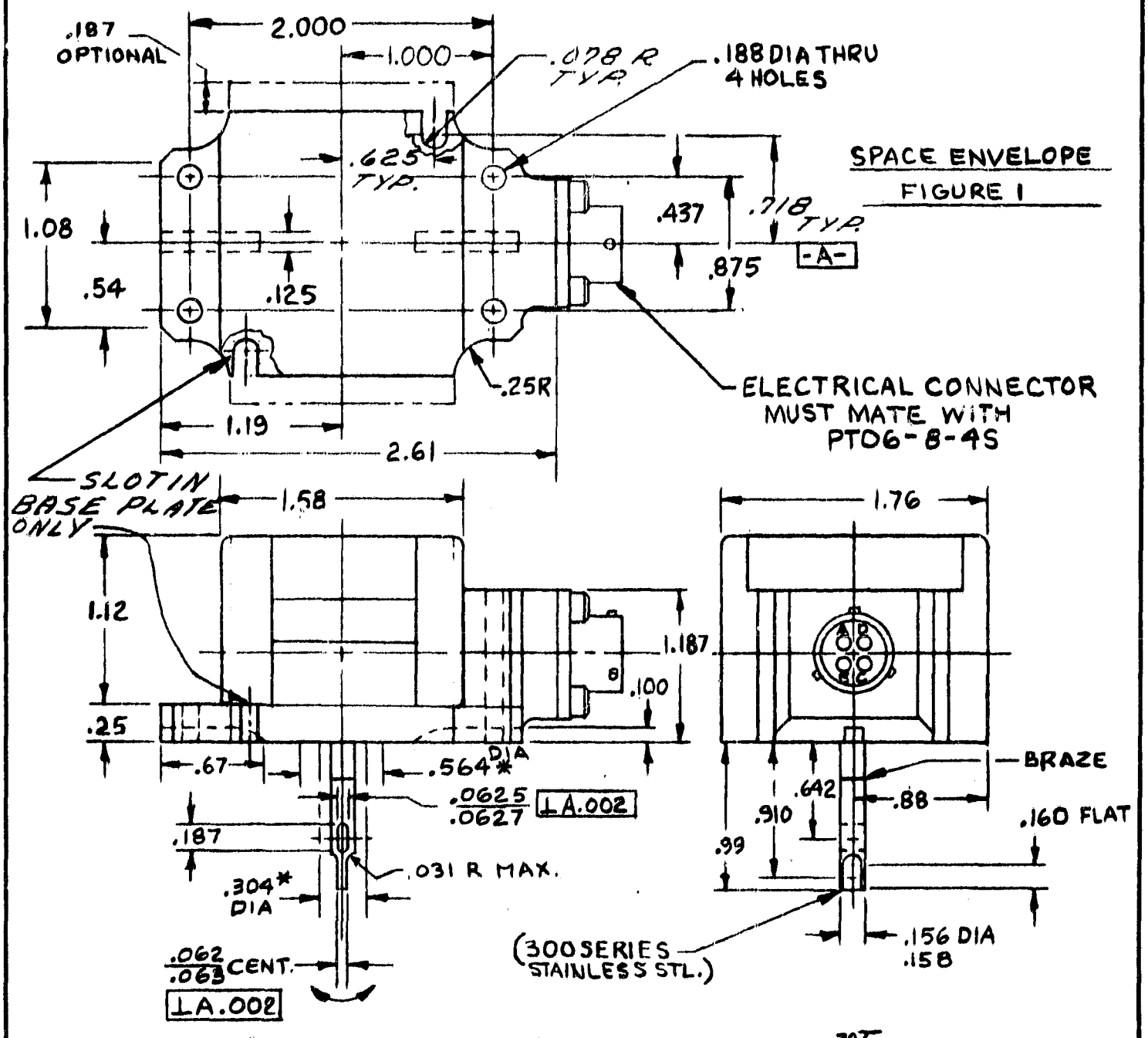

* "O" RING SEAL SURFACE $\frac{32}{}$ GROOVE TO BE PROVIDED IN MATING PART

PREPARED BY	CHECKED BY	APPROVED BY
R. P. Jacobs		T. A. Phillips

REVISIONS

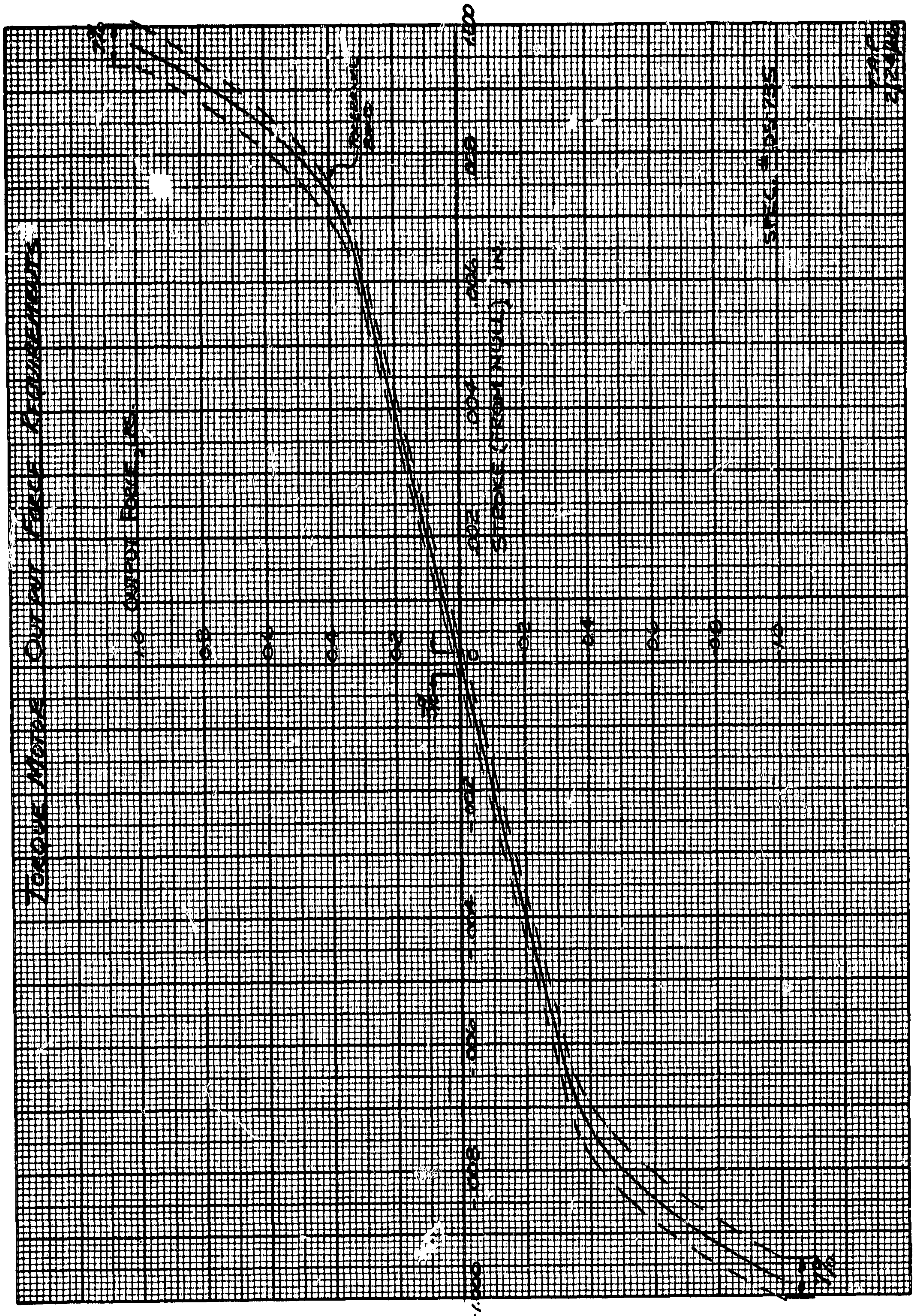

FIGURE 2

PAGE 7 OF 7

APPENDIX D

EFFECT OF TANGENTIAL HOLE ORIFICE COEFFICIENT ON VALVE PERFORMANCE

The hydraulic vortex valve performance is affected by the discharge coefficient of the tangential holes. The orifice coefficient should be maximized or made to approach a value of unity as close as possible. Since the control flow vena contracta has the highest momentum of any position in the tangential hole channel, this is the point at which momentum exchange with the supply fluid should occur. Because the tangential hole channels have had a high length-to-diameter ratio (approximately 5 to 1), the flow has normally expanded to fill the channel before leaving the channel. Therefore, the stream velocity was reduced from the vena contracta velocity by a factor equal to the apparent orifice coefficient of the tangential holes. The injected momentum is also reduced by a like amount as can be seen from the following equation:

$$M_{c_i} = C_d(M_{vc})$$

where

M_{c_i} = momentum injected

C_d = orifice coefficient

M_{vc} = vena contracta momentum

The variation in the performance of a given hydraulic vortex valve which may be expected from a change in the tangential hole orifice coefficient is summarized below:

(1) Turndown will be increased by the ratio of the new over the original orifice coefficient if the control pressure at turndown is held constant. This requires that the total control port area be decreased. The subscript "o" denotes original conditions.

$$\frac{Q_s}{Q_c} = \left(\frac{C_D}{C_{Do}}\right)\left(\frac{Q_{s_o}}{Q_{c_o}}\right)$$

and

$$A_c = \left(\frac{C_{D_o}}{C_D}\right) A_{c_o}$$

(2) The control Pressure ratio will be decreased at full turndown by the square of the ratio of the original to the new orifice coefficient, as shown below, if the turndown ratio is held constant. This is the condition for an existing vortex valve whose tangential hole entrances are modified to change the orifice coefficient, while the diameter of the holes is unchanged.

$$\frac{P_c}{P_s} = \left[\frac{Q_{s_o}}{Q_{c_o}} X \frac{C_{D_o}}{C_D} X \frac{M_{c_o}}{M_{s_o}}\right]^2 + 1$$

Experiments to data with typical vortex valve tangential holes with canted, sharp-edged entrances indicate orifice coefficients averaging around 0.67. It is expected that the coefficient can be raised to 0.90 by reshaping the entrance to the tangential holes. A typical set of hydraulic vortex valve performance characteristics are a turndown ratio of 5 to 1, a P_c/P_s ratio of 1.2, and a momentum ratio of 0.089.

As shown previously, the apparent momentum ratio may be decreased by the ratio of the original to the new orifice coefficient or,

$$\frac{M_c}{M_s} = \frac{0.67}{0.90} (0.089)$$

$$= 0.0662$$

If the P_c/P_s ratio was kept at 1.2, the new turndown ratio would be,

$$\frac{Q_s}{Q_c} = \left(\frac{0.90}{0.67}\right) 5$$

$$= 6.74$$

and the new tangential control hole area would be,

$$A_c = \frac{0.67}{0.90} A_{c_o}$$

$$= 0.74\ A_{c_o}$$

That is, the new control holes would be 86% of the diameter of the original holes.

The P_c/P_s ratio would be reduced if the turndown were kept constant by reshaping the tangential holes to increase the orifice coefficient.

$$\frac{P_c}{P_s} = \left[\frac{Q_{s_o}}{Q_{c_d}} \frac{C_{D_o}}{C_D} \frac{M_{c_o}}{M_{s_o}}\right]^2 + 1$$

$$= \left[5 \left(\frac{0.67}{0.90}\right) 0.089\right]^2 + 1$$

$$= 1.11$$

Therefore, it is concluded that a substantial increase in the hydraulic vortex valve performance can be realized by maximizing the tangential hole orifice coefficient.

APPENDIX E

DYNAMIC ANALYSIS OF REVERSED-FLOW FLAPPER-NOZZLE PILOT STAGE

A complete analytical model of the reversed-flow flapper-nozzle system is needed. The results of this analysis could be correlated with the experimental data recorded to date and could be utilized to formulate new pilot stage design criteria. A preliminary analysis was performed during the course of the present program in order to obtain a "first look" at conditions for stability.

The pilot stage configuration is shown schematically in Figure 130. As explained previously, supply pressure is admitted to the flapper-nozzle cavity. Control flow to the vortex valve power stage exits from the cavity through the flapper nozzle. The pressure differential across the flapper varies in such a way that the resultant force on the flapper is in the direction of flapper motion. A positive rate auxiliary spring is added to the system, so that when combined with this negative hydraulic rate, the system is statically stable. The torque motor is sized to drive this small net positive spring rate load.

In order to derive the differential equations of the pilot stage system, the mechanical analogy of Figure 131 is utilized. The symbols used in Figure 131 are defined in the attached nomenclature. For simplicity, the derivation of the equations assumes linear motions only. The negative hydraulic rate, K_3, is shown as a linear spring. Experimental determination of the flapper forces, as shown in Figure 132, reveals that the curves are reasonably linear.

The differential equation relating the input force, F_i, and the flapper stroke, X_o, is shown in Figure 133. A block diagram representation of the system is also shown in Figure 133. The block diagram also includes an external disturbance at X_o, to investigate the unstable condition, which has been encountered with the torque motor de-energized.

The differential equation of the system indicates that with no magnetic damping ($B_m = 0$), the coefficients of s^3 and s will vanish. The system is unstable under these conditions. If damping is added to the output flapper, this will be included in the s term of the characteristic equation. Therefore, if there is no magnetic damping, no amount of damping on the flapper will produce a stable system since the s^3 term will still be zero. Finally, from the coefficient of s, it can be seen that, since K_3 is negative, K_2 must always be greater than K_3 for the system to remain stable.

This preliminary analysis of the system characteristic equation has indicated some of the conditions for instability in the present pilot stage. An analog computer analysis must be formulated with actual physical data. The results must be correlated with experimental observations in order to verify the mathematical model.

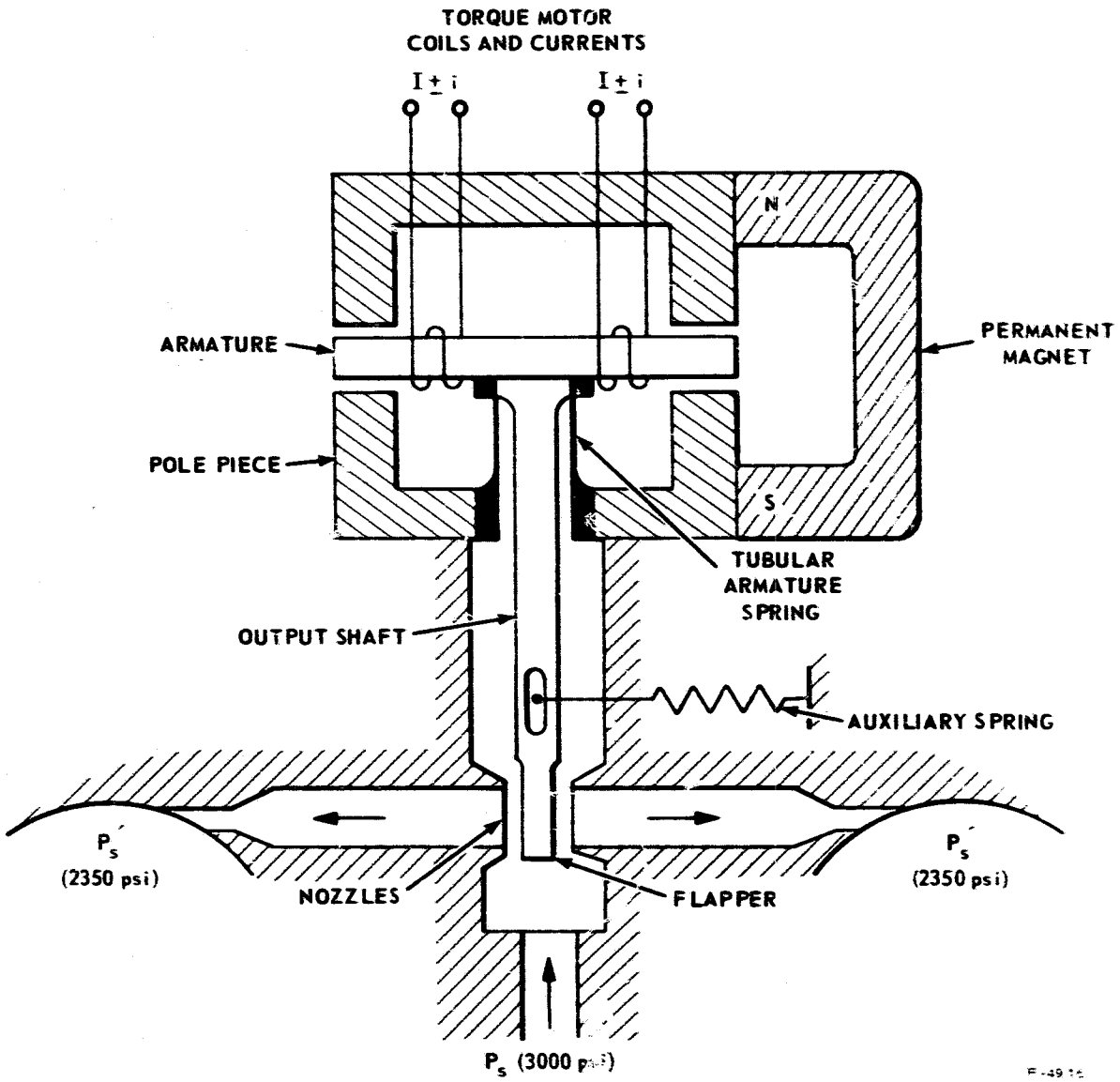

Figure 130 - Schematic of Model 2834 Vortex Servovalve Pilot Stage

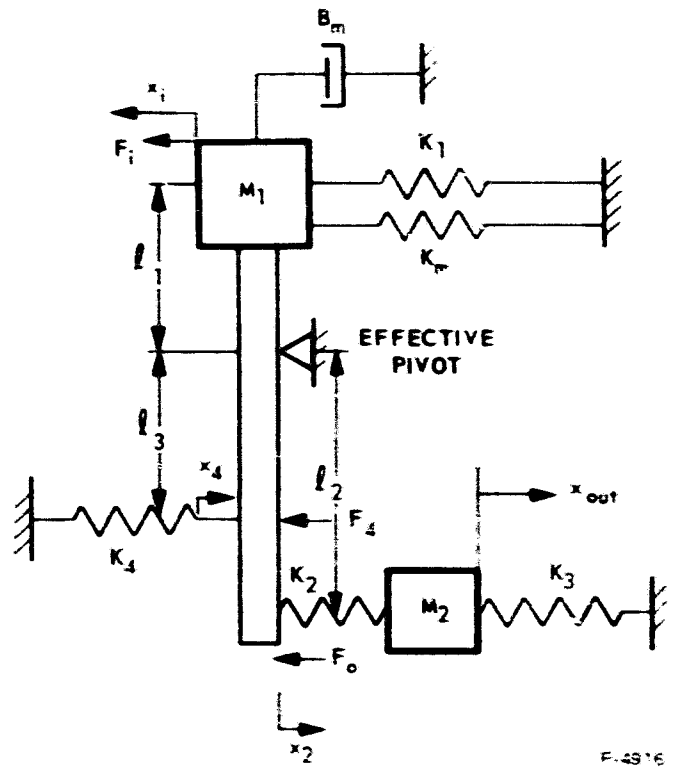

Figure 131 - Mechanical Analogy of Reversed-Flow Flapper-Nozzle Pilot Stage

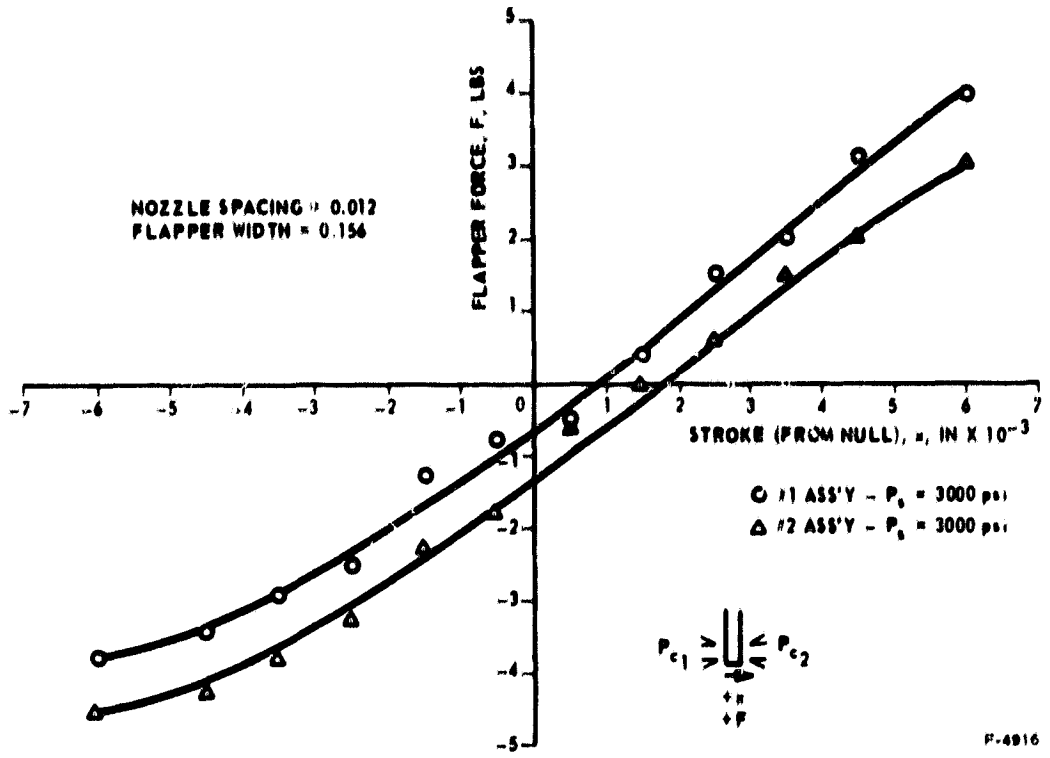

Figure 132 - Flapper Force Versus Stroke for Reversed-Flow Flapper-Nozzle Pilot Stage

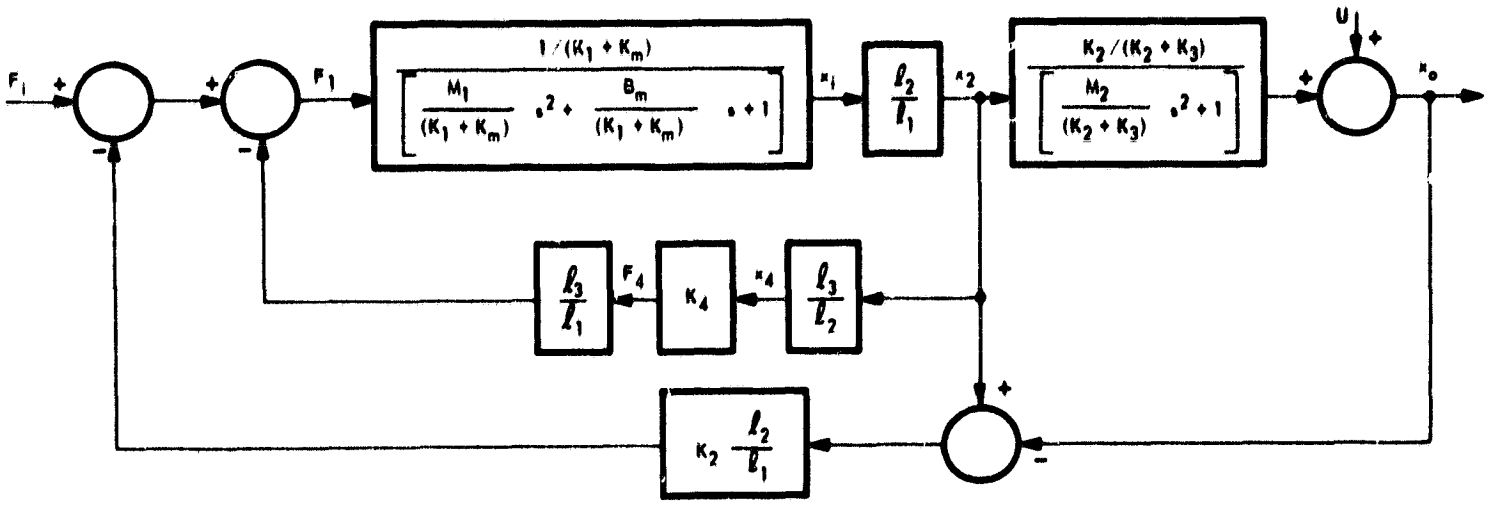

$$F_i = \left\{ \left[\left(\frac{M_1 M_2}{K_2} \right) \frac{\ell_1}{\ell_2} \right] s^4 + \left[\left(\frac{M_2 B_m}{K_2} \right) \frac{\ell_1}{\ell_2} \right] s^3 + \left[\frac{M_1 (K_2 + K_3)\ \ell_1^2 + M_2 (K_1 + K_m)\ \ell_1^2 + (M_2 K_2)\ \ell_2^2 + (M_2 K_4)\ \ell_3^2}{K_2 (\ell_1\ \ell_2)} \right] s^2 \right.$$

$$\left. + \left[B_m \left(\frac{K_2 + K_3}{K_2} \right) \frac{\ell_1}{\ell_2} \right] s + \left[\frac{(K_1 + K_m)(K_2 + K_3)\ \ell_1^2 + (K_2 K_3)\ \ell_2^2 + (K_4)(K_2 + K_3)\ \ell_3^2}{K_2 (\ell_1\ \ell_2)} \right] \right\} x_o$$

Figure 133 - Block Diagram Representation of the Reversed-Flow Flapper-Nozzle Pilot Stage

The effect of parameter variations can be readily observed on the computer. Thus, the required torque motor static and dynamic characteristics can be determined and the correct torque motors specified.

Nomenclature

B_m	-	Torque motor magnetic damping coefficient	lb-sec/in
F_i	-	Force developed by torque motor	lb
F_o	-	Reaction force on armature due to flapper mass, flapper spring rate and hydraulic reaction forces on flapper	lb
F_1	-	Reaction force at torque motor armature due to armature mass, spring rate and magnetic damping	lb
F_4	-	Reaction force on flapper due to auxiliary spring	lb
K_m	-	Torque motor spring rate due to armature displacement (negative)	lb/in
K_1	-	Tubular armature spring rate	lb/in
K_2	-	Output shaft rate	lb/in
K_3	-	Hydraulic reaction equivalent spring rate on flapper (negative)	lb/in
K_4	-	Auxiliary spring rate	lb/in
ℓ_1	-	Distance from armature flapper pivot to centerline of armature	in.
ℓ_2	-	Distance from armature flapper pivot to nozzle centerline	in.
ℓ_3	-	Distance from armature flapper pivot to auxiliary spring centerline	in.
M_1	-	Effective mass of armature	$lb\text{-}sec^2/in$
M_2	-	Effective mass of output shaft and flapper	$lb\text{-}sec^2/in$
s	-	Laplace Operator (complex)	sec^{-1}

U	-	Flapper displacement due to dynamic flow disturbance	in.
x_1	-	Displacement of torque-motor armature	in.
x_o	-	Displacement of flapper	in.
x_2	-	Displacement of torque-motor armature referred to the flapper	in.
x_4	-	Displacement of auxiliary spring	in.

APPENDIX F

GLOSSARY OF SYMBOLS

A_{ann} - Vortex valve annulus area, in^2

A_c - Vortex valve control port area, in^2

A_o - Vortex valve outlet hole area, in^2

C_{d_c} - Control port flow coefficient, dimensionless

C_{d_o} - Outlet hole flow coefficient, dimensionless

D_B - Vortex valve button diameter, in.

D_c - Vortex valve control port diameter, in.

D_{ch} - Vortex valve chamber diameter, in.

D_o - Vortex valve outlet hole diameter, in.

D_R - Flow receiver diameter, in.

f - Frequency, cps

F - Force, lb

K - Spring rate, lb/in

L_R - Flow receiver spacing, in.

L_1 - Vortex valve chamber spacing, in.

m_c - Control flow momentum, lb-sec

m_s - Supply flow momentum, lb-sec

P_c - Vortex valve control pressure, psi

P_o - Vent pressure, psi

P_R - Flow receiver pressure, psi

P_s - Vortex valve supply pressure, psi

Q_c - Vortex valve control flow, in^3/sec or gal/min

Q_o, Q_T - Vortex valve output flow, in^3/sec or gal/min

Q_R - Flow receiver flow, in^3/sec or gal/min

Q_s - Vortex valve supply flow, in^3/sec or gal/min

$Q_{s_{max}}$ - Maximum vortex valve supply flow, in^3/sec or gal/min

x - Torque motor flapper stroke, in.

Δi - Torque motor differential current, ma

ΔP - Pressure differential, psi